

Injury Risk Functions Based on Responses of Population-Based Finite Element Models:
Application to Femurs under Dynamic Loading

A Dissertation

Presented to
the faculty of the School of Engineering and Applied Science
University of Virginia

in partial fulfillment
of the requirements for the degree

Doctor of Philosophy

by

Gwansik Park

May

2017

APPROVAL SHEET

The dissertation
is submitted in partial fulfillment of the requirements
for the degree of
Doctor of Philosophy

Gouansik Park

AUTHOR

The dissertation has been read and approved by the examining committee:

Jeff R. Crandall

Advisor

Richard Kent

Jason R. Kerrigan

Matthew B. Panzer

Seth R. Yarboro

Accepted for the School of Engineering and Applied Science:



Craig H. Benson, Dean, School of Engineering and Applied Science

May
2017

© Copyright by
Gwansik Park
All rights reserved
May 2017

ABSTRACT

A fundamental purpose of biomechanical testing and the field of injury biomechanics is the development of injury risk functions (IRFs). Up to the present, IRFs have usually been developed in a “top-down” approach by relating injury outcomes in cadaveric tests to dummy measures in matched crash conditions. While IRFs developed in the top-down approach have been commonly used in the automobile safety field, future initiatives for the development of IRFs may need to address 1) the limited number of cadaveric specimens available for testing and 2) the limited ability of scaling techniques to capture the complexity of the human body.

The central idea of this study is that population-based finite element (FE) models, whose input distributions are based on subject-specific finite element (SS-FE) and statistical modeling approaches, may hold the key to overcoming the challenges facing the development of IRFs. SS-FE models, incorporating specific skeletal geometry of specimens into the models, help researchers verify the predictive capability of FE models with given material properties and their parameter distributions by minimizing the geometric error between cadaveric specimens and the models. If accurate subject-specific modeling technique can be developed and validated, this may facilitate the development of statistical models that can analyze geometric variations across the population. In the end, assigning probabilistic distributions as input variables instead of a single value allows generation of population-based FE models which captures variabilities across the population. Among other applications, these population-based FE models could be utilized to develop IRFs whose range of variabilities are informed by observations from the population-based

FE model responses. In other words, the population-based FE modeling approach allows us to develop the IRFs in a “bottom-up” manner rather using the current “top-down” approach.

The goal of this dissertation was to explore a framework for developing IRFs in a “bottom-up” approach based on the responses of parametrically-variable finite element (FE) models representing exemplar populations. To illustrate the process, first, subject-specific FE models of human femurs were developed and validated. Next, principal component analysis and regression were used to identify parametric geometric descriptors of the human femur and the distribution of those factors for three target occupant sizes (5th, 50th, and 95th percentile males). Also, distributions of material parameters of cortical bone were obtained using regression analysis based on the literature for three target occupant ages (25, 50, and 75 years). A Monte-Carlo method was then implemented to generate populations of FE models of the femur for target occupant sizes and ages. In total, 100 femur models incorporating the variation in the population of interest were generated for each target occupant and simulations were conducted with each of these models under three-point dynamic (1.5m/s) bending. In the end, model-based IRFs were developed using logistic regression analysis, based on the 500,000 observations (each 100 femur models with 5,000 ultimate strains) of moment-at-fracture in the population-simulation dataset for each target occupant. In addition, to exemplify an application of the proposed framework, this dissertation developed a closed-form of model-based IRFs for the human femur under a frontal oblique car crash test, whose loading conditions were analyzed from the publicly-available NHTSA crash test database, using survival analysis with a multivariate logistic model based on 27 million observations of moment-at-fracture in the population-simulation dataset.

The framework proposed in this dissertation would be beneficial for developing IRFs in a bottom-up manner, whose range of variabilities are informed by the observations of moment-at-fracture in population-based FE model responses. This method would be able to address challenges facing the current development procedure of IRFs for diverse or specialized populations: specifically, this method mitigates the uncertainties in applying empirical scaling and may improve IRF fidelity when a limited number of experimental specimens are available.

To my first, my last, my everything “Eunyoung Hwang”

TABLE OF CONTENTS

ABSTRACT.....	i
TABLE OF FIGURES.....	viii
TABLE OF TABLES.....	xiii
CHAPTER1: INTRODUCTION.....	2
Background.....	2
Motivation.....	5
Research Goal and Overview.....	12
CHAPTER 2: DEVELOPMENT OF SUBJECT-SPECIFIC FINITE ELEMENT MODELS OF THE FEMURS.....	14
2.1 Introduction.....	14
2.2 Methods.....	16
2.3 Results.....	23
2.4 Discussion.....	24
CHAPTER 3: VALIDATION OF SUBJECT-SPECIFIC FINITE ELEMENT MODELS.....	30
3.1 Introduction.....	30
3.2 Methods.....	33
3.3 Results.....	39
3.4 Discussion.....	44
CHAPTER 4: STATISTICAL SHAPE ANALYSIS.....	51
4.1 Introduction.....	51
4.2 Methods.....	53

4.3 Results.....	57
4.4 Discussion.....	62
CHAPTER 5: GENERATION OF POPULATION-BASED FINITE ELEMENT MODELS AND INJURY RISK FUNCTIONS.....	65
5.1 Introduction.....	65
5.2 Methods.....	67
5.3 Results.....	71
5.4 Discussion.....	77
CHAPTER 6: A CLOSED-FORM OF MODEL-BASED INJURY RISK FUNCTIONS FOR APPLICATION TO FEMURS OF ANTHROPOMETRIC TEST DEVICES UNDER A FRONTAL OBLIQUE CAR CRASH TEST	82
6.1 Introduction.....	82
6.2 Methods.....	84
6.3 Results.....	87
6.4 Discussion.....	92
CHAPTER 7: CONCLUSIONS	95
7.1 Concluding Remarks.....	95
7.2 Contributions.....	98
7.3 Future Research Directions and Limitations.....	100
REFERENCES	102
APPENDIX A: BIOMECHANIAL TEST DATA	106
APPENDIX B: EVALUATION OF ACCURACY MORPHED FEMUR FE MODEL	113

APPENDIX C: MATERIAL PARAMETER IDENTIFICATION	150
APPENDIX D: DISTRIBUTIONS FOR POPULATION-BASED FE MODELS	153
APPENDIX E: DEVELOPED VPM AND INJURY RISK FUNCTIONS.....	163
APPENDIX F: CRASH DATABASE.....	198

TABLE OF FIGURES

Figure 1 Motor vehicle crash fatalities (left axis) and fatality rate per 100K registered vehicles (right axis) from 1966 to 2013	2
Figure 2 Anthropomorphic test device (ATD) – Hybrid III series (left) and ATD used in car crash test (right).....	3
Figure 3 Example of the assessment of injury using IRFs: 10kN of the peak femur load represents a 35% risk of sustaining an AIS 2+ injury	4
Figure 4 Current Procedure for Developing Injury Risk Functions	5
Figure 5 Geometrically similar objects; in the above cases, the model ratio is ½.....	7
Figure 6 Schematic comparison between the top-down and the bottom-up approaches for developing IRFs	9
Figure 7 Development of parametric statistical FE human body models and application of model-based IRF	11
Figure 8 Overview of the dissertation.....	12
Figure 9 Subject-specific FE in orthopedic biomechanics: proximal femur (left) (Nishiyama et al., 2013), lumbar spine (right) (Giambini et al., 2015).....	14
Figure 10 Subject-specific FE models for whole human body: 50 th percentile male (Jolivet et al., 2015) (left), 95 th percentile male (Vavalle et al., 2014) (right)	15
Figure 11 Steps to develop the SS-FE models of the femurs	16
Figure 12 Developed template FE model	17
Figure 13 Five femur FE models with different number and shape of elements for mesh sensitivity analysis.....	19

Figure 14 pre-defined anatomical patches to select control points for the proximal and the distal regions.....	21
Figure 15 Manipulation of corresponding control points using parametrization and re-parametrization	22
Figure 16 comparison of the geometry between target subject and developed SS-FE models and control points used for the morphing for one of the specimens (F2012-M01) as an example	24
Figure 17 Large geometric error in proximal and distal region using the limited number of control points represented by anatomical landmarks: (Klein et al., 2015) (left), (Park et al., 2017) (right)	26
Figure 18 Template FE femur model used (left) and accurate morphed FE model (middle) in Bryan et al. (2010). Morphed surface geometry in surface registration in this study (right)	27
Figure 19 difficulty in finding corresponding points between target and template geometries ...	28
Figure 20 Example of 3D parameterization of non-spherical topology using sphere (Davies, 2002)	28
Figure 21 Biomechanical tests (left) and FE simulations (right): three-point bending test conducted by Forman et al. (2012a) (top) and by Funk et al. (2004) (bottom).....	34
Figure 22 Schematic diagram for evaluation of predictive capability of FE model according to model complexity.....	38
Figure 23 Evaluation of scaling techniques and contribution of geometric variabilities to structural response (left) and fracture response (right) variations	39
Figure 24 Comparison of impact force histories between test, SS-FE and SS-FE models with a material fit for femur specimens of Forman et al. (2012a). X indicates the femur fracture	40

Figure 25 Comparison of impact force histories between test, SS-FE and SS-FE models with a material fit for femur specimens of Funk et al. (2004). X indicates the femur fracture	42
Figure 26 Comparison of material parameters (top) and distributions of the material parameters for three target occupant ages: coupon tests from literature (circle) and material fit using SS-FE (triangle).....	43
Figure 27 Distributions of the Elastic modulus (left), ultimate strain (middle), and yield stress (right)	43
Figure 28 Violation of assumption of geometric similarity: the relationship between the normalized length and normalized square root area (left) and variation of area along the longitudinal femur direction (right)	47
Figure 29 Distribution of height (left), weight (middle), and age (right) of the training set	54
Figure 30 Landmarks points used in PCA	58
Figure 31 percentage of shape variance: first 13 modes explains 95% of shape variance	59
Figure 32 First three principal modes: 1 st mode=size of femur (left), 2 nd mode=slenderness of femur(middle), 3 rd mode= curvature of the shaft in the anterior-posterior direction (right),	59
Figure 33 Reconstruction errors in relation to the different number of principal components included in PCA-FE model: geometric error (left), structural response (middle), and fracture force difference (right). The number in % indicates the percentage of variance explained by the principal components	60
Figure 34 geometric reconstruction error: RMS error vs. percentage of variance (top) and RMS error outer surface of F2004-M03 as an example (bottom).....	61

Figure 35 regression analysis for the geometric descriptors (left) and the distributions of the geometric descriptors (right) for three occupant sizes: example of first three factors – 1 st GD (top), 2 nd GD (middle), and 3 rd GD (bottom).....	61
Figure 36 boundary conditions for the FE simulations.....	68
Figure 37 histograms of the principle scores of the GDs.....	71
Figure 38 histograms of the input material parameters	72
Figure 39 Model-based Injury risk functions for femurs under dynamic pure bending (lateral-medial direction)	73
Figure 40 Compare to the scared IRF.....	74
Figure 41 cross-section of intertrochanteric and femoral shaft of VPM #1 (M05) (left) and VPM#100 (right).....	75
Figure 42 Comparing cross-sectional areas of the VPMs to those from 13,615 patients in NHANES	75
Figure 43 Comparison of the model-based IRF to the IRF developed in a top-down approach ..	76
Figure 44 Convergence test: the principal scores of GD, elastic modulus, and yield stress (left) and ultimate strain (right)	76
Figure 45 Correlation analysis between material parameters.....	81
Figure 46 sign convention for the femur load cell of Hybrid III	84
Figure 47 Biomechanical tests (left) and FE simulations (right) for combined loading test conducted by Ivarsson et al. (2009)	85
Figure 48 femur loads during car crash: forces (upper) and moments (lower)	87
Figure 49 Accuracy of SS-FE models for the specimens of Ivarsson et al. (2009).....	88

Figure 50 Comparison of impact force histories between test, SS-FE and SS-FE models with a material fit for femur specimens of Ivarsson et al. (2009). X indicates the femur fracture..... 89

Figure 51 comparison of material parameters: coupon tests from literature (circle) and material fit using SS-FE (triangle). Elastic modulus (left) and ultimate strain (right) 91

Figure 52 Example of model-based IRF for different covariates: baseline case (M50, 50years, 0kN axial load, lateral-medial direction) 92

TABLE OF TABLES

Table 1 Element quality check for developed template femur FE model.....	18
Table 2 Summary of mesh sensitivity analysis using five FE models with different number of elements	19
Table 3 Summary of the geometric accuracy and the element quality of developed SS-FE models	23
Table 4 Common cortical bone material parameters for the SS-FE models identified by parametric study	36
Table 5 the level of model complexity defined in this study	37

CHAPTER1: INTRODUCTION

Background

Advancement in Occupant Safety under Car Crashes

A recent investigation of the fatality rate (per 100K registered vehicles) in motor vehicle crashes shows that the rate has declined by more than 75% since 1975 (Figure 1) (NHTSA, 2013). One of the main contributing factors to this remarkable achievement is increased knowledge of injury biomechanics, resulting in the development of injury countermeasures, changes in the vehicle structures and design, and incorporation of automobile safety standards.

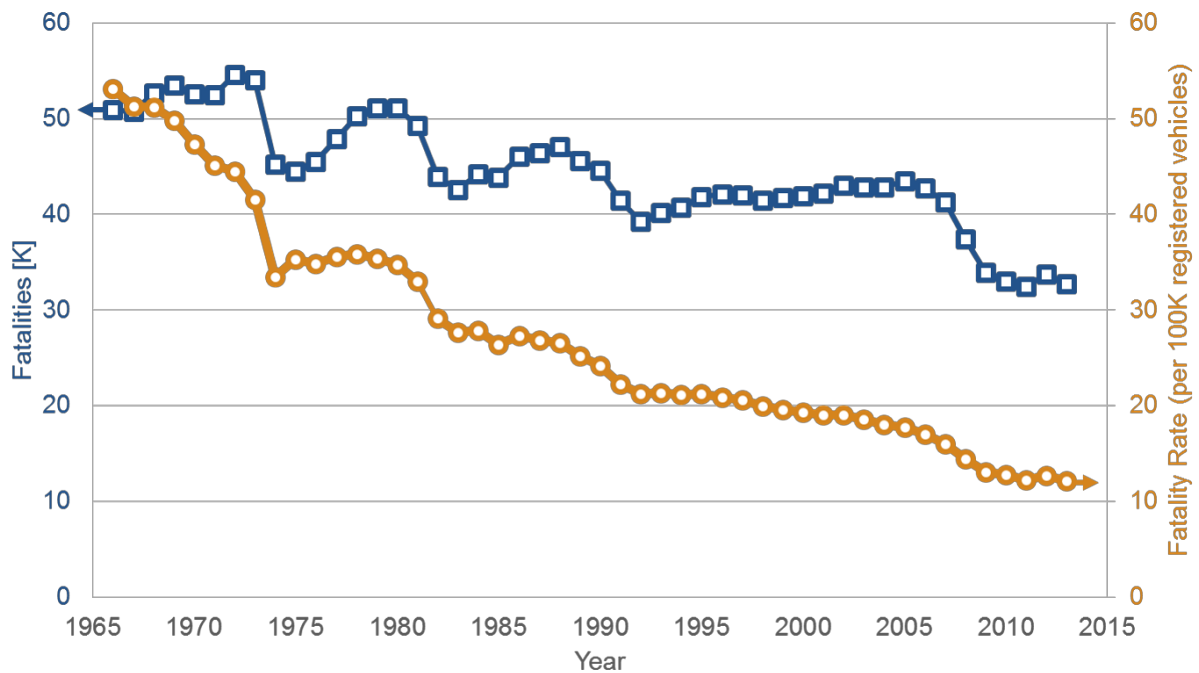


Figure 1 Motor vehicle crash fatalities (left axis) and fatality rate per 100K registered vehicles (right axis) from 1966 to 2013

Injury Biomechanics and Anthropomorphic Test Devices (ATDs)

Injury biomechanics applies the principles of mechanics to the analysis of human response with the goal of identifying injury mechanism and tolerance (Crandall et al., 2011). Given an identified injury mechanism and tolerance, anthropomorphic test devices (ATDs) have been developed to be used for regulatory or consumer tests in the automobile safety field (Figure 2). The ATDs are synthesized mechanical devices - often called “dummies” - which have a simplified anatomical structure targeted at replicating the occupant responses under car crash conditions. Those ATDs enable engineers to develop effective injury countermeasures and to change the vehicle structures. The 50th percentile male ATD, nominally representing the average adult male, has served as the standard size ATD (Crandall et al., 2011). In addition to the standard size ATD, various sizes of ATDs have been developed to cover the anthropometric variability in size and gender of the population (Figure 2). Although ATDs play an important role in the advancement of automobile safety, they do not have the capability to assess failure directly. Rather, ATDs require the use of injury risk functions (IRFs) to predict the likelihood of injury using recorded measurements, such as force, acceleration, and deflection.

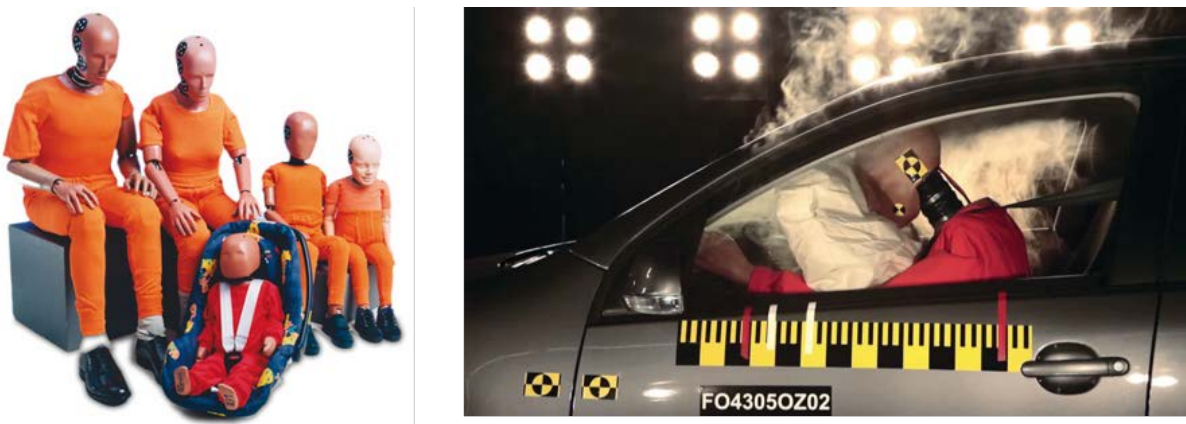


Figure 2 Anthropomorphic test device (ATD) – Hybrid III series (left) and ATD used in car crash test (right)

Injury Risk Functions (IRFs)

A fundamental purpose of biomechanical testing and the field of injury biomechanics is the development of risk functions (Kent & Funk, 2004). These IRFs are generally expressed as probability curves, rather than absolute thresholds or limits, since the likelihood of being injured varies by individual and are dependent on age, gender, physiologic condition, and other factors. (Crandall et al., 2011). For example, if 10kN of the peak femur axial load is recorded from a Hybrid III 50th percentile male dummy during a crash test, it represents a 35% risk of sustaining an AIS 2+ injury according to the injury risk function proposed for that dummy (Eppinger et al., 1999) (Figure 3). Since the assessment of injury using ATDs highly relies on which IRFs were being used, the importance of IRFs should not be underestimated.

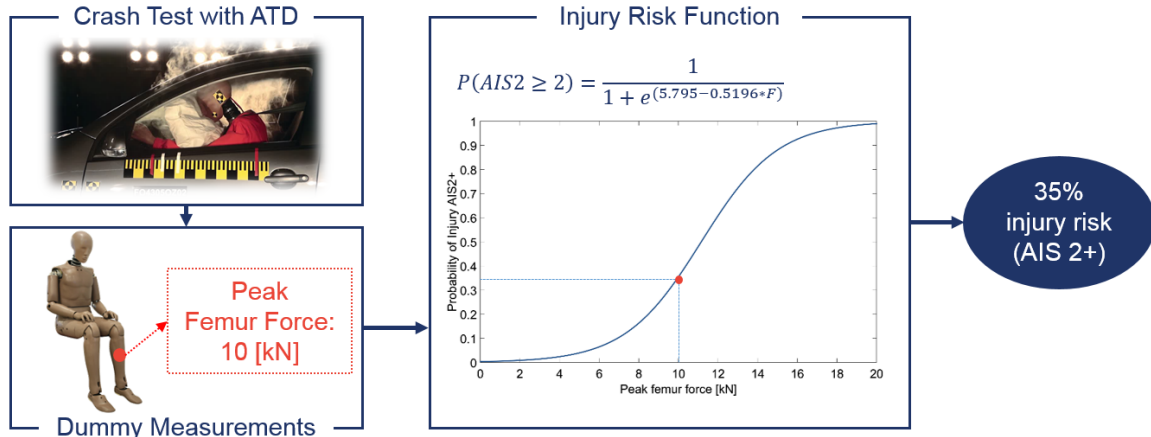


Figure 3 Example of the assessment of injury using IRFs: 10kN of the peak femur load represents a 35% risk of sustaining an AIS 2+ injury

The conventional procedure for the development of IRFs is shown in Figure 4. The first step of the development is the biomechanical tests using surrogates (mostly the Post-Mortem Human Surrogates (PMHS) or specimens from the PMHS) subjected to loading conditions comparable to

an occupant in car crashes to record mechanical responses (such as force, accelerations, and deflection, etc.) and to observe injuries from them. After conducting the biomechanical tests, the responses of each specimen are generally normalized to standard size subject responses to compensate for the anthropometric differences using scaling techniques. Usually, peak values of the measured responses are used as predictors for IRFs. Finally, IRFs are generated using regression or survival analysis as a function of the predictor. Some IRFs are developed with consideration of specimen characteristics (such as age, height, or weight, etc.) as covariates.

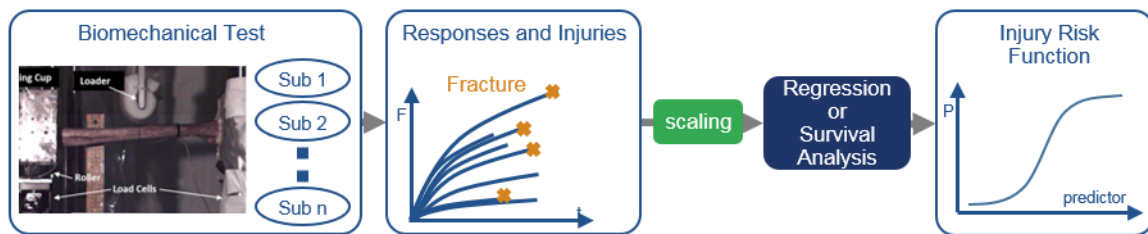


Figure 4 Current Procedure for Developing Injury Risk Functions

Motivation

While IRFs for the application to the ATDs have been developed and widely used in the automobile safety field, there are some challenges that need to be addressed in the current development procedure of IRFs.

Challenges in Development of IRFs using Current Procedure

Up to the present, IRFs have usually been developed in a “top-down” approach by relating injury occurrence in cadaveric tests to dummy measures in matched crash conditions (Forman et al., 2012b). The usage of a top-down approach stems from a lack of knowledge of the relationship

between the human variabilities and the variation of injury outcome. The variabilities observed in the human population are the root cause of the variation of injury outcome between individuals. However, researchers usually do not have a clear understanding of the relationship between the variabilities and the injury outcome variation due to the complexity of the human body. Thus, researchers observe the injury outcome first from biomechanical tests using a number of specimens and apply probabilistic analysis to come up with IRFs. In other words, the human variabilities have been considered an “uncontrollable” factor.

Scaling techniques are usually applied to compensate for anthropometric variability (which is likely to affect the injury outcome variation) between specimens. One of the main challenges in the development of IRFs in the top-down approach involves the usage these scaling techniques. The responses and injuries from biomechanical test data usually have a large variation due to the complexity of the human body, including anthropometric differences, local geometric differences, and other physical characteristics of specimens used in tests. Thus, various scaling techniques are sometimes used to normalize subject responses to estimate the response of a target subject size prior to developing injury risk functions. At present, a mass-based scaling technique is the most commonly used method in the field of injury biomechanics. This scaling technique normalizes human subject responses based on the mass ratio between the subjects assuming a constant density and modulus of elasticity among subjects between the scaled objects (Eppinger et al., 1984). Recently, a structure-based scaling technique has also been proposed, which assumes additional structural similarity by using idealized mechanical models to account for specific anatomy and expected loading condition (Nie et al., 2016). Although scaling techniques are applied in other engineering fields (such as ships and airplanes), the validity and effectiveness of those scaling

techniques for application to the field of injury biomechanics are still questionable (Moorhouse, 2013); Since scaling techniques represent complex human structure and composition using a limited number of parameters, such as stature or mass, based on the assumption of geometric similarity (Figure 5), they are limited in their ability to capture the effect of variabilities in human body that may affect the responses of a human under car crash conditions.

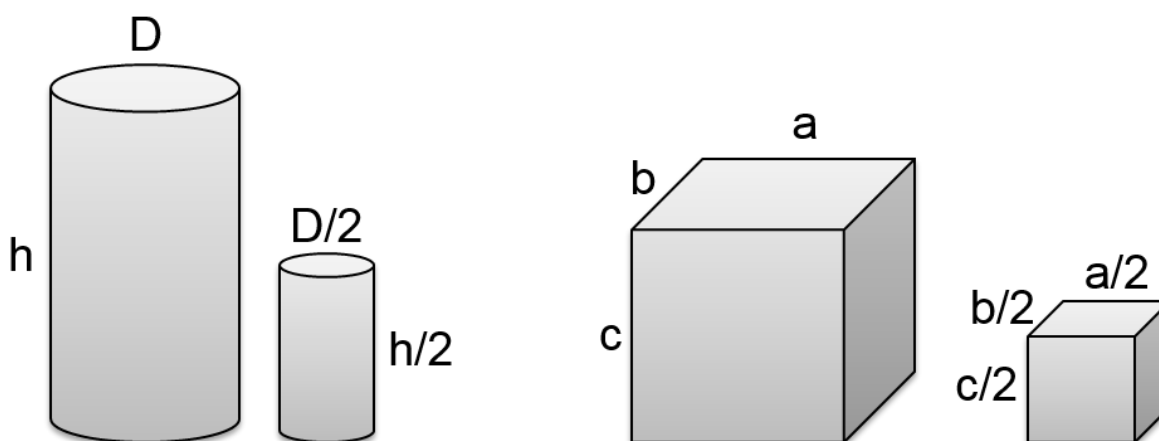


Figure 5 Geometrically similar objects; in the above cases, the model ratio is $1/2$.

Following the uncertainty of the scaling techniques, the limited number of biomechanical tests available for developing IRFs is another challenge that needs to be addressed. Since the development of IRFs relies on probabilistic analysis, increasing the number of specimens unequivocally improves the statistical power of the analysis. However, increasing the number of specimens is not easy with the usage of biological materials. Biomechanical tests are expensive, and it is hard to get specimens with particular characteristics, such as pediatric specimens or those with restricted anthropometry or age range; it may take years to get specimens with particular characteristics (Kent et al., 2011). Thus, the developed IRFs, so far, usually have large confidence intervals, which gives uncertainty bounds for the location of the true population parameter. Also,

the question of the required number of tests for generation of IRFs is largely unanswered (Cutcliffe et al., 2012).

Most of all, the uncertainty on scaling techniques and the limited number of specimens available are challenges intrinsic to the studying of the complex human body and the use of biological specimens, which may be difficult to overcome by just relying on the conventional top-down approach. Thus, there needs to be a consideration of new approaches to overcome the challenges facing the development of IRFs.

Central Idea of the Study

The central idea of this study is that population-based finite element (FE) models, whose input distributions are based on subject-specific finite element (SS-FE) and statistical modeling approaches, may hold the key to overcoming the challenges facing the development of IRFs. SS-FE models, incorporating specific skeletal geometry of specimens into the models, help researchers verify the predictive capability of FE models with given material properties and their parameter distributions by minimizing the geometric error between cadaveric specimens and the models. If accurate subject-specific modeling technique can be developed and validated, this may facilitate the development of statistical models that can analyze geometric variations across the population. In the end, assigning probabilistic distributions as input variables instead of a single value allows generation of population-based FE models which captures variabilities across the population. Since the population-based FE models incorporate the variabilities across the population, the usage of the population-based FE modeling approach makes human variability a “controllable” factor. Most of all, since the variabilities in the human body are incorporated in the

FE models, researchers no longer need to rely on scaling techniques to compensate for anthropometric differences between individuals. Among other applications, this approach could be utilized to develop IRFs whose range of variabilities are informed by the population-based FE model responses. In other words, the population-based FE modeling approaches allows us to develop the IRFs in a “bottom-up” manner rather using the current “top-down” approach (Figure 6).

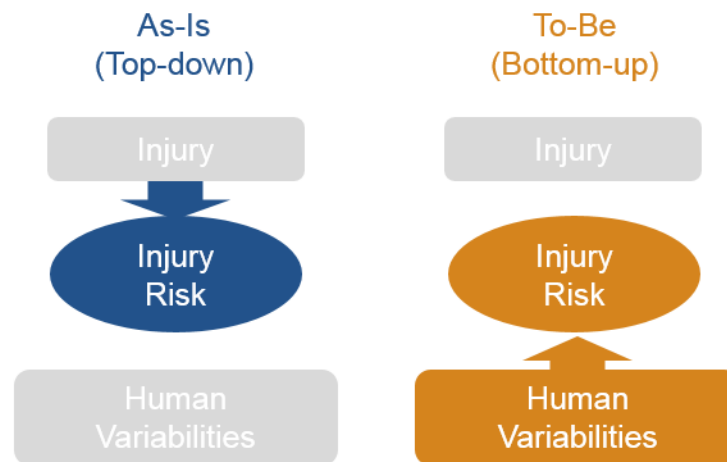


Figure 6 Schematic comparison between the top-down and the bottom-up approaches for developing IRFs

To identify the geometric variabilities in the human body, statistical shape analysis using a medical image database can be introduced. Statistical shape analysis has the capability to analyze the shape variabilities among specimens to find the reduced-parametric representation of the variabilities in a large number of data sets based on a dimensionality reduction analysis, such as principal component analysis (PCA). It allows researchers not only to identify important parameters representing the variabilities in the human body but also to increase the number of data analyzed;

in general, the availability of the medical image database is greater than the ability to obtain specimens for biomechanical tests resulting in improved statistical power.

Furthermore, the versatility of computational models can also enable engineers to develop IRFs with modified or additional loading conditions (such as different impact direction or speeds) for a given set of biomechanical test data within a range of conditions of which the models were validated. Designing a loading condition using a biological specimen to be comparable to that of an occupant in a car crash can be sometimes difficult due to the physical limitations of testing. If accurately validated computational models for that test condition are developed, the boundary conditions used in the test would be modified using the computational models.

To sum up, the usage of subject-specific and statistical FE modeling approaches will be beneficial to developing IRFs, especially, by generating IRFs in a “bottom-up” manner: this method will be able to 1) incorporate variabilities across the population by using probabilistic distributions as input variables in FE models, 2) eliminate the uncertainties of using scaling techniques, 3) increase the number of data using an available medical image database resulting in improved statistical power, and 4) modify or add loading conditions for a given set of biomechanical test data.

Application of Model-Based IRFs in conjunction with Parametric FE Human Body Models

The parametric FE human body models (HBMs) are being developed in an effort to represent a wider range of the occupant population with rapid development time (Schoell et al., 2015; Shi et al., 2014). These parametric FE HBMs are aimed at the substitution of current ATDs. Even with these parametric FE HBMs available in the near future, IRFs still need to be developed to consider the effect of local variabilities in the human body because the models are targeting to predict the

average response of given occupant characteristics - even within the same target occupant characteristics, the human responses must have variations. Ideally, development of population-based FE HBMs is the ultimate solution to represent all variabilities in the human body. However, it may not be feasible due to extremely increased computational costs for calculation. Hence, the parametric FE human body models in conjunction with IRFs developed in bottom-up approach would be an appropriate approach for assessment of injury risk of the human body under car crashes (Figure 7).

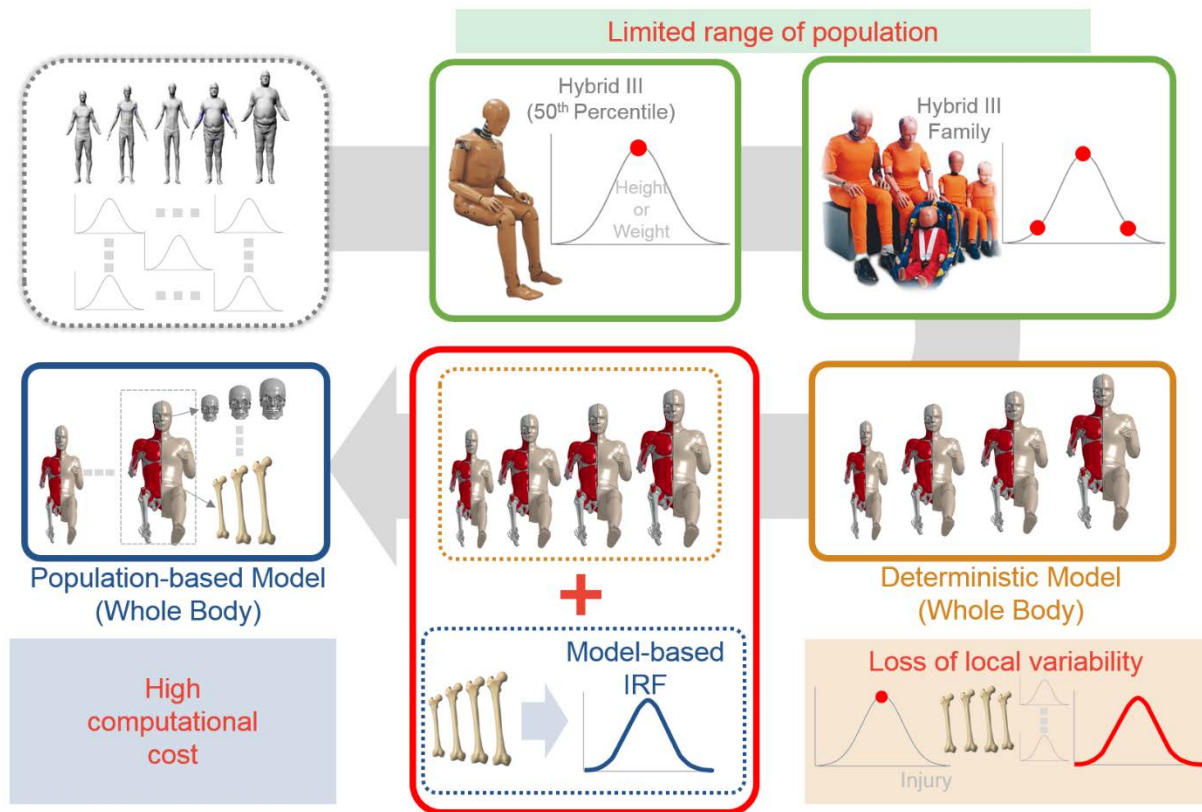


Figure 7 Development of parametric statistical FE human body models and application of model-based IRF

Research Goal and Overview

The goal of this dissertation was to explore a framework for developing injury risk functions (IRFs) in a bottom-up approach based on responses of population-based finite element models. To exemplify the proposed framework, this dissertation developed a closed-form of model-based IRFs for application to the femur of the ATDs under a frontal oblique car crash test. Figure 8 presents the overview of this dissertation.

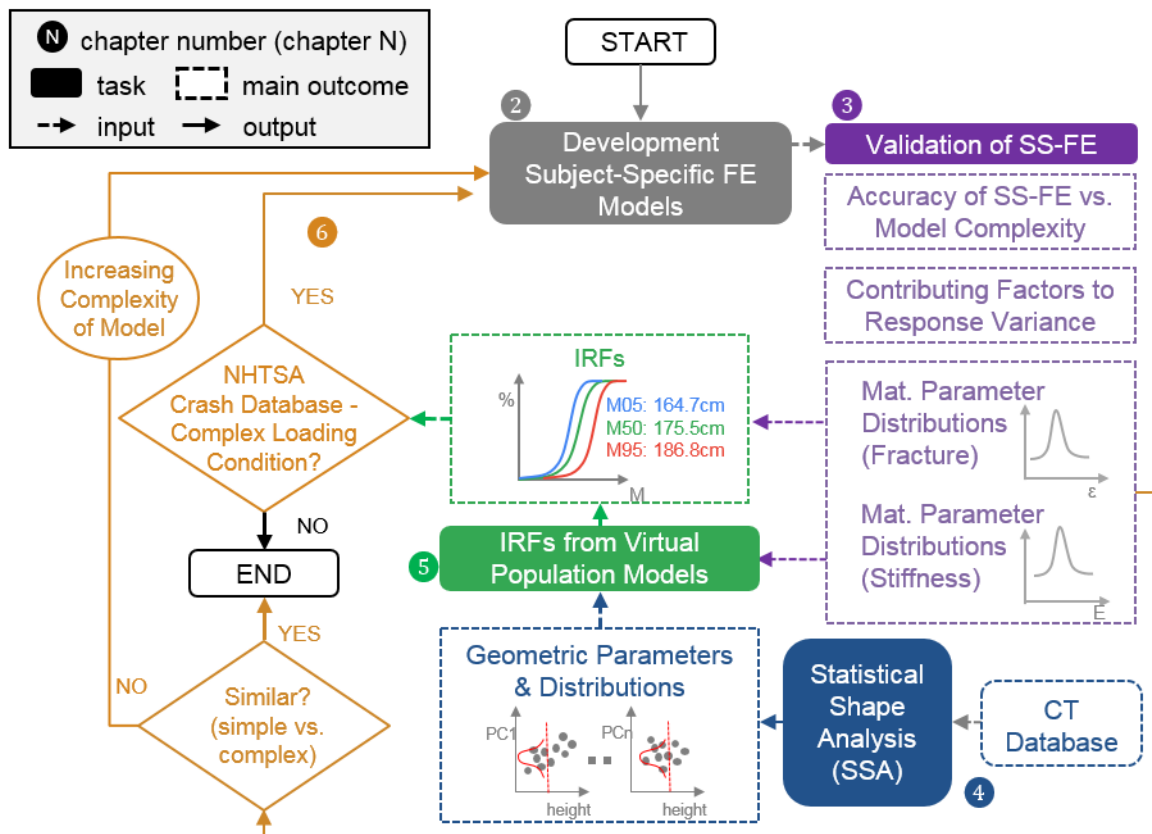


Figure 8 Overview of the dissertation

Chapter 2 developed a method for developing the subject-specific finite element (SS-FE) models of the femurs by transforming the template femur FE model to the target subject geometry from

medical images. Chapter 3 validated the SS-FE models developed in Chapter 2 by comparing the response of the models to those of cadaveric specimens obtained from the biomechanical tests. In addition, material parameters for individual SS-FE models was estimated and compared to those from the literature. Then, distributions of the material parameters for three target occupant ages (25, 50, and 75 years) were obtained using a regression analysis. Once the accurate SS-FE models were developed and validated from Chapter 3, Chapter 4 conducted principal component analysis (PCA) and regression to identify parametric geometric descriptors of the human femur, and the distribution of those factors for three target occupant sizes (5th, 50th, and 95th percentile males). A Monte-Carlo method was then implemented to generate populations of FE models of the femur for target occupants in Chapter 5. In total, 100 femur models incorporating the variation in the population of interest were generated for each target occupant. Simulations were then conducted with each of these models under 3-point dynamic bending. Model-based IRFs were then developed using logistic regression analysis, based on 500,000 observations (each 100 femur models with 5,000 ultimate strains) of the moment-at-fracture in the FE simulation. Finally, in Chapter 6, the framework proposed in this study was employed to develop a closed-form of model-based IRFs for application to the femurs of ATDs under a frontal oblique crash condition, whose loading conditions sustained were analyzed from the publicly-available NHTSA crash test database, using survival analysis with a multivariate logistic model using the occupant height, age, axial loading, and loading direction as covariates.

CHAPTER 2: DEVELOPMENT OF SUBJECT-SPECIFIC FINITE ELEMENT MODELS OF THE FEMURS

To develop population-based FE models, as the first step, the predictive capability of subject-specific FE (SS-FE) models for individual specimens needs to be ensured. The goal of this chapter is to construct a programmatic way of developing SS-FE models of the femur specimens using a template femur FE model and medical images, prior to evaluating the predictive capability of SS-FE models in Chapter 3.

2.1 Introduction

The development of SS-FE models has been studied primarily in the field of orthopedic biomechanics (Giambini et al., 2015, An et al., 2015; Helgason et al., 2008; Nishiyama et al., 2013) (Figure 9). The studies in the field of orthopedic biomechanics mainly focused on proximal femurs since they were attempting to predict the risk of fracture during falls or were interested in implant design. However, SS-FE models focusing on the femoral shaft, which is commonly injured in automobile collisions, have not been addressed.

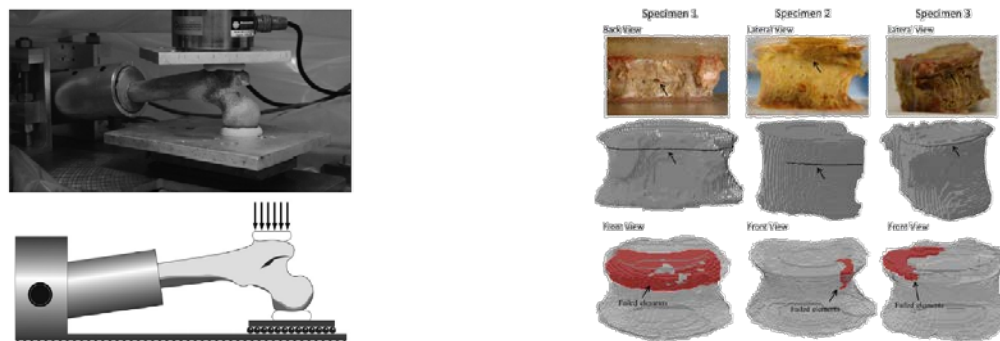


Figure 9 Subject-specific FE in orthopedic biomechanics: proximal femur (left) (Nishiyama et al., 2013), lumbar spine (right) (Giambini et al., 2015)

In the field of injury biomechanics, SS-FE modeling techniques have been studied focusing on the development of parametric FE human body models (HBMs) using morphing techniques in an effort to represent a wider range of the occupant population with rapid development time (Jolivet et al., 2015; Schoell et al., 2015; Vavalle et al., 2014) (Figure 10); these FE HBMs targeting to predict the average response of given target occupant characteristics, such as height, BMI, and age. Those studies have investigated a method to transform the geometry of template FE HBMs to target subject geometries on a whole-body level. Also, several researchers have demonstrated the benefit of using SS-FE models for the prediction of individual specimen responses in component level impact tests (Li et al., 2013; Untaroiu et al., 2008) and whole body level impact tests (Poulard et al., 2016); however, the number of specimens used in those studies was limited.

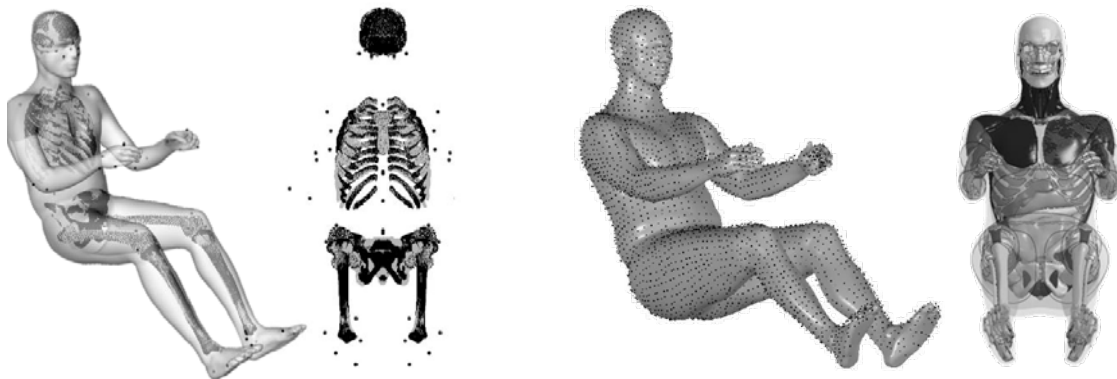


Figure 10 Subject-specific FE models for whole human body: 50th percentile male (Jolivet et al., 2015) (left), 95th percentile male (Vavalle et al., 2014) (right)

Also, in the morphing technique, digitizing the control points is extremely laborious and varies greatly between operators. Thus, there needs to be a consideration for developing a programmatic selection of control points. The goal of this task was to develop SS-FE models of the femur specimens with a programmatic selection of control points.

2.2 Methods

The SS-FE models of the femur specimens used in two biomechanical tests (Forman et al., 2012a; Funk et al., 2004) were developed using the computed tomography (CT) images recorded prior to the tests. In total, 20 specimens were introduced to develop SS-FE models (Table A1). The development of the SS-FE models of the femur specimens was divided into four steps: 1) model preparation, 2) registration, 3) selection of control points, and 4) morphing and evaluation (Figure 11).

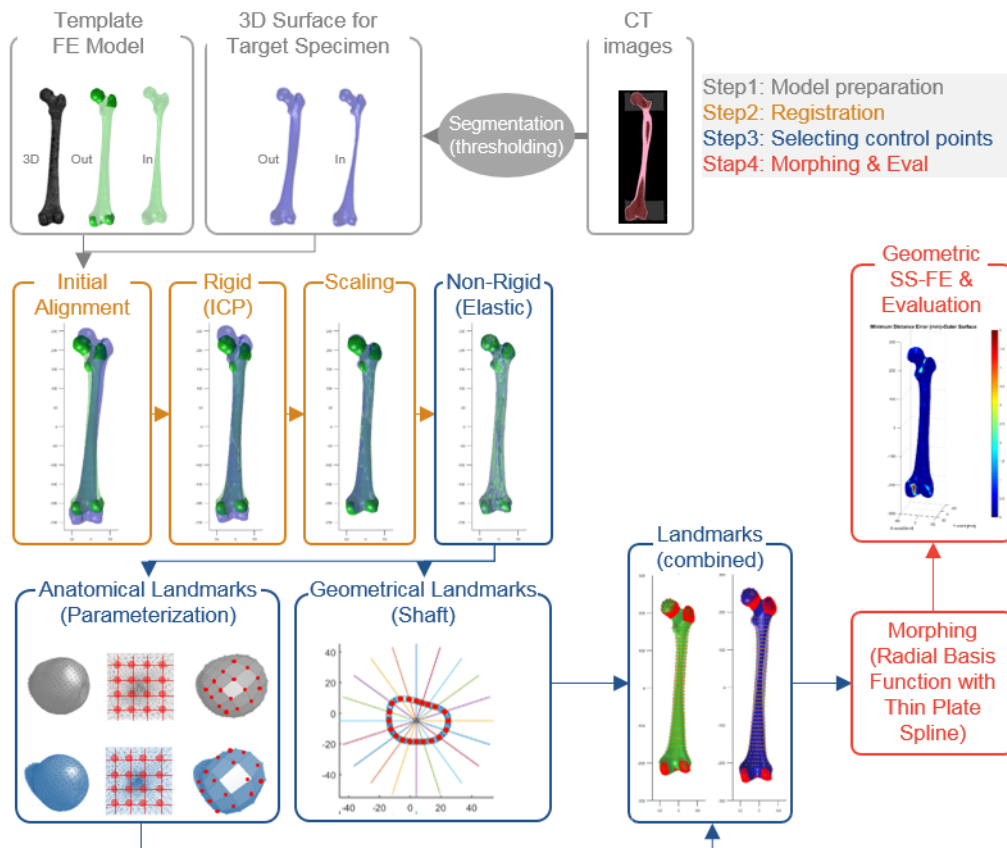


Figure 11 Steps to develop the SS-FE models of the femurs

The first step to developing the SS-FE models of the femurs was to develop the template FE model based on the femur geometry of the Global Human Body Model Consortium-owned GHBMC M50 Seated Occupant Model (GHBMC) (Figure 12).

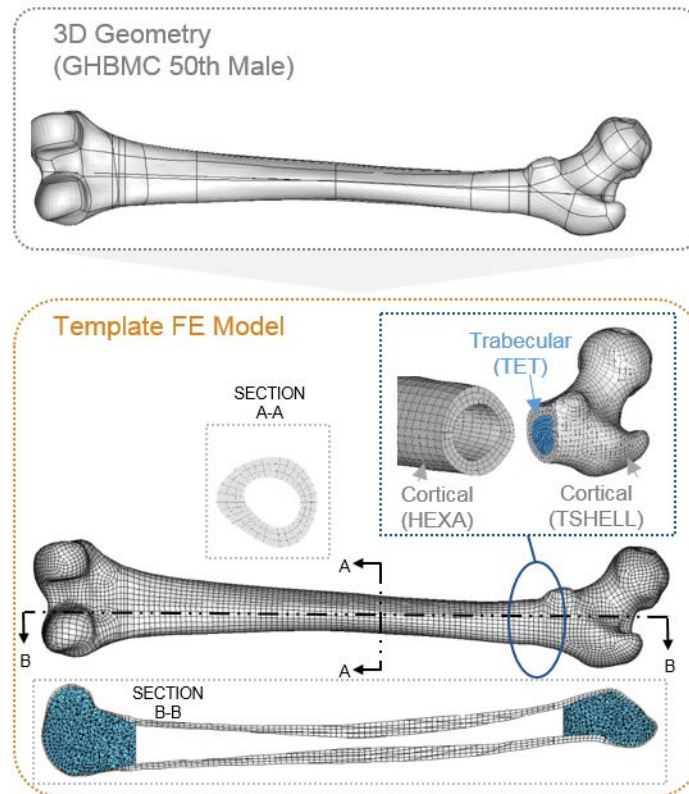


Figure 12 Developed template FE model

The femoral shaft region, mostly consisting of cortical bone, was modeled using hexahedral/pentahedral elements with three-layer along the radial direction. The proximal and distal parts of cortical bone, which were not regions of interest in this study due to the potting during the tests (Forman et al., 2012a; Funk et al., 2004), were modeled with thick shell elements with two-layer. The transition regions between the femoral shaft with three-layer elements and

proximal/distal end regions with two-layer were connected with pentahedral elements. Trabecular bones at a proximal and a distal region of the femur were modeled using tetrahedral elements, and the outside surface of the trabecular bone and the inside surface of cortical bone share the nodes. The femur FE models were covered by membrane elements, which were used as dummy elements only to calculate surface strain of the femurs. There are, in total, 14,926 hexa/pentahedral elements for cortical bone and 75,758 tetrahedral elements for trabecular bone. No element violated the criteria for element quality in the shaft region (Table 1).

Table 1 Element quality check for developed template femur FE model

Element Type	Standard	Failure Criteria	Total number of elements	Total number of elements not meeting criteria	Failure ratio [%]
HEX-PENTA (Femoral Shaft)	Jacobian	< 0.3	7328	0	0.0
	Warpage	> 50		0	0.0
	Aspect ratio	> 8		0	0.0
	Skew	> 70		0	0.0
HEX-PENTA (All)	Jacobian	< 0.3	14926	23	0.2
	Warpage	> 50		21	0.1
	Aspect ratio	> 8		650	4.4
	Skew	> 70		9	0.1
TETRA	Tet collapse	< 0.2	75758	6958	9.2
	Aspect ratio	> 8		0	0.0
	Skew	> 70		42	0.1
	Vol skew	> 90		5752	7.6

The number and shape of elements were determined based on the results of simulations, so-called the mesh sensitivity analysis, for Forman et al.'s test condition (Forman et al., 2012), which will be the target biomechanical test data for the validation of SS-FE models in Chapter 3, using five femur FE models with different number and shape of elements (Figure 13); the impact force time history and maximum principal strain of exterior femur surface at mid-shaft region were compared

(Table 2 and Figure B1). Based on the results, the element number and shape of elements for the template FE model was determined as they were located between those of the SENS3 and SENS4 models.

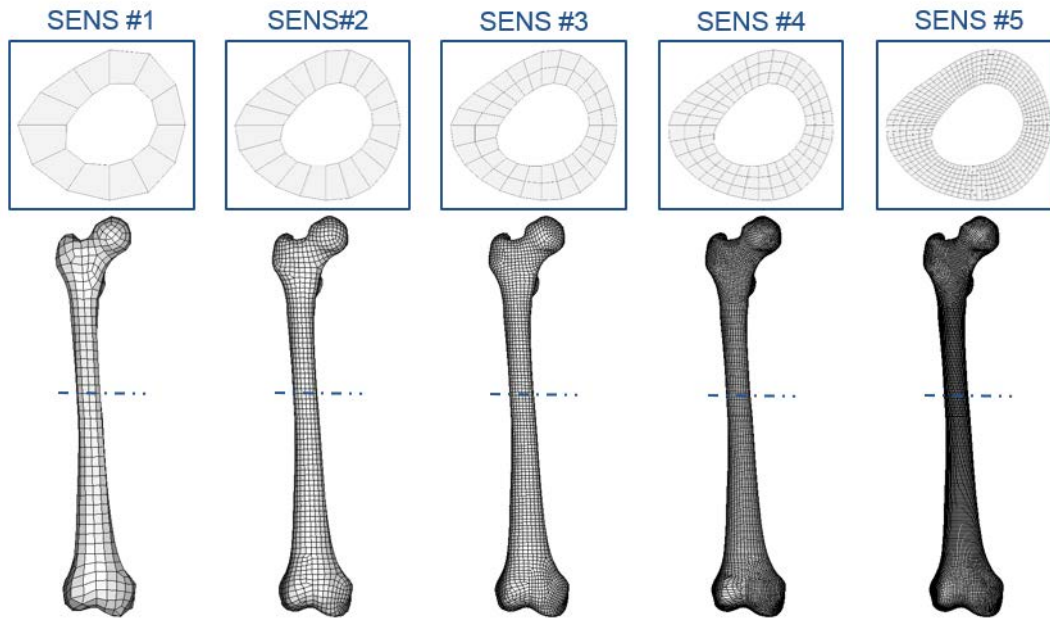


Figure 13 Five femur FE models with different number and shape of elements for mesh sensitivity analysis

Table 2 Summary of mesh sensitivity analysis using five FE models with different number of elements

	# of elements	Impact Force [kN]	Max. Principal Strain [%]
SENS #1	681	Peak [kN]	5.7
		difference [%]	1.38
SENS #2	1195	Peak [kN]	5.72
		difference [%]	1.04
SENS #3	8228	Peak [kN]	5.72
		difference [%]	1.04
SENS #4	38535	Peak [kN]	5.73
		difference [%]	0.87
SENS #5	154693	Peak [kN]	5.78
		difference [%]	0.00

Next, the geometry of each femur specimen was reconstructed from computed tomography (CT) images by a segmentation-with-thresholding method using Mimics (14.01, Materialise, Plymouth, MI). Based on a histogram analysis, voxels above 500 Hounsfield Unit (HU) value are marked as cortical bone; previous study recommended 600 of HU value for thresholding the cortical bone region of the femoral shaft (Aamodt et al., 1999). Whereas thresholding HU value exceeding 300 was not sensitivity to the change of cross-sectional area of femoral shaft (Table B1), using HU=600 as thresholding resulted in a poor segmentation due to a resolution of clinical CT scan. Thus, Thresholding HU value was reduced to 500 in this study.

For the segmentation of the femur, an outer surface and an inner surface of the specimen were generated separately. Due to the resolution of CT images (pixel size of 0.289mm), proximal and distal regions of the femurs, which has a thin cortical thickness (usually less than 1 mm) were difficult to segment the inner surface. Thus, regions with a cortical thickness less than three voxels of CT images were assumed as a constant cortical thickness of size of three voxels.

Before transforming the template FE model to target reconstructed subject geometry, a registration between two geometries was conducted (Figure 11); both geometries were centered and rigidly transformed using an iterative closest point (ICP) algorithm (Besl & McKay, 1992); the ICP algorithm finds a rigid-body transformation which aligns the template model geometry to a target geometry by finding the closest points in the target geometry to the template geometry. After applying the ICP, the target subject geometry was scaled in three directions (x, y, and z) to the template FE model to minimize the size difference between the two geometries. The scaling factors were recorded to scale-back the target subject geometry after searching control points for morphing.

Given aligned geometries of the template FE model and the target subject geometry, control points for morphing were selected using in-house MATLAB scripts (R2015a, The MathWorks Inc., Natick, MA). To select control points, first, the surface registration technique proposed by Bryan et al. (2010) was employed. This technique is based on the three-dimensional generalization of Burr's elastic registration algorithm (Bryan et al., 2010). Prior to implementing this surface registration, the outer surface of the template FE model was divided into eight patches of the anatomical parts (femoral head, greater trochanter, lesser trochanter, medial/lateral condyles, medial/lateral epicondyles, and center of the condyle) (Figure 14). Then, the outer surface of the template FE model was transformed to the outer surface of the target subject geometry using the surface registration algorithm (Figure 11).

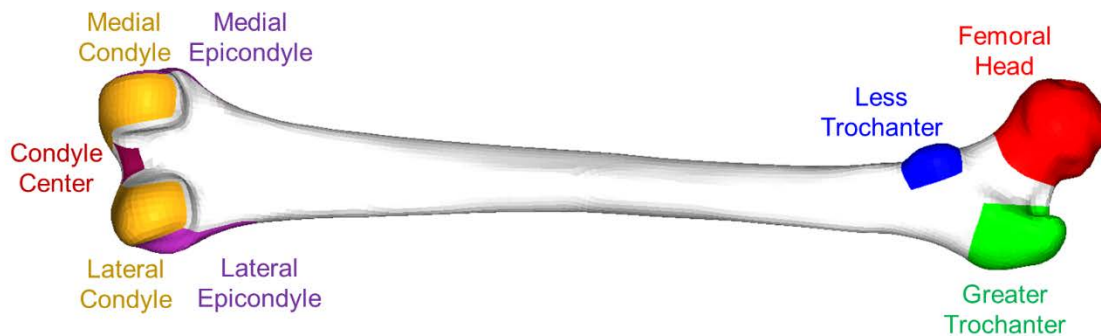


Figure 14 pre-defined anatomical patches to select control points for the proximal and the distal regions

After completion of the surface registration, control points for the femoral shaft and proximal and distal regions were selected. For the femoral shaft region, which has relatively simple geometry (hollow cylindrical shape), 39 sections, from the 12 percentile to the 88 percentile along the

longitudinal direction of the femur were selected, and each section had evenly distributed 40 pseudo-landmarks (based on angle) around the outer and inner outlines of the section (Figure 11). To select control points for the proximal and distal regions, the parameterization and re-parameterization of surfaces (Davies et al., 2008) were employed to manipulate correspondence between the pre-defined anatomical patches of the template FE model and the target subject geometry (Figure 15). After selection of control points for both the femoral and distal/proximal regions, all control points of the target subject geometry were scaled back using the scaling factors recorded during the previous scaling step.

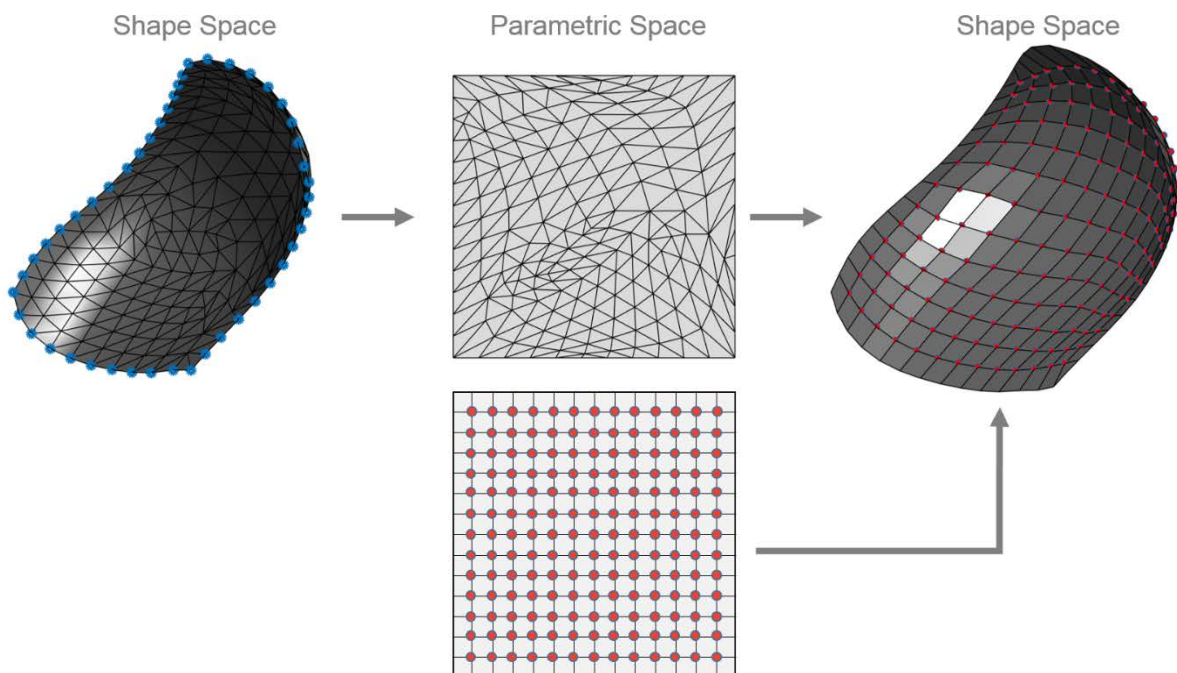


Figure 15 Manipulation of corresponding control points using parametrization and re-parametrization

Finally, with selected control points, the geometry of the template femur FE model was transformed to the target subject geometry of each specimen using a morphing technique,

implementing a thin-plate spline with a radial basis function, an extension of the original thin-plate spline proposed by Bookstein (1989) to take into account landmark localization errors, (Rohr et al., 2001).

The accuracy of developed SS-FE models was evaluated regarding the average minimum distance error (MDE) (the average distance between nodes on the surface of the FE model and the surface of the target subject geometry) and three cross-sectional areas (25, 50, 75 percentile along the long bone direction). Also, the element quality (Jacobian, warpage, aspect ratio, and skew) was evaluated for the shaft region which consists of hexa/pentahedral elements.

2.3 Results

Table 3 summarizes the geometric error analysis and the percentage of elements not meeting the target element quality of the developed SS-FE models. The difference in cross-sectional area was less than 3%, and the average minimum distance error was less than 1mm between the developed SS-FE models and the target subject geometries. The developed SS-FE models satisfied the element quality criteria about Jacobian, warpage, and skew while it showed 0.4% of the elements not meeting a criterion of aspect ratio. The errors of each SS-FE model are presented in Table B2. Figure 16 shows a visual comparison regarding the geometric accuracy of one of the developed SS-FE model and control points used as an example.

Table 3 Summary of the geometric accuracy and the element quality of developed SS-FE models

	Area [%]			Min. distance [mm]		% of elements not meeting target: HEX-PENTA (shaft) [%]			
	25%	50%	75%	Outer	Inner	Jacobian	Warpage	Aspect ratio	skew
Average	2.9	3.0	0.9	0.33	0.84	0.00	0.00	0.37	0.00
1 STD	2.7	0.7	0.8	0.03	0.19	0.00	0.00	0.80	0.00

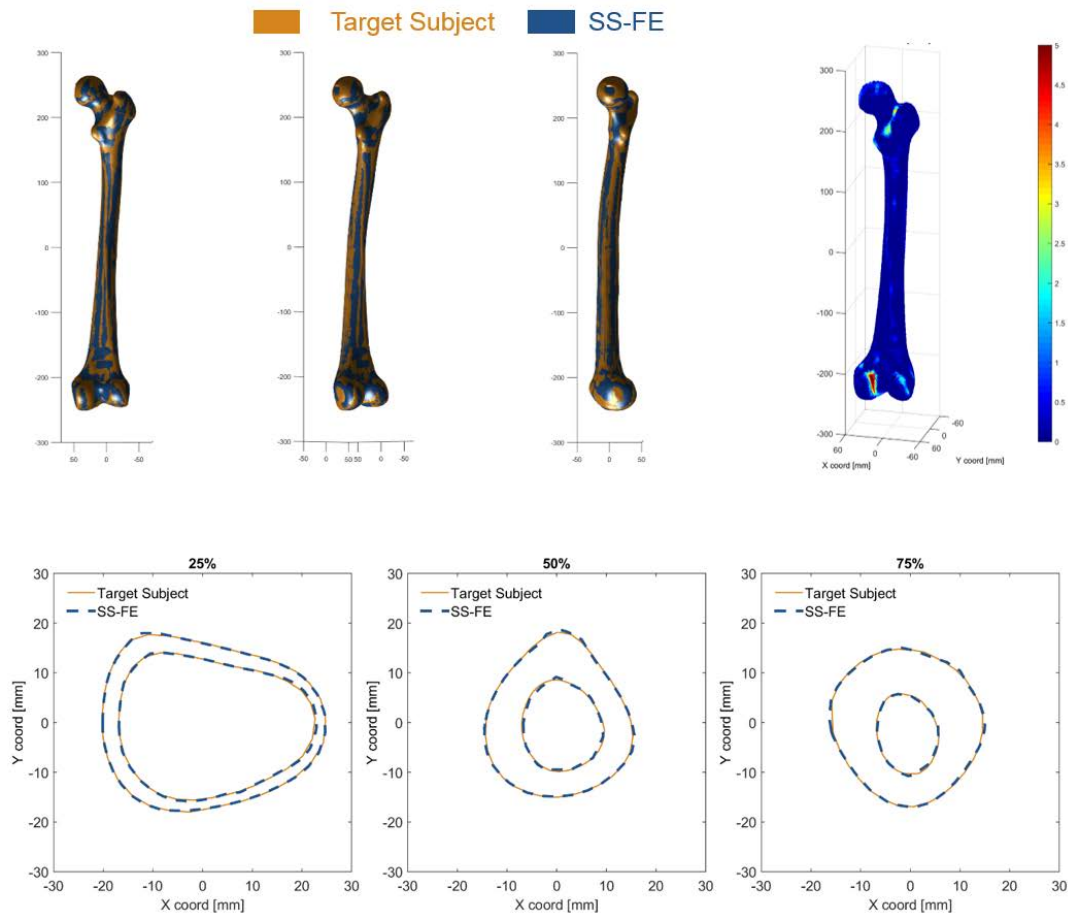


Figure 16 comparison of the geometry between target subject and developed SS-FE models and control points used for the morphing for one of the specimens (F2012-M01) as an example

2.4 Discussion

In this chapter, geometrically accurate SS-FE models were created from CT images of the target specimens using the algorithm developed; the differences in cross-sectional area between the SS-FE model and the target subject geometries were less than 3%, and the average minimum distance between the outer and inner surfaces of those two geometries was less than 1 mm. More importantly, the developed algorithm only requires a reconstructed geometry from CT images and

a template FE model. Then, given those two geometries, the SS-FE models were programmatically generated, which means the researcher does not need to manually select control points, which are laborious and the result largely varies between operators. This could be done by implementing several different algorithms from the literature: ICP, elastic registration, thin-plate spline, and parametrization/re-parametrization; implementing just one algorithm from the literature was not applicable for developing SS-FE models of the femurs in this study.

The greatest difficulty in developing the algorithm for SS-FE models of the femurs in this study comes from the way control points are selected to ensure a geometrically corresponding location between the template and the target subject geometries. The selection of corresponding control points was easily made for a simple geometry, such as a hollow cylindrical shape in the femoral shaft, using evenly distributed control points with a programmatic selection of them. However, application of this method became difficult with complex geometry, such as the proximal and distal regions of the femurs. Thus, for those regions with complex geometries, anatomical landmarks have been manually picked as control points; however, the number of control points represented by only anatomical landmarks may not be sufficient to characterize the complex geometry. Klein et al. (2015) incorporated an extension of the thin plate spline method to morph the template femur FE models for statistical shape analysis. For the femoral shaft region, Klein et al. programmatically digitized control points using the equal distance method similar to the one used in this study. For proximal and distal regions, the authors manually selected 13 anatomical landmarks which were easily distinguishable. Due to the limited number of control points available, the reconstructed surfaces had large geometric differences compared to the target geometries in distal and proximal regions (maximum of 6mm error of average nodal distance) (Figure 17). A

similar approach was also initially adopted for this study (Park et al., 2017). However, this resulted in a large geometric error in the proximal and distal regions as shown in Klein et al.'s study.

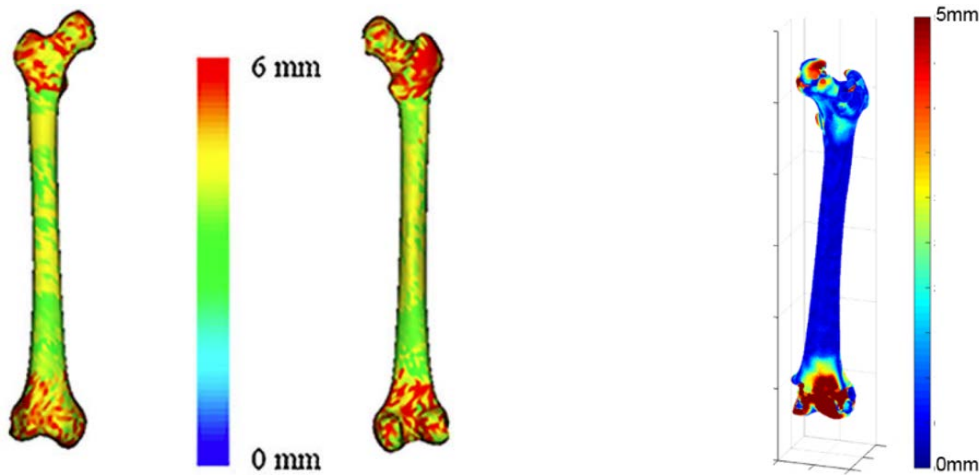


Figure 17 Large geometric error in proximal and distal region using the limited number of control points represented by anatomical landmarks: (Klein et al., 2015) (left), (Park et al., 2017) (right)

An alternative way of selecting control points for complex geometries, instead of the selection of anatomical landmarks, is to use all surface nodes as control points, rather than using a limited number of anatomical landmarks. In the field of orthopedic biomechanics, Bryan et al. (2010) developed statistical shape models of the femurs using a template FE model with 615,523 tetrahedral elements, which had six times more elements than this study (Figure 18). Bryan et al. demonstrated that Burr's elastic registration algorithm was successfully implemented to morph the surface of the template femur model to target geometries including proximal and distal regions in the femurs (Figure 18). It is noted that this algorithm was only applicable for the transformation of 2D surface geometry; application of this algorithm was not applicable to the morphing of the 3D template FE model, which mostly consists of hexa/pentahedral elements, resulting in severely

distorted elements. Thus, Bryan et al. adopted an additional step to morph 3D geometry using the thin plate spline algorithm using nodes on the morphed surface as control points.

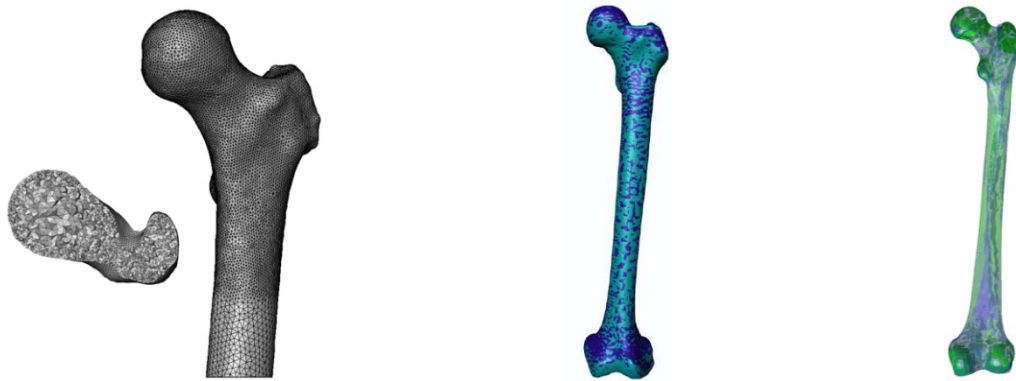


Figure 18 Template FE femur model used (left) and accurate morphed FE model (middle) in Bryan et al. (2010). Morphed surface geometry in surface registration in this study (right)

Even though the usage of directly morphed nodal points as control points successfully generated subject-specific geometries, control points used in the transformation do not guarantee a corresponding location between the two geometries. Correspondence between control points does not necessarily need to be ensured for the creation of SS-FE models. Besides, the correspondence between control points is a necessary condition for generation of parametric statistical models. Since the way of selecting control points will be used to statistical shape analysis in Chapter 4, corresponding points between the two geometries needs to be ensured in this chapter. However, correspondence between control points in two different geometries becomes more difficult to be ensured as geometry becomes complex or has the local geometric difference (Figure 19). This difficulty could be overcome by finding an explicit parameterization of the surfaces than equally spacing points in parameter space (Davies et al., 2008), as was done in this study. (Figure 15).



Figure 19 difficulty in finding corresponding points between target and template geometries

To apply the developed algorithm in this chapter to other body regions, the algorithm should be adopted to each specific body region depending on the shape characteristics of the part. For example, for the kidney, an algorithm implementing 3D parametrization using a sphere or a cube would be a better algorithm than using a square (2D), as was used in this study (Figure 20).

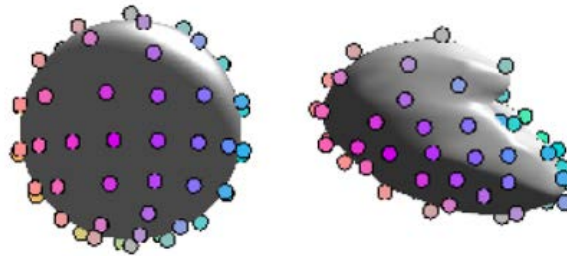


Figure 20 Example of 3D parameterization of non-spherical topology using sphere (Davies, 2002)

The developed SS-FE models in this chapter incorporated all aspects of geometric variability into the models. Thus, the models would have the potential, at least, of capturing the response variation shown in biomechanical tests attributed to its geometric variability. In other words, using the developed SS-FE models allows analysis of the contribution of geometric variability relative to the other factors (mainly, material variability) contributing to the response and injury outcome

variations, which would be a necessary step to develop population-based FE models which require information of effective variabilities to the response and injury outcome variations.

In Chapter 3, the SS-FE models developed in this chapter will be validated by comparing the model responses to those of cadaveric specimens. Most of all, the contribution of geometric variability to the response variation will be analyzed by decomposing the geometrical error using the SS-FE models. Also, the distribution of material parameters identified for individual specimens using the SS-FE models will be compared to those from the literature.

CHAPTER 3: VALIDATION OF SUBJECT-SPECIFIC FINITE ELEMENT MODELS

In Chapter 2, a method for developing the SS-FE models of the femurs was developed. Given the models, this chapter validated the models under a dynamic three-point bending condition by comparing the response of the models to those of cadaveric specimens from biomechanical tests. In addition, material parameters were identified for individual specimens via material parameter identifications with SS-FE models and compared to those from the literature. Then, distributions of the material parameters for three target occupant ages (25, 50, and 75 years) were obtained using a regression analysis. The results of this verified the predictive capability of the model for individual specimen responses with given material models and their parameter distributions and the required level of model complexity to capture the response variations shown in the tests. The distributions of the material parameters obtained from this chapter will be used as the input parameters for generation of the population-based FE models in Chapter 5.

3.1 Introduction

With the contemporary development of computational modeling and imaging technology, SS-FE models have been increasingly employed in the field of biomechanics. Since SS-FE models are able to incorporate detailed skeletal geometry as well as a spatial density distribution of specimens, they have the potential to predict the response of each specimen by capturing all aspects of geometric and compositional variabilities. If accurate subject-specific modeling techniques can be developed and validated, this may facilitate the development of parametric population-based FE models that can capture the effects of variabilities across the population. This approach will be able to 1) take into account variabilities across the population rather than considering the limited

range of the population, 2) eliminate uncertainties inherent to scaling techniques, 3) increase the amount of data available to the field using models developed from available medical images. To develop parametric population-based FE models, as the first step, the predictive capability of SS-FE models needs to be evaluated.

Even though SS-FE models have a potential to incorporate variabilities in the human body, one question still remains regarding SS-FE models, “how specific should SS-FE models be?” This issue has been largely unanswered and needs to be addressed to develop biofidelic SS-FE models with feasible model complexity. A recent study addressed the question using the FE HBMs under the side impact condition (Hwang et al., 2016). Hwang et al. compared the biofidelity of the full FE HBM using three different HBM (original generic HBM representing 50th percentile male size, a parametric HBM with occupant characteristics, and a subject-specific HBM) and demonstrated that the subject-specific HBM model showed the best biofidelity among three models. Also, through sensitivity analysis, Hwang et al. pointed out important contributing factors for the biofidelity of FE model: the body posture, the skeleton and body shape geometries. Whereas this study using whole body level HBM have provided insight into the potential of SS-FE modeling technique, validation of component-level test data would be a useful supplement for those studies to identify key validation goals for SS-FE models in more specific. Also, SS-FE modeling needs to be applied for various loading conditions because the answer of the posed question would be different case-by-case.

Developed SS-FE models can be further utilized to decompose the contribution of geometric variability to response variations. The response variations shown in biological specimens mainly come from two variabilities: geometric variability and material property variability. Since the

developed SS-FE models incorporated all geometric information into the models, the response variations attributed to the geometric variability would be mostly reduced by the usage of the SS-FE models. In other words, the SS-FE models allow decomposition of the contribution of the geometric variability from the response variations. Up to the present, some efforts to decompose the contribution of the geometric variability from the response variations have been made using analytical models (Forman et al., 2012a; Ivarsson et al., 2009). Forman et al. (2012a) analyzed the contributing effects of changes in bone geometry by a component decomposition using a simplified beam model. Ivarsson et al. (2009) estimated individual values of elastic modulus for the specimens using a developed analytical model characterizing the femurs as the curved beam. Since those analytical models employed femurs characterized using a limited number of factors, adopting SS-FE models for the decomposition analysis would better identify the contributing factors to the response variations.

Most of all, SS-FE models, incorporating specific skeletal geometry of specimens into the models, help researchers verify the predictive capability of FE models with given material properties and their parameter distributions by minimizing the geometric error between cadaveric specimens and the models.

The goals of this chapter were 1) to predict the structural response and the fracture of the femoral shaft under dynamic loading conditions using the SS-FE models, 2) to evaluate the predictive capability of the models with respect to the complexity of the model and 3) to obtain distributions of the material parameters for three target occupant ages by verifying that material parameters for individual SS-FE models are in the range of those from the literature.

First, dynamic three-point bending tests of fifteen bare femurs, described by Forman et al. (2012a), were simulated using the SS-FE models developed from Chapter 2. Second, the prediction capabilities of four different levels of model complexity were defined and evaluated: baseline, mass-based scaled, structure-based scaled, and the SS-FE models. Third, to ensure the robustness of developed SS-FE models, dynamic three-point bending tests of five bare femurs, described by Funk et al. (2004), were simulated and compared to the experimental results. Finally, individual material parameters for specimens were obtained by fitting material parameters to minimize the response errors between the SS-FE models and specimens tested. The material parameters for individual SS-FE models were then compared to those from the literature to verify the feasibility of using the material parameter distributions from the literature as input variables for generation of population-based FE models. Finally, the distributions of the material parameters were generated for target occupant ages using a regression analysis.

3.2 Methods

FE simulations

Dynamic three-point bending tests of bare femurs (Forman et al., 2012a) were simulated (Figure 21). The distal and proximal ends of the femur specimens were potted into cups, and the specimens were loaded at the mid-span in the latero-medial direction by an impactor at 1.5 m/s. In total, tests performed on 15 specimens (Table A1) were simulated using the SS-FE models developed in Chapter 2.

In addition to the fifteen simulations for Forman et al.'s test, the robustness of the models for different loading directions with a wider range of the age span was checked using simulations of

the dynamic three-point bending tests of the femur specimens described by Funk et al. (2004) (Figure 21). The simulation condition was similar to that of Forman et al.'s with the exception that the impact speed was at 1.2 m/s and specimens with posterior-anterior loading direction were included. In total, tests performed on five specimens (Table A1) were simulated using the SS-FE models.

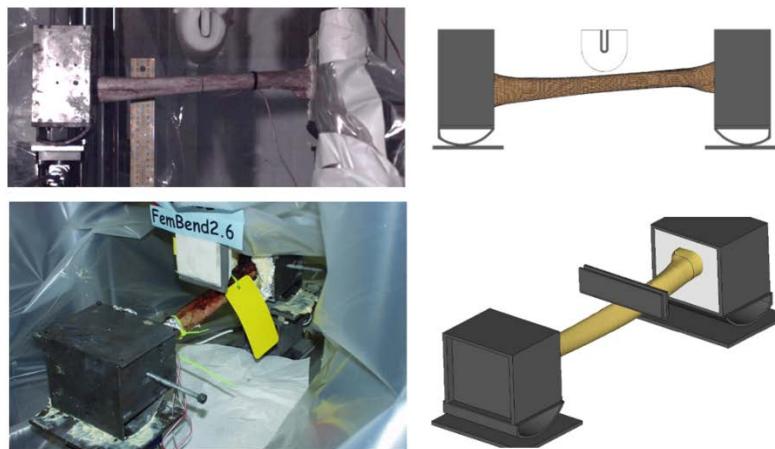


Figure 21 Biomechanical tests (left) and FE simulations (right): three-point bending test conducted by Forman et al. (2012a) (top) and by Funk et al. (2004) (bottom)

The inertia properties of the test apparatus were taken into account by using the 3D CAD geometry and density of each component. The potting material, inside the blocks of proximal and distal ends of the femur with a density of $1.0 \text{ [g/cm}^3\text{]}$, impactor, and test fixtures were assumed as rigid bodies. Also, the elements of femur inside the volume of potting material were assumed as a rigid body constrained by the potting volume. The friction coefficient between the block and bottom plates for Forman's and Funk's test conditions were defined as 0.2 and 0.0, respectively; friction coefficients were estimated by calculating the ratio of the normal force to the tangential force from the load cells placed under the plates in the tests.

Data Processing

The impact force time histories were used as the reference curves for comparison, and the root mean square (RMS) errors between the responses of models and the tests were calculated to quantify the prediction error (the RMS errors were calculated until fracture occurred in the test data). To evaluate fracture prediction, differences in the impact force at the timing of fracture were calculated. The RMS errors and the fracture force differences between the baseline model, the mass-based and structure based scaled responses, and the SS-FE models were compared to evaluate the predictive capability of the models regarding the complexity of the FE models. Also, a paired student t-test was performed to check statistical differences between the responses. Time zero was assumed to be the time at which the impact force exceeded 0.4kN, and all model and experimental responses were shifted in time to match that time zero. All the test and model responses were filtered using the same filter class (CFC180) (SAE, 2003).

Material Parameter Identification of SS-FE models and Determination of Fracture

A piecewise linear plastic material model (LSTC, 2013) was selected as the material model for the femur SS-FE models (Table 4), and the fracture was identified if the maximum principal strain exceeded the ultimate strain during post-processing. Since a wide range of elastic moduli of cortical bone has been reported (McCalden et al., 1993; Zioupos, 2001), material parameter identification was conducted to assign estimated generalized material properties to the SS-FE models. In other words, a single common set of material parameters was identified from via parametric study and was assigned to all the SS-FE models (Table 4). The details of material parameter identification are presented in [Appendix C](#).

Table 4 Common cortical bone material parameters for the SS-FE models identified by parametric study

	Elastic Modulus [GPa]	Yield Stress [GPa]	Tangent Modulus [GPa] ^{*a}	Ultimate Strain ^{*b}	Poisson's Ratio	Density [kg/mm ³]
Piecewise linear plasticity	17	0.125	0.935	0.045	0.3	2000

*a: 5.5% of elastic modulus was assumed for tangent modulus based on the literature (Burstein et al., 1976)

*b: Fracture strain was not directly assigned in the material model. Rather, the bone fracture was determined if the maximum principal strain of elements exceed a strain tolerance during the post-processing.

In addition to identifying generalized material properties to the SS-FE models, individual material parameters, which minimize the RMS error and the fracture force difference, for specimens were obtained. The SS-FE models with material parameters obtained for individual specimen are referred to as “*the SS-FE models with a material fit.*”. Obtained material parameters were compared to those from coupon tests using human cortical bones in the literature (Kemper et al., 2007, 2008; McCalden et al., 1997; Zioupos, 2001) to evaluate the validity of the SS-FE models.

Linear regression analysis was conducted to obtain the distributions of the material parameters (elastic modulus and ultimate strain) as a function of the age using the material parameters from the literature which would be used to generate the population-based FE models in Chapter 5. Due to the limited data on the distribution of yield stress from the literature, yield stresses estimated for the individual specimens using the SS-FE models with a material fit were used to estimate the distribution of yield stress. Normal distribution was assumed as underlying the distribution of three material parameters. The normality of the samples was tested by using the Anderson-Darling normality test with 5% significance level.

Model Complexity

To evaluate the predictive accuracy of the models in relation to the model complexity, the level of model complexity was defined as Table 5.

Table 5 the level of model complexity defined in this study

Level	Model	Description
1	Baseline	single generic response prediction
2	Mass-based Scaled	subject-specific response prediction using one parameter
3	Structure-based Scaled	subject-specific response prediction using two parameters
4	SS-FE	subject-specific response prediction using all geometric factors

Level 1 was defined as using the baseline template model for prediction; this level reflects the response that would be predicted by one generic model that does not consider variations in geometry between specimens. The model complexity Level 2 and 3 were defined as using scaling techniques to compensate for the geometric variability. Scaling techniques attempt to represent the geometric variability shown in specimens using a reduced number of geometric or mass parameters, mostly one or two. Each selected baseline response was scaled to the other fourteen target specimens using two scaling techniques: mass-based scaling (Eppinger et al., 1984) and structure-based scaling (Nie et al., 2016). For mass-based scaling, the scaling factors were derived from the ratio of mass between the target femur specimen and the baseline model (Eq. 1). This scaled response using the mass-based scaling technique is, hereafter, referred to as “*the mass-based scaled response.*” The scaling factors for structure-based scaling were obtained using the ratio of mid-section area and femur length between the baseline model and target specimen (Eq. 2). This response is referred to as “*the structure-based scaled response.*”

$$\lambda_{\text{force}} = \lambda_{\text{mass}}^{2/3}, \quad \lambda_{\text{time}} = \lambda_{\text{mass}}^{1/3} \quad \text{Eq. 1}$$

$$\lambda_{\text{force}} = \frac{\lambda_{\text{Area}}^{3/2}}{\lambda_{\text{length}}}, \quad \lambda_{\text{time}} = \lambda_{\text{length}} \quad \text{Eq. 2}$$

The SS-FE models were defined as Level 4, as the SS-FE model incorporates all available detailed geometric factors into the model.

To gain insight into how the overall comparison would change based on the choice of baseline geometry, each of the fifteen geometric SS-FE model responses was selected in series to serve as “the baseline response” against which all other models (of all other specimens) were compared. The results from each set of analyses (with different “baselines”) were then aggregated to determine mean and standard deviation error predictions (Figure 22).

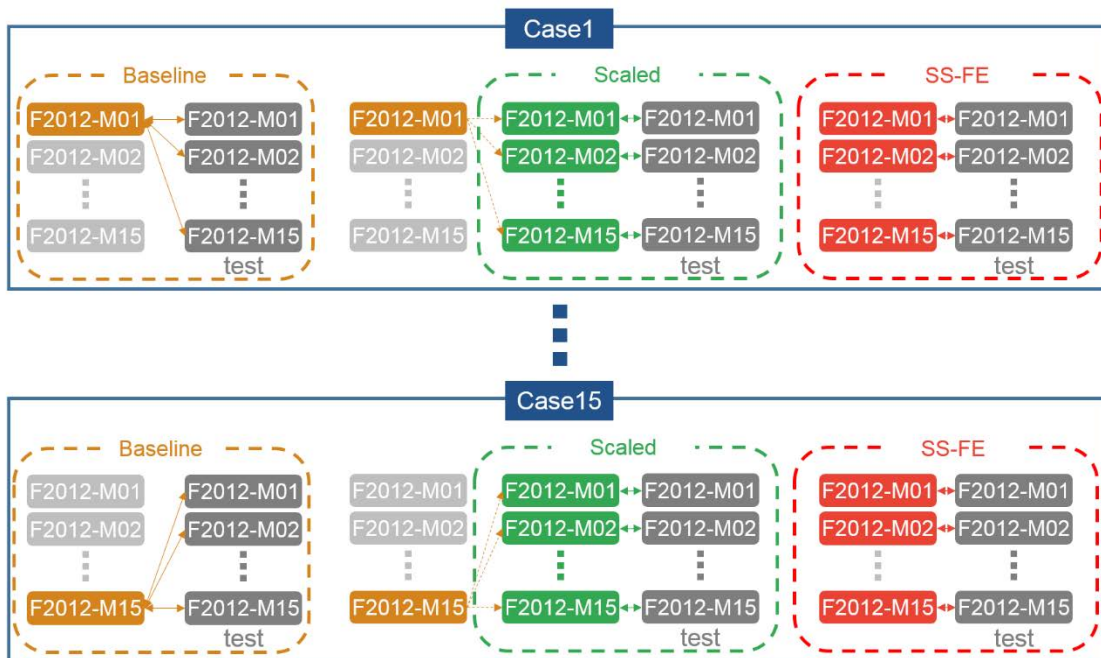


Figure 22 Schematic diagram for evaluation of predictive capability of FE model according to model complexity

3.3 Results

The structural response and fracture prediction capabilities of four model complexities (the baseline, mass-based scaled, structure-based scaled, and SS-FE models) were evaluated using the RMS error and the fracture force difference (Figure 23). The SS-FE models showed a statistically significant ($p < 0.05$) reduction of both the RMS error and the fracture force difference compared to those of baseline models. Both scaled responses using the mass-based, and the structure-based techniques did not show a statistically significant reduction in both the RMS error and the fracture force difference.

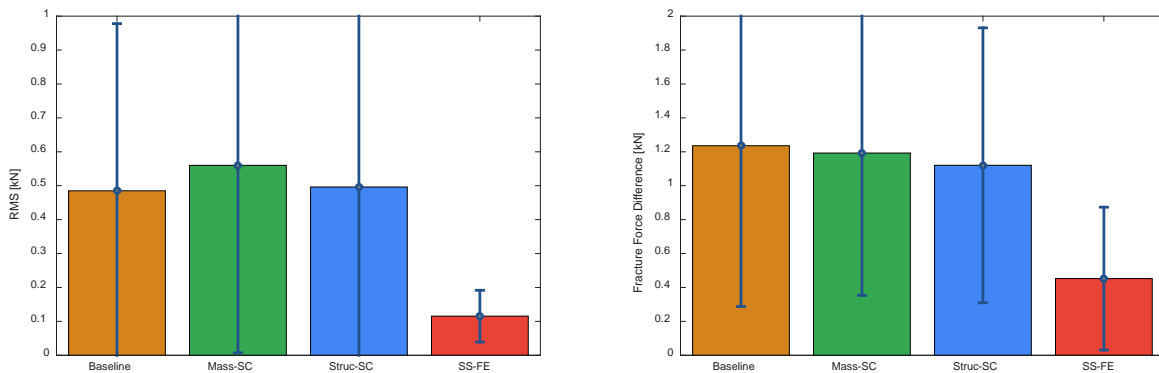


Figure 23 Evaluation of scaling techniques and contribution of geometric variabilities to structural response (left) and fracture response (right) variations

Figure 24 and Figure 25 compare the impact force time histories between the SS-FE models, the SS-FE models with a material fit, and femur specimens from the tests conducted by Forman et al. (2012a) and Funk et al. (2004).

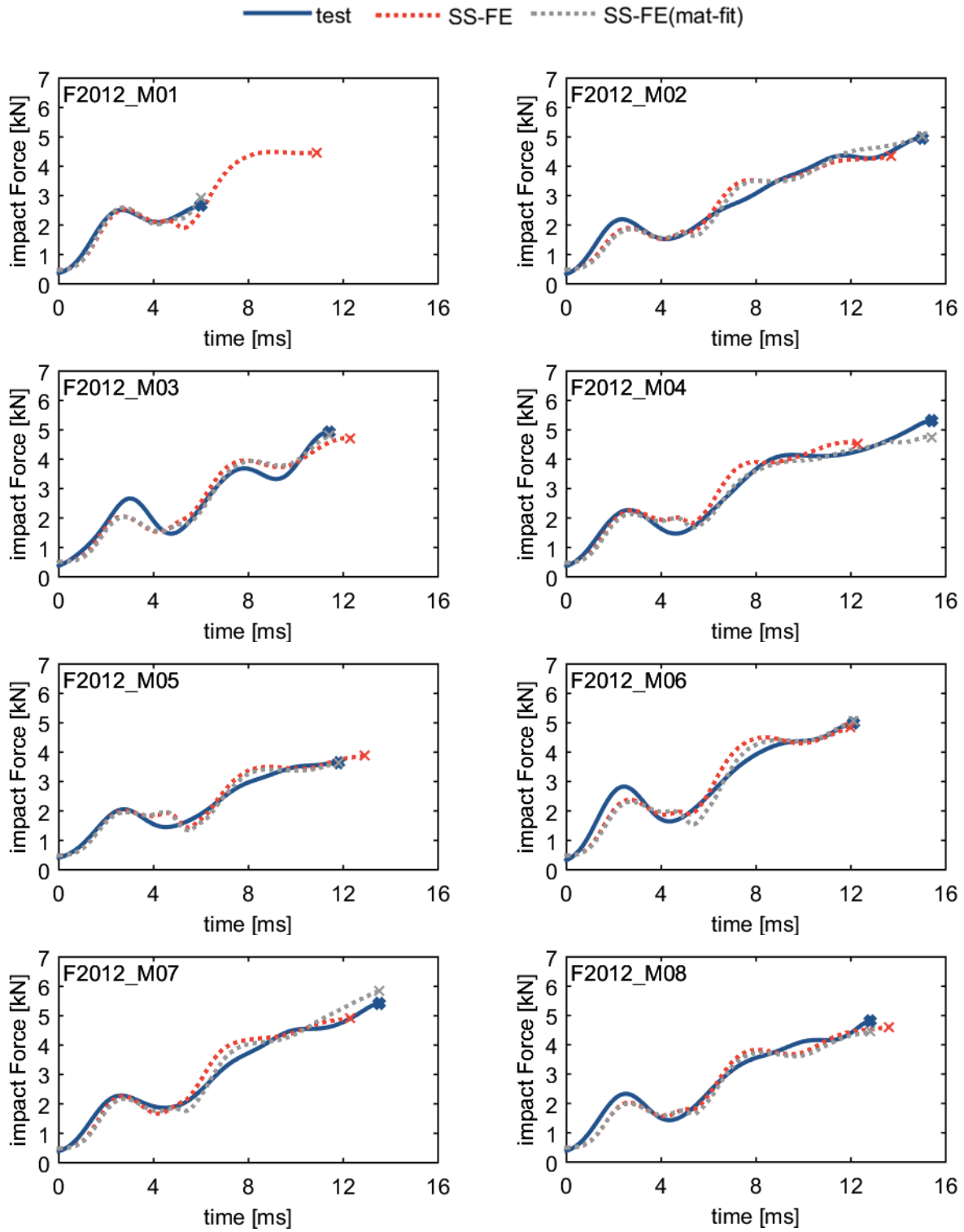


Figure 24 Comparison of impact force histories between test, SS-FE and SS-FE models with a material fit for femur specimens of Forman et al. (2012a). X indicates the femur fracture

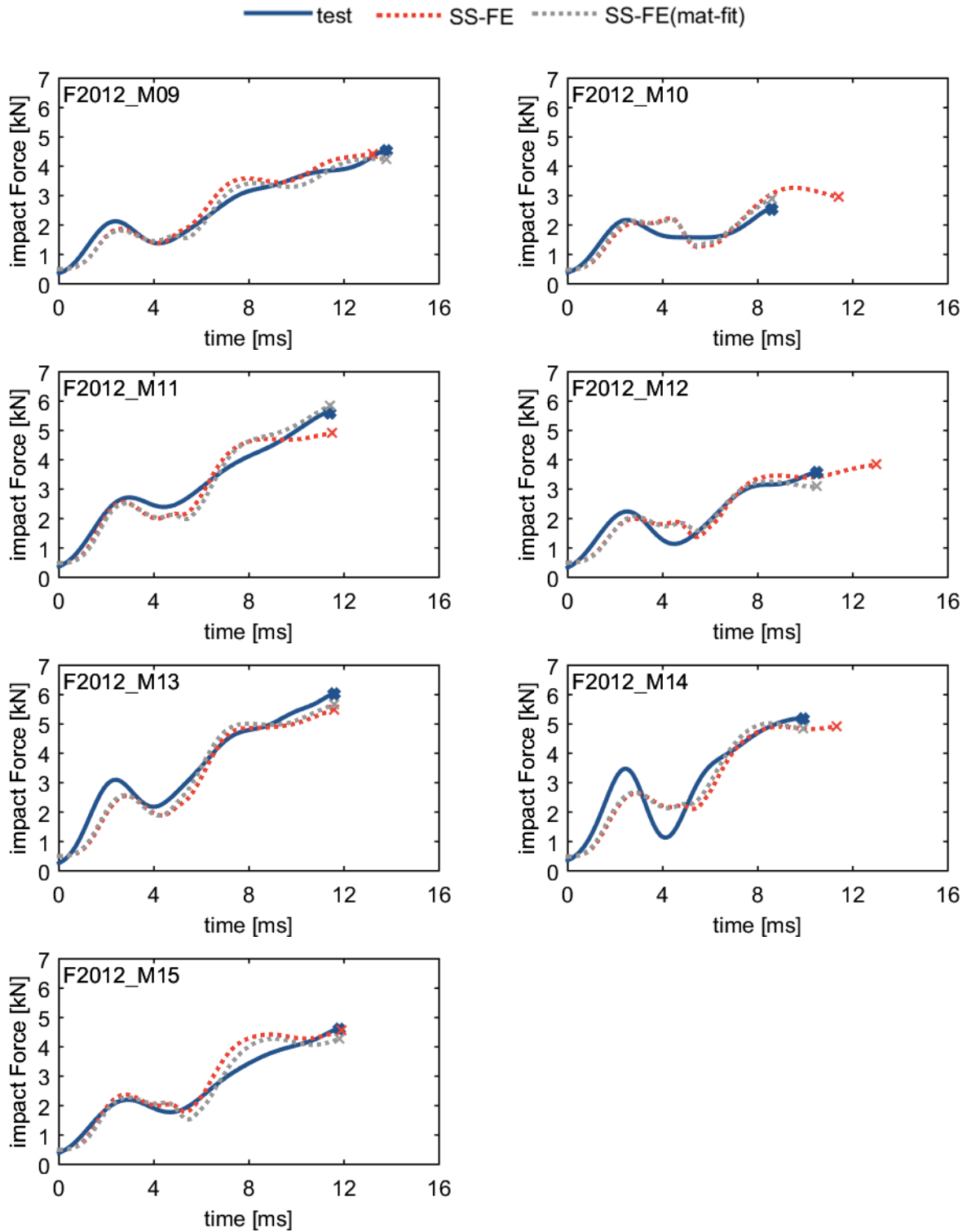


Figure 24 Comparison of impact force histories between test, SS-FE and SS-FE models with a material fit for femur specimens of Forman et al. (2012a). X indicates the femur fracture (continued)

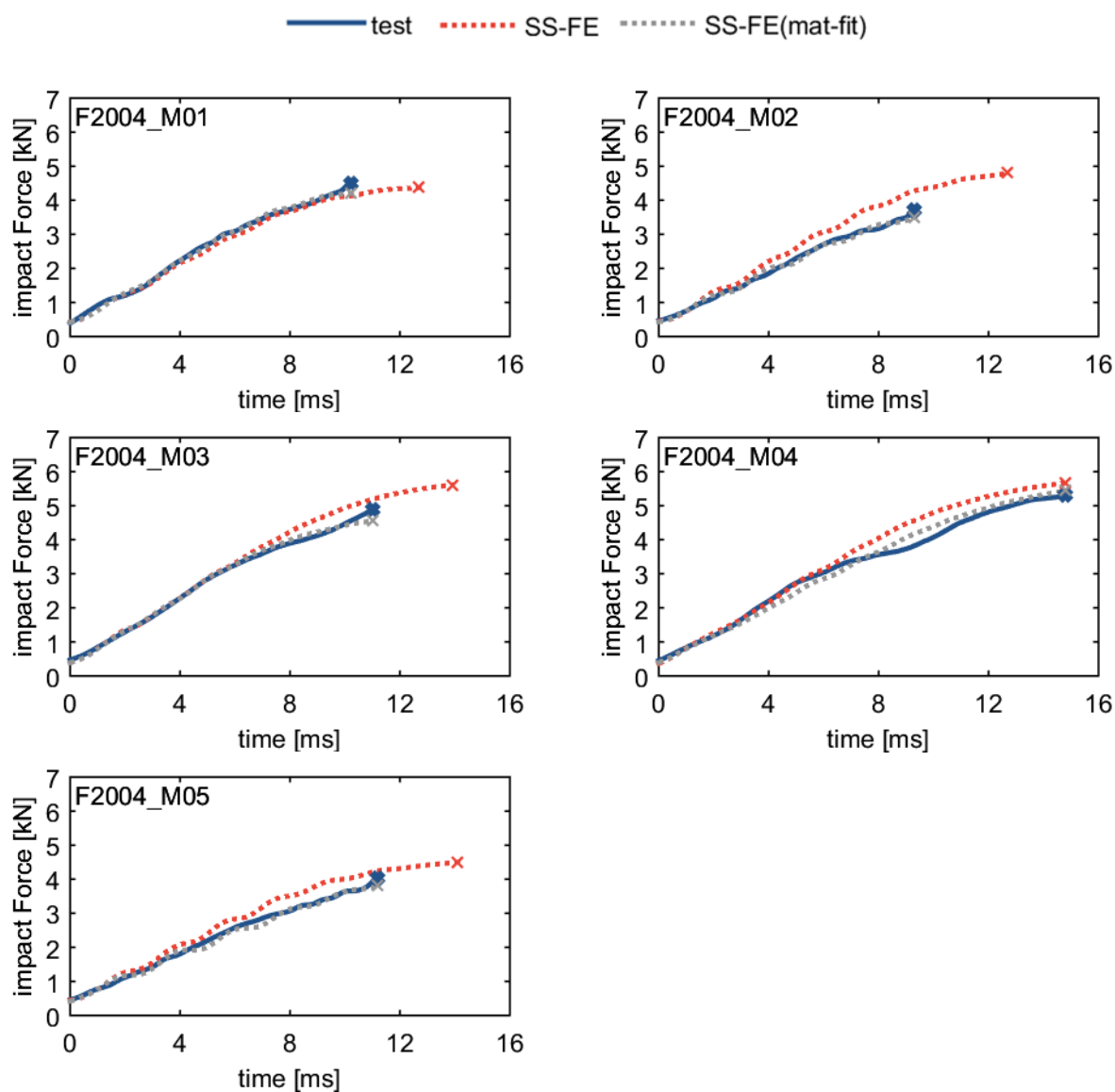


Figure 25 Comparison of impact force histories between test, SS-FE and SS-FE models with a material fit for femur specimens of Funk et al. (2004). X indicates the femur fracture

The material parameters fitted to individual specimens from the SS-FE models with a material fit were in the range of those from the literature (Figure 26). The material parameters of individual specimens are presented in Table C4. A regression analysis demonstrated that the ultimate strain was only a significant variable ($p < 0.05$) and showed a strong negative correlation with age ($r=-$

0.59) while the elastic modulus ($p=0.15$, $r=-0.13$) and the yield stress ($p=0.21$, $r=0.21$) did not. Thus, only the distribution of ultimate strain was generated for three different target age occupants (Figure 27). The ultimate strain and the elastic modulus showed normal distributions ($p > 0.05$) while the hypothesis on the normality of the yield stress was rejected ($p < 0.05$) (Table D1).

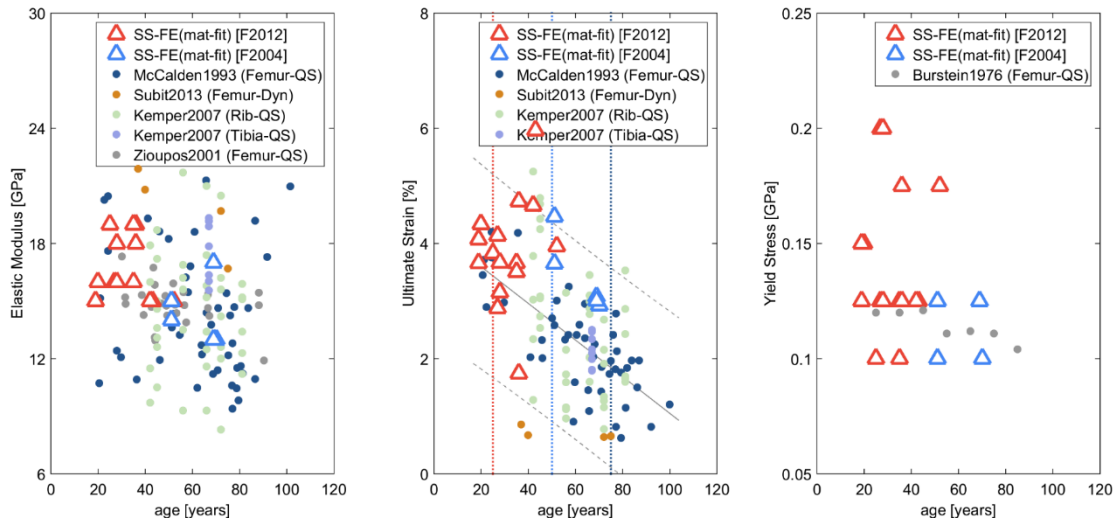


Figure 26 Comparison of material parameters (top) and distributions of the material parameters for three target occupant ages: coupon tests from literature (circle) and material fit using SS-FE (triangle)

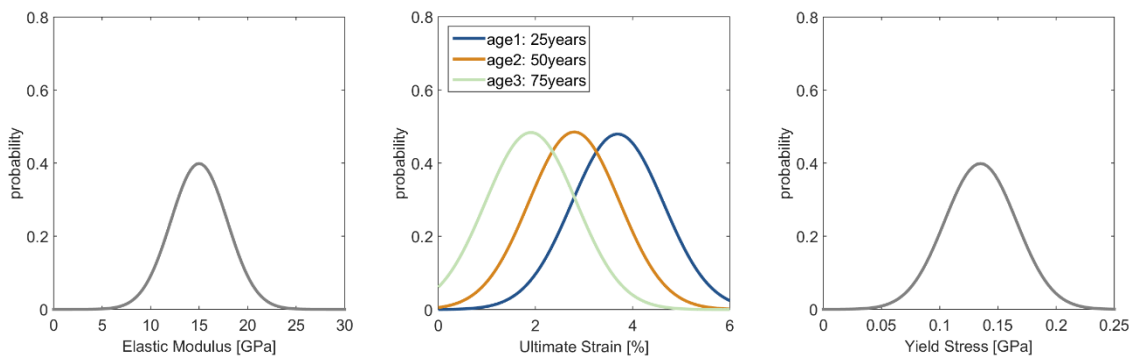


Figure 27 Distributions of the Elastic modulus (left), ultimate strain (middle), and yield stress (right)

3.4 Discussion

Advantage of using the SS-FE Models for Prediction of the Structural Response and Fracture

The SS-FE models showed a statistically significant improvement in the predictive capability of structural response and fracture compared to the baseline model ($p < 0.05$) (Figure 23). This result demonstrates the advantage of incorporating all aspects of the geometric variability into the model using the SS-FE modeling over using a single baseline model to predict the responses of individual femur specimens.

Required Level of Model Complexity for Prediction of the Structural Response and Fracture

Computational models always experience a trade-off between efficiency and accuracy. Given the fact that the cortical bone has a complex hierarchical composite structure spanning from a nano-scale to macro-scale structure (Launey et al., 2010), identifying the required level of model complexity to predict the response of cortical bone, especially to capture the response and fracture variation between the subjects, is of great importance to developing the SS-FE models.

The SS-FE models tended to result in significantly improved predictive capability for structural response and fracture compared to the mass-based or the structure-based scaled responses. The results showed that scaling techniques were not effective to reduce the prediction errors (Figure 23). Thus, these results suggest that scaling techniques would not meet a level of model complexity needed to accurately predict the structural response and fracture of specific femur specimens under the type of loading studied here. In other words, increased model complexity, at least, to the SS-FE models, is required to capture the response and injury outcome variation shown in the femur specimens.

In addition to model complexity regarding the geometric aspect, the result of this study informed the required complexity of the material model used. Specifically, the results suggested that a piecewise linear plasticity material model could be used to predict the structural response and fracture of the femoral shaft under a dynamic three-point bending loading condition if subject-specific geometries are used. It is well known that cortical bone is rate-dependent and an anisotropic material as well showing asymmetric response between the loading under tension and compression. Thus, selection of a constitutive model to characterize the bone is one of the major factors for developing SS-FE models. This study used the piecewise linear plasticity material (with an elastic modulus, yield stress, and ultimate strain as material parameters) to characterize cortical bone, and the developed SS-FE models captured the force-time histories of the bare femur and the fracture (Figure 24 and Figure 25) for all 20 specimens. This result was consistent with previous studies on constitutive model regarding anisotropy of the human femur (Krone & Schuster, 2006; Untaroiu et al., 2006). Krone and Schuster (2006) reported that the global structural response of a femur subjected to bending is sufficiently described by isotropic elastic material, and more complex materials (non-linear isotropic, linear transversely isotropic, and linear orthotropic materials) do not improve the predictive capability of the model. However, Krone and Schuster postulated that consideration of the directional property of the material model enhances the predictive capability of the femur FE model under the torsional loading condition. Also, Untaroiu et al. (2006) demonstrated that both isotropic elastic-plastic and elastic transversally isotropic constitutive models showed a good structural response and fracture prediction of the human femur specimen under three-point dynamic bending condition. Furthermore, the individual material parameters that were obtained through the inverse FE modeling technique were in the range of

values in the literature with cortical bone coupon tests (Figure 27). Thus, the results of this study demonstrated that the piecewise linear plasticity would be the required level of material model complexity for the prediction of structural response and fracture of the femurs, at least, under the dynamic three-point bending condition. More importantly, the results showed that the femur FE model has a capability for prediction of structural response and fracture of individual femur specimens if subject-specific geometry and a material model/parameters were accurately incorporated.

For different body regions and loading conditions, a different level of model complexity may be required. It is well known that cortical bone is rate dependent and an anisotropic material. Also, bone has a different structure according to its function in the body. For example, the proximal region of the femur consists of the trabecular bone inside of a thin cortical shell to offer stability against compressive force. Hence, this SS-FE modeling technique should be extended to apply to various loading rates, loading methods, and other body regions.

Violation of Geometric Similarity in Femur Specimens

The reason for increased error in both scaled responses might arise from a violation of the fundamental assumption of scaling techniques: geometric similarity. Scaling techniques try to represent differences in complex geometries with one or two parameters using an assumption of geometric similarity. If the geometric similarity is not applicable for femur specimens, those techniques would be in error.

The geometric similarity of the femur specimens was investigated in two ways (Figure 28). One way was to investigate the relationship between the length and square root area normalized by

their average of all fifteen specimens. For geometric similarity to hold, the length and the square root area should be correlated. The femur specimens were not correlated ($R^2=0.32$). The other way to investigate geometric similarity was by analyzing a variation of the cross-sectional area along the longitudinal femur direction (normalized by the area of each specimen's mid-section). For geometric similarity to hold, the cross-sectional area variation in the specimen should be similar between the specimens. The results indicate that the specimens showed up to 40% variation of the area along the longitudinal femur direction. Those results indicate a violation of the assumption of the geometric similarity of femur specimens. In other words, more geometric factors need to be incorporated into the FE model to capture the response variation attributed to the geometric variability.

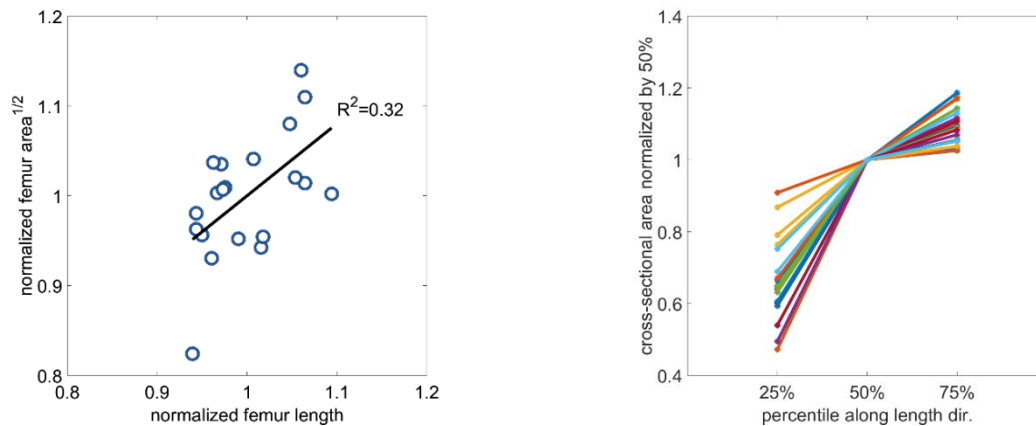


Figure 28 Violation of assumption of geometric similarity: the relationship between the normalized length and normalized square root area (left) and variation of area along the longitudinal femur direction (right)

Decomposition of Geometric Contribution to Response Variation

The results of this study showed the significant contributions of the geometric variability to the structural response and fracture variations relative to those of material variability and other sources of modeling error. Since the SS-FE models incorporated all the geometric variability into the

model, the improvement in the predictive capability would be interpreted as the contribution of the geometric variability to the response variations. By comparing the RMS errors and the fracture force differences, the contribution of the geometric variability to structural response and fracture variations were about 80% and 50% respectively. This result indicated that the geometry dominates the structural response, at least for a femur under the specific loading condition in this study. Contribution of the other factors, mainly material property, increased when it comes to the fracture outcome variation.

Distribution of Material Parameters

The results of this chapter demonstrated the biofidelity of the femur FE model with a given material model and material parameter distributions. Since the usage of SS-FE models minimizes the geometric error between the FE model and cadaveric specimens, the material parameters were estimated for each individual specimen to minimize the RMS error and the fracture force differences. Those estimated individual material parameters were in the range of those from cortical bone coupon tests in the literature (Figure 27), which confirmed the biofidelity of the FE model, at least under the loading condition used in this study.

Linear regression was performed to predict material parameters as a function of the age, and the result showed that only the ultimate strain showed a statistically significant correlation with age ($p < 0.05$). Therefore, the distribution of the ultimate strain was obtained for three different target ages (25, 50, and 75 years) and the distributions of the other two were generated regardless of the age.

This different correlation with age between elastic modulus and ultimate strain also demonstrate the difficulty of applying scaling techniques for generation of injury risk functions. Currently, for mechanical systems, the scaling factors for structural characteristics of the model are established by the ratios of three fundamental properties: the length, mass density and Elastic modulus (Nie et al., 2016). Even though the scaling factor for elastic modulus as a function of age was determined, this scaling factor could not be applicable for scaling the fracture force or moment.

The underlying assumption on the assumed linear relationship between the material parameters and age could be enhanced by applying non-linear regression. Forman et al. (2012a) demonstrated that the ultimate stress of bone tended to be relatively consistent for the first 40 years followed by a decline. Thus, further investigation of the relationship between the material parameters and age needs to be addressed. Also, the distributions of the material parameters may need to be refined by sex. The material parameters obtained from the literature in this study did not consider the sex. However, the cortical bone tends to show a different ultimate stress (McCalden et al., 1993) and viscoelastic property (Wu et al., 2011) between male and female. Especially, the significant bone loss observed in older women, especially after menopause (Zebaze et al., 2010). Since this study targets male occupants, the result of this study was likely to overestimate the effect of age on the degradation of the ultimate strain.

The sample distribution of the ultimate strain and elastic modulus were normally distributed ($p > 0.05$ from Anderson-Darling test) while the yield stress was not. Non-normality of the yield stress may come from the limited number of data points. Material parameters (elastic modulus, ultimate strain, and yield stress) were obtained from the literature and estimated material parameters using the SS-FE models with a material fit. The average yield stress obtained from the SS-FE models

with a material fit in this study (135 MPa) was comparable to that from material testing in the literature (114 MPa) (Burstein et al., 1976); however, due to the limited information on the yield stress in the literature, the distribution of yield stress was generated only relying on the material parameters from the SS-FE models with a material fit which have fewer data points when compared to the other two material parameters.

Application of the SS-FE models

The distributions of the material parameters obtained from this chapter will be used to generate the population-based FE models in Chapter 5. In Chapter 4, statistical shape analysis with regression will be employed to analyze geometric descriptors explaining the geometric variability in the femur and their distributions. Given the geometric and material variables and their distributions, a Monte-Carlo method will be implemented to synthesize the population-based FE models in Chapter 5.

CHAPTER 4: STATISTICAL SHAPE ANALYSIS

In Chapter 2 and Chapter 3, the SS-FE models were developed and validated, which confirms the biofidelity of the femur FE model with a given material model and parameter distributions. In this Chapter, the geometric variability in the human femurs was analyzed from clinical computed tomography (CT) images to identify significant geometric factors of the human femur using principal component analysis (PCA). The distributions of principal scores of the identified geometric descriptors for three target male occupant sizes (5th, 50th, and 95th) were then obtained using a regression analysis. The distributions of principal scores of the geometric descriptors obtained from this chapter will be used as input parameters for generation of the population-based FE models in Chapter 5.

4.1 Introduction

Statistical shape analysis has received attention from the field of biomechanics due to its ability to analyze the shape and densitometry variabilities among specimens; it has been used to find reduced-parametric representations of the variabilities in a large number of data sets based on the dimensionality reduction analysis, such as principal component analysis (PCA). Given the information about geometric descriptors obtained from the statistical shape analysis, the geometric variability in the human body can be employed directly in computational FE models: a statistical finite element (FE) modeling approach; the models are assigned probabilistic distributions of subject characteristics as input variables instead of a single characteristic value. Thus, these statistical FE models allow researchers to overcome the intrinsic limitation of using biomechanical test data - the limited number of specimens - by using a large number from a medical image

database, such as clinical CT images, and generating large datasets of bones using statistical models.

Several studies have been conducted to develop statistical models of femurs (Bryan et al., 2010; Zhang et al., 2016). Most of them were focused on the proximal region of the femur due to the intentions to predict the risk of fracture in falls or for use in the implant biomechanics. Since the proximal femur contains trabecular bone, the intensity information of CT images was also incorporated to generate statistical models in addition to the geometric information. While those studies give valuable insight and offer a methodology to analyze medical CT images, a study focused on the femoral shaft region, which is likely injured during a car crash or pedestrian impact, is of limited benefit.

Recently, Klein et al. (2015) developed parametric statistical models - from clinical CT scan data of 62 men and 36 women, as functions of the age, body mass index (BMI), and femur length - using PCA and regression analysis. This study not only analyzed the shape of the proximal region but also focused on the femoral shaft region, especially the cross-sectional shape of the femoral shaft. This study claimed that the average error in mid-shaft cortical bone areas between the geometry from developed statistical models and that of CT scan data was 4.4%; While this study indicates the potential of parametric statistical models for capturing effects of anthropometric differences throughout the population using PCA analysis and regression, the authors did not report detailed information about the results of the PCA analysis, such as the principal components and the percentage of shape variance explained by each principal component. Also, the geometrical error of the reconstructed geometry of the proximal and the distal regions (maximum 6 mm difference between surfaces) needed to be improved in Klein et al.'s study.

The goal of this chapter was to conduct a statistical shape analysis to obtain geometric descriptors explaining the geometric variability in the human femurs. Also, the chapter was aimed at obtaining the distributions of principal scores of the geometric descriptors for three target male occupant sizes (5th, 50th, 95th percentiles). First, CT images of 122 male specimens were reconstructed using a thresholding based method. Second, landmark points were selected using the method developed in Chapter 2 ensuring corresponding points between the specimens. PCA was then employed to analyze the geometric variability in the human femur. Among principal components obtained from PCA, the required number of principal components (referred to as the geometric descriptors in this study) to reconstruct the geometry, the structural response, and fracture was identified using PCA-based FE models. Finally, the distributions of principal scores of the geometric descriptors were generated for three target male occupant sizes (5th, 50th, 95th percentiles) using a regression analysis.

4.2 Methods

Clinical CT Images

In total, the CT images from 122 male specimens at the Center for Applied Biomechanics Lab were introduced to analyze geometric variability between specimens. The specimens are referred to as “the training set.” The average age, height, and weight of the training set were 61 ± 13 years, 178 ± 7 cm, 81 ± 16 kg, respectively (Figure 29 and Table A3). For the convenience of analysis, the left femurs were reflected to the right femur with respect to the mid-sagittal plane.

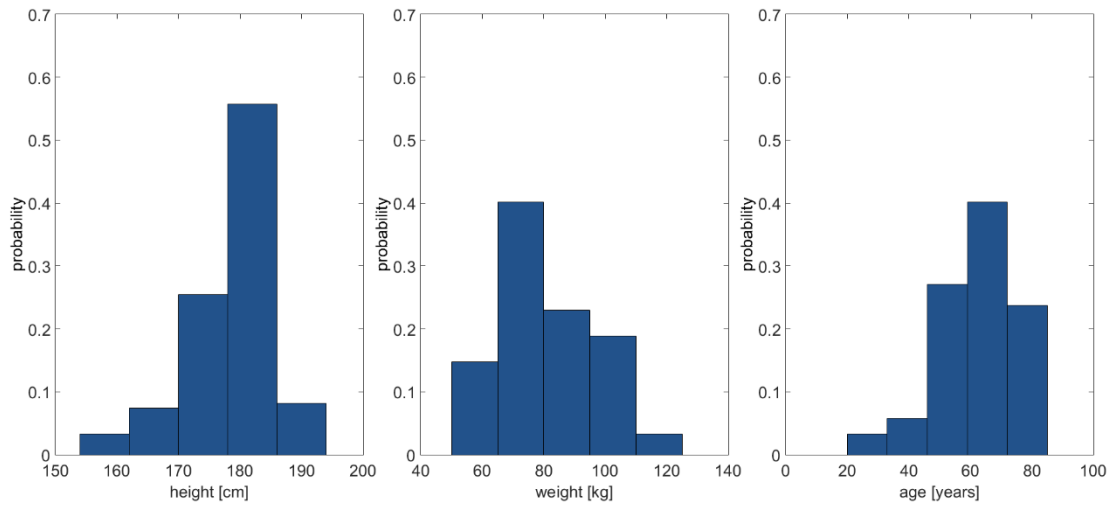


Figure 29 Distribution of height (left), weight (middle), and age (right) of the training set

Data Preparation (Establishing Point to Point Correspondence)

The first step to conducting a statistical shape analysis is to establish a correspondence between subjects in such a way that the location at any given point in one model can be directly related to an equal point in another model (Bryan et al., 2010). The correspondence between femurs of the training set was established by employing the method developed for the development of SS-FE models in Chapter 2: 1) 3D shape models of the training set were generated from the CT images based on a segmentation-with-thresholding method. 2) 3D shape models were registered to the template FE model geometry and 3) landmarks were selected (Figure 11), refer to Chapter 2 for details). Then, the landmarks were considered as corresponding points between the femurs of the training set.

Statistical Shape Analysis

Given the corresponding points between the femurs of the training set, statistical shape analysis (SSA) was conducted using principal component analysis (PCA) to analyze important geometric descriptors, which explain the shape variability of the femurs in the training set. PCA is a statistical technique to reduce the dimensionality of data to provide significant components of the variability in the large data set. A correlation based PCA was adopted in this study since the dimension of the long bone direction is greater than other directions (Bryan et al., 2010).

First, \mathbf{x}_i was defined for each femur using nodal coordinates (x, y, and z) of the landmark points in series (Eq. 3).

$$\mathbf{x}_i = [x_{1i} \ y_{1i} \ z_{1i} \ x_{2i} \ y_{2i} \ z_{2i} \ \cdots \ x_{ni} \ y_{ni} \ z_{ni}]^T, \quad 1 \leq i \leq N \quad \text{Eq. 3}$$

Where N is the number of specimens in the training set and n is the number of landmarks points in each femur. Then, the matrix \mathbf{X} was established by combining \mathbf{x}_i (Eq. 4)

$$\mathbf{X} = [x_1 \ x_2 \ x_3 \ \cdots \ x_N]^T, \quad \mathbb{R}^{N \times 3n} \quad \text{Eq. 4}$$

Second, matrix \mathbf{X} converted matrix \mathbf{Z} by calculating the z-score of each row and PCA was applied using the function “PCA” implemented in MATLAB (R2015a, The MathWorks Inc., Natick, MA), which centers the data and uses the singular value decomposition algorithm by default. Applying PCA returns the principal component coefficients matrix, the principal component scores, the principal component variance, the percentage of the total variance explained by each principal component, and the mean of \mathbf{x} . Each column of the principal component coefficients matrix

$(\boldsymbol{\psi}_m, m = 1, 2, \dots, N)$ contains coefficients for one principal component. The principal component variance vector is denoted by \boldsymbol{v} .

The shape of m^{th} principal component was identified by adding and subtracting 1.96 standard deviations of each principal component to the mean shape of the femur (Eq. 5). Finally, PCA with \mathbf{Z} was returned back to nodal coordinates by using the mean and standard deviation of \boldsymbol{x} .

$$\boldsymbol{P}_m = \bar{\boldsymbol{x}} \pm 1.96v_m\boldsymbol{\psi}_m \quad \text{Eq. 5}$$

Reconstruction Error using PCA-based models

The five femurs of the specimens used in Funk et al. (2004), whose SS-FE models were developed and validated in Chapter 2 and Chapter 3, were reconstructed using the different number of principal components (Eq. 6). These reconstructed models are referred to as “*the PCA-FE*” models.

$$\boldsymbol{P} = \bar{\boldsymbol{x}} \pm \sum_{i=1}^k v_k \boldsymbol{\psi}_k \quad \text{Eq. 6}$$

Where k denotes the number of principal components included in the models. For example, including the first 22 principal components, which explains 95% of shape variance, loses the information of 5% shape variance in the reconstruction of the femur models. The effect of loss of 5% shape variation by including the limited number of principal components was analyzed in two aspects: the geometrical reconstruction error and the response reconstruction error. The average minimum distance error between the SS-FE and the PCA-FE models were calculated to evaluate the geometrical reconstruction error. For the response reconstruction error, the PCA-FE models were simulated as those of SS-FE models in Chapter 3, and the structural responses with the RMS

errors and the fracture force differences were calculated. Given the errors according to the number of principal components included in the PCA-FE models, the required number of principal components for generation of the population-based FE models was determined, and the reduced number of selected principal components are referred to as “*the geometric descriptors*” in this study.

Principal Score Distributions of the Geometric descriptors

Given the geometric descriptors selected, a linear regression analysis was employed to obtain the principal score distributions of the geometric descriptors (GDs) for three target male occupant sizes in terms of height (5th percentile: 164.7cm, 50th percentile: 175.5cm, 95th percentile: 186.8cm). The GDs whose principal scores showed statistically significant correlation with occupant height ($p < 0.05$) were identified, and the distributions of their principal scores as a function of height were obtained. For the GDs whose principal scores were not correlated with height, the probabilistic distributions of principal scores were generated regardless of the occupant height. Normal distributions were assumed as underlying distribution, and the normality of distributions was tested by the Anderson-Darling normality test with 5% significance level. The distributions which showed non-normality were generated using their empirical distributions instead of assuming a normal distribution.

4.3 Results

Figure 30 shows the landmarks registered in the coordinate system of the template FE model. The landmarks were used as corresponding points for statistical shape analysis.

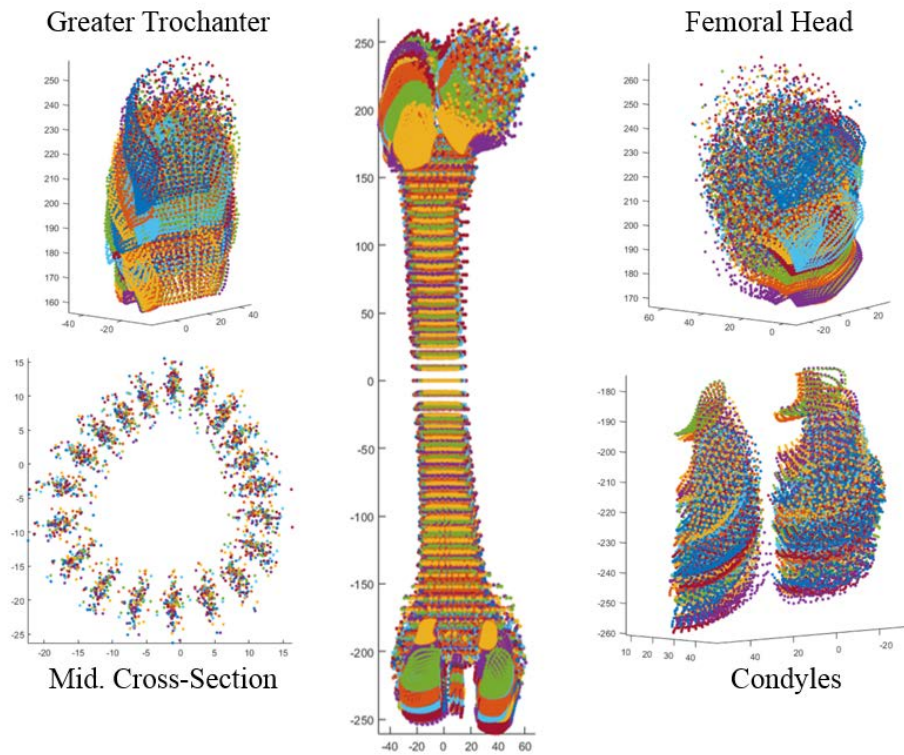


Figure 30 Landmarks points used in PCA

The results of PCA showed that 95% of the geometric variability was explained by the 22 principal components; the first principal component explained 40% of the geometric variability while 99% of the variability was captured by the first 54 principal components (Figure 31). Figure 32 shows principal shape modes of the first three principal components. The first mode was explained by the size of the femur; as increasing the length of the femur, cross-sectional areas of the femur increases radially. The second mode was related to the slenderness of femur. Unlike the first shape mode, increasing the length of the femur results in decreasing the size of the proximal femur region. The third mode was related to the cross-sectional shape and curvature of the femurs in the anterior-posterior direction.

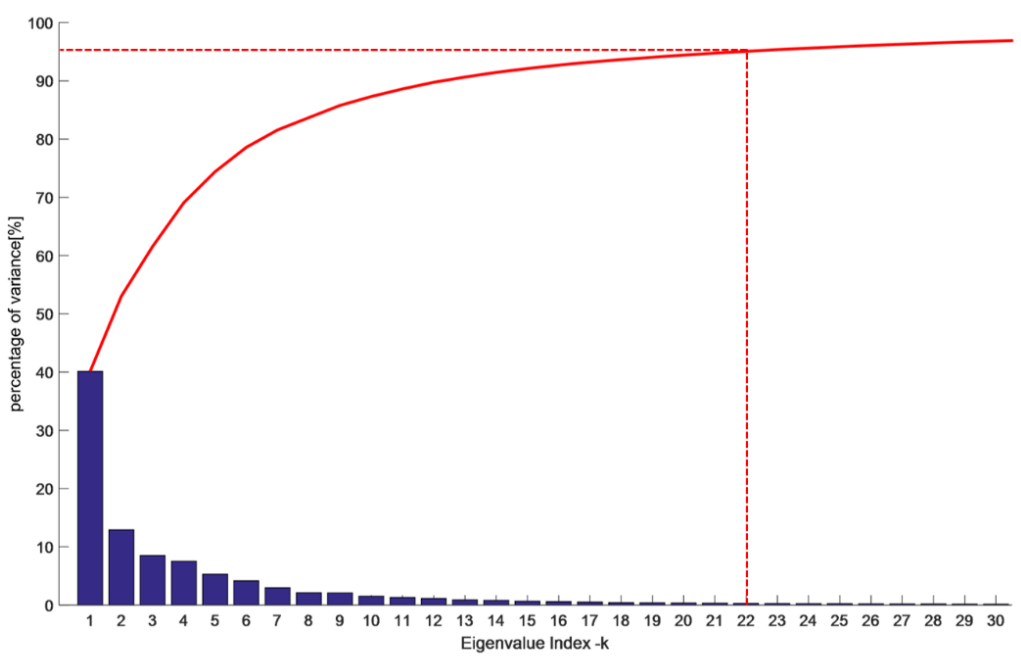


Figure 31 percentage of shape variance: first 13 modes explains 95% of shape variance

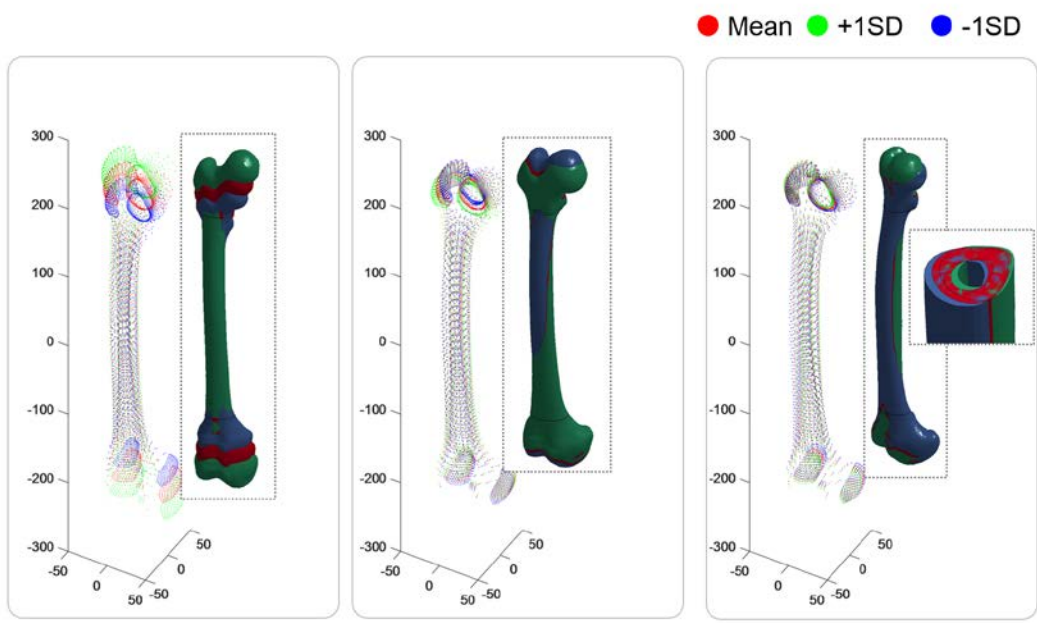


Figure 32 First three principal modes: 1st mode=size of femur (left), 2nd mode=slenderness of femur (middle), 3rd mode=curvature of the shaft in the anterior-posterior direction (right),

The reconstruction error using the PCA-FE models in relation to the different number of principal components included are analyzed in Figure 33. Regarding the geometric reconstruction error, including 22 principal components explaining 95% of the geometric variability resulted in 0.56 ± 0.08 mm of the average minimum distance error. This error reduced up to 0.38mm as increasing the number of the principal components up to 54, which explains 99% of the geometric variability. For the response prediction error aspect, the reconstructed models using 22 principal components showed less than 0.02 ± 0.02 [kN] (0.4% of the peak fracture force) and 0.13 ± 0.09 [kN] (2.5% of the peak fracture force) of the RMS error and the fracture force difference, respectively. Figure 34 presents the average minimum distance error and the impact force time histories in relation to the different number of the selection of principal components for generation of PCA-FE model for one of the specimens as an example. Based on the results, the first 22 principal components were selected as the GDs in this study. Finally, the distributions of principal scores of the GDs were generated using a linear regression analysis and Figure 35 presents the distributions of the first three GDs as an example. The distributions of all GDs are presented in Figure D2.

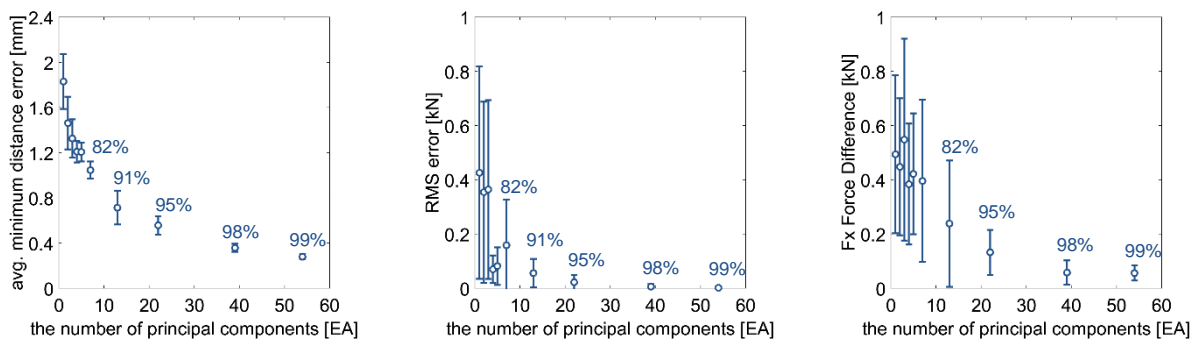


Figure 33 Reconstruction errors in relation to the different number of principal components included in PCA-FE model: geometric error (left), structural response (middle), and fracture force difference (right). The number in % indicates the percentage of variance explained by the principal components

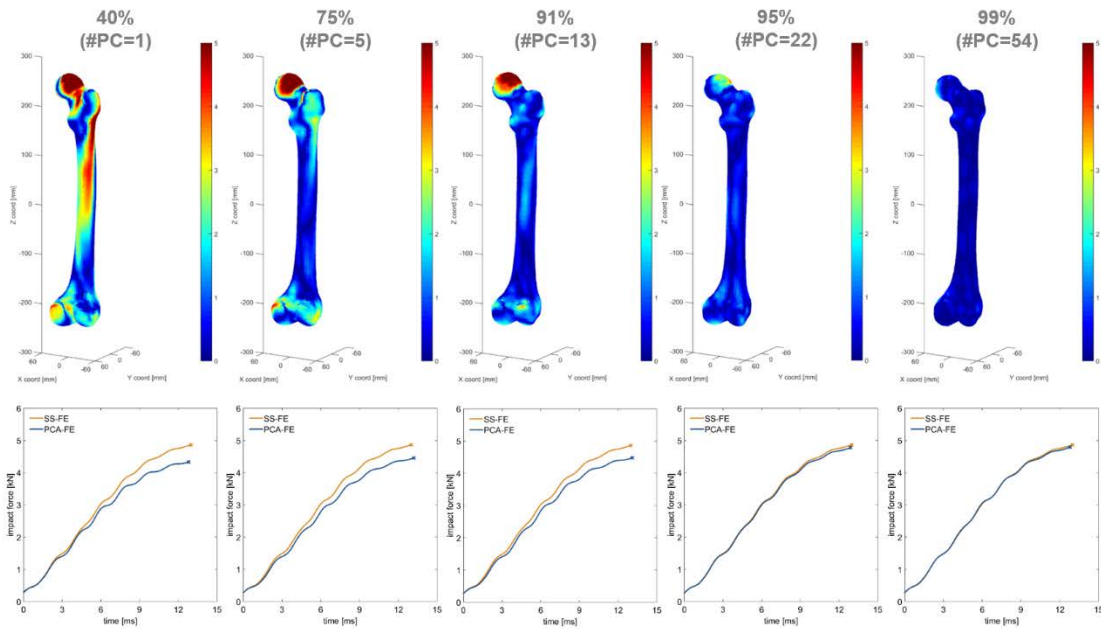


Figure 34 geometric reconstruction error: RMS error vs. percentage of variance (top) and RMS error outer surface of F2004-M03 as an example (bottom)

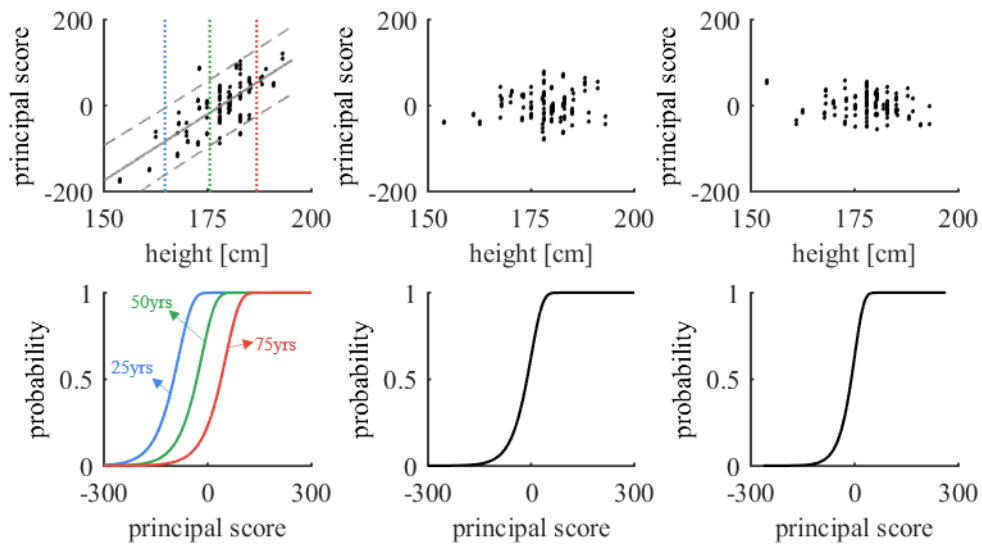


Figure 35 regression analysis for the geometric descriptors (left) and the distributions of the geometric descriptors (right) for three occupant sizes: example of first three factors – 1st GD (top), 2nd GD (middle), and 3rd GD (bottom)

4.4 Discussion

This chapter conducted statistical shape analysis and identified the geometric descriptors and their principal score distributions to explain the geometric variability across the population.

Principal Component Analysis (PCA)

Analysis of the principal components showed that 40% of the geometric variance in the human femur was explained by the first principal component and the first mode was mainly explained by the size of the femurs (Figure 32). Other researchers reported similar conclusion as this study (Bryan et al., 2010; Zhang et al., 2016); Bryan et al. demonstrated that the first principal component in the human femurs is mainly explained by the length and it explains 45% of the geometric variance. Also, Zhang et al. showed that the first principal component explains 35% of the shape variance and the mode was related to the length, anteversion angle, and cortical thickness of the femur.

While the first principal component obtained from PCA in this study was in line with that from the literature, the second and third principal components were varied between the research groups. The second principal component of this study was related to the slenderness of the femur, and the third principal component exhibited the variation of the curvature of the femoral shaft in the anterior-posterior direction. On the other hand, Bryan et al. (2010) reported the second mode dominated by a bone thickness and the third mode was explained by some subtle geometric traits (head diameter, anteversion angle, etc.). Zhang et al. (2016) demonstrated that the second principal and the third components were dominated by anteversion angle and neck-shaft angle variations,

respectively. These different observations between the research groups might come from the difference in the sample distribution of medical images or the region of interests.

Geometric descriptors (GDs) and Distributions

In this study, 22 principal components explaining the 95% shape variation were considered as the geometric descriptors (GDs). How many principal components needed to be included for the generation of the population-based FE models would be different for different loading conditions and body regions. To identify the required number of principal components included for the generation of the population-based FE models for this study, the significance of the principal components was analyzed by three factors: geometric reconstruction, the structural response, and fracture force prediction errors. As expected, increasing the number of principal components reduced the errors (Figure 33). The slope of the average and the standard deviation of the errors largely decreased from the consideration of 95% shape variance. Thus, we decided to set 95% of shape variance, which includes the first 22 principal components, as the tolerance for selection of the GDs.

Given the identified GDs, the distributions of them were generated using linear regression analysis (Figure 35 and Figure D1). Several geometric factors (5 out of 22) did not show the normality. In Chapter 5, to take into account the non-normal distribution of some of the GDs for generation of the population-based FE models, a sampling technique using an empirical distribution will be applied instead of assuming the normal distribution.

Subject Characteristics of Medical Image Database

The principal components of the geometric variability would depend on medical images used for the analysis. Since only the CT images of male subjects were considered in this study, introducing female images for the analysis and identifying the difference between sexes would be a possible research topic following this study. Also, the effects of age and race may need to be further investigated; the age of subjects tended toward elderly (61 ± 13 years) white subjects. Thus, investigation of change in shape variability according to aging and the differences between races could be a topic for future investigation.

On top of the needs for consideration of the differences in sex, race, and age, the effects of the number of medical images need further investigation. While increasing the number of images unequivocally improves the statistical power of the analysis, the question on the required number is still unknown. Thus, analysis of the requirement of the number of subjects analyzed would help improve accuracy and efficiency of the analysis.

Application

This chapter identified the GDs and the principal score distributions of the factors from the set of CT images. These distributions of principal scores of the GDs will be used to synthesize the population-based FE models of the human femurs with a Monte-Carlo method in Chapter 5.

CHAPTER 5: GENERATION OF POPULATION-BASED FINITE ELEMENT MODELS AND INJURY RISK FUNCTIONS

Using SS-FE modeling technique, the capability of the femur FE models for prediction of structural responses and fracture forces of individual specimens was validated, and the distributions of material parameters were identified in Chapter 3. Also, the geometric descriptors, explaining the shape and response variabilities, and their principal score distributions were identified in Chapter 4.

In this chapter, the population-based FE models of the femurs were generated for target occupants using a Monte-Carlo method by sampling points from identified distributions. FE simulations were then conducted with each of the population-based FE models under 3-point dynamic bending in lateral-medial direction. Model-based injury risk functions (IRFs) were then developed using logistic regression analysis, based on the moment-at-fracture observed in the FE simulations.

5.1 Introduction

A fundamental purpose of biomechanical testing and the field of injury biomechanics is the development of risk functions (Kent & Funk, 2004). Up to the present, IRFs have usually been developed in a “top-down” approach by relating injury occurrence in cadaveric tests to dummy measures in matched crash conditions (Forman et al., 2012b). While IRFs have been developed and widely used in the automotive safety field, there are some challenges that need to be addressed in the current development procedure of the IRFs: 1) a lack of understanding of the relationship between the human variabilities and the variation of injury outcome, 2) the uncertainty of the

scaling techniques used for compensating anthropometric differences between subjects, and 3) the limited number of biomechanical tests available.

The central idea of this study is that IRFs could be developed in a bottom-up approach utilizing population-based FE models instead of being developed in the top-down approach. Contrary to the top-down approach, a range of variabilities of IRFs developed in the bottom-up approach would be informed by the population-based FE model responses. This method would be able to address challenges facing the current development procedure of IRFs for diverse or specialized populations: specifically, this method mitigates the uncertainties in applying empirical scaling and may improve IRF fidelity when a limited number of experimental specimens are available.

The goal of this chapter was to demonstrate a framework for the generation of IRFs in a bottom-up approach using the responses of the population-based FE models. To exemplify the framework, this chapter generated IRFs for the human femur under dynamic (1.5 m/s) 3-point bending in the lateral-medial direction for three target occupant sizes (5th percentile: 164.7cm, 50th percentile: 175.5cm, 95th percentile: 186.8cm) with three ages (25, 50, 75 years).

5.2 Methods

Generation of the Population-Based FE Models

In Chapter 4, the geometric descriptors (GDs) of the human femur were identified, and the distributions of principal scores of the GDs were obtained. Also, the distributions of the material parameters (elastic modulus, ultimate strain, and yield stress) were generated using the data from the literature in Chapter 3 with regression analysis. In this chapter, given those distributions of principal scores of the GDs and the material parameters, A Monte-Carlo method was implemented to generate population-based FE models of the femur for target occupants: three occupant sizes (5th, 50th, and 95th percentile males) and three occupant ages (25, 50, and 75 years).

The principal scores of the GDs, the elastic modulus, and the yield stress were randomly sampled from the distributions for 100 trials. Given the principal scores and material parameters sampled, in total, 100 femur models were generated by using the way of reconstructing the PCA-FE models in Chapter 3 (see details in the [Method section](#) in Chapter 3). Also, the ultimate strain was randomly sampled for 5000 trials. These ultimate strains were used to determine the fracture of the femur during a post-processing step of the FE simulations. Therefore in total, the fractures of the 500,000 population-based FE models were analyzed (applying 5000 ultimate strains for each 100 femur FE model) for each target occupant characteristics. These synthesized models are referred to as “*the virtual population models (VPMs)*.”

FE simulation and Data Processing

Using the VPMs, dynamic 3-point bending tests of bare femurs were simulated (Figure 36). The boundary conditions were simplified from the test described by Forman et al. (2012a) (Figure 21);

the distal and proximal ends of the femur specimens were assumed as a rigid body, whose regions were potted into cups during the test. The distal and proximal ends of the femurs were only allowed to rotate along the x-axis. The specimens were loaded at the mid-span in the latero-medial direction by an impactor at 1.5 m/s. Foam, which was modeled with *MAT_LOW_DENSITY_FOAM in LS-DYNA (LSTC, 2013), covered the impactor to release the stress concentration. A stress-strain curve for the material model is presented in Figure E2.

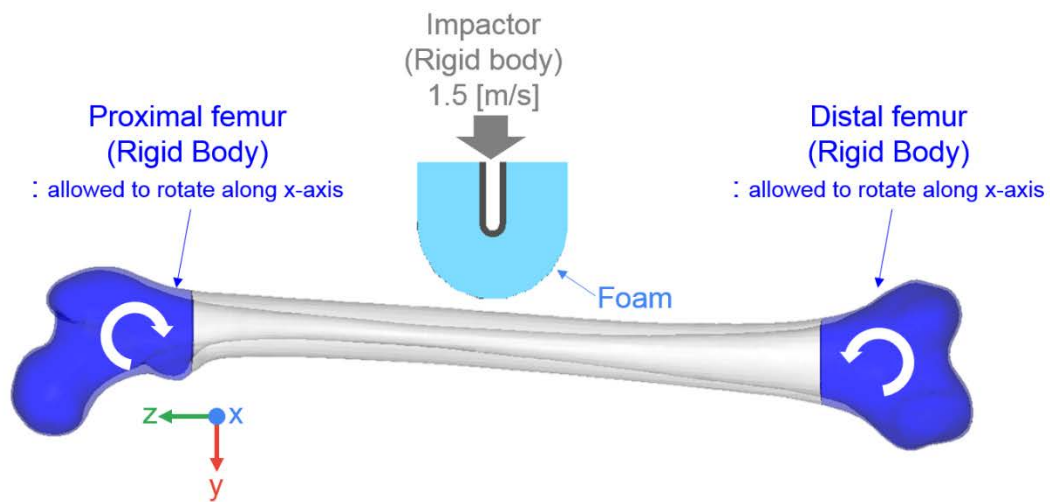


Figure 36 boundary conditions for the FE simulations

After the FE simulations, the moment-at-fracture of the femurs was observed. The moment at the mid-section was estimated by the half of impact force times half of the initial length between the distal and proximal center of rotations. The time of fracture was determined as the maximum principal strain of any element in the femoral shaft region to exceed the ultimate strain sampled from the distribution.

Generation of Injury Risk Functions

Given the moment-at-fracture from the FE simulations, the model-based IRFs were generated using logistic and Weibull regressions for three different occupant sizes (M05: 164.7cm, M50: 175.5cm, M95: 186.8cm) with three different ages (25, 50, and 75 years).

Comparison of Femur Geometry between VPMs and Anthropometry Database

To examine how the geometries of the VPMs similar to those of the actual population, the intertrochanteric (along the bisector of the neck-shaft angle) and the femoral shaft cross-sectional areas (20mm distal to the lesser trochanter) measured from DXA scans of 13,615 patients in the National Health and Nutrition Examination Survey (NHANES) (Beck, 2002) were compared to those of the VPMs. The femoral shaft and the intertrochanteric areas were automatically identified using an in-house MATLAB script (R2015a, The MathWorks Inc., Natick, MA); the location and angles of the planes of the cross-sectional areas were obtained using the center of the pre-defined patches of the femoral head, the lesser trochanter, and the femoral neck.

Validation of Developed IRFs

To check the validity of the model-based IRFs based on the responses of the VPMs, an IRF was generated from the cadaveric test data using logistic regression: the fracture moment of cadaveric specimens in the literature were compiled from previous biomechanical tests; in total, 23 male femurs loaded in lateral-medial direction were included (Forman et al., 2012a). The average age and weight of the specimens were 62.4years and 90.2kg, respectively (Table A4).

Since the geometric distributions of this study were developed with the subject height information, for the purpose of comparison, the VPMs of the occupant with 62.4years and 90.2kg, the average

occupant characteristics of the test set, were re-generated, and the model-based IRF was then generated using logistic regression, based on the moment-at-fracture observed in the FE simulations.

In addition, to answer the question about the required number of the VPMs for generation of IRFs, the coefficient of variation (CV) of the average of moment-at-fracture was calculated as increasing the number of sampling points for the VPMs. For the sampling of the principal scores of GDs, the elastic modulus, and the yield stress, 1000 femurs were regenerated assuming 3% of the ultimate strain as the fracture criterion (common fracture criterion was applied to all 1000 femurs). Then, responses of the VPMs were randomly sampled assuming a uniform distribution without replacement as increasing the number of sampling from 10 to 1000 for 100 trials. Using the mean and one standard deviation of the moment-at-fracture of each trial, the CVs were calculated. For the sampling of the ultimate strain, the number of sampling was increased up to 10000 for 100 trials using one of the VPMs (randomly selected one common VPM was used for all ultimate strains).

Evaluation of IRFs using Scaling Techniques

To check the effectiveness of the current scaling techniques for generation of IRFs, the model-based IRF for 5th percentile subject developed in this chapter was scaled to that of the 95th percentile subject using the mass-based scaling technique (Eq. 1, in Chapter 3) using two different measures for calculation of the scaling factor: occupant height and femur length. These scaled IRFs for 95th percentile subject were compared to the model-based IRF.

5.3 Results

The histograms of the principal scores of the GDs and the material parameters sampled from the Monte-Carlo method are presented in Figure 37 and Figure 38 and, respectively.

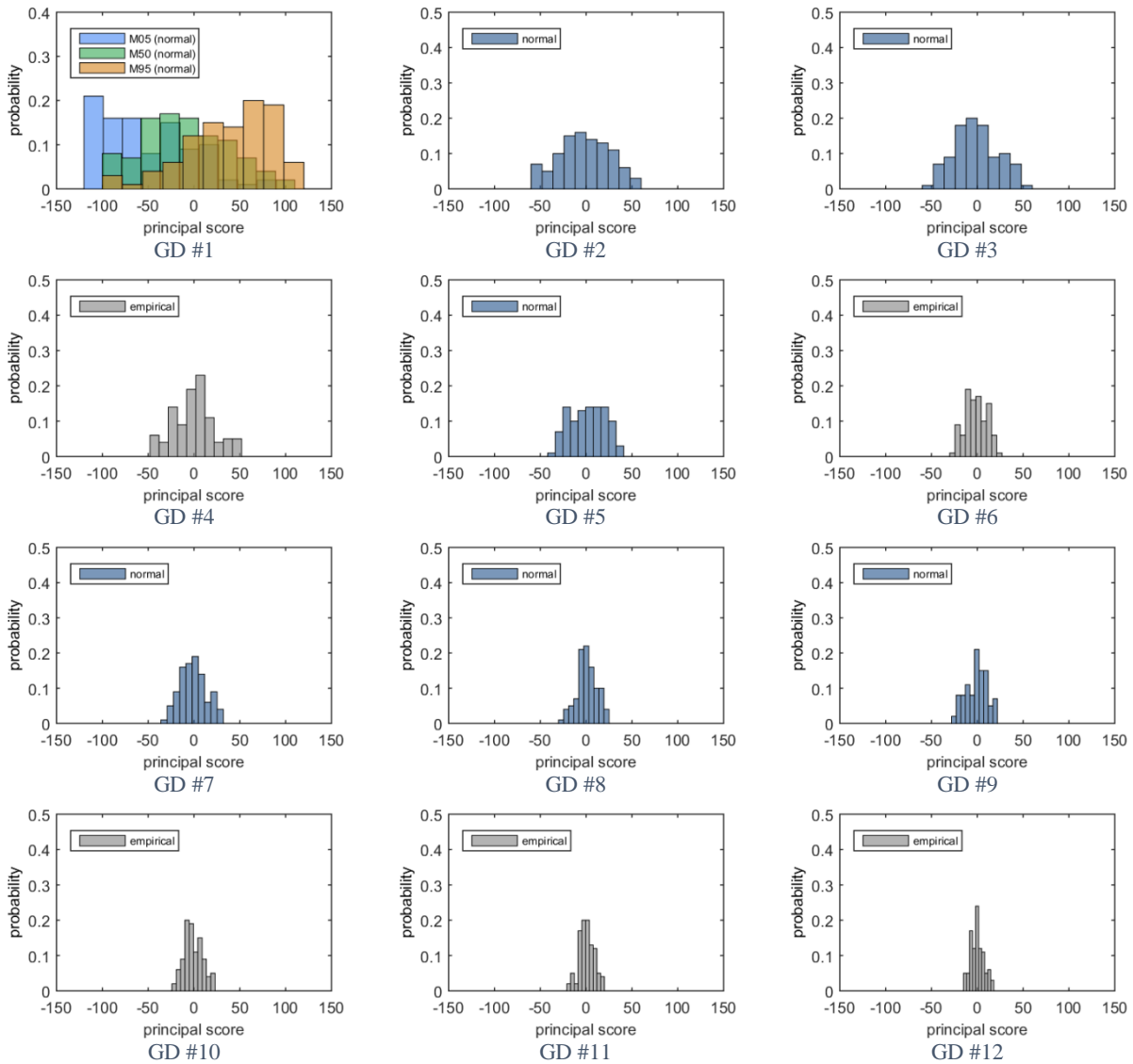


Figure 37 histograms of the principle scores of the GDs

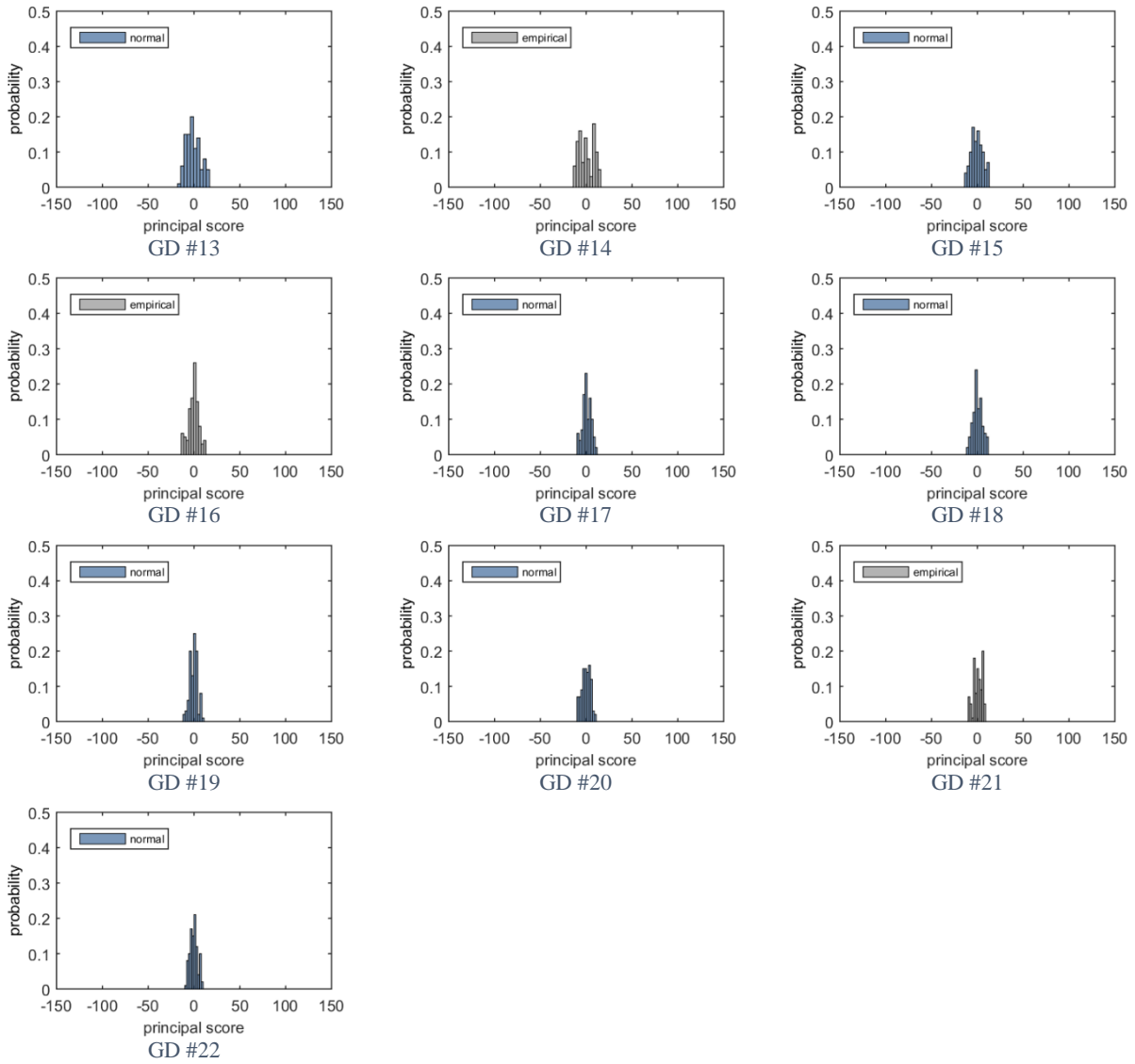


Figure 37 histograms of the principle scores of the GDs (continued)

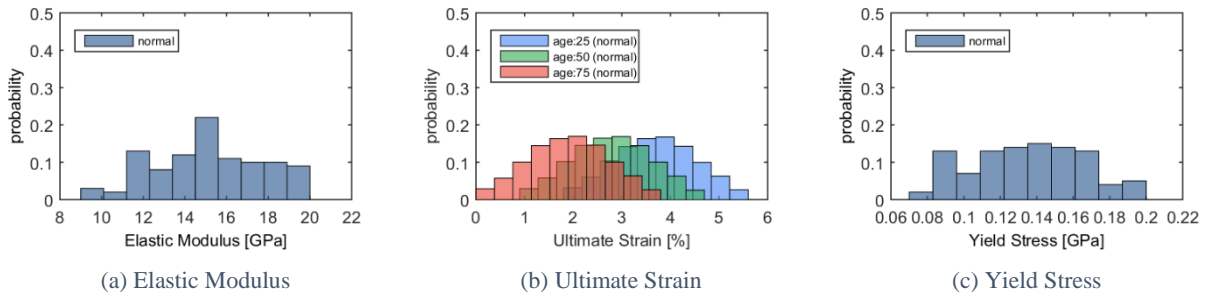
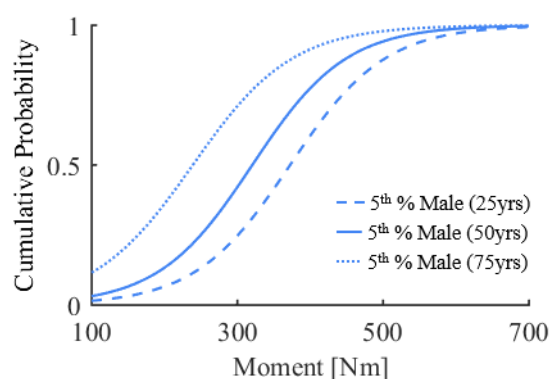
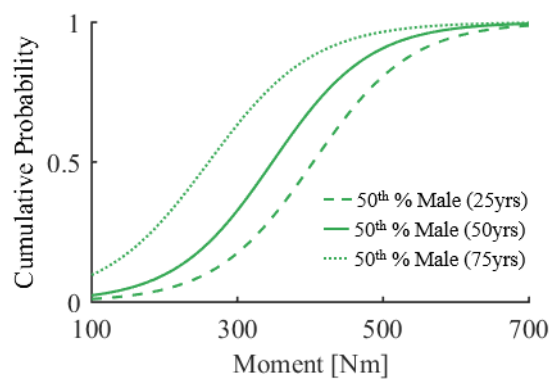


Figure 38 histograms of the input material parameters

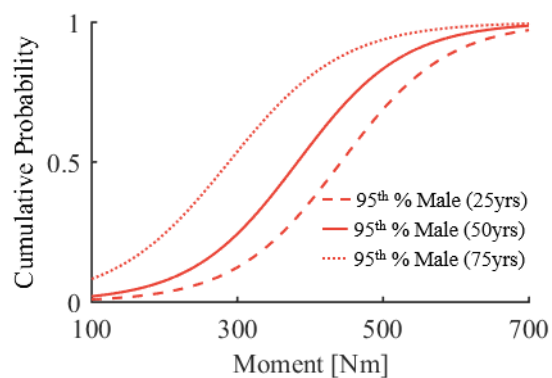
The model-based IRFs developed for dynamic 3-point bending of the human femur in the lateral-medial direction for three occupant sizes and ages are presented in Figure 39; injury risks increased as increasing age and decreasing occupant size of the specimen.



(a) 5th percentile male: height=164.7cm



(b) 50th percentile male: height=175.5cm



(c) 95th percentile male: height=186.8cm

Figure 39 Model-based Injury risk functions for femurs under dynamic pure bending (lateral-medial direction)

The scaled IRFs using the occupant height and the femur height for the calculation of the scaling factor showed a 26% and a 4% higher fracture moment of 50% injury risk than that of the model-based IRF, respectively (50% injury risk in VPM: 451Nm, Scaled w/ occupant height: 568Nm, and Scaled w/ femur height: 471Nm) (Figure 40).

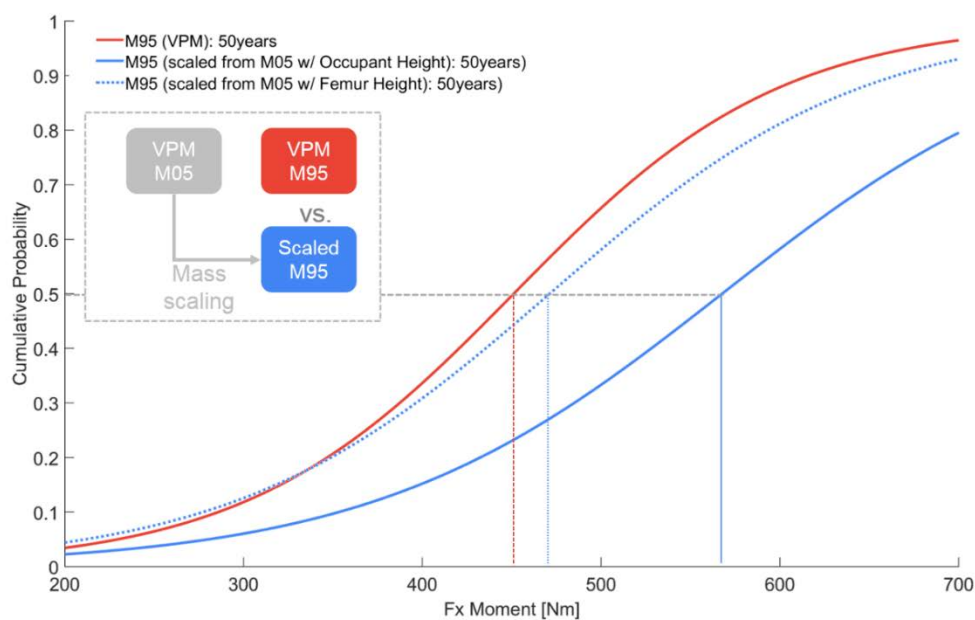


Figure 40 Compare to the scaled IRF

The cross-sectional areas of the intertrochanteric and the femoral shaft of the VPMs (Figure 41) varied from 251 mm to 735 mm and 332 mm to 669 mm, respectively. The range of distributions of the cross-sectional areas of the VPMs was compared to those from 13,615 patients (Figure 42). The cross-sectional shapes and areas of all VPMs (n=300) are presented in (Figure E1).

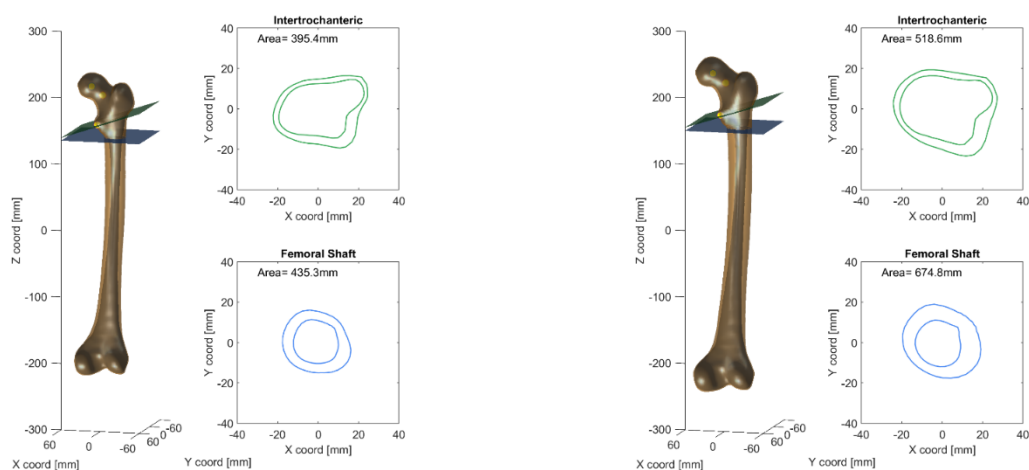


Figure 41 cross-section of intertrochanteric and femoral shaft of VPM #1 (M05) (left) and VPM#100 (right)

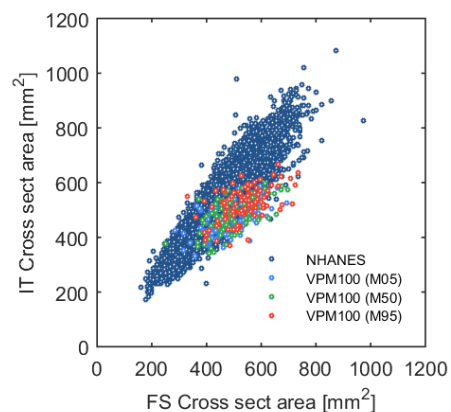


Figure 42 Comparing cross-sectional areas of the VPMs to those from 13,615 patients in NHANES

The model-based IRF for the male occupant with the weight of 90.2kg and age of 62years was located in the 95% confidence interval of the IRF generated from the biomechanical test data (Figure 43) for the range of 15% to 70% injury risks. The 95% confidence interval of the developed IRF was almost in line with the mean curve due to the large number (500,000) of data points.

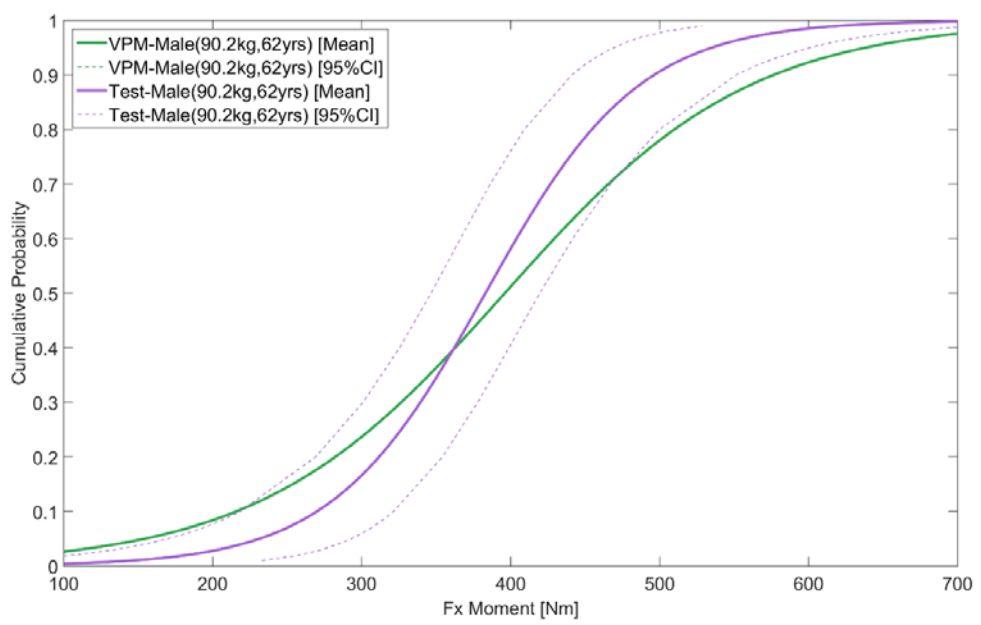


Figure 43 Comparison of the model-based IRF to the IRF developed in a top-down approach

As increasing the number of sampling points, the coefficient of variations was decreased. Less than 2% of the CVs were observed for 5000 trials for the sampling of the ultimate strain and 100 trials for the sampling of the principal scores of GDs, the elastic modulus, and the yield stress (Figure 44).

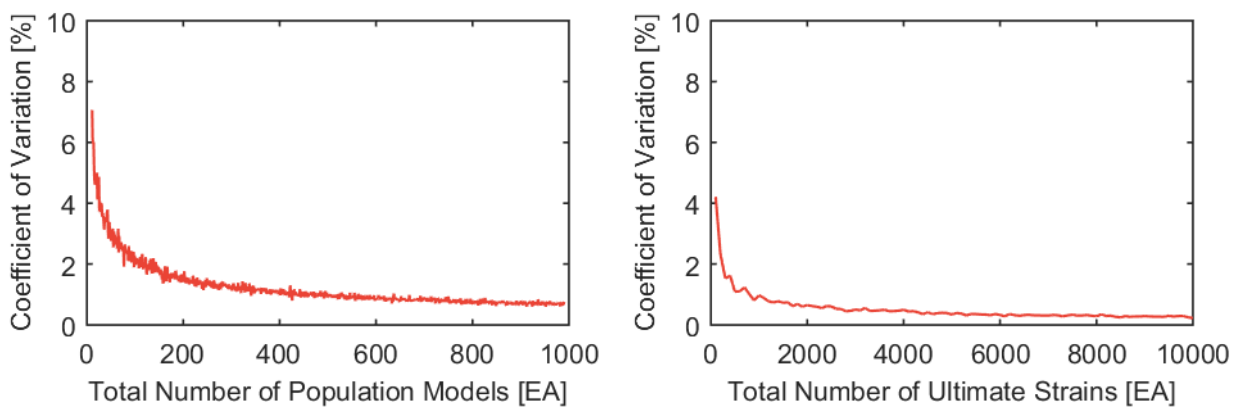


Figure 44 Convergence test: the principal scores of GD, elastic modulus, and yield stress (left) and ultimate strain (right)

5.4 Discussion

This chapter demonstrated the framework for developing IRFs based on the VPM responses. A Monte-Carlo method was implemented to generate populations of FE models of the femur for target occupant characteristics (three different male sizes with three different ages). In total, 100 femur models incorporating the variation in the population of interest were generated for each target occupant. The model-based IRFs were then developed for the femurs subjected to dynamic 3-point bending for target populations.

Significance of Model-Based IRFs

One of the greatest benefits of model-based IRFs was that the range of variabilities was informed by VPM responses. The usage of a top-down approach for developing IRFs, which has been a conventional way of developing IRFs, comes from a lack of knowledge of the relationship between the human variabilities and response (or injury outcome) variations due to the complexity of the human body. In other words, the human variabilities have been considered an “uncontrollable” factor. Contrary to the top-down approach, the model-based IRFs developed in a bottom-up approach already incorporate the information of the human variabilities. Hence, the usage of population-based FE models for the generation of IRFs makes human variability a “controllable” factor. This method would be able to address challenges facing the current development procedure of IRFs for diverse or specialized populations: specifically, this method mitigates the uncertainties in applying empirical scaling and may improve IRF fidelity when a limited number of experimental specimens are available.

Evaluation of the Scaling Techniques Using Model-Based IRFs

Since the information of variabilities in the human femur was already incorporated into the model-based IRFs, the IRFs could be used as a tool for evaluating the effectiveness of applying the scaling techniques for generation of IRFs. The mass-based scaling technique was evaluated in two different ways: using the occupant height and the femur height to calculate the scaling factor.

This result was somewhat obvious because 1) the femur length, in conjunction with the cross-sectional moment of inertia, governs the response of the femur under bending and 2) the first geometric descriptor of the human femur explained 40% of shape variance (Figure 31) and varied up to 50mm length difference even in the same size occupant height. In other words, the mass-based scaling with the occupant height to compensate for anthropometric differences between individuals ends up losing the key geometric variability in the human femur. On the other hand, the mass-based scaling using the femur height resulted in a 4% difference in the fracture moment for 50% injury risk to the model-based IRFs. This result demonstrated that applying the mass-based scaling using the femur height would be a feasible way developing IRFs of the human femur (if the 4% difference is considered as an acceptable range).

Model-Based IRFs for Diverse or Specialized Population

Even though applying the mass-based scaling technique with the femur height would result in similar injury risks (4% difference in the fracture moment for 50% injury risk) to those of the model-based IRF, the model-based IRFs still have an advantage over IRFs developed in the top-down approach. First, model-based IRFs would be able to result in a better fit for “tail” regions than IRFs developed in a top-down approach. The result of this study showed that the model-based

IRF showed more deviation in injury risk from that of the IRF developed in top-down approach as it approaches tail regions (Figure 43). This result may stem from a narrow range of distribution of specimens available. In other words, biomechanical specimens obtained for testing may tend to populate closer to the median of distribution than the tail of distributions. Contrary to IRFs developed in a top-down approach, the observations for developing model-based IRFs were sampled from probabilistic distributions covering up to 1.96 standard deviations.

More importantly, the model-based IRF would become more beneficial when it comes to generating IRFs for diverse or specialized populations. It is noted that the scaling technique in this chapter was applied to the scaling of the fracture moment between the same sex and age. In other words, the assumption on material property similitude in the mass-scaling technique would be valid. However, if the scaling were applied to specimens with different sex or ages, the assumption on material property similitude would not be feasible. Since the model-based IRFs are able to incorporate the range of variabilities of the material parameters, this method would become more promising for generation of IRFs for diverse or specialized populations. Hence, further studies need to focus on investigating material parameters in those populations.

Validity of VPMs and Model-Based IRFs

The synthesized VPMs showed a similar range of shape variabilities (the cross-sectional areas of the intertrochanteric and the femoral shaft, 20mm distal to the lesser trochanter) to those from measurements of patients as well as the correlation between two geometric shapes (Figure 42). This result demonstrates the feasibility of the VPMs for representing the geometry of the target populations.

The model-based IRF for the male occupant with the weight of 90.2kg and age of 62years was generated and compared to the IRF developed based on responses of the femur from the tests to check the validity of the framework. The model-based IRF predicted a similar fracture moment for 50% injury risk to that of the IRF based on test responses. Also, the model-based IRF was located in the 95% confidence interval of the IRF based on test responses for the range of 15% to 70% injury risks. It was noted that the 95% confidence interval of the model-based IRF was almost duplicated with the line of the IRF. These results not only confirmed the validity of the proposed framework but also showed a significantly improved IRF fidelity compared to the test-based IRF due to the large number of the dataset (the number of the dataset in the model-based IRF: 500,000 and test-based IRF:23).

In this study, 100 points were sampled from the distributions of principal scores of the GDs, the elastic modulus, and the yield stress and 5000 points were sampled from the ultimate strain. To answer the question on effects of the number of sampling points, the coefficient variations (CVs) were calculated as increasing the number of VPMs (Figure 44). Even though the number of sampling points for the principal scores of GDs, the elastic modulus, and the yield stress increased up to 1000 from 100, the injury risk showed a 1% difference in CV. Also, increasing the number of sampling points up to 10000 for the ultimate strain resulted in less than a 0.1% difference in CV compared to the case of 5000 sampling points. Besides, increasing the number of sampling points for three variables (geometric descriptors, the elastic modulus, and the yield stress) requires a significant increase in computational cost. Hence, the number of sampling points used in this study would be feasible with the consideration of both accuracy and efficiency of the models.

This study assumed the independence between the geometric descriptors and the material parameters. Thus, further analysis needs to address the correlation between them. On the other hand, the independence between the material parameters were valid since the correlation between the material parameters showed either the independence or weak correlation between the parameters (Figure 45): the elastic modulus and the ultimate strain showed a statistically significant ($p < 0.05$) but weak negative correlation ($r = -0.23$) while the correlation between the elastic modulus and ultimate strain, and the ultimate strain and the yield strain, did not show statistically significant correlation ($p > 0.05$).

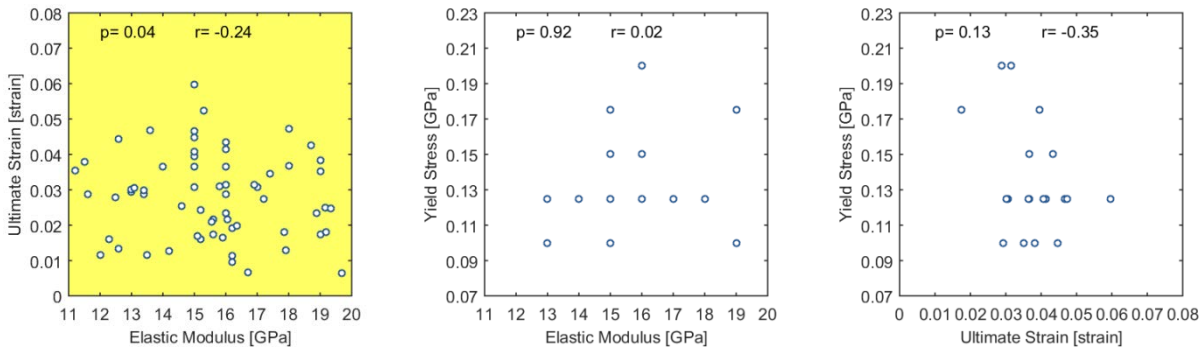


Figure 45 Correlation analysis between material parameters

This study sampled ultimate strains separately from the sampling for the generation of population-based femur FE models to improve the efficiency of the analysis. Rather, the sampling of the ultimate strain was conducted during the post-processing step; this method allowed to increase the number of observations without increasing the number of FE simulations. Thus, further study needs to be investigated focusing the effect of the separation of sampling of the ultimate strain from the generation of population-based FE models.

CHAPTER 6: A CLOSED-FORM OF MODEL-BASED INJURY RISK FUNCTIONS FOR APPLICATION TO FEMURS OF ANTHROPOMETRIC TEST DEVICES UNDER A FRONTAL OBLIQUE CAR CRASH TEST

Chapter 5 demonstrated the framework for developing injury risk functions (IRFs) in the bottom-up approach based on the responses of the population-based FE models. Using the framework demonstrated, this chapter generated a closed-form of IRFs for application to the femur of the ATDs under a frontal oblique car crash test.

6.1 Introduction

The recent analysis of types of injuries from car crashes showed that lower extremities were the leading injured body region, and femur fractures, as part of the knee-thigh-hip (KTH) complex, were observed for occupants in car crashes; injury to the KTH complex accounted for approximately 55% of AIS 2+ lower extremity injuries (Kuppa et al., 2001) and femoral shaft fractures explained 32% of the KTH injuries (Rupp, 2006). To assess the risk of femur fracture, the only injury criterion currently introduced in FMVSS208 and in NCAP is 10kN of axial femur force for the 50th percentile male (Kennedy et al., 2004). The assessment of the femur fracture using a peak femur axial load of the ATDs is based on the injury mechanism, an axial load transferred through the knee impacting the knee bolster, under frontal and offset test conditions. Although the current regulation has assessed the femur fracture solely relying on the axial femur force, it may not be sufficient to evaluate the femur fracture under car crash conditions. Specifically, the major loading path of the human femurs would be not only the axial load through the knee but also 1) the sagittal bending in frontal crashes due to the knee into the dash, slipping

below the lower dash, and impact of the thigh against the steering wheel or steering column (States, 1986) and 2) the lateral bending in oblique or offset crashes, which has become of interest in the automobile safety field. On December 16th 2015 NHTSA released a Request for Comments (RFC) announcing the intension to introduce another USNCAP update. NHTSA announced the intention to introduce a new frontal oblique test. Hence, there needs to be a consideration of new femur injury criteion incorporated more loading components for the assessment of femur fracture under the new test condition.

There is one study available focusing on the effect of bending with axial compression on femoral shaft fracture (Ivarsson et al., (2009); Ivarsson et al. investigated the effect of combined loading condition using cadaveric specimens and concluded that the bending of the femur in the posterior-anterior direction reduces the tolerances of the femoral shaft to axial compression which would contribute to the high prevalence of femoral shaft fracture in frontal crashes. While this biomechanical test helps clarify the underlying mechanism of the femoral fracture under car crash conditions, IRFs for the human femur under car crash conditions resulting in complex loading modes to the femur have not been addressed.

The goal of this chapter was to develop IRFs for application to the femur of the ATDs under a frontal oblique car crash condition. First, loading conditions of the femur sustained during car crashes were identified through the publicly-available NHTSA crash test database. Second, the SS-FE models of the femur under combined loading (bending with axial compression) conditions were developed and validated as the way conducted in Chapter 3. FE simulations of the human femur were then performed for various loading conditions according to the loading conditions

identified in the first step of this chapter. Finally, a closed-form of IRFs was generated based on the responses of the VPMs using survival analysis with a multivariate logistic model.

6.2 Methods

NHTSA Crash Database

To elucidate the loading conditions of the human femur during a car crash, an analysis of crash tests in the publicly-available NHTSA crash test database was performed. The NHTSA crash test database was compiled for frontal and oblique full vehicle crash tests with NCAP-style barriers either with the THOR dummy or with the Hybrid III dummy. The sensor data collected from the femur load cell of the ATDs in the frontal driver seat and a range of forces and moments were analyzed for 75 tests (Table F1). The polarity of the femur load cell is presented in Figure 46 (SAE, 1994).

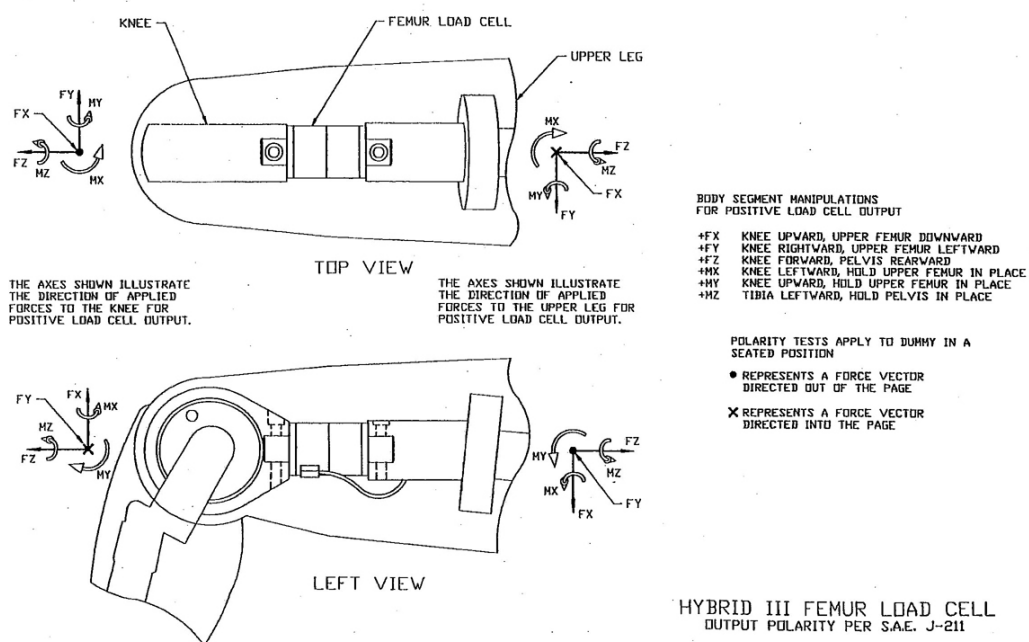


Figure 46 sign convention for the femur load cell of Hybrid III

Validation of the SS-FE Models for Combined Loading Conditions

To ensure the fidelity of developed SS-FE models in Chapter 2 for complex loading conditions, the SS-FE models of the femurs under combined loading tests (bending with axial loading up to 8kN) of twelve bare femurs (described by Ivarsson et al. (2009)) were generated (Figure 47). FE simulations were then conducted, and the results of the simulations were compared to the experimental results. The simulation condition was similar to that of the pure bending cases (Forman et al., 2012a) with the exception that three levels (0kN, 4kN, 8kN) of axial compression were added to the bending. In total, tests performed on 12 specimens (Table A2) were simulated using the SS-FE models. The inertia properties of the test apparatus were taken into account by using the 3D CAD geometry and density of each component. The potting material, inside the blocks of proximal and distal ends of the femur with a density of $1.0 \text{ [g/cm}^3\text{]}$, impactor, and test fixtures were assumed as a rigid body. Also, the elements of femur inside the volume of potting material were assumed as a rigid body constrained by the potting volume.

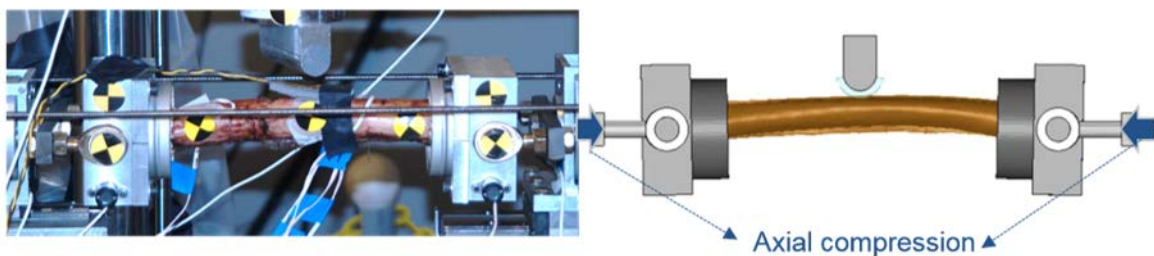


Figure 47 Biomechanical tests (left) and FE simulations (right) for combined loading test conducted by Ivarsson et al. (2009)

A piecewise linear plastic material model (LSTC, 2013) was used as the material model for the SS-FE models, and the maximum principal strain was used as fracture criterion for the analysis. The material parameters for the SS-FE model with a material fit were determined which minimized

the RMS error and the fracture force difference for each individual specimen. The identified material parameters were compared to those from the literature and the SS-FE models with material fit under dynamic bending in Chapter 3 (Figure 27).

Generation of IRFs

Given validated SS-FE models of the femurs under combined loading conditions, FE simulations were conducted using the VPMs of three target male occupant sizes (5th, 50th, 95th in height) and three ages (25, 50, 75 years) developed in Chapter 5. Two directions of bending (MX+ and MX-) with three levels of axial loading (0, 4, 8kN) were applied to the femur VPMs based on an analysis of the NHTSA crash database (see results section). Using the moment-at-fracture of VPMs under combined loading conditions from the FE simulations, a closed-form of the IRFs was generated using survival analysis with a multivariate logistic model using height, age, axial loading, and direction of loading as covariates. The MX- direction bending was coded as “0” and MX+ direction bending was coded as “1” in a regression model.

6.3 Results

The loading conditions that the femur of the ATDs sustained during car crashes are presented in Figure 48. Axial compression (FZ-) and moment in the lateral-medial or medial-lateral directions (MX-) were the two main loading paths to the femurs followed by posterior-anterior bending (MY+).

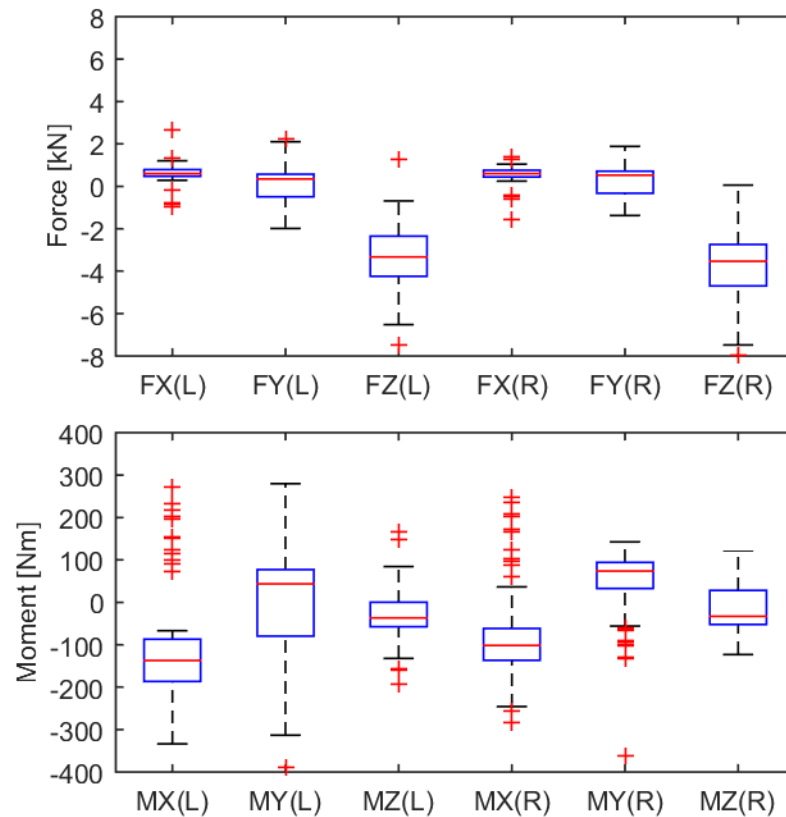


Figure 48 femur loads during car crash: forces (upper) and moments (lower)

Figure 49 represents a visual illustration of the accuracy of the SS-FE models. The average minimum distance error is less than 1mm for both the outer and inner surfaces, and the difference in cross-sectional areas are less than 3% (Table B3).

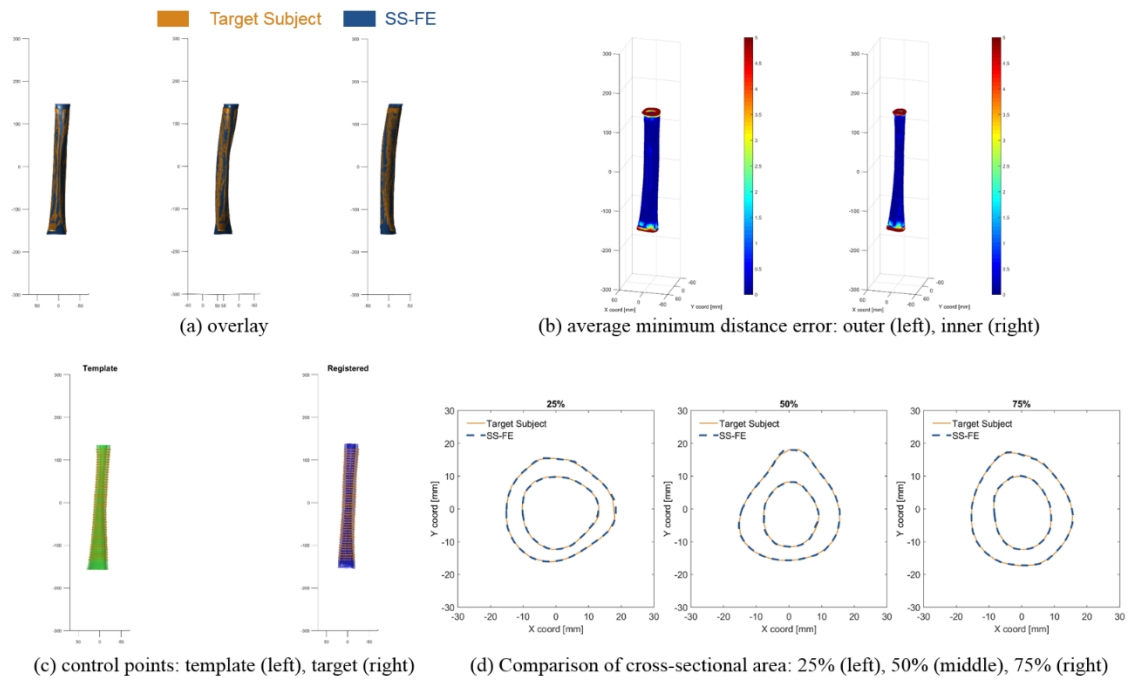


Figure 49 Accuracy of SS-FE models for the specimens of Ivarsson et al. (2009)

Figure 50 compares the impact force time histories between the SS-FE models with a material fit and femur specimens from the tests conducted by Ivarsson et al. (2009). The impact force time histories of the SS-FE models with a material fit showed a good correlation with those from the test specimens.

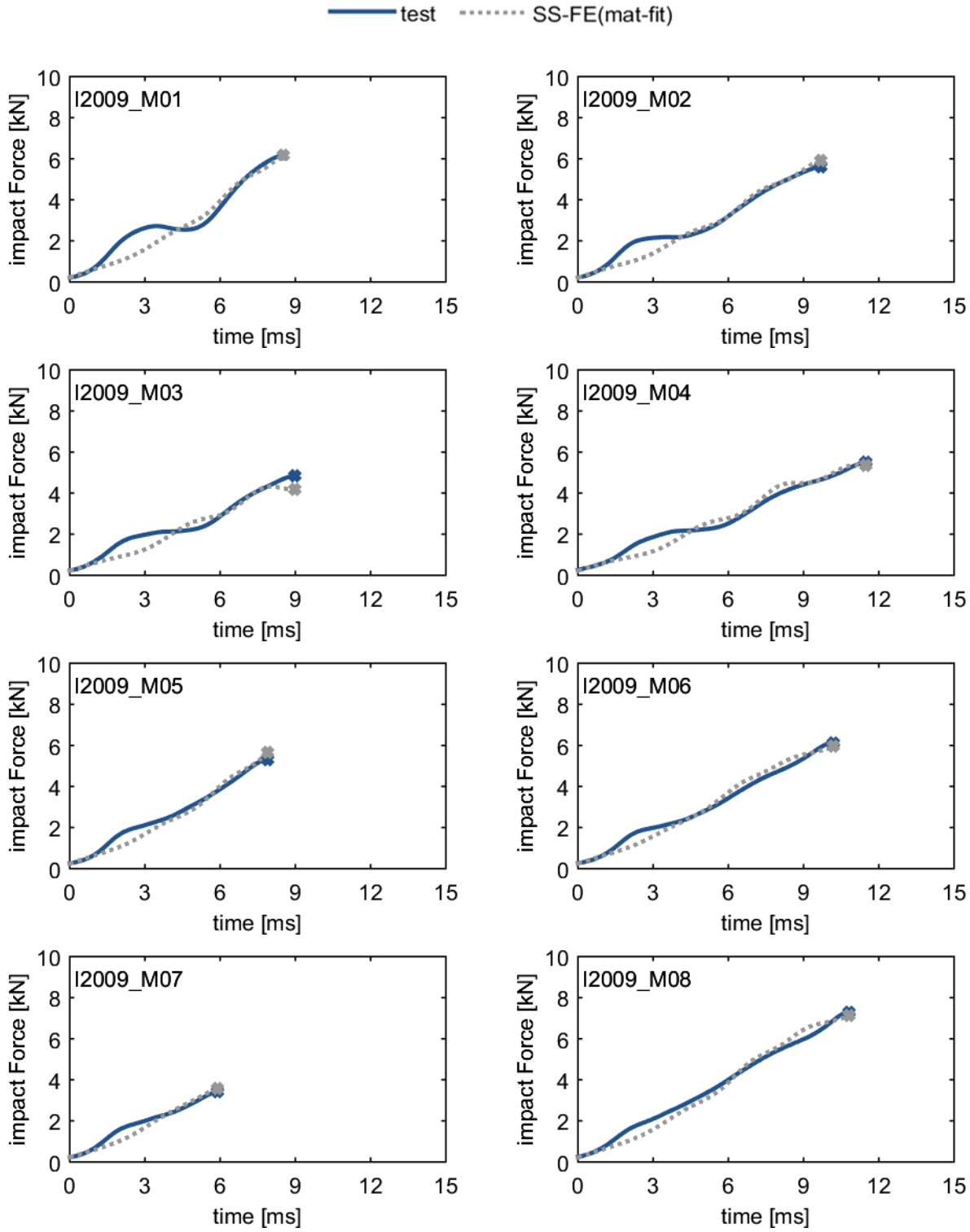


Figure 50 Comparison of impact force histories between test, SS-FE and SS-FE models with a material fit for femur specimens of Ivarsson et al. (2009). X indicates the femur fracture

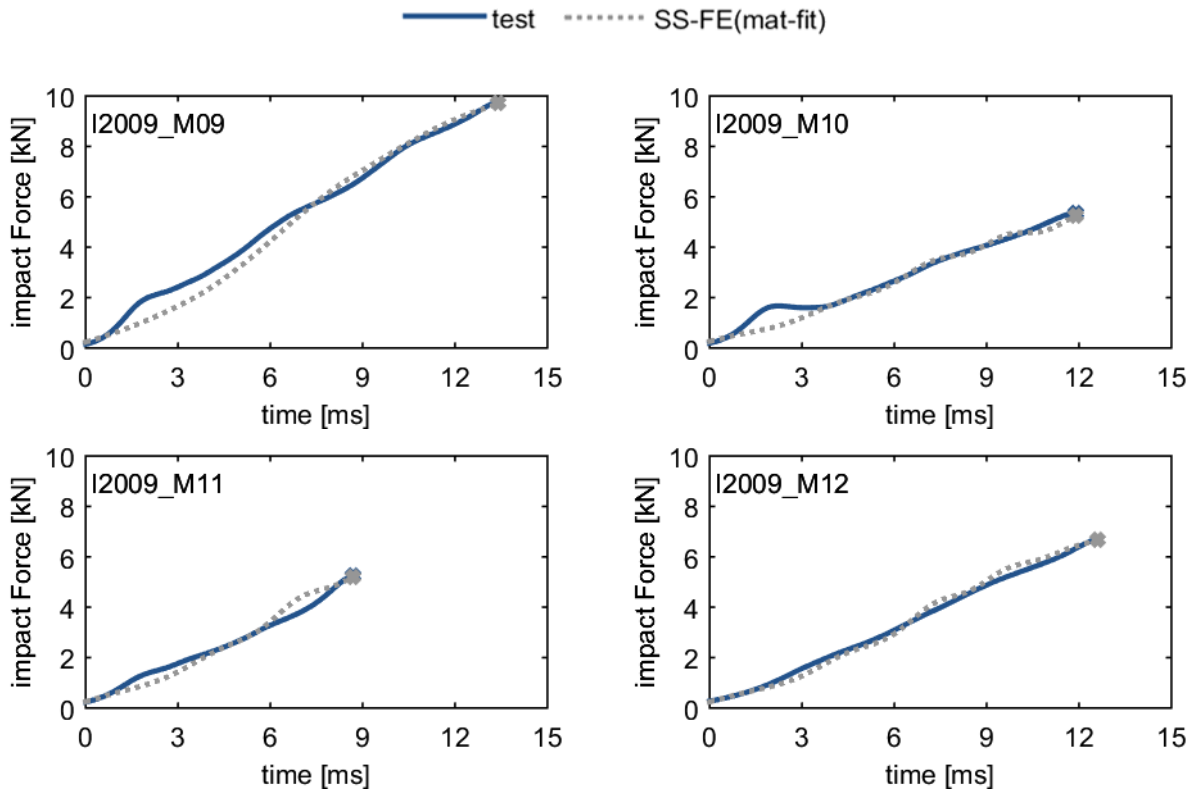


Figure 50 Comparison of impact force histories between test, SS-FE and SS-FE models with a material fit for femur specimens of Ivarsson et al. (2009). X indicates the femur fracture (continued)

The material parameters identified for individual specimens showed a similar range of distributions to those from the literature and to those identified from specimens under pure bending cases using the SS-FE model with a material fit in Chapter 3 (Figure 51).

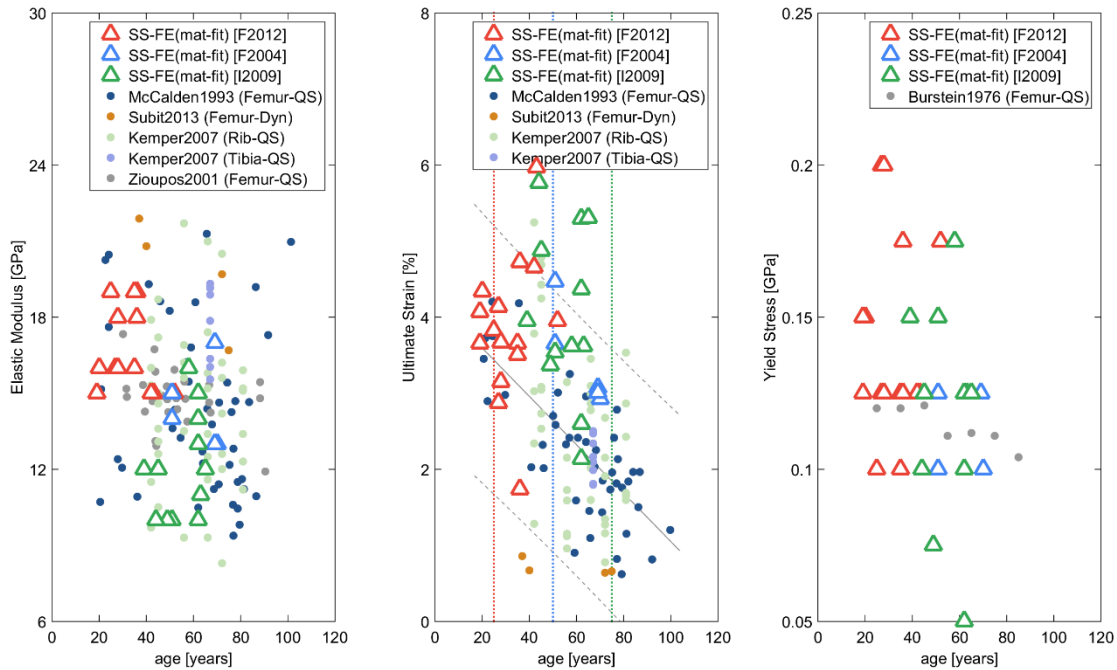


Figure 51 comparison of material parameters: coupon tests from literature (circle) and material fit using SS-FE (triangle). Elastic modulus (left) and ultimate strain (right)

The closed-form of IRFs for the application to the femur of the human surrogates (such as ATDs and FE HBMs) under a car crash was developed from 27 million observations (50k observations for each 9 target occupants with 6 loading cases) (Eq. 7). The moment-at-fracture (M) about x-axis was used as a predictor in the equation. All four covariates (occupant height [H], age [A], level of axial compression [AC], and loading direction [D]) showed statistically significant effects on the response (p-value < 0.05). Figure 52 presents the effect of each covariate in Eq. 7 as an example.

$$P = 1 - \left[\frac{1}{1 + e^{\{0.0140 \cdot M - 2.2494 - 0.0327 \cdot (H) + 0.0393 \cdot (A) + 0.1844 \cdot (AC) + 0.6240 \cdot (D)\}} \right] \quad \text{Eq. 7}$$

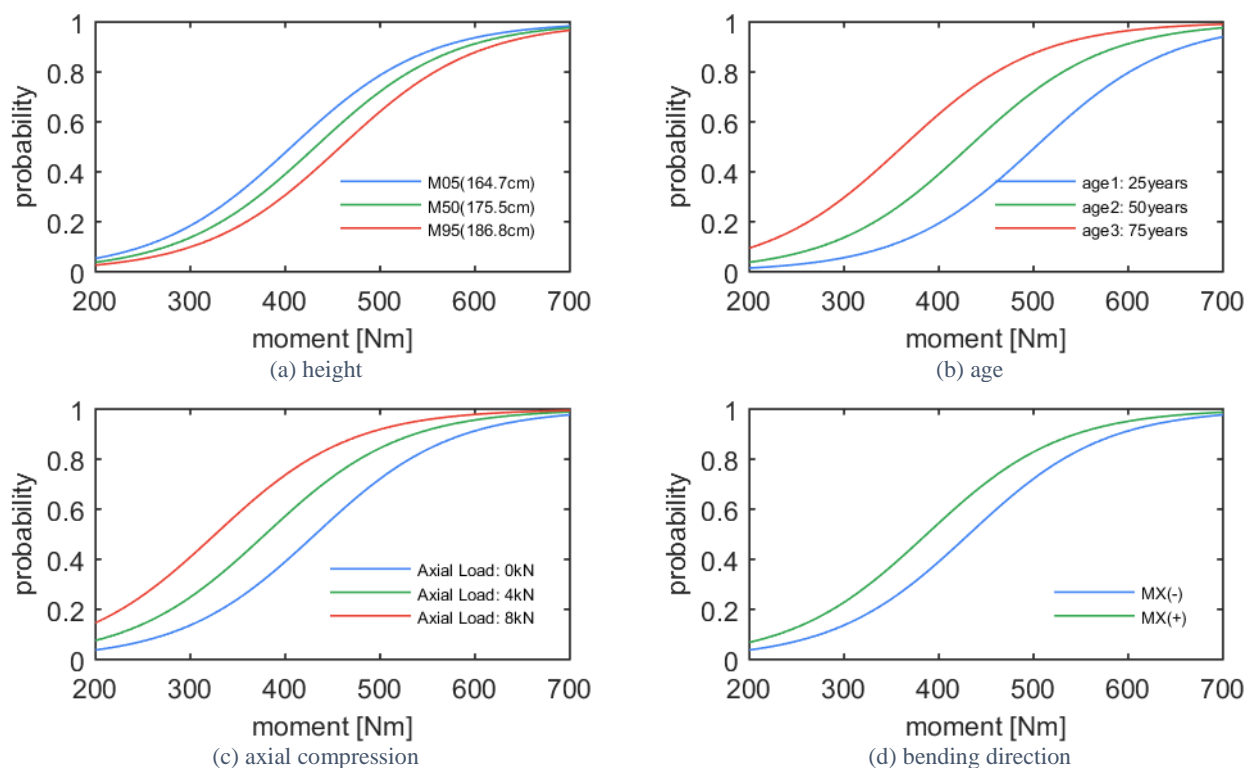


Figure 52 Example of model-based IRF for different covariates: baseline case (M50, 50years, 0kN axial load, lateral-medial direction)

6.4 Discussion

In this chapter, the closed-form of IRF for application to the femur of the human surrogates under car crash conditions was developed using survival analysis with a multivariate logistic model.

Loading Conditions of the Femur under Car Crashes

Based on the loading conditions identified, the femur of the ATDs was mainly loaded by axial loading and the bending moment in lateral-medial direction. The loading conditions identified from the NHTSA crash database included the oblique, offset, and frontal test conditions. Thus, axial loading might result from the interaction between knee and knee bolster or knee airbag, and the bending moment may mainly come from the interaction of the femur with side door panel or

occupant lateral/yaw motion due to inertia effect. Hence, these identified loading conditions from the NHTSA crash database demonstrated the limitation of using the axial compression for injury criterion to assess the femur fracture during car crashes.

Application of Developed IRF

The developed closed-form of IRFs could be used for the femurs of the ATDs (such as Hybrid III M50 and THOR M50 implemented with six-axis load cell) or parametric FE human body models. It is noted that this IRF is only applicable for male ATDs with different sizes. In other words, IRFs for female ATDs needs to be developed through the proposed framework in this study by consideration of female geometry in a statistical shape analysis and identification of material parameters.

The closed-form of IRFs developed in this chapter took into account two main loading paths; axial compression and the lateral-medial direction bending. The third dominant loading path, the posterior-anterior direction bending, and the interaction effect between the bending directions needs to be further investigated following this study.

Validation of the Femur SS-FE Models under Combined Loading

The closed-form of IRFs developed in this chapter intended to include not only a bending moment but also an axial compression to represent the loading condition femur sustained during a frontal oblique crash test. Since the femur FE model was validated under the pure bending condition in Chapter 3, the validity of the femur FE model under the combined loading condition, a bending with an axial compression, was verified prior to developing the model-based IRFs using the framework in this study.

The femur FE models in this chapter implemented the piecewise linear plasticity model with the maximum principal strain as a fracture criterion. Previous studies demonstrated that the cortical bone showed asymmetric response under tension and compression (Burstein et al., 1976; Hansen et al., 2008). Even with this asymmetric characteristics of the cortical bone, the results of distributions of material parameters identified for individual SS-FE models, which is under the range of those from the literature, demonstrated that the piecewise linear plasticity model was still applicable for, at least, the loading conditions considered in this chapter. It may come from a little contribution of axial compression to offset the stress state in the femur. The level of axial loading (maximum: 8kN) induced 15 [MPa] compression stress for the femur, whose average mid-shaft cross-sectional is around 540 [mm²] based on the VPMs developed in Chapter 5. This levels of axial compression is 8% of the ultimate stress of the cortical bone under compression. In addition, even with the bending stress offset due to 15 [MPa] axial compression, the fracture was likely to occur at the tension side based on 45% ultimate stress difference in the cortical bone under tension and under compression (ultimate stress (tension) = 190 [MPa] / ultimate stress (compression) = 130 [MPa]) (Burstein et al., 1976). Thus, the constitute model used in this chapter would be still valid under the loading condition of this chapter. Under the loading condition with more contribution of axial loading, the constitutive model considering asymmetric plasticity implemented in LS-DYNA (*MAT_PLASTICITY_COMPRESSION_TENSION, MAT124) would help model the asymmetric bone characteristic (Khor et al., 2016; LSTC, 2013).

CHAPTER 7: CONCLUSIONS

7.1 Concluding Remarks

The goal of this dissertation was to explore a framework for developing injury risk functions (IRFs) in a bottom-up approach based on responses of parametrically variable finite element (FE) models representing exemplar populations. To achieve the goal of the dissertation, in Chapter 2, the femur FE modeling tool was first developed to generate the subject-specific femur models using the geometric information from the medical images in a programmatic way. Given the template femur FE model and medical images of the target subject, the femur FE modeling tool automatically finds correspondence between two geometries and transformed the template model geometry to that of the target subject. The transformed femur FE models showed the average minimum distance error to the target surface less than 1mm for both inner and outer surfaces and less than 5% difference of cross-sectional area of the femoral shaft.

Then in Chapter 3, using the femur FE modeling tool developed in Chapter 2, the FE models of the femur subjected to dynamic 3-point bending were validated through a SS-FE modeling approach. The results of SS-FE modeling confirmed the predictive capability of the femur FE model for the structural response and fracture force of individual specimens. Distributions of material parameters of the individual specimen from the SS-FE models with a material fit were compared to those from the literature; they were located in the range of material parameters from the literature. Thus, the result of the SS-FE modeling demonstrated that the femur FE models could predict the individual response and fracture of the femur under dynamic loading conditions if the models properly capture the geometric and material property variabilities of the human femurs.

Finally, the distributions of material parameters of cortical bone for three target occupant ages (25, 50, and 75 years) were generated from distributions of the material parameters in the literature using regression analysis for the purpose of generation of population-based FE models in Chapter 5.

Following the SS-FE modeling approach, in Chapter 4, principal component analysis and regression were used to identify parametric geometric descriptors of the human femur, and the principal score distributions of those factors for three target occupant sizes (5th, 50th, and 95th percentile males). The results demonstrated that the first principal component (related to the size of the femur) explains 40% of the geometric variance shown in the femurs and the first 22 principal components account for 95% of the geometric variance. In addition, this study demonstrated that including the first 22 principal components, referred to as the geometric descriptors (GDs) in this study, for synthesizing a new femur shape (PCA-FE model), resulted in good reconstruction results regarding the geometry (0.56mm of the minimum distance error), the structural response (0.02kN of RMS error – 0.4% of the peak fracture force), and the fracture prediction (0.13kN of fracture force – 2.5% of the peak fracture force).

Using the identified distributions of material parameters (Chapter 3) and principal scores of GDs (Chapter 4), a Monte-Carlo method was then implemented to generate populations-based FE models of the femur for target occupants in Chapter 5. In total, 100 femur models incorporating the variation in the population of interest were generated for each target occupant. Simulations were then conducted with each of these models under 3-point dynamic bending. Model-based IRFs were then developed using logistic regression analysis, based on 500,000 observations (100 femur models with 5,000 ultimate strains) of the moment-at-fracture in the FE simulations dataset. The

range of intertrochanteric and femoral shaft areas of the synthesized population models showed them to be in the similar range as the 13,614 patients in the National Health and Nutrition Examination Survey. The validity of the model-based IRF was confirmed; the model-based IRF was located in the 95% confidence interval of the IRF developed in a top-down approach using test data except for the tail regions. Also, the model-based IRF was utilized to evaluate the effectiveness of the mass-based scaling for generation of IRFs, and the results showed that using the femur height for calculation of the scaling factor resulted in a better accuracy (4% fracture force difference from that of model-based IRF) than using the occupant height (26% fracture force difference).

Finally, in Chapter 6, the closed-form of the IRFs for the application to the femur of the ATDs under a frontal oblique crash condition was developed using survival analysis with a multivariate logistic model using the occupant height, age, axial loading, and loading direction as covariates. To identify the loading conditions of the femur during car crashes, the NHTSA crash test database was compiled. The result demonstrated the two main loading paths of the femur (axial loading, and the x-axis bending) and the need for consideration of combined loadings for assessment of femur fracture, rather than only using axial compression as the current injury criterion in regulations. Simulations were then conducted using the population-based FE models under the identified main loading paths. The closed-form of model-based IRFs was developed based on 27 million observations of moment-at-fracture from the FE simulations. The closed-form of the IRFs was developed in a bottom-up approach that the range of injury outcome variation was informed by the population-based FE models, which incorporated the femur geometric and material variabilities of target occupant characteristics into the models. Also, it considered combined

(lateral bending with axial compression) loading conditions femur sustained during car crashes, instead of only considering axial force, as well as the occupant characteristics (the height and the age) for injury assessment.

7.2 Contributions

The main contribution of this dissertation is the demonstration of the framework for developing IRFs in a bottom-up approach using the population-based FE model responses, which has not been addressed in the field of injury biomechanics. The main benefit of the proposed framework over the conventional way of developing IRFs is that the model-based IRFs can incorporate the information about the range of variabilities informed by the population-based FE model responses. In other words, the variabilities in the human become controllable using the proposed framework. Most of all, this method mitigates the uncertainties in applying empirical scaling and may improve IRF fidelity when a limited number of experimental specimens are available, especially for the case of diverse or specialized populations. It is noted that if empirical scaling techniques were applied to scale the response between specimens with different sex or ages, the assumption on material property similitude may not be valid. Since model-based IRFs are able to incorporate different distributions of material parameters for target occupants with different sex or ages, this method would become more promising for generation of IRFs for diverse or specialized populations. Also, the model-based IRFs would be able to result in a better injury prediction for “tail” regions than the test-based IRFs. The result of this study showed that the model-based IRF showed more deviation in injury risk from that of the test-based IRF as it approaches tail regions. This result may stem from that the cadaveric specimens obtained for testing tend to populate closer to the median of distributions than the tail of distributions. Contrary to the test-based IRFs

developed in a top-down approach, the observations for developing model-based IRFs were sampled from probabilistic distributions covering the tail regions which would result in a better prediction for tail regions. Also, it was noted that the 95% confidence interval of the model-based IRF was almost duplicated with the line of the IRF due to the large number of the dataset (the number of the dataset in the model-based IRF: 500,000 and the test-based IRF:23), which indicates a significantly improved fidelity of injury prediction compared to the test-based IRF.

Second contribution would be that this dissertation has developed the tool for the population-based FE modeling and the generation of model-based IRFs of the femur. Data required for analysis is only the outer and the inner surfaces of the femur in STL format from medical images. Given more medical images for different gender and wide age spans, this tool could be easily utilized for the future study of the population-based FE modeling of the femur.

To exemplify the framework, this dissertation has developed the closed-form of model-based IRFs for the application of the femur of the ATDs and parametric FE HBMs under car crash conditions. So far, the assessment of the femur has relied solely on the axial compression. Due to increased interests in oblique and offset crash conditions in the automobile safety field, the IRF developed in this study would offer a better assessment of the risk of femur fracture than the current criterion.

Also, this dissertation addressed the validation of the FE model using a component level SS-FE modeling technique. In the field of injury biomechanics, SS-FE modeling techniques have been studied by many researchers focusing on the development of morphed human body FE models. While previous studies on the morphed human body FE models have provided insight into the potential of these techniques, validation of component-level test data as the way conducted in this

study would be a useful supplement for those studies to identify key validation goals for SS-FE and population-based FE models.

7.3 Future Research Directions and Limitations

Following this study, further research on statistical shape analysis and material testing of female and pediatric specimens needs to be addressed to develop IRFs for a diverse population. Klein et al. (2015) showed the difference in the geometry of the femur regarding the cross-sectional area along the long bone direction. In addition to the geometric difference, McCalden et al. (1993) and Wu et al. (2011) claimed there was a difference in ultimate stress and viscoelastic property between male and female. Especially, the significant bone loss is observed in older women after menopause (Zebaze et al., 2010). Also, the material property of pediatric specimens would be quite different from that of adults. Hence, further analysis needs to focus on obtaining the geometric descriptors and material parameters of females and pediatrics.

The subject-specific FE modeling approach in the framework proposed in this study needs to be extended to various loading rates, loading conditions, and other body regions. It is well known that cortical bone is rate dependent and an anisotropic material. Also, bone has a different structure according to its function in the body. For example, the proximal region of the femur consists of trabecular bone inside of a thin cortical shell to offer stability against compressive force. For different body regions and loading conditions, a different level of model complexity may be required.

This study assumed an independence between geometric descriptors and material parameters. A further study focused on the correlation between them could refine the results of this study. This

work could be done by obtaining medical images of bulk specimens of coupons and applying a statistical shape analysis for them in addition to material testing to analyze a correlation between the material parameters and geometric descriptors. If the variables showed the correlation, sampling techniques for dependent variables, such as adding the constraint of the covariance matrix, needs to be introduced.

This study sampled ultimate strains separately from the sampling for the generation of population-based femur FE models to improve the efficiency of the analysis. Rather, the sampling of the ultimate strain was conducted during the post-processing step; this method allowed to increase the number of observations without increasing the number of FE simulations. Thus, further study needs to be investigated focusing the effect of the separation of sampling of the ultimate strain from the generation of population-based FE models.

Further research on statistical shape analysis may need to be done using a larger number of medical images with closer sampling distributions to the actual occupant population. Due to the nature of the CT image database of PMHS used in this study, the age of subjects tended to toward elderly (61 ± 13 years) white subjects. Also, this study did not focus on the effect of the number of medical images. While increasing the number of images unequivocally improves the statistical power of the analysis, the optimal number needed for the best results is still unknown. Thus, analysis of the requirement of the number of subjects analyzed would help improve accuracy and efficiency of the analysis.

REFERENCES

- Aamodt, a, Kvistad, K. a, Andersen, E., Lund-Larsen, J., Eine, J., Benum, P., & Husby, O. S. (1999). Determination of Hounsfield value for CT-based design of custom femoral stems. *The Journal of Bone and Joint Surgery. British Volume*, 81(1), 143–147.
- Beck, T. J. (2002). *Hip Structural Analysis (HSA) Program*.
- Besl, P., & McKay, N. (1992). A Method for Registration of 3-D Shapes. In *IEEE Transactions on Pattern Analysis and Machine Intelligence* (Vol. 14, pp. 239–256). Los Alamitos, CA, USA.
- Bryan, R., Mohan, P. S., Hopkins, A., Galloway, F., Taylor, M., & Nair, P. B. (2010). Statistical modelling of the whole human femur incorporating geometric and material properties. *Medical Engineering & Physics*, 32(1), 57–65.
- Burstein, A. H., Reilly, D. T., & Martens, M. (1976). Aging of bone tissue: mechanical properties. *J Bone Joint Surg Am*, 58(1), 82–86.
- Burstein, A. H., Reilly, D. T., Martens, M., Joint, J. B., & Am, S. (1976). Aging of bone tissue : mechanical properties. *J Bone Joint Surg Am.*, 58, 82–86.
- Crandall, J. R., Bose, D., Forman, J., Untaroiu, C. D., Arregui-Dalmases, C., Shaw, C. G., & Kerrigan, J. R. (2011). Human surrogates for injury biomechanics research. *Clinical Anatomy (New York, N.Y.)*, 24(3), 362–71.
- Cutcliffe, H. C., Schmidt, A. L., Lucas, J. E., & Bass, C. R. (2012). How few? Bayesian statistics in injury biomechanics. *Stapp Car Crash J*, 56(October), 349–386.
- Davies, R. H. (2002). Learning shape: optimal models for analysing natural variability.
- Davies, R., Twining, C., & Taylor, C. (2008). *Statistical Models of Shape: Optimisation and Evaluation*. Springer.
- Eppinger, R., Marcus, J., & Morgan, R. (1984). Development of dummy and injury index for NHTSAs Thoracic Side Impact Protection Research Program. *SAE Technical Paper*.
- Eppinger, R., Sun, E., Bandak, F., Haffner, M., Khaewpong, N., Maltese, M., ... Saul, R. (1999). Development of Improved Injury Criteria for the Assessment of Advanced Automotive Restraint Systems - II. *NHTSA*, (November).
- Forman, J. L., Dios, E. del P. de, Symeonidis, I., Duarte, J., Kerrigan, J. R., Salzar, R. S., ... Kent, R. W. (2012). Fracture Tolerance Related to Skeletal Development and Aging Throughout Life: 3-Point Bending of Human Femurs. In *IRCOBI Conference*.
- Forman, J. L., Kent, R. W., Mroz, K., Pipkorn, B., Bostrom, O., & Segui-Gomez, M. (2012). Predicting rib fracture risk with whole-body finite element models: development and preliminary evaluation of a probabilistic analytical framework. In *56th AAAM Annual Conference* (Vol. 56, pp. 109–124). Seattle, WA, United States.
- Funk, J. R., Kerrigan, J. R., & Crandall, J. R. (2004). Plastic Material Properties of the Human Femur. *Association for the Advancement of Automotive Medicine*, 48.
- Giambini, H., Qin, X., Dragomir-Daescu, D., An, K.-N., & Nassr, A. (2015). Specimen-specific vertebral fracture modeling: a feasibility study using the extended finite element method. *Medical & Biological Engineering & Computing*.
- Hansen, U., Zioupos, P., Simpson, R., Currey, J. D., & Hynd, D. (2008). The effect of strain rate on the mechanical properties of human cortical bone. *J Biomech Eng*, 130(1), 11011.

- Helgason, B., Taddei, F., Pálsson, H., Schileo, E., Cristofolini, L., Viceconti, M., & Brynjólfsson, S. (2008). A modified method for assigning material properties to FE models of bones. *Medical Engineering and Physics*, 30(4), 444–453.
- Hwang, E., Hu, J., Chen, C., Klein, K. F., Miller, C. S., Reed, M. P., ... Hallman, J. J. (2016). Development, Evaluation, and Sensitivity Analysis of Parametric Finite Element Whole-Body Human Models in Side Impacts. *Stapp Car Crash Journal*, 60(November), 473–508.
- Ivarsson, B. J., Genovese, D., Crandall, J. R., Bolton, J. R., Untaroiu, C. D., & Bose, D. (2009). The tolerance of the femoral shaft in combined axial compression and bending loading. *Stapp Car Crash Journal*, 53(November), 251–290.
- Jolivet, E., Lafon, Y., Petit, P., & Beillas, P. (2015). Comparison of Kriging and Moving Least Square Methods to Change the Geometry of Human Body Models. *Stapp Car Crash Journal*, 59, 337–357.
- Kemper, A. R., McNally, C., Kennedy, E., Manoogian, S., Tech, V., Forest, W., & Biomechanics, I. (2008). The material properties of human tibia cortical bone. *Biomedical Sciences Instrumentation*, 44(1976), 419–427.
- Kemper, A. R., McNally, C., Pullins, C. A., Freeman, L. J., Duma, S. M., & Rouhana, S. M. (2007). The biomechanics of human ribs: material and structural properties from dynamic tension and bending tests. *Stapp Car Crash Journal*, 51(October), 235–273.
- Kennedy, E. a, Hurst, W. J., Stitzel, J. D., Cormier, J. M., Hansen, G. a, Smith, E. P., & Duma, S. M. (2004). Lateral and posterior dynamic bending of the mid-shaft femur: fracture risk curves for the adult population. *Stapp Car Crash Journal*, 48(November), 27–51.
- Kent, R. W., & Funk, J. R. (2004). Data Censoring and Parametric Distribution Assignment in the Development of Injury Risk Functions from Biomechanical Data Reprinted From: *Biomechanics. Engineering*, 2004(724), 1.
- Kent, R. W., Lopez-Valdes, F. J., Dennis, N. J., Lessley, D., Forman, J., Higuchi, K., ... Arbogast, K. (2011). Assessment of a three-point restraint system with a pre-tensioned lap belt and an inflatable, force-limited shoulder belt. *Stapp Car Crash Journal*, 55(November), 141–159.
- Kerrigan, J., AK, B., NJ, M., JR, F., Bose, D., & JR, C. (2003). Experiments for establishing pedestrian-impact lower limb injury criteria. *SAE International Technical Paper Series*, 2003-01-08, 1–19.
- Khor, F., Watson, B., Gierczycka, D., Malcolm, S., Panzer, M. B., & Cronin, D. (2016). Effect of Cortical Bone Material Asymmetry Using a 3-Point Bend Test Simulation. In *IRCOBI Asia Conference*. Seoul, South Korea.
- Klein, K. F., Hu, J., Reed, M. P., Hoff, C. N., & Rupp, J. D. (2015). Development and Validation of Statistical Models of Femur Geometry for Use with Parametric Finite Element Models. *Annals of Biomedical Engineering*, 43(10), 2503–2514.
- Krone, R., & Schuster, P. (2006). An Investigation on the Importance of Material Anisotropy in Finite-Element Modeling of the Human Femur. *SAE Technical Paper 2006-01-0064*.
- Kuppa, S., Wang, J., Haffner, M., & Eppinger, R. (2001). Lower extremity injuries and associated injury criteria. *17th ESV Conference*, 4, 1–15.
- Launey, M. E., Buehler, M. J., & Ritchie, R. O. (2010). *On the Mechanistic Origins of Toughness in Bone. Annual Review of Materials Research* (Vol. 40).
- Li, Z., Kindig, M. W., Kerrigan, J. R., Kent, R. W., & Crandall, J. R. (2012). Development and

- validation of a subject-specific finite element model of a human clavicle. *Computer Methods in Biomechanics and Biomedical Engineering*, 16(8), 819–29.
- LSTC. (2013). LS-DYNA keyword user's manual: version971.
- McCalden, R. W., McGeough, J. A., Barker, M. B., & Court-Brown, C. M. (1993). Age-related changes in the tensile properties of cortical bone. The relative importance of changes in porosity, mineralization, and microstructure. *J Bone Joint Surg Am*, 75(8), 1193–1205.
- McCalden, R. W., McGeough, J. A., & Court-Brown, C. M. (1997). Age-related changes in the compressive strength of cancellous bone. The relative importance of changes in density and trabecular architecture. *J Bone Joint Surg Am*, 79(3), 421–427.
- Moorhouse, K. (2013). An improved normalization methodology for developing mean human response curves.
- NHTSA. (2013). Traffic Safety Facts 2013: A Compilation of Motor Vehicle Crash Data from the Fatality Analysis Reporting System and the General Estimates System. *NHTSA, DOT HS 812*, 1–238.
- Nie, B., Kim, T., Wang, Y., Bollapragada, V., Daniel, T., & Crandall, J. R. (2016). Comparison of two scaling approaches for the development of biomechanical multi-body human models. *Multibody System Dynamics*.
- Nishiyama, K. K., Gilchrist, S., Guy, P., Cripton, P., & Boyd, S. K. (2013). Proximal femur bone strength estimated by a computationally fast finite element analysis in a sideways fall configuration. *Journal of Biomechanics*, 46(7), 1231–1236.
- Park, G., Kim, T., Forman, J., Panzer, M. B., & Crandall, J. R. (2017). Prediction of the Structural Response of the Femoral Shaft under Dynamic Bending Loading using Subject-Specific Finite Element Models. *Computer Methods in Biomechanics and Biomedical Engineering (under Review)*.
- Poulard, D., Chen, H., & Panzer, M. (2016). Geometrical personalization of pedestrian finite element models using morphing increases the biofidelity of their impact kinematics. *SAE Technical Paper 2016-01-1506*.
- Rohr, K., Stiehl, H. S., Sprengel, R., Buzug, T. M., Weese, J., & Kuhn, M. H. (2001). Landmark-based elastic registration using approximating thin-plate splines. *IEEE Transactions on Medical Imaging*, 20(6), 526–34.
- Rupp, J. D. (2006). Biomechanics of hip injuries in frontal motor-vehicle crashes. *University of Michigan, Ann Arbor, MI*.
- SAE. (1994). *Sign Convention for Vehicle Crash Testing (SAE-J1733)*.
- SAE. (2003). Surface Vehicle Recommended Practice J211-1 – Instrumentation for Impact Test – Part 1 – Electronic Instrumentation.
- Schoell, S. L., Weaver, A. A., Urban, J. E., Jones, D. A., Stitzel, J. D., Hwang, E., ... Rupp, J. D. (2015). Development and Validation of an Older Occupant Finite Element Model of a Mid-Sized Male for Investigation of Age-related Injury Risk. *Stapp Car Crash Journal*, 59(November), 359–383.
- Shi, X., Cao, L., Reed, M. P., Rupp, J. D., & Hu, J. (2014, March 25). Effects of obesity on occupant responses in frontal crashes: a simulation analysis using human body models. *Computer Methods in Biomechanics and Biomedical Engineering*. Taylor & Francis.
- States, J. D. (1986). Adult occupant injuries of the lower limb. *SAE International*, 861927, 97–107.

- Untaroiu, C., Genovese, D., Ivarsson, J., & Crandall, J. (2008). A Finite Element Analysis of Mid-Shaft Femoral Tolerance under Combined Axial-Bending Loading. *10th International LS-DYNA® Users Conference*, (3), 13-1-13–10.
- Untaroiu, C., Kerrigan, J., & Crandall, J. (2006). Material Identification using Successive Response Surface Methodology , with Application to a Human Femur Subjected to Three-Point Bending Loading. *Response*, 2006(724).
- Vavalle, N. A., Schoell, S. L., Weaver, A. A., Stitzel, J. D., & Gayzik, F. S. (2014). Application of Radial Basis Function Methods in the Development of a 95th Percentile Male Seated FEA Model. *Stapp Car Crash Conference*, 58(November).
- Zebaze, R. M., Ghasem-Zadeh, A., Bohte, A., Iuliano-Burns, S., Mirams, M., Price, R. I., ... Seeman, E. (2010). Intracortical remodelling and porosity in the distal radius and post-mortem femurs of women: a cross-sectional study. *Lancet*, 375(9727), 1729–1736.
- Zhang, J., Hislop-Jambrich, J., & Besier, T. F. (2016). Predictive statistical models of baseline variations in 3-D femoral cortex morphology. *Medical Engineering and Physics*, 38(5).
- Zioupos, P. (2001). Ageing Human Bone: Factors Affecting Its Biomechanical Properties and the Role of Collagen. *Journal of Biomaterials Applications*, 15(3), 187–229.

APPENDIX A: BIOMECHANICAL TEST DATA

Table A1 Subject characteristics for biomechanical tests of femurs subjected to dynamic pure bending from Forman et al. (2012a) and Funk et al. (2004) (n=20)

code* ^a	aspect	age	gender	stature (cm)	weight (kg)	Loading Type	Loading Direction * ^b
F2012-M01	L	36	M	N/A	N/A	Bend	LM
F2012-M02	R	20	M	N/A	N/A	Bend	LM
F2012-M03	R	27	M	N/A	N/A	Bend	LM
F2012-M04	R	43	M	N/A	N/A	Bend	LM
F2012-M05	L	35	M	N/A	N/A	Bend	LM
F2012-M06	L	19	M	N/A	N/A	Bend	LM
F2012-M07	R	52	M	N/A	N/A	Bend	LM
F2012-M08	L	27	M	N/A	N/A	Bend	LM
F2012-M09	L	42	M	N/A	N/A	Bend	LM
F2012-M10	L	25	M	N/A	N/A	Bend	LM
F2012-M11	L	28	M	N/A	N/A	Bend	LM
F2012-M12	R	35	M	N/A	N/A	Bend	LM
F2012-M13	R	36	M	N/A	N/A	Bend	LM
F2012-M14	R	28	M	N/A	N/A	Bend	LM
F2012-M15	R	19	M	N/A	N/A	Bend	LM
F2004-M01	R	69	M	162.6	91.6	Bend	PA
F2004-M02	R	70	M	167.6	73.0	Bend	LM
F2004-M03	R	51	M	188.0	123.4	Bend	LM
F2004-M04	L	51	M	188.0	123.4	Bend	PA
F2004-M05	L	69	M	162.6	91.6	Bend	LM

N/A = not available

*a: F2012 = Forman et al., 2012a, F2004 = Funk et al., 2004

*b: LM = lateral-medial, AP = anterior-posterior, PA = posterior-anterior

Table A2 Subject characteristics for biomechanical tests of femurs subjected to dynamic combined loading from Ivarsson et al. (2009) (n=12)

Code	Aspect	Age	Gender	Height (cm)	Weight (kg)	Loading Type ^b	Loading Direction ^a
I2009-M01	L	39	M	184.0	79.4	Bending	AP
I2009-M02	R	63	M	180.3	89.0	Bending	AP
I2009-M03	R	51	M	175.0	54.9	Bending	PA
I2009-M04	L	45	M	175.3	68.1	Bending	AP
I2009-M05	L	62	M	177.8	81.8	Comb-4kN	AP
I2009-M06	R	62	M	185.4	100.0	Comb-4kN	AP
I2009-M07	L	62	M	182.9	90.9	Comb-4kN	PA
I2009-M08	R	62	M	177.8	81.8	Comb-4kN	PA
I2009-M09	R	58	M	182.9	141.0	Comb-8kN	AP
I2009-M10	L	65	M	182.9	90.9	Comb-8kN	AP
I2009-M11	L	49	M	193.0	100.0	Comb-8kN	PA
I2009-M12	R	44	M	193.0	81.8	Comb-8kN	PA

a: LM=lateral-medial, AP=anterior-posterior, PA=posterior-anterior

b: comb = combined loading (bending + pre-axial loading)

Table A3 Subject characteristics of clinical CT image specimens

Code	Side	CT#	Gender	Race	Age (yrs)	Height (cm)	Weight (kg)	Femur Height (mm)
CABCT-M01	L	677	male	W	54	180.0	54.0	477.29
CABCT-M02	R	677	male	W	54	180.0	54.0	479.73
CABCT-M03	L	682	male	W	54	183.0	57.0	472.51
CABCT-M04	R	682	male	W	54	183.0	57.0	471.71
CABCT-M05	L	684	male	W	65	175.0	59.0	481.60
CABCT-M06	R	684	male	W	65	175.0	59.0	482.94
CABCT-M07	L	696	male	W	49	175.0	61.0	483.74
CABCT-M08	R	696	male	W	49	175.0	61.0	483.49
CABCT-M09	L	747	male	W	70	178.0	56.7	502.03
CABCT-M10	R	747	male	W	70	178.0	56.7	498.76
CABCT-M11	L	675	male	W	73	182.0	65.0	520.25
CABCT-M12	R	675	male	W	73	182.0	65.0	516.14
CABCT-M13	L	679	male	W	56	185.0	68.0	496.47
CABCT-M14	R	679	male	W	56	185.0	68.0	498.70
CABCT-M15	L	680	male	W	58	175.0	63.0	480.85
CABCT-M16	R	680	male	W	58	175.0	63.0	485.06
CABCT-M17	L	686	male	W	72	173.0	66.0	515.10
CABCT-M18	R	686	male	W	72	173.0	66.0	510.49
CABCT-M19	L	693	male	W	47	173.0	68.0	475.26
CABCT-M20	R	693	male	W	47	173.0	68.0	475.81
CABCT-M21	L	707	male	W	36	180.0	62.0	479.21
CABCT-M22	R	707	male	W	36	180.0	62.0	479.70
CABCT-M23	L	717	male	W	65	178.0	68.0	474.52
CABCT-M24	R	717	male	W	65	178.0	68.0	469.54
CABCT-M25	L	720	male	W	61	170.0	68.0	446.90
CABCT-M26	R	720	male	W	61	170.0	68.0	450.53
CABCT-M27	L	721	male	W	60	178.0	64.0	466.72
CABCT-M28	R	721	male	W	60	178.0	64.0	468.07
CABCT-M29	L	730	male	W	77	178.0	63.0	493.15
CABCT-M30	R	730	male	W	77	178.0	63.0	490.64
CABCT-M31	L	745	male	W	84	167.6	65.3	430.76
CABCT-M32	R	745	male	W	84	167.6	65.3	430.26
CABCT-M33	L	767	male	B	67	172.7	77.1	496.05
CABCT-M34	R	767	male	B	67	172.7	77.1	492.71
CABCT-M35	L	673	male	W	67	180.0	72.0	480.84
CABCT-M36	R	673	male	W	67	180.0	72.0	485.28

Table A3 Subject characteristics of clinical CT image specimens (continued)

Code	Side	CT#	Gender	Race	Age (yrs)	Height (cm)	Weight (kg)	Femur Height (mm)
CABCT-M37	L	674	male	W	67	178.0	72.0	474.33
CABCT-M38	R	674	male	W	67	178.0	72.0	483.31
CABCT-M39	L	695	male	W	74	178.0	73.0	490.12
CABCT-M40	R	695	male	W	74	178.0	73.0	490.42
CABCT-M41	L	703	male	W	76	183.0	73.0	511.27
CABCT-M42	R	703	male	W	76	183.0	73.0	526.02
CABCT-M43	L	722	male	W	64	185.0	73.0	506.06
CABCT-M44	R	722	male	W	64	185.0	73.0	511.78
CABCT-M45	L	724	male	W	73	189.0	73.0	519.09
CABCT-M46	R	724	male	W	73	189.0	73.0	520.16
CABCT-M47	L	736	male	W	67	170.0	70.0	464.90
CABCT-M48	L	749	male	W	22	182.9	69.4	495.90
CABCT-M49	R	749	male	W	22	182.9	69.4	501.33
CABCT-M50	L	758	male	W	69	168.0	72.0	475.58
CABCT-M51	R	758	male	W	69	168.0	72.0	475.01
CABCT-M52	L	760	male	W	74	170.2	71.7	443.28
CABCT-M53	R	760	male	W	74	170.2	71.7	440.27
CABCT-M54	L	785	male	W	55	177.8	75.0	476.03
CABCT-M55	R	785	male	W	55	177.8	75.0	471.17
CABCT-M56	L	725	male	W	53	178.0	78.0	471.54
CABCT-M57	R	725	male	W	53	178.0	78.0	466.05
CABCT-M58	L	727	male	B	54	183.0	82.0	520.71
CABCT-M59	R	727	male	B	54	183.0	82.0	515.56
CABCT-M60	L	733	male	W	74	178.0	84.0	490.32
CABCT-M61	R	733	male	W	74	178.0	84.0	489.30
CABCT-M62	L	737	male	W	50	191.0	95.0	488.68
CABCT-M63	R	737	male	W	50	191.0	95.0	489.72
CABCT-M64	L	750	male	W	66	172.7	76.2	433.09
CABCT-M65	R	750	male	W	66	172.7	76.2	435.51
CABCT-M66	L	756	male	W	67	180.3	79.8	484.64
CABCT-M67	R	756	male	W	67	180.3	79.8	485.87
CABCT-M68	L	764	male	W	65	182.9	86.2	478.63
CABCT-M69	R	764	male	W	65	182.9	86.2	481.61
CABCT-M70	L	770	male	W	72	182.9	68.0	456.17
CABCT-M71	R	770	male	W	72	182.9	68.0	454.11
CABCT-M72	R	698	male	W	41	175.0	84.0	465.18

Table A3 Subject characteristics of clinical CT image specimens (continued)

Code	Side	CT#	Gender	Race	Age (yrs)	Height (cm)	Weight (kg)	Femur Height (mm)
CABCT-M73	L	702	male	W	42	178.0	86.0	473.36
CABCT-M74	R	702	male	W	42	178.0	86.0	475.19
CABCT-M75	L	732	male	W	57	175.0	88.0	446.52
CABCT-M76	R	732	male	W	57	175.0	88.0	445.57
CABCT-M77	R	746	male	W	74	180.3	87.5	490.58
CABCT-M78	L	759	male	W	66	185.0	88.0	504.47
CABCT-M79	R	759	male	W	66	185.0	88.0	510.55
CABCT-M80	L	765	male	W	67	177.8	85.3	437.35
CABCT-M81	R	765	male	W	67	177.8	85.3	445.15
CABCT-M82	L	771	male	W	68	168.0	82.0	463.58
CABCT-M83	R	771	male	W	68	168.0	82.0	463.79
CABCT-M84	L	783	male	W	67	180.3	85.3	490.66
CABCT-M85	R	783	male	W	67	180.3	85.3	488.11
CABCT-M86	L	699	male	W	50	175.0	89.0	480.78
CABCT-M87	R	699	male	W	50	175.0	89.0	483.08
CABCT-M88	L	755	male	W	37	183.0	91.0	460.58
CABCT-M89	R	755	male	W	37	183.0	91.0	457.31
CABCT-M90	R	701	male	W	67	180.0	99.0	483.88
CABCT-M91	L	748	male	W	75	185.4	98.0	496.26
CABCT-M92	R	748	male	W	75	185.4	98.0	494.01
CABCT-M93	L	752	male	W	27	183.0	97.0	493.58
CABCT-M94	R	752	male	W	27	183.0	97.0	496.95
CABCT-M95	L	763	male	B	48	178.0	99.0	497.56
CABCT-M96	R	763	male	B	48	178.0	99.0	492.66
CABCT-M97	L	676	male	W	73	193.0	105.0	528.87
CABCT-M98	R	676	male	W	73	193.0	105.0	521.00
CABCT-M99	L	692	male	W	65	180.0	104.0	480.61
CABCT-M100	R	692	male	W	65	180.0	104.0	483.64
CABCT-M101	L	706	male	W	76	188.0	106.0	492.38
CABCT-M102	R	706	male	W	76	188.0	106.0	489.47
CABCT-M103	L	735	male	W	54	185.0	103.0	503.38
CABCT-M104	R	735	male	W	54	185.0	103.0	502.34
CABCT-M105	L	754	male	W	59	185.0	103.0	461.22
CABCT-M106	R	754	male	W	59	185.0	103.0	466.27
CABCT-M107	L	769	male	W	61	177.8	106.6	476.20
CABCT-M108	R	769	male	W	61	177.8	106.6	478.63

Table A3 Subject characteristics of clinical CT image specimens (continued)

Code	Side	CT#	Gender	Race	Age (yrs)	Height (cm)	Weight (kg)	Femur Height (mm)
CABCT-M109	L	784	male	W	82	180.3	105.2	481.61
CABCT-M110	R	784	male	W	82	180.3	105.2	479.45
CABCT-M111	L	705	male	W	46	180.3	113.4	488.66
CABCT-M112	R	705	male	W	46	180.3	113.4	491.87
CABCT-M113	L	326	male	W	62	154.0	72.6	419.37
CABCT-M114	R	326	male	W	62	154.0	72.6	422.95
CABCT-M115	L	352	male	W	64	161.0	86.2	419.17
CABCT-M116	R	352	male	W	64	161.0	86.2	422.25
F2004-M01	R	116	male	W	69	162.6	91.6	453.46
F2004-M02	R	146	male	W	70	167.6	73.0	453.71
F2004-M03	R	139	male	W	51	188.0	123.4	499.76
F2004-M04	L	139	male	W	51	188.0	123.4	502.10
F2004-M05	L	116	male	W	69	162.6	91.6	458.78

Table A4 Femur fracture moments from the biomechanical tests (Funk et al., 2004; Kennedy et al., 2004; Kerrigan et al., 2003) to generate IRFs

Fracture Moment [Nm]	Aspect	Age	Gender	Reference
275	65	68.9	M	Kennedy et al. 2004
384	49	106.6	M	Kennedy et al. 2004
468	62	89.1	M	Kennedy et al. 2004
371	83	66.4	M	Kennedy et al. 2004
376	65	84.7	M	Kennedy et al. 2004
343	64	65.8	M	Kennedy et al. 2004
384	62	99.3	M	Kennedy et al. 2004
279	71	71.2	M	Kennedy et al. 2004
242	61	107.1	M	Kennedy et al. 2004
355	61	116.6	M	Kennedy et al. 2004
429	64	90.7	M	Kennedy et al. 2004
302	78	104.8	M	Kennedy et al. 2004
358	62	99.3	M	Kennedy et al. 2004
319	61	107.1	M	Kennedy et al. 2004
309	61	116.6	M	Kennedy et al. 2004
435	67	64	M	Funk et al. 2004
497	59	108	M	Funk et al. 2004
528	40	70	M	Funk et al. 2004
389	55	64	M	Funk et al. 2004
356	70	73	M	Funk et al. 2004
419	69	92	M	Funk et al. 2004
543	51	124	M	Funk et al. 2004
632	55	85	M	Kerrigan et al. 2003

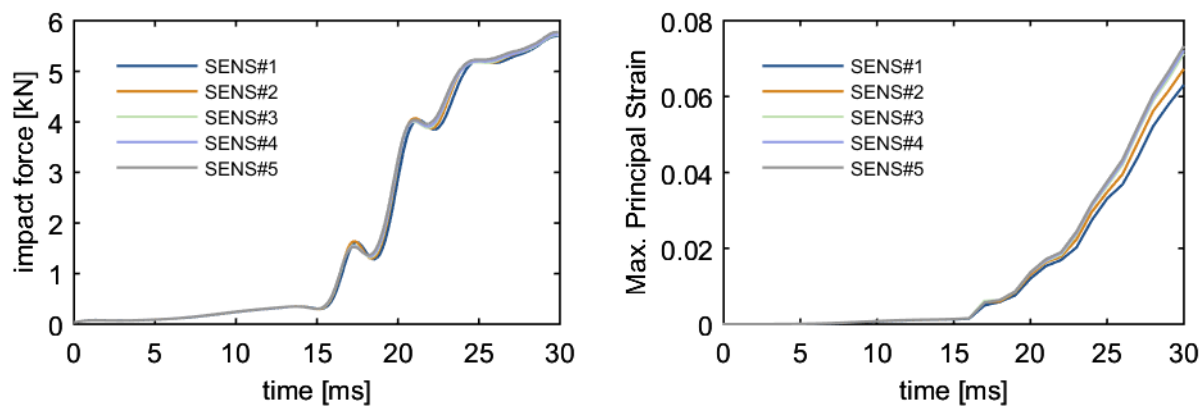
APPENDIX B: EVALUATION OF ACCURACY MORPHED FEMUR FE MODEL

Figure B1 Impact force (left) and maximum principal strain (right) time histories for Mesh sensitivity analysis using five FE models with different number of elements

Table B1 Sensitivity of thresholding HU value for one of the specimens (Forman2012-M01)

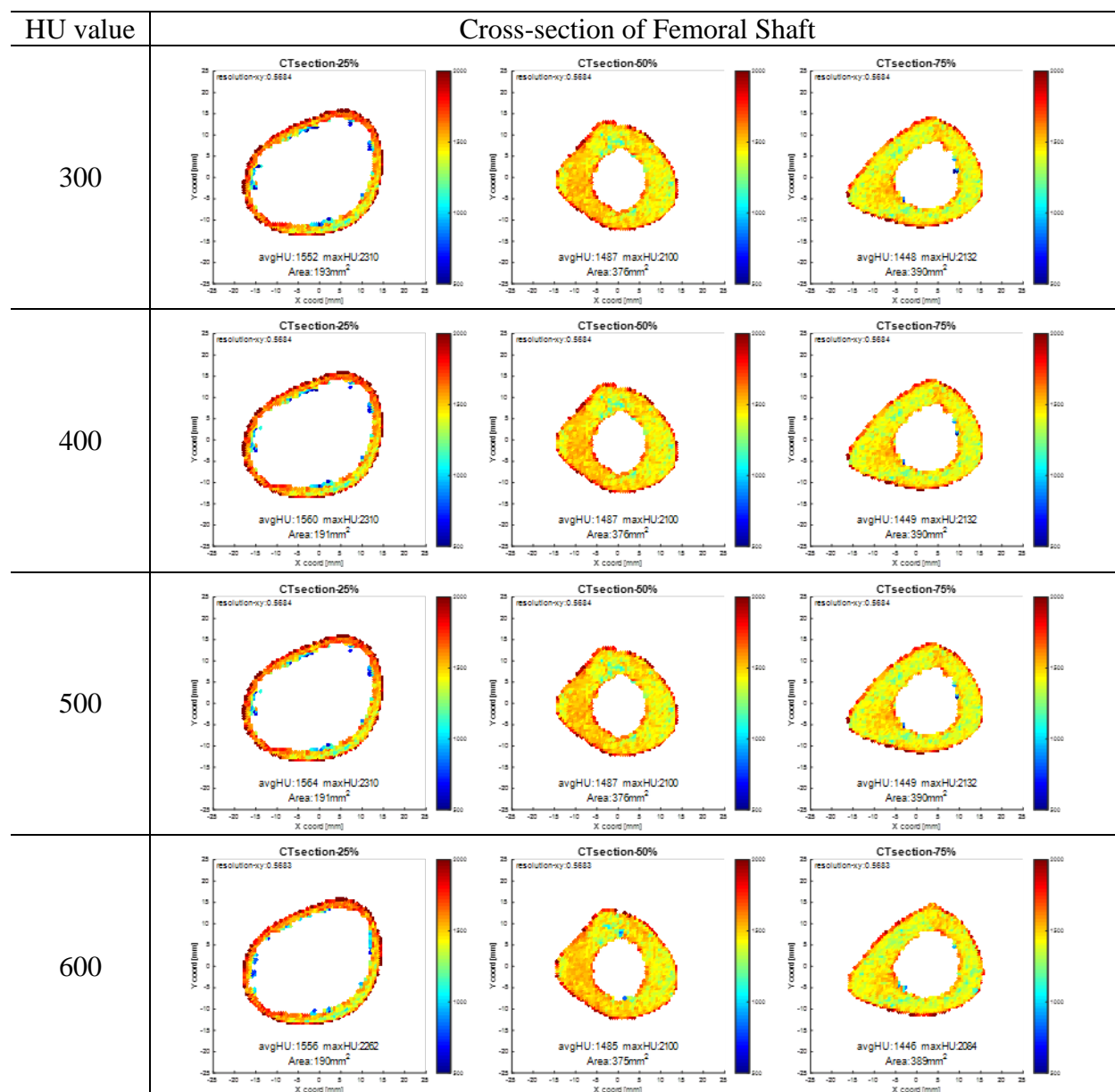


Table B2 Morphing accuracy

code		Area [mm ²]			Minimum distance Error [mm]		% of elements not meeting target: HEX-PENTA (shaft)			
		25%	50%	75%	Outer	Iner	J ^{*a}	W ^{*b}	A ^{*c}	S ^{*d}
F2012-M01	CT	267.2	450.0	533.8						
	SS-FE	270.1	434.7	553.9	0.35	0.88	0.00	0.01	3.40	0.00
	error[%]	1.1	3.4	3.8						
F2012-M02	CT	238.7	506.5	554.6						
	SS-FE	269.3	490.8	549.6	0.35	0.80	0.00	0.00	1.23	0.00
	error[%]	12.8	3.1	0.9						
F2012-M03	CT	497.6	574.0	625.7						
	SS-FE	482.3	552.5	622.3	0.35	0.83	0.00	0.00	0.03	0.00
	error[%]	3.1	3.7	0.5						
F2012-M04	CT	288.7	445.6	498.1						
	SS-FE	283.4	430.1	495.6	0.31	0.60	0.00	0.00	0.35	0.00
	error[%]	1.8	3.5	0.5						
F2012-M05	CT	282.5	437.1	510.8						
	SS-FE	271.7	422.9	506.9	0.33	0.66	0.00	0.00	0.93	0.00
	error[%]	3.8	3.2	0.8						
F2012-M06	CT	304.2	500.9	518.7						
	SS-FE	311.7	483.4	516.2	0.33	0.75	0.00	0.00	0.00	0.00
	error[%]	2.5	3.5	0.5						
F2012-M07	CT	320.8	533.2	589.5						
	SS-FE	329.9	516.1	581.0	0.36	0.67	0.00	0.00	0.00	0.00
	error[%]	2.8	3.2	1.5						
F2012-M08	CT	339.9	511.9	558.6						
	SS-FE	345.2	502.7	555.2	0.38	0.72	0.00	0.00	0.00	0.00
	error[%]	1.6	1.8	0.6						
F2012-M09	CT	331.4	493.9	579.1						
	SS-FE	342.0	482.1	572.9	0.36	0.75	0.00	0.00	0.08	0.00
	error[%]	3.2	2.4	1.1						
F2012-M10	CT	264.1	333.8	362.9						
	SS-FE	266.4	326.1	363.3	0.33	0.98	0.00	0.00	0.11	0.00
	error[%]	0.9	2.3	0.1						
F2012-M11	CT	303.3	473.0	506.3						
	SS-FE	306.9	463.9	503.2	0.32	0.58	0.00	0.00	0.00	0.00
	error[%]	1.2	1.9	0.6						

*a = Jacobian, *b = Warpage, *c = Aspect Ratio, *d = Skew

Table B1 Morphing accuracy (continued)

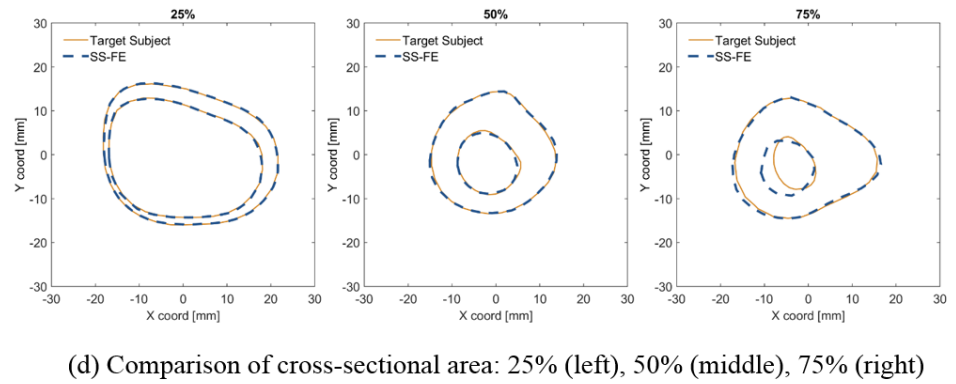
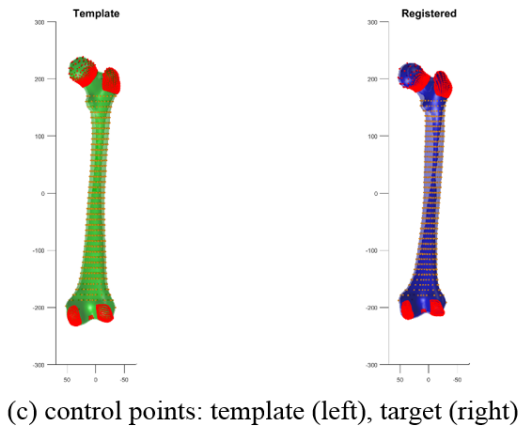
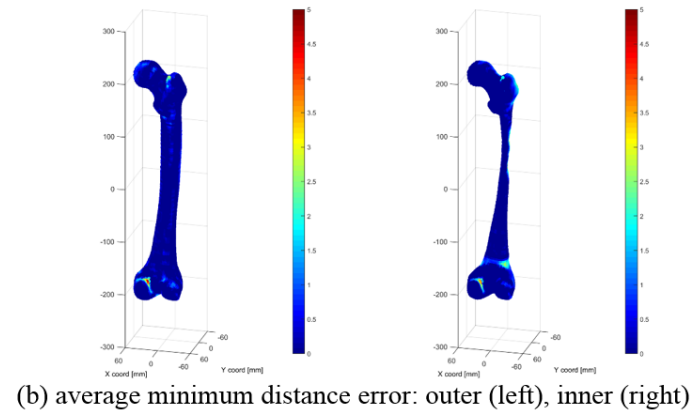
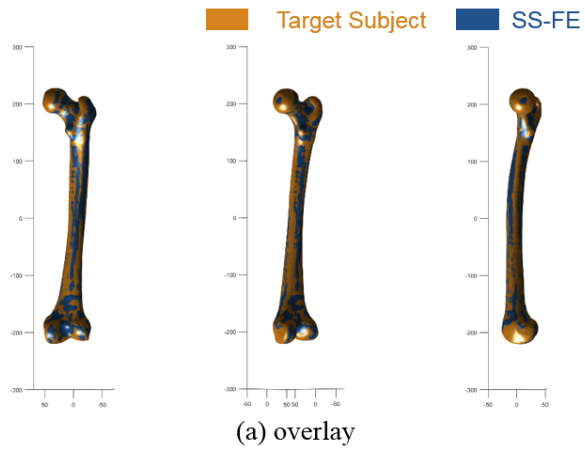
code		Area [mm ²]			Minimum distance Error [mm]		% of elements not meeting target: HEX-PENTA (shaft)			
		25%	50%	75%	Outer	Iner	J ^{*a}	W ^{*b}	A ^{*c}	S ^{*d}
F2012-M12	CT	283.0	447.8	511.9						
	SS-FE	286.4	433.3	505.6	0.34	1.27	0.00	0.00	0.11	0.00
	error[%]	1.2	3.2	1.2						
F2012-M13	CT	267.2	450.0	533.8						
	SS-FE	270.1	434.7	553.9	0.35	0.83	0.00	0.00	0.00	0.00
	error[%]	1.1	3.4	3.8						
F2012-M14	CT	267.2	450.0	533.8						
	SS-FE	270.1	434.7	553.9	0.26	0.69	0.00	0.00	0.00	0.00
	error[%]	1.1	3.4	3.8						
F2012-M15	CT	238.7	506.5	554.6						
	SS-FE	269.3	490.8	549.6	0.34	0.71	0.00	0.00	0.00	0.00
	error[%]	12.8	3.1	0.9						
F2004-M01	CT	497.6	574.0	625.7						
	SS-FE	482.3	552.5	622.3	0.28	1.21	0.00	0.00	0.00	0.00
	error[%]	3.1	3.7	0.5						
F2004-M02	CT	288.7	445.6	498.1						
	SS-FE	283.4	430.1	495.6	0.29	1.10	0.00	0.00	0.00	0.00
	error[%]	1.8	3.5	0.5						
F2004-M03	CT	282.5	437.1	510.8						
	SS-FE	271.7	422.9	506.9	0.31	0.88	0.00	0.00	0.00	0.00
	error[%]	3.8	3.2	0.8						
F2004-M04	CT	304.2	500.9	518.7						
	SS-FE	311.7	483.4	516.2	0.30	0.99	0.00	0.00	0.31	0.00
	error[%]	2.5	3.5	0.5						
F2004-M05	CT	320.8	533.2	589.5						
	SS-FE	329.9	516.1	581.0	0.30	0.99	0.00	0.00	0.80	0.00
	error[%]	2.8	3.2	1.5						

*a = Jacobian, *b = Warpage, *c = Aspect Ratio, *d = Skew

Table B3 Morphing accuracy for combined loading (Ivarsson et al. (2009))

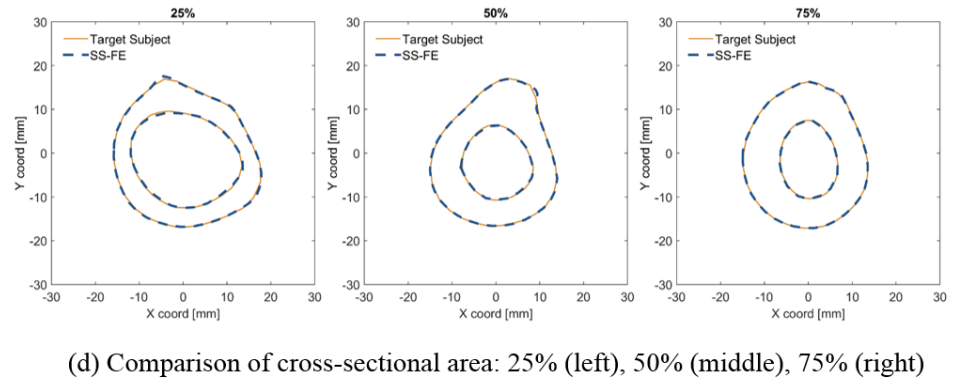
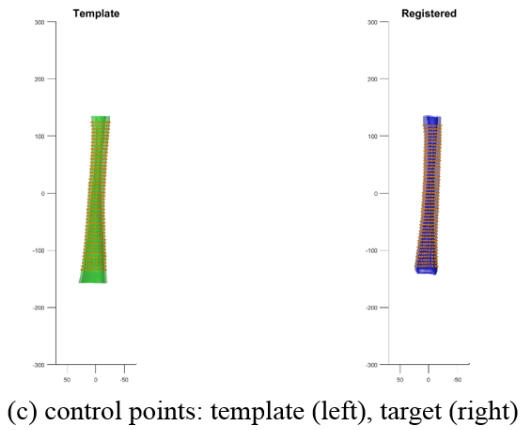
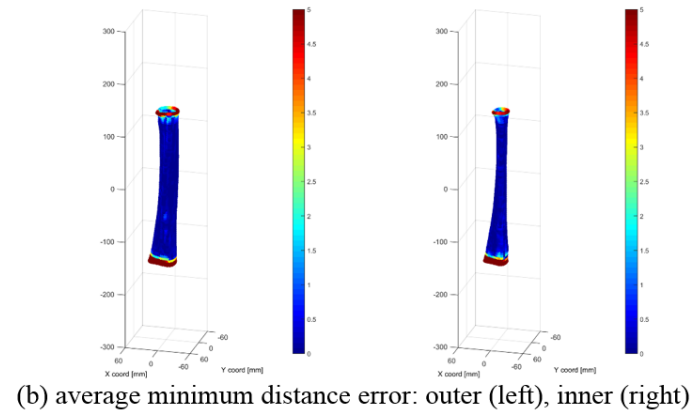
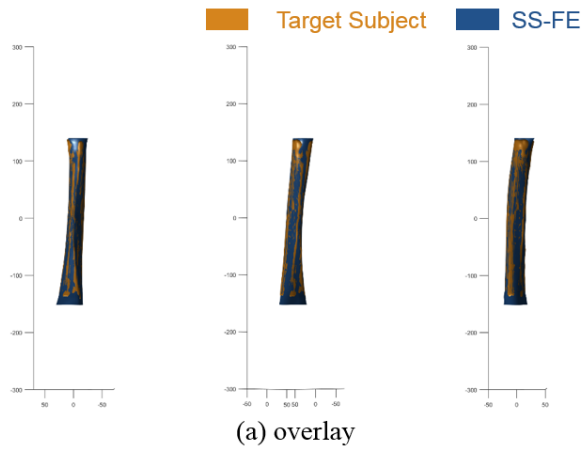
code		Area [mm ²]			Minimum distance Error [mm]		% of elements not meeting target: HEX-PENTA (shaft)			
		25%	50%	75%	Outer	Iner	J ^{*a}	W ^{*b}	A ^{*c}	S ^{*d}
I2009-M01	CT	411.0	456.0	533.9						
	SS-FE	400.8	452.4	533.7	0.51	0.60	0.00	0.00	0.00	0.00
	error[%]	2.5	0.8	0.0						
I2009-M02	CT	401.4	491.2	506.3						
	SS-FE	392.0	489.9	508.3	0.48	0.49	0.00	0.00	0.00	0.00
	error[%]	2.3	0.3	0.4						
I2009-M03	CT	436.4	470.8	467.3						
	SS-FE	425.8	466.2	464.2	0.53	0.65	0.00	0.00	0.00	0.00
	error[%]	2.4	1.0	0.6						
I2009-M04	CT	390.4	450.9	477.8						
	SS-FE	380.0	443.1	476.4	0.66	0.76	0.00	0.00	0.30	0.00
	error[%]	2.7	1.7	0.3						
I2009-M05	CT	430.7	503.5	541.6						
	SS-FE	419.2	498.1	540.8	0.58	0.61	0.00	0.00	0.07	0.00
	error[%]	2.7	1.1	0.2						
I2009-M06	CT	397.1	470.6	539.0						
	SS-FE	391.6	469.2	537.5	0.42	0.46	0.00	0.00	0.23	0.00
	error[%]	1.4	0.3	0.3						
I2009-M07	CT	465.1	561.1	624.2						
	SS-FE	451.1	554.4	622.1	0.56	0.57	0.00	0.00	0.00	0.00
	error[%]	3.0	1.2	0.3						
I2009-M08	CT	428.4	508.4	558.5						
	SS-FE	417.6	503.0	560.2	0.59	0.63	0.00	0.00	0.00	0.00
	error[%]	2.5	1.1	0.3						
I2009-M09	CT	535.8	656.0	692.1						
	SS-FE	524.2	649.1	688.5	0.57	0.56	0.00	0.00	0.00	0.00
	error[%]	2.2	1.1	0.5						
I2009-M10	CT	376.9	446.0	488.7						
	SS-FE	368.6	440.8	486.6	0.50	0.50	0.00	0.00	0.00	0.00
	error[%]	2.2	1.2	0.4						
I2009-M11	CT	455.3	547.2	610.5						
	SS-FE	442.5	540.3	610.6	0.58	0.57	0.00	0.00	0.00	0.00
	error[%]	2.8	1.3	0.0						
I2009-M12	CT	418.0	491.7	528.4						
	SS-FE	408.3	486.1	528.2	0.52	0.55	0.00	0.00	0.67	0.00
	error[%]	2.3	1.1	0.0						

*a = Jacobian, *b = Warpage, *c = Aspect Ratio, *d = Skew



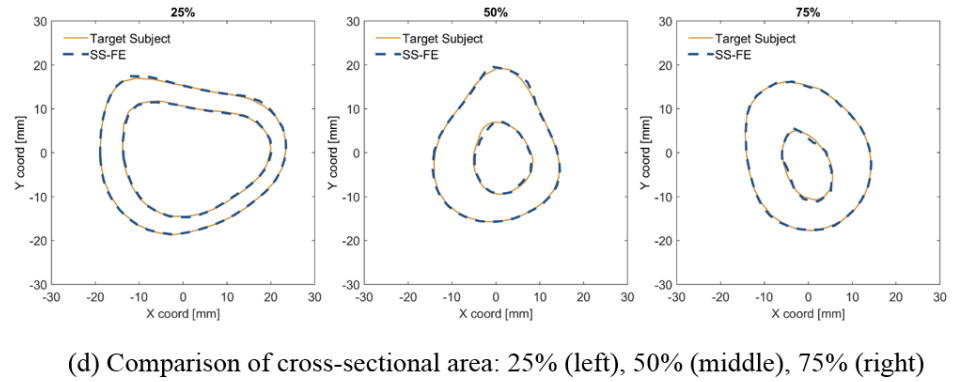
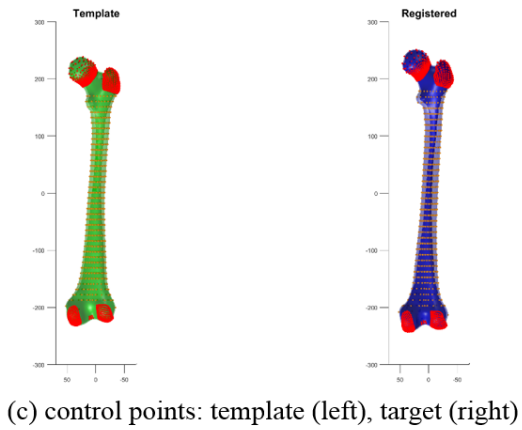
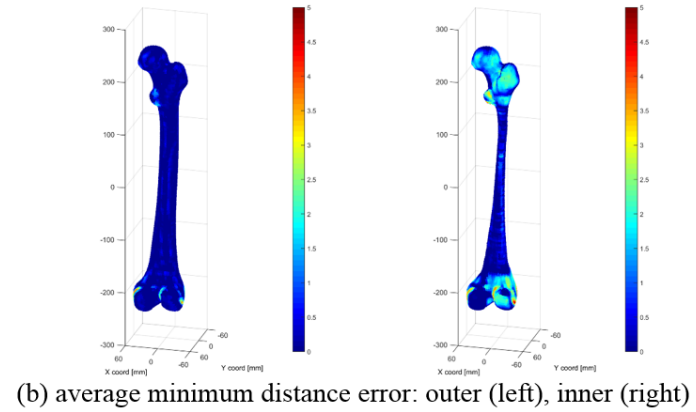
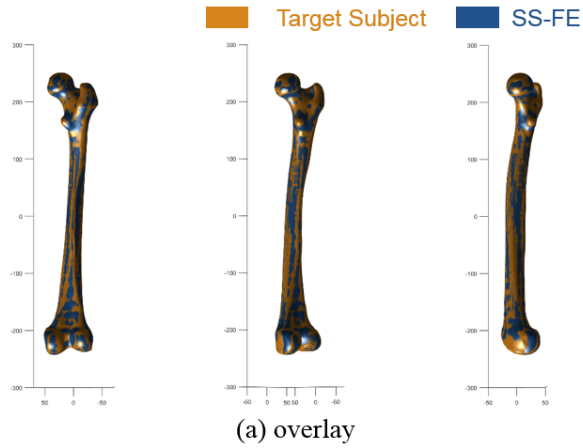
F2012-M01 (age=36)

Figure B2 Comparison of CT and Morphed FE model



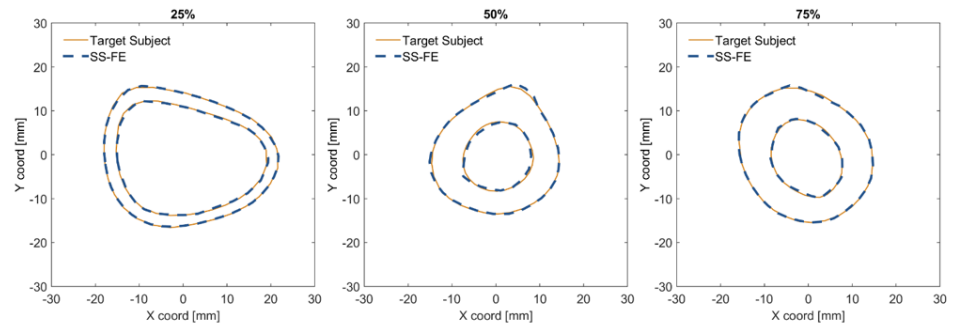
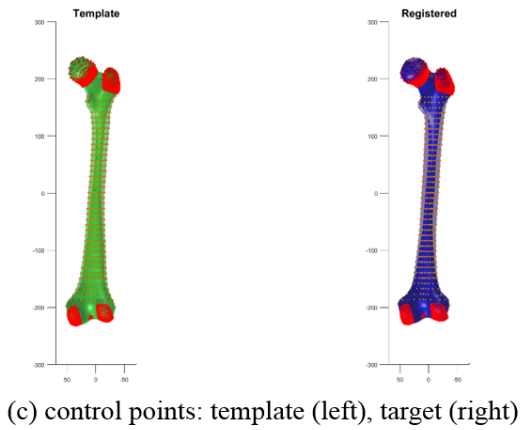
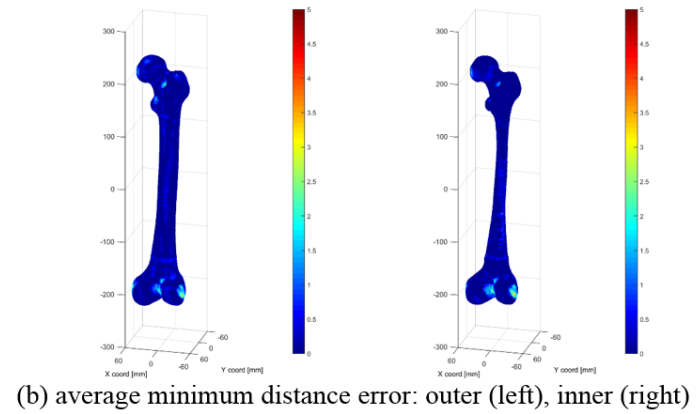
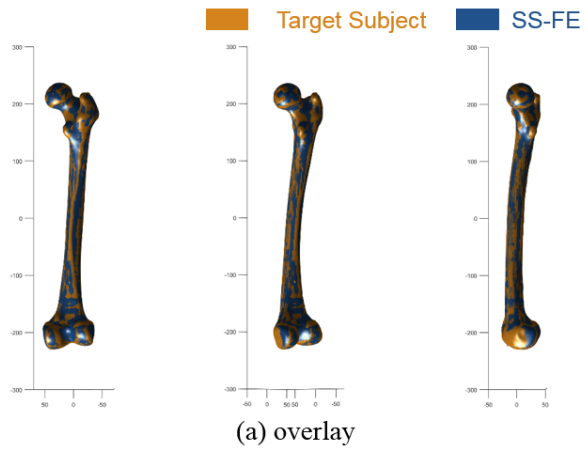
F2012-M02 (age=20)

Figure B1 Comparison of CT and Morphed FE model (continued)



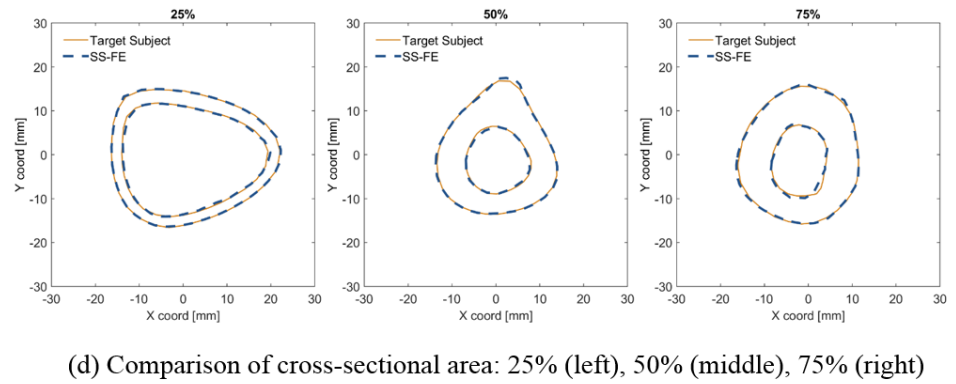
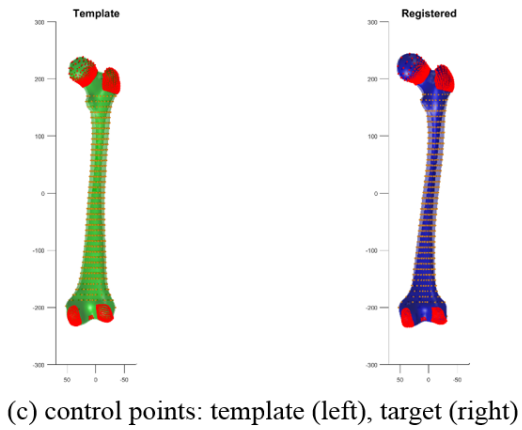
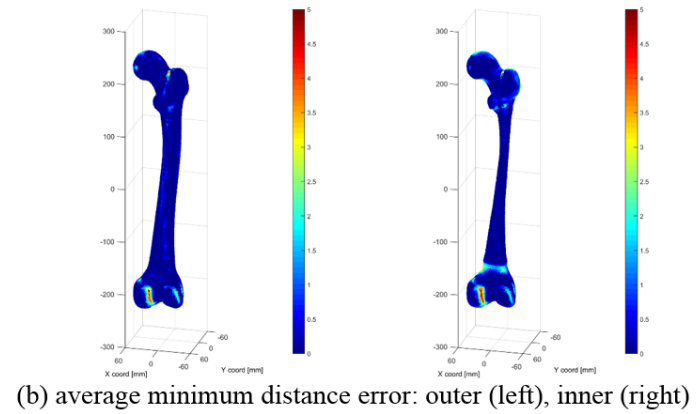
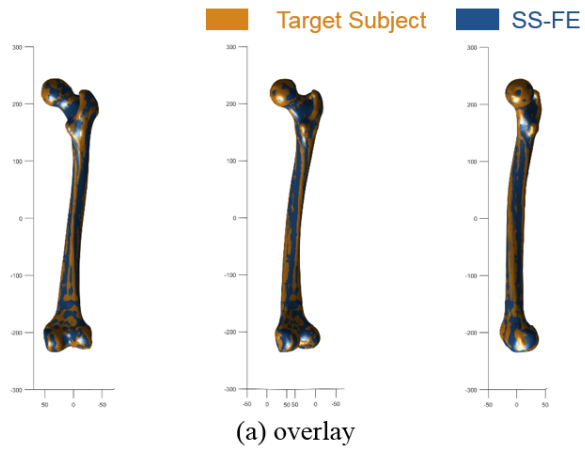
F2012-M03 (age=27)

Figure B1 Comparison of CT and Morphed FE model (continued)



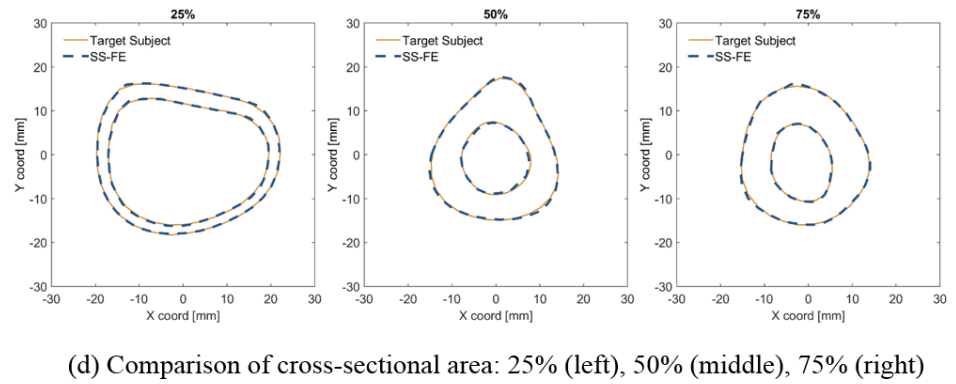
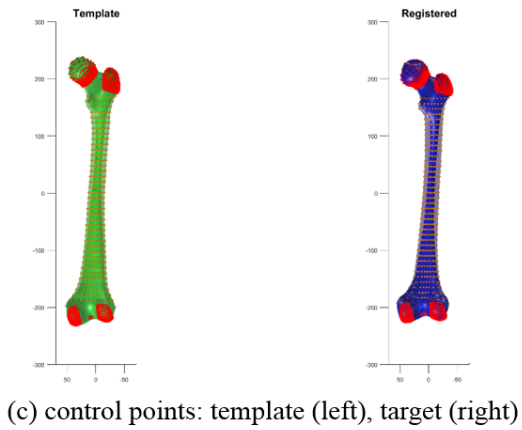
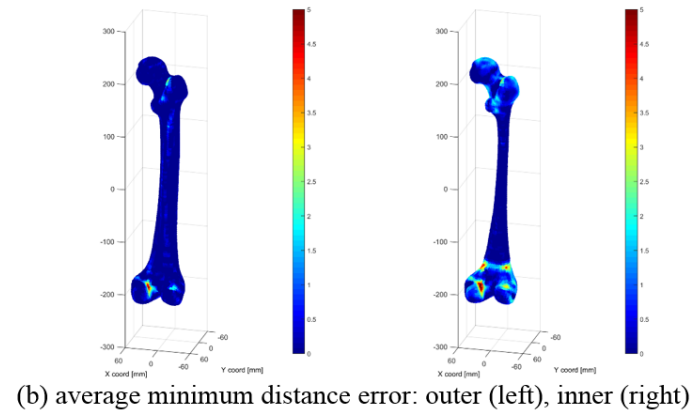
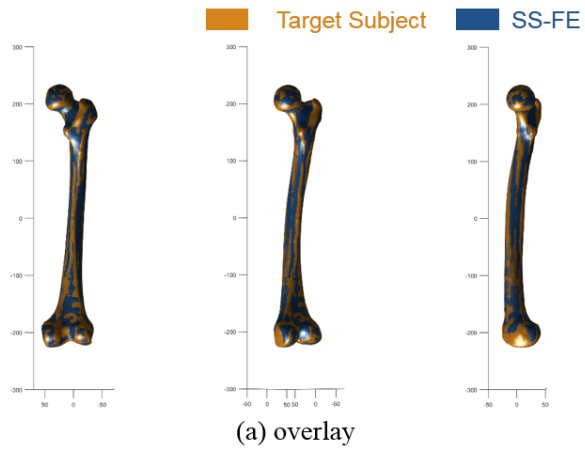
F2012-M04 (age=43)

Figure B1 Comparison of CT and Morphed FE model (continued)



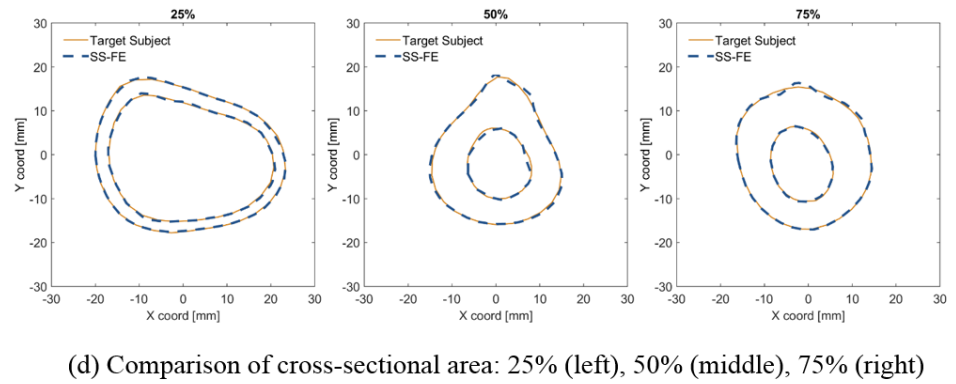
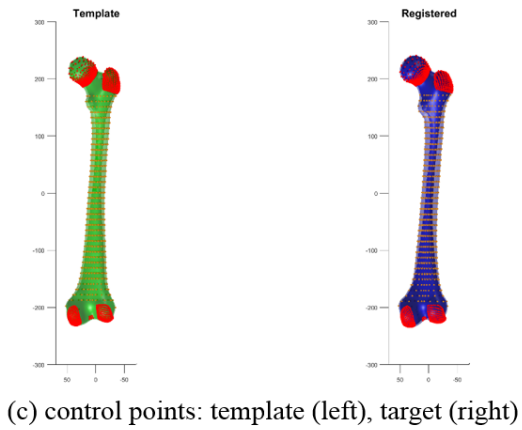
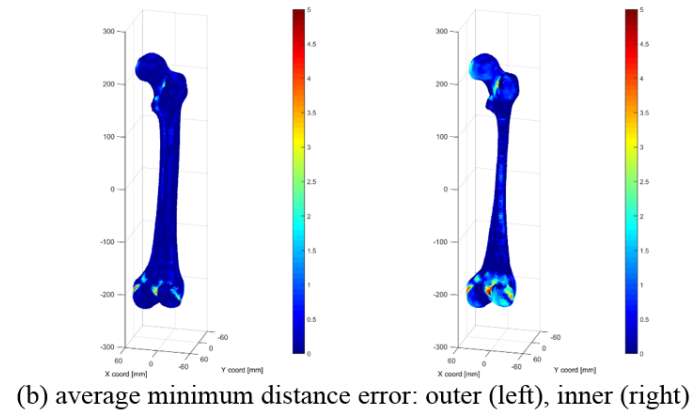
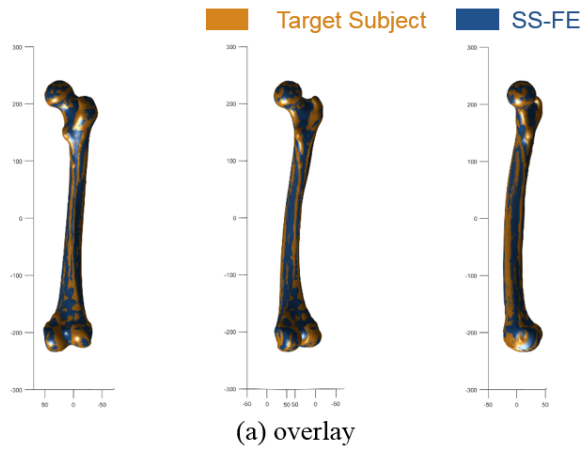
F2012-M05 (age=35)

Figure B1 Comparison of CT and Morphed FE model (continued)



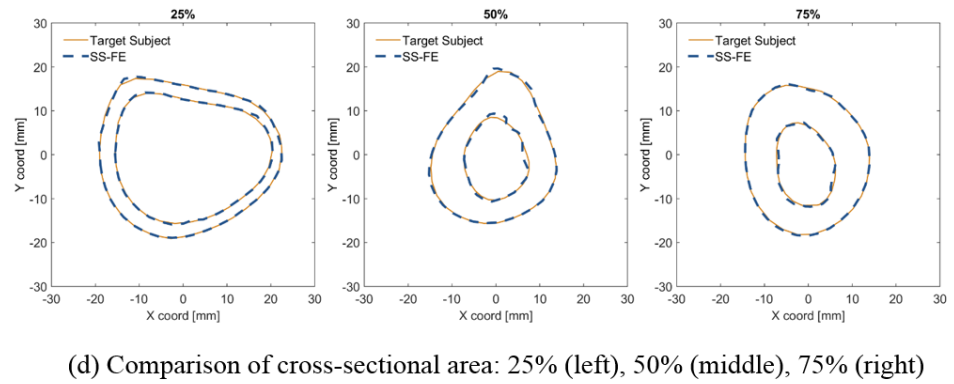
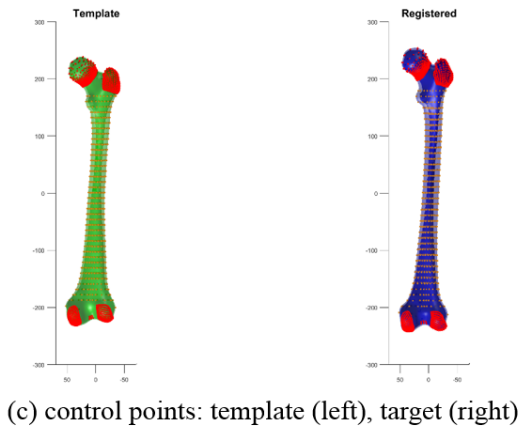
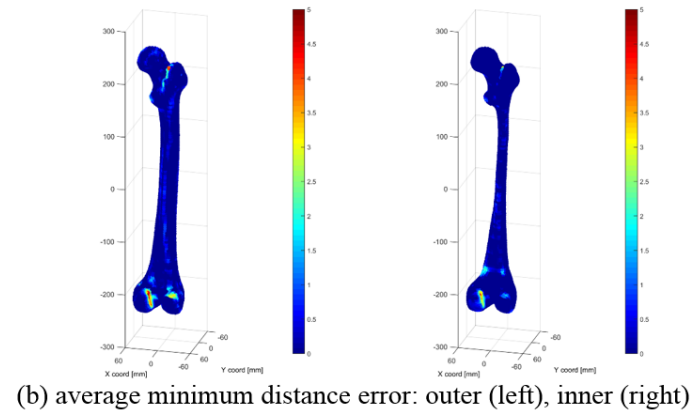
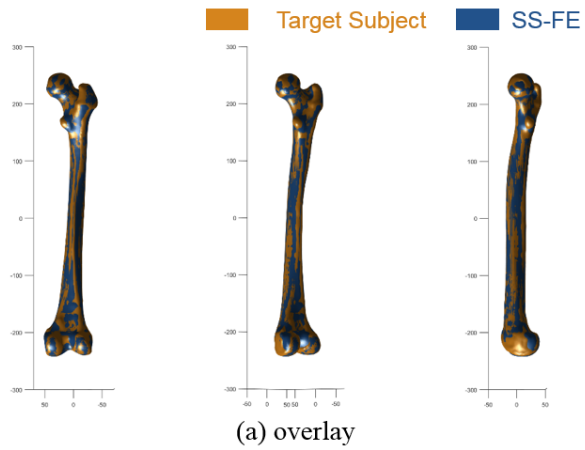
F2012-M06 (age=19)

Figure B1 Comparison of CT and Morphed FE model (continued)



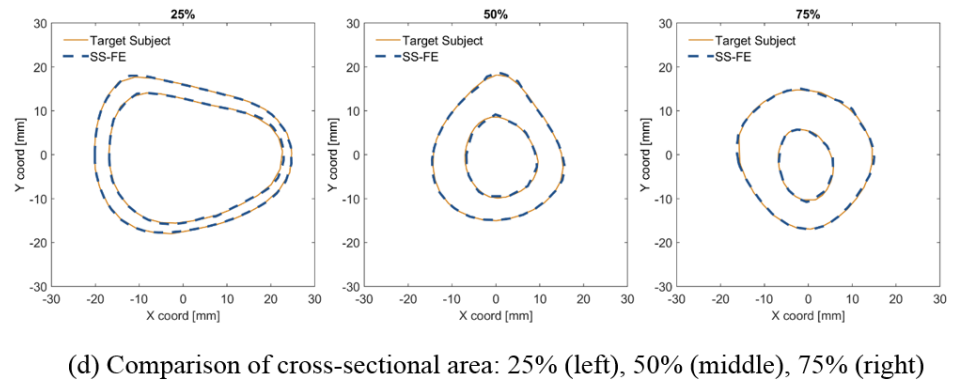
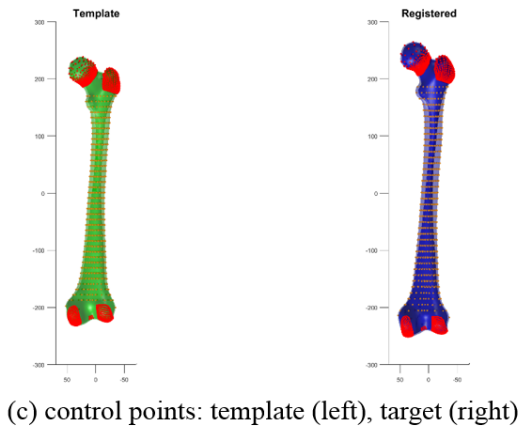
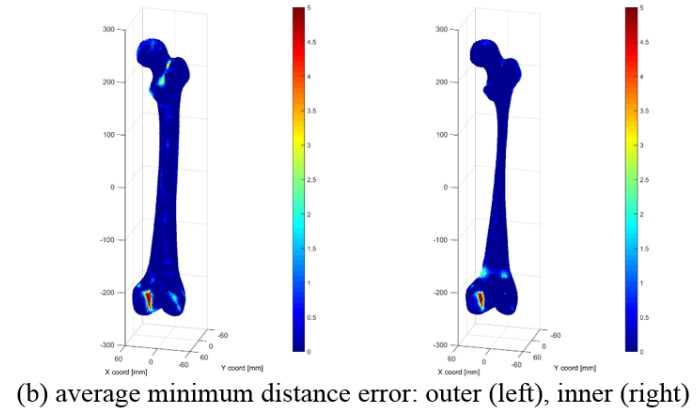
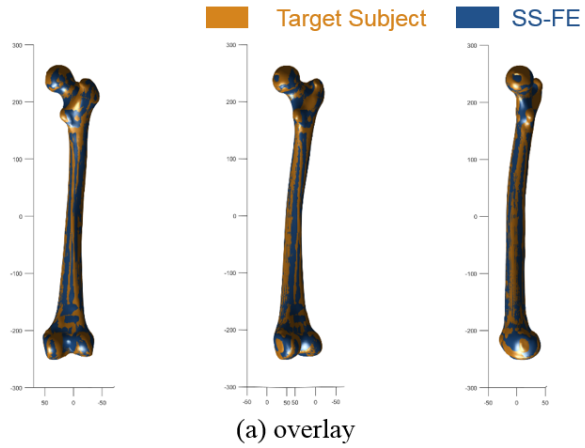
F2012-M07 (age=52)

Figure B1 Comparison of CT and Morphed FE model (continued)



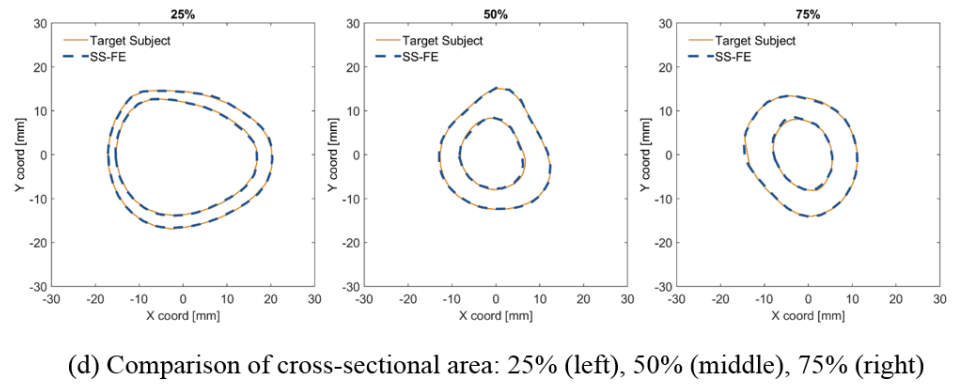
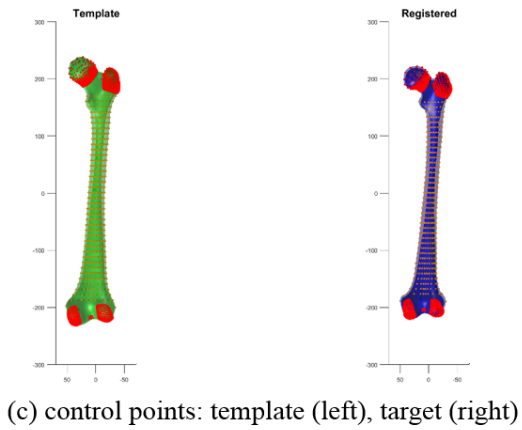
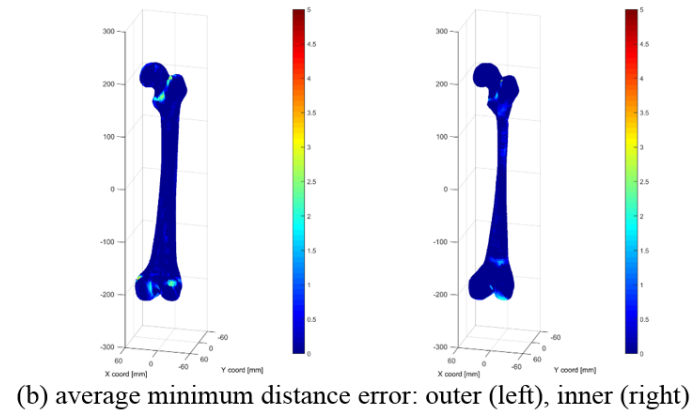
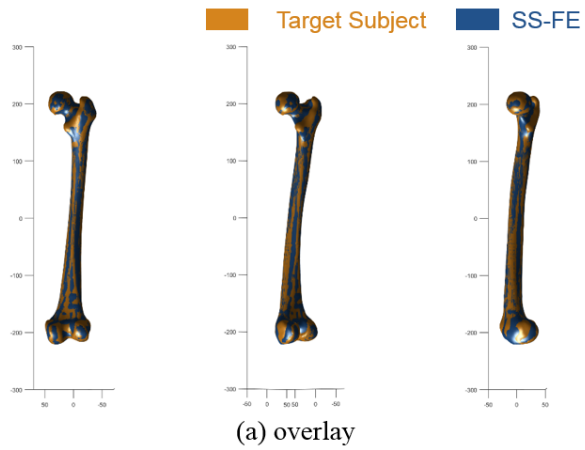
F2012-M08 (age=27)

Figure B1 Comparison of CT and Morphed FE model (continued)



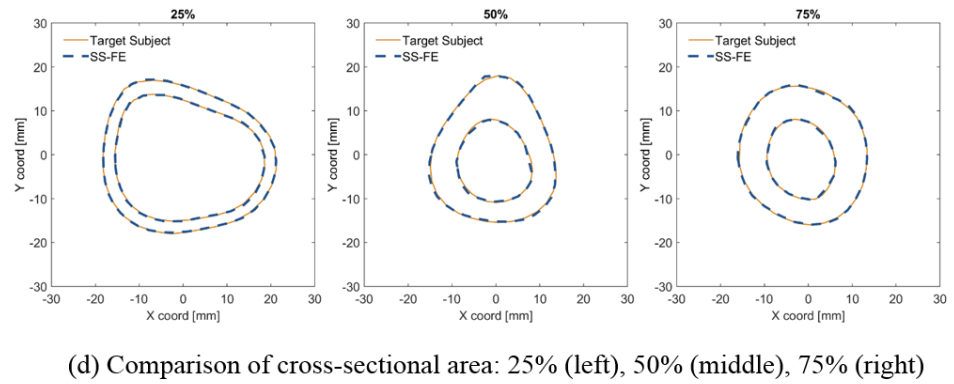
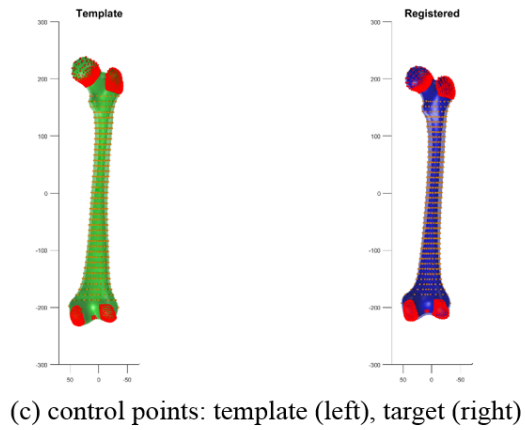
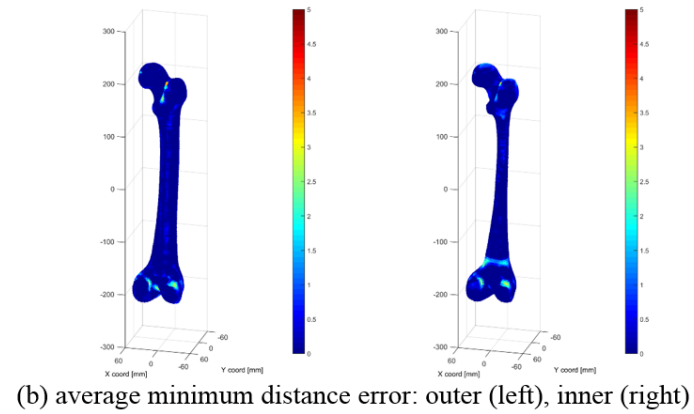
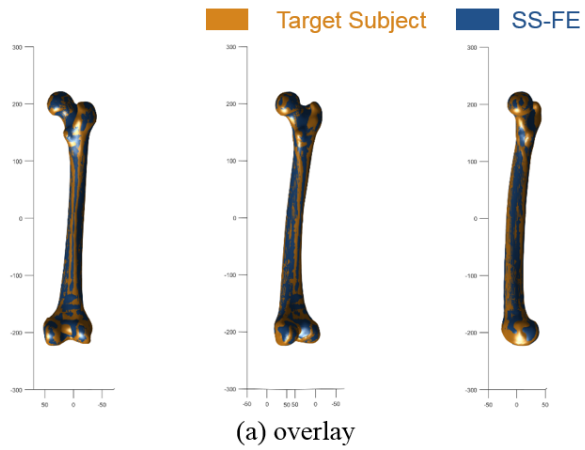
F2012-M09 (age=42)

Figure B1 Comparison of CT and Morphed FE model (continued)



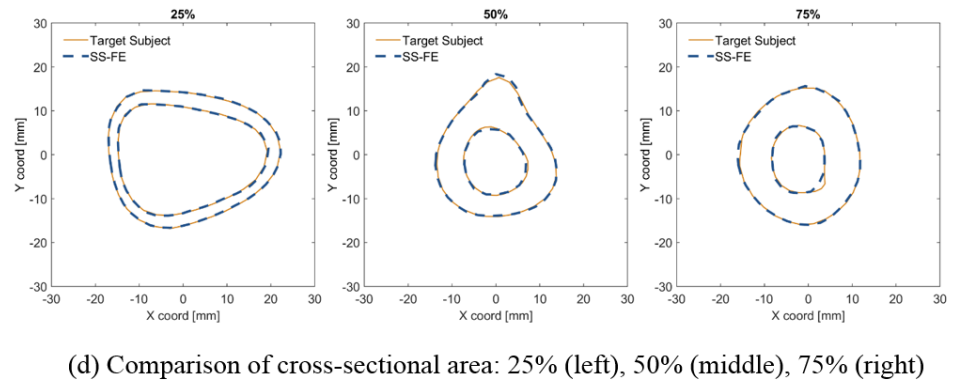
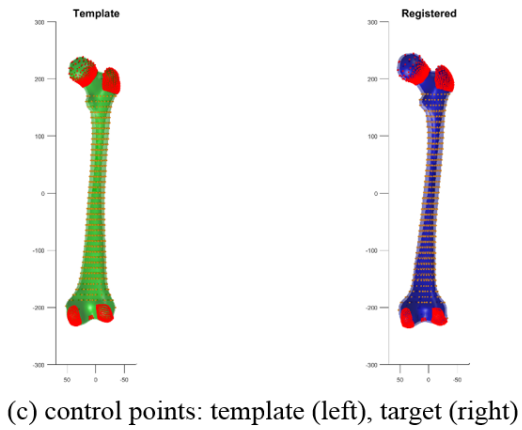
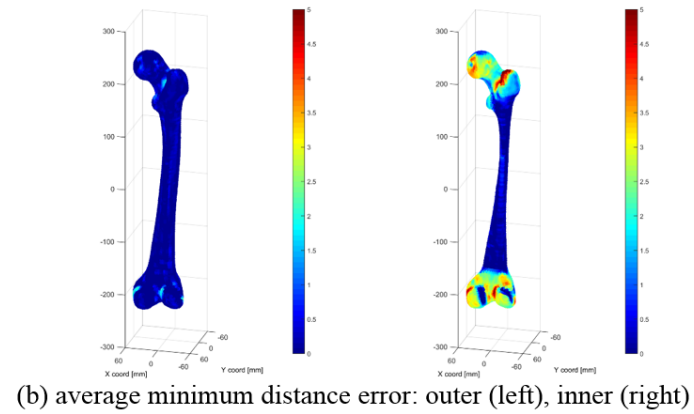
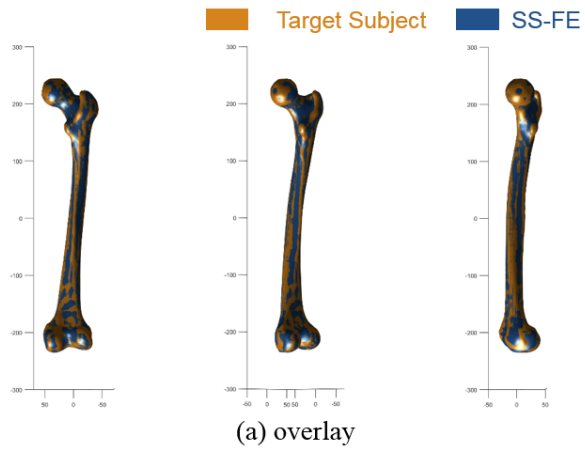
F2012-M10 (age=25)

Figure B1 Comparison of CT and Morphed FE model (continued)



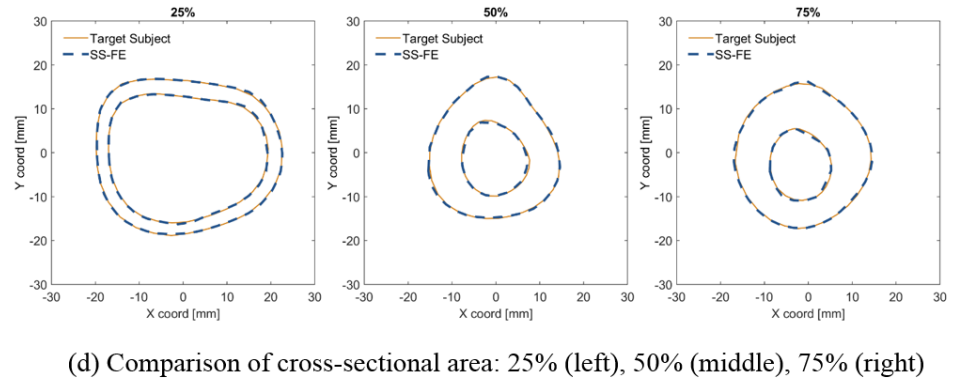
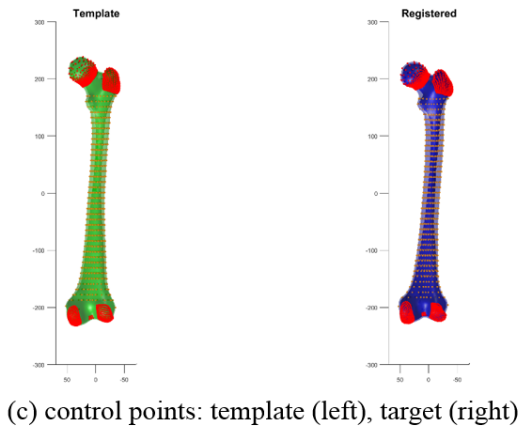
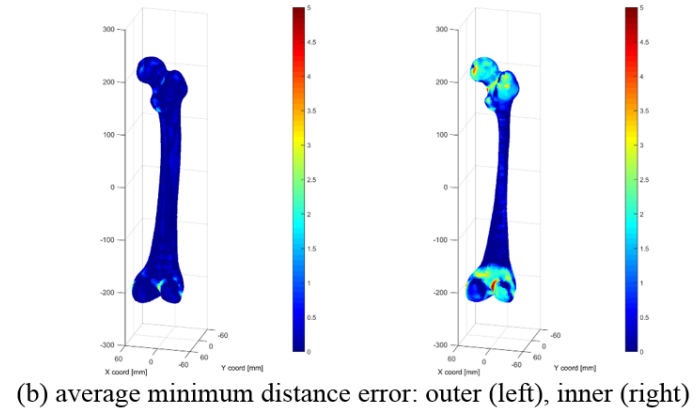
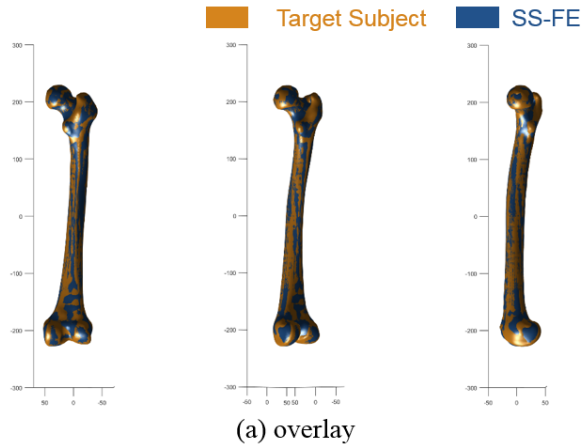
F2012-M11 (age=28)

Figure B1 Comparison of CT and Morphed FE model (continued)



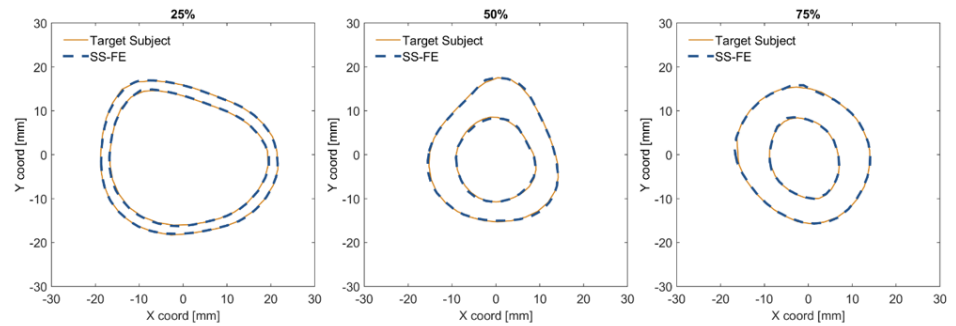
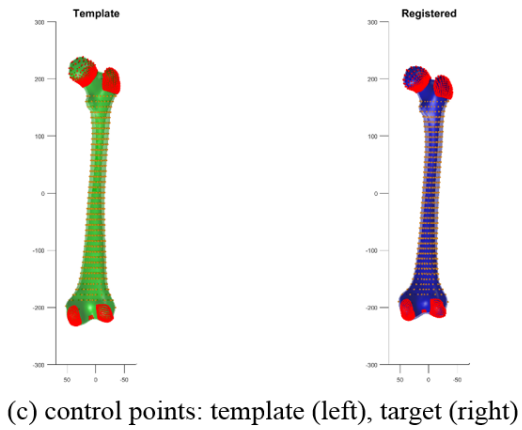
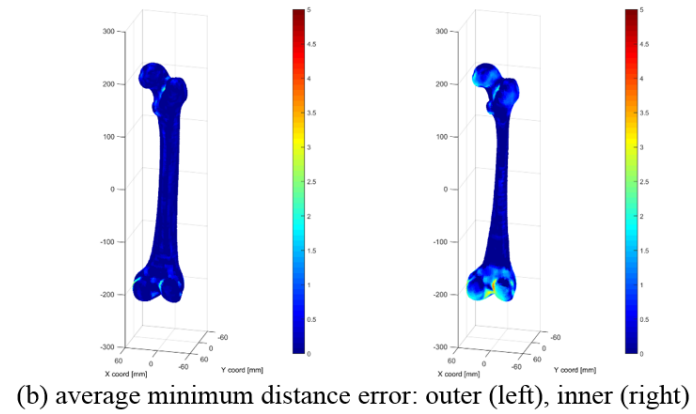
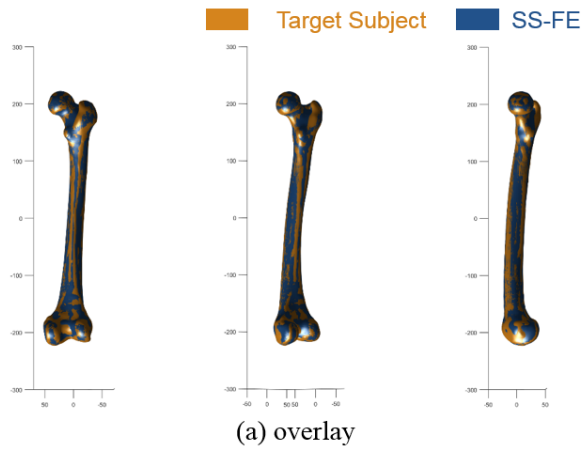
F2012-M12 (age=35)

Figure B1 Comparison of CT and Morphed FE model (continued)



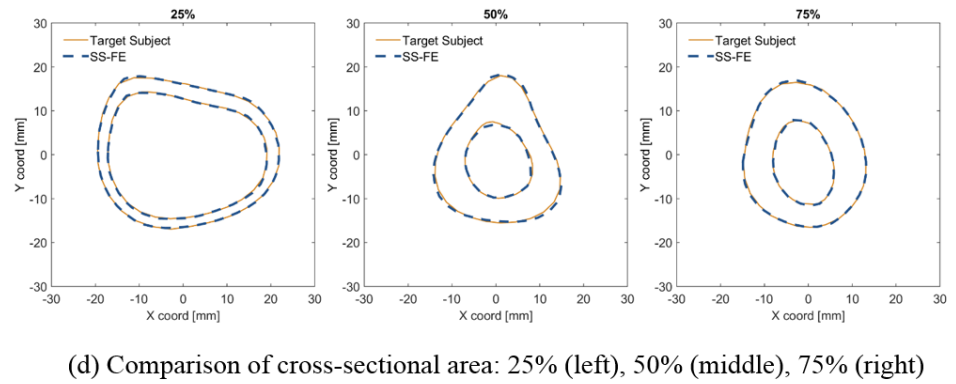
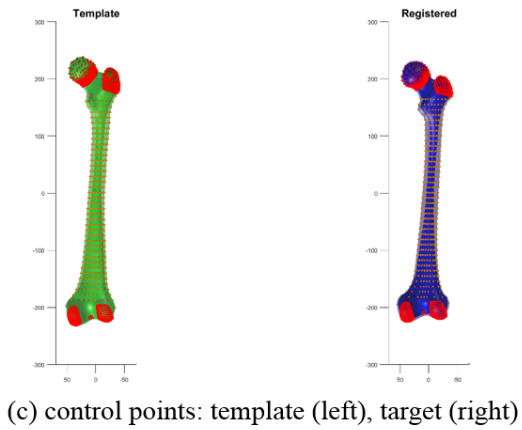
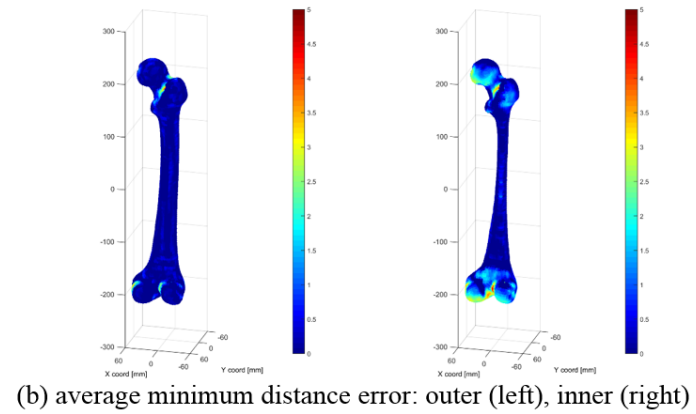
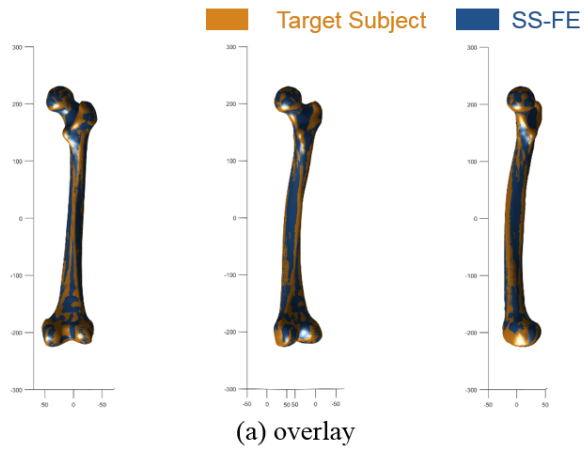
F2012-M13 (age=36)

Figure B1 Comparison of CT and Morphed FE model (continued)



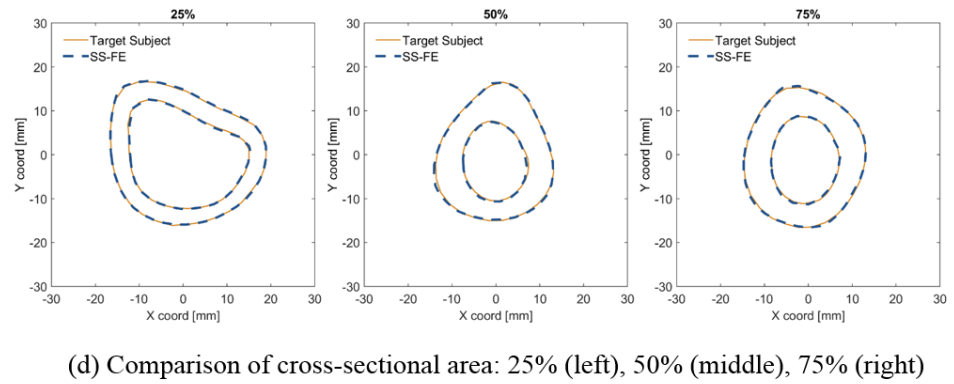
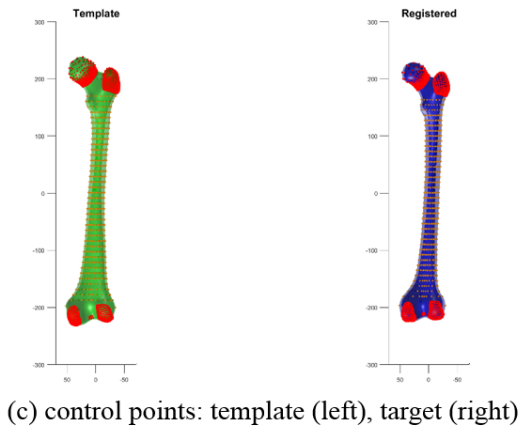
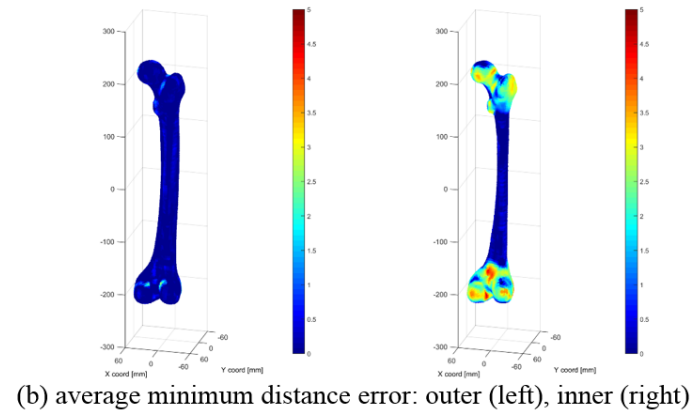
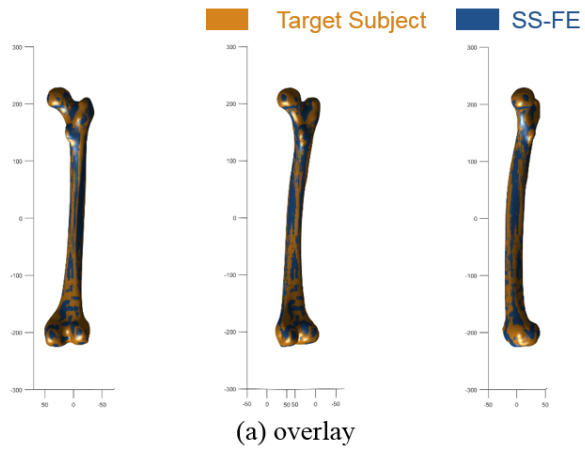
F2012-M14 (age=28)

Figure B1 Comparison of CT and Morphed FE model (continued)



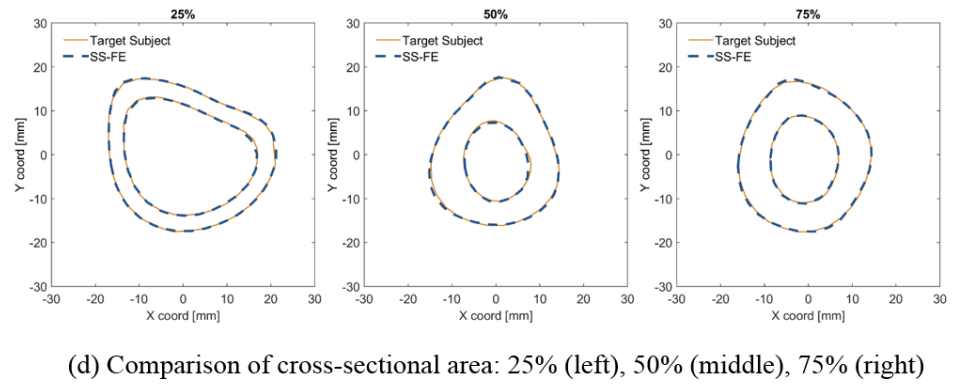
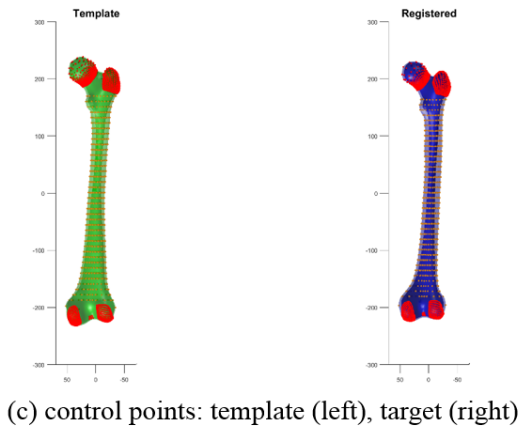
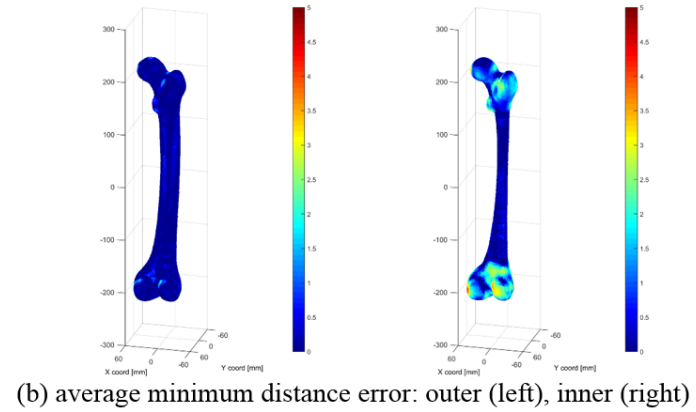
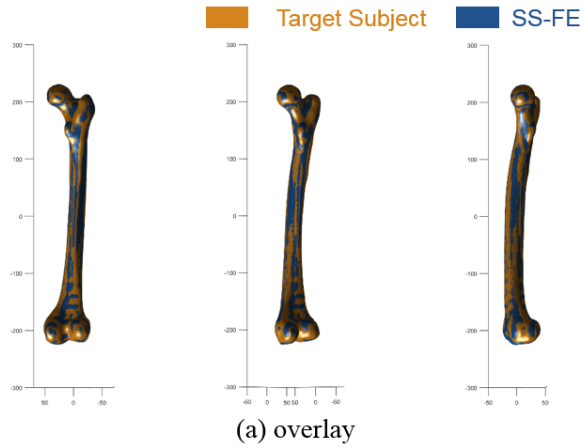
F2012-M15 (age=19)

Figure B1 Comparison of CT and Morphed FE model (continued)



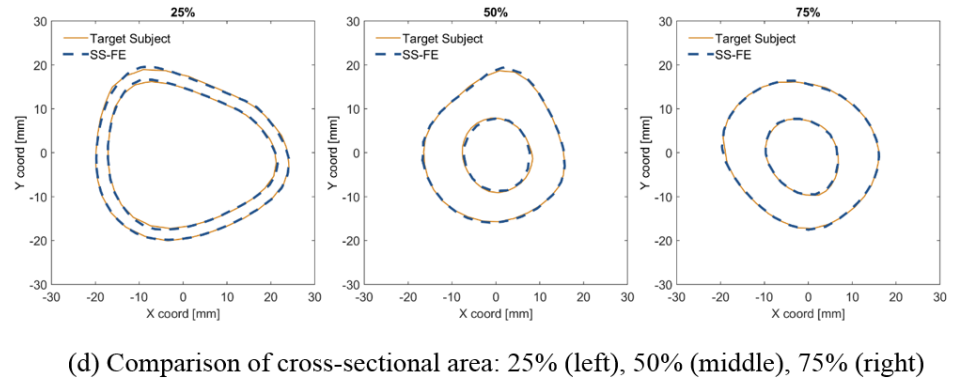
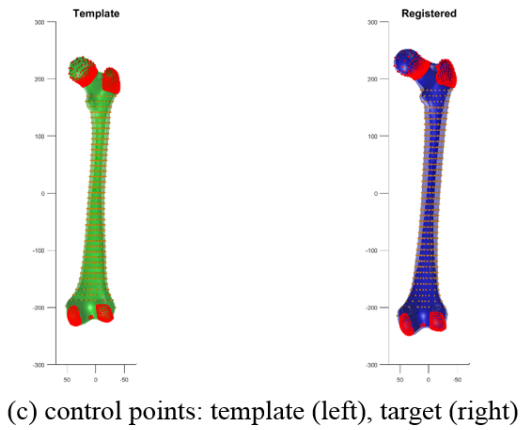
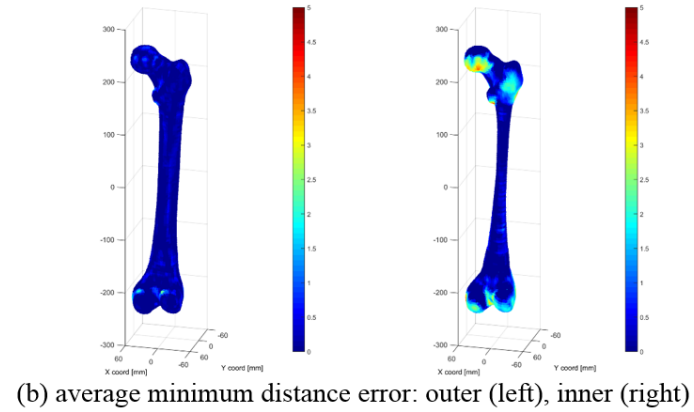
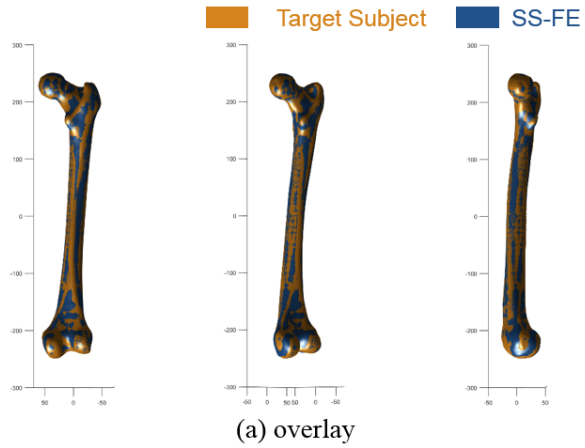
F2004-M01 (age=69)

Figure B1 Comparison of CT and Morphed FE model (continued)



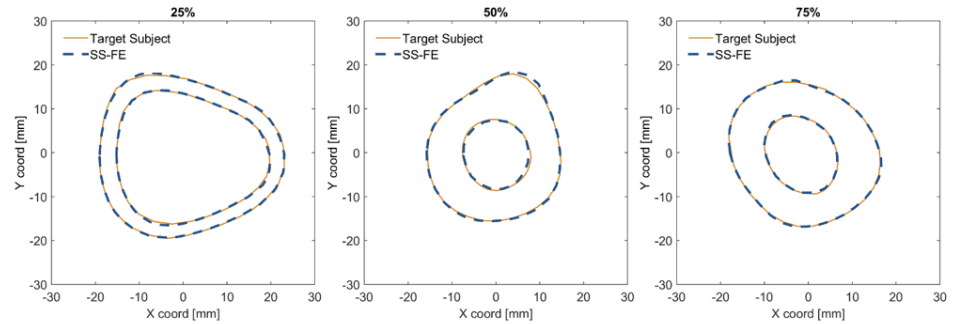
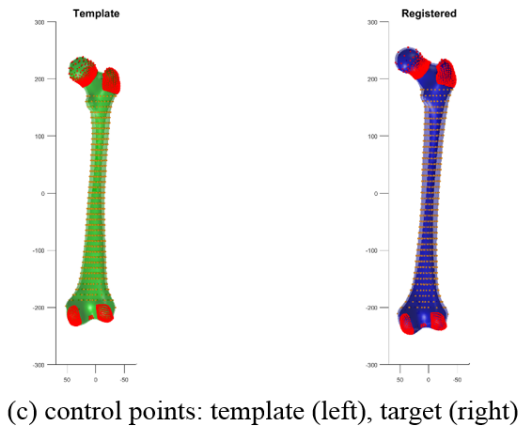
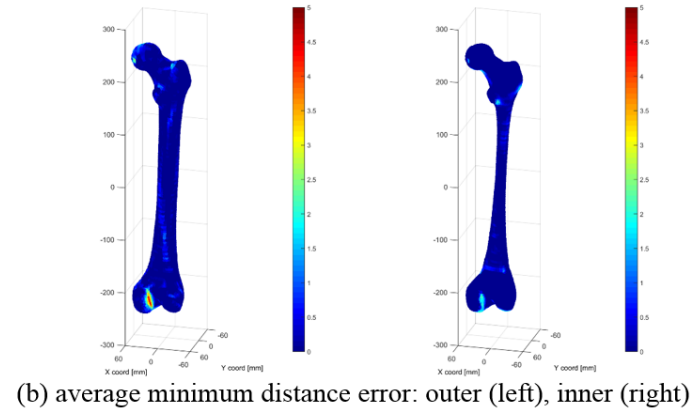
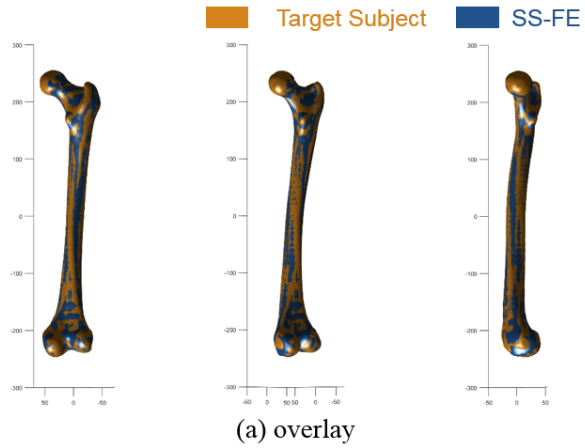
F2004-M02 (age=70)

Figure B1 Comparison of CT and Morphed FE model (continued)



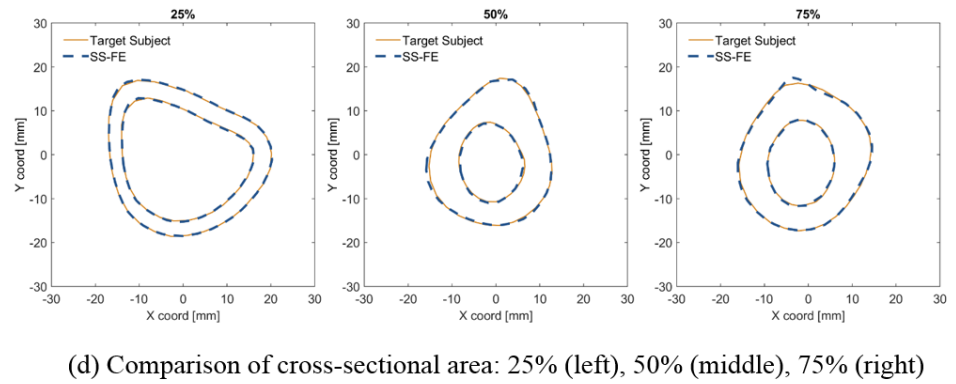
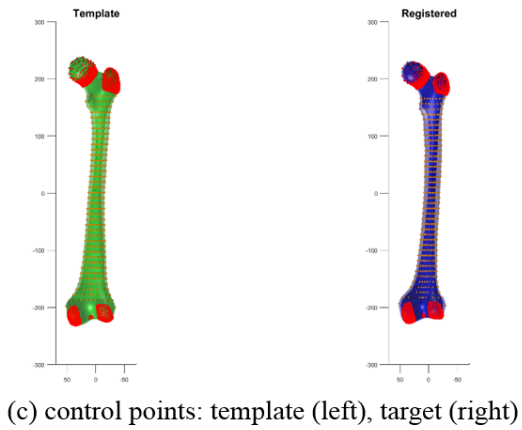
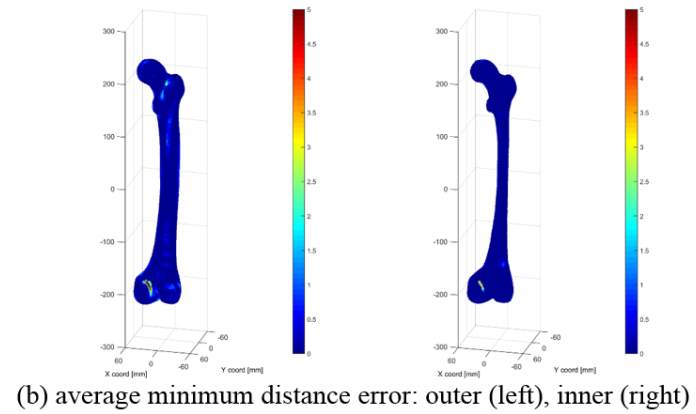
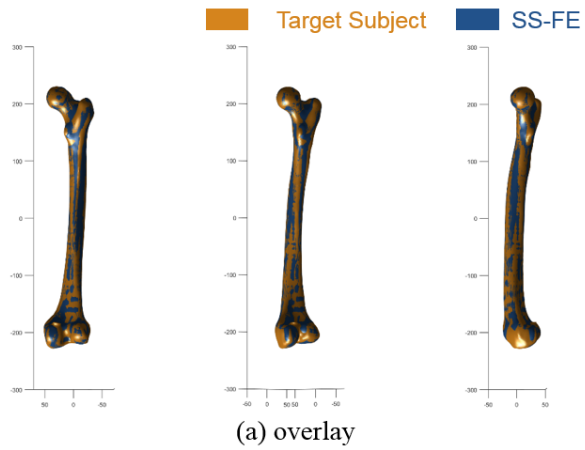
F2004-M03 (age=51)

Figure B1 Comparison of CT and Morphed FE model (continued)



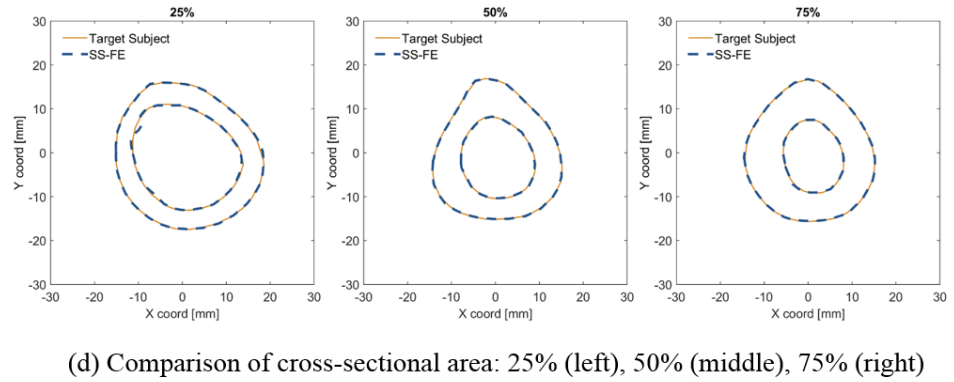
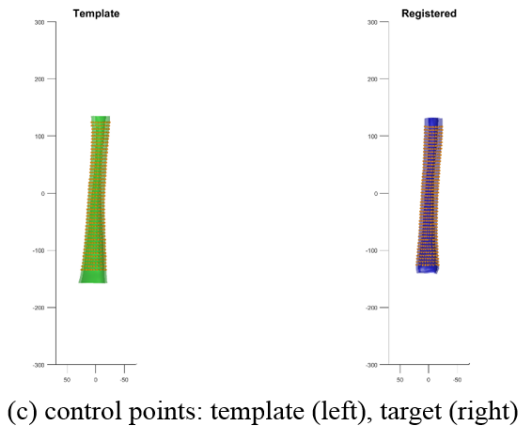
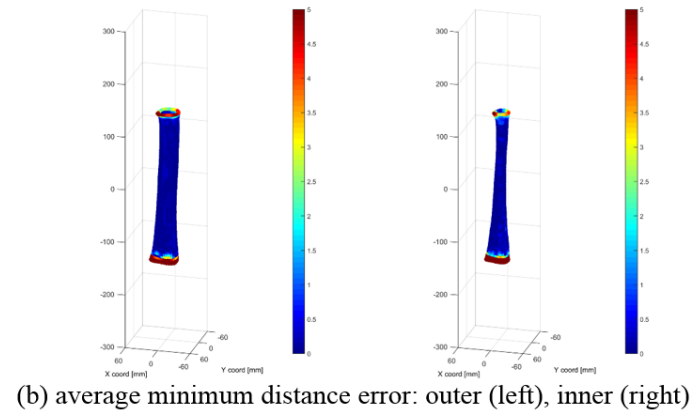
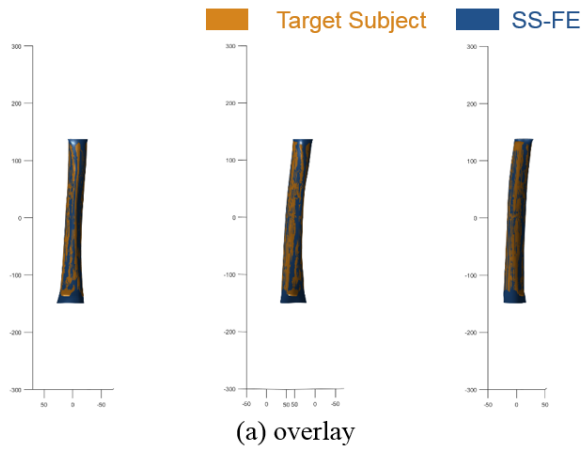
F2004-M04 (age=51)

Figure B1 Comparison of CT and Morphed FE model (continued)



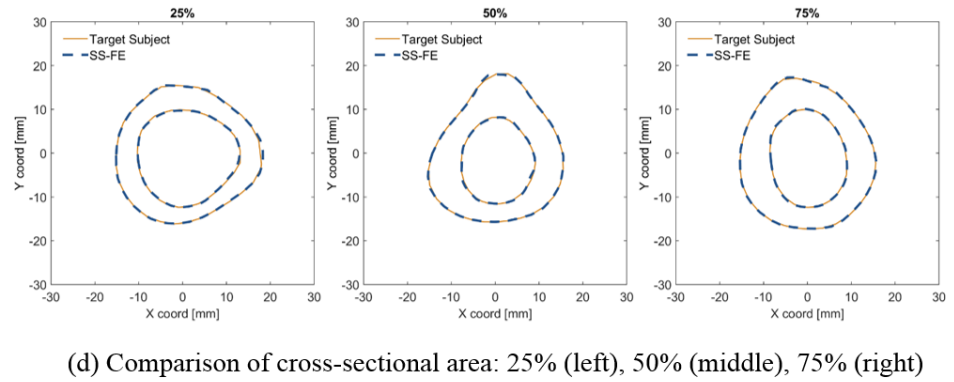
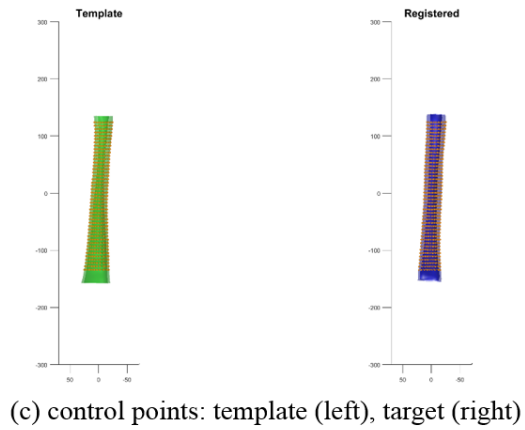
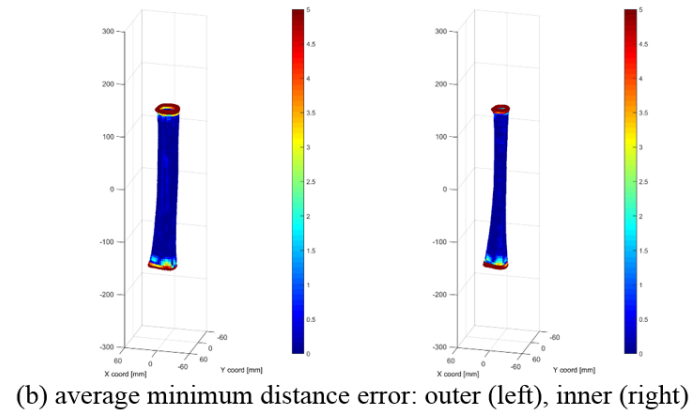
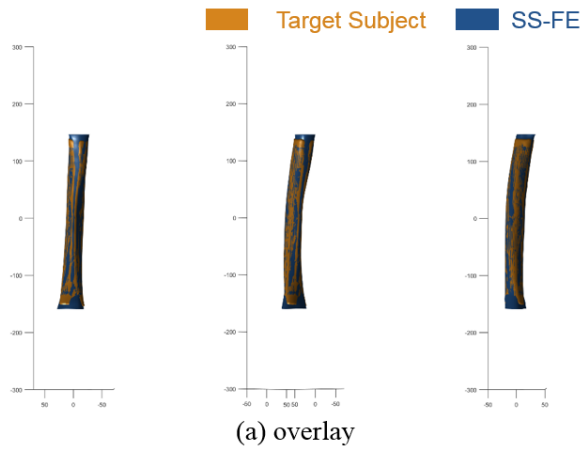
F2004-M05 (age=69)

Figure B1 Comparison of CT and Morphed FE model (continued)



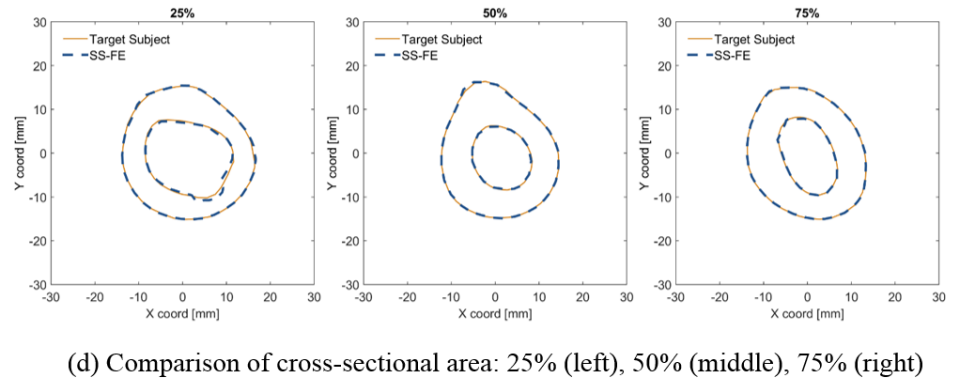
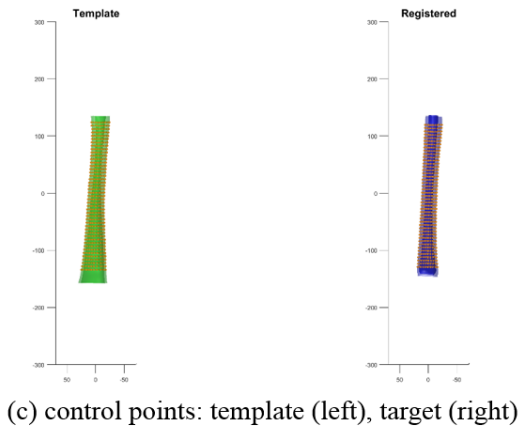
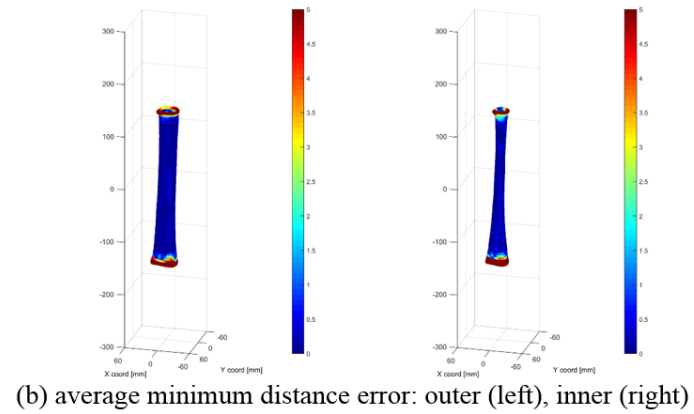
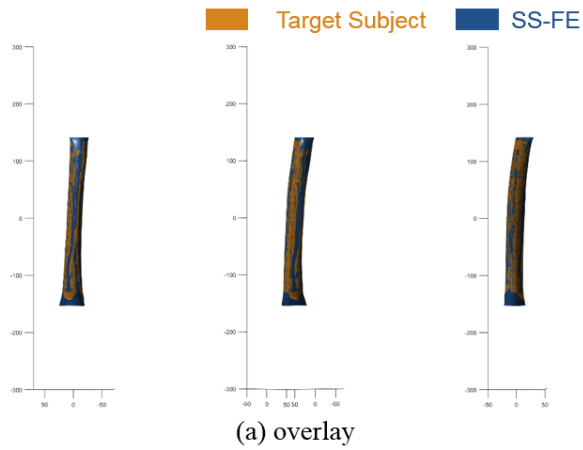
I2012-M01 (age=39)

Figure B3 Comparison of CT and Morphed FE models for combined loadings



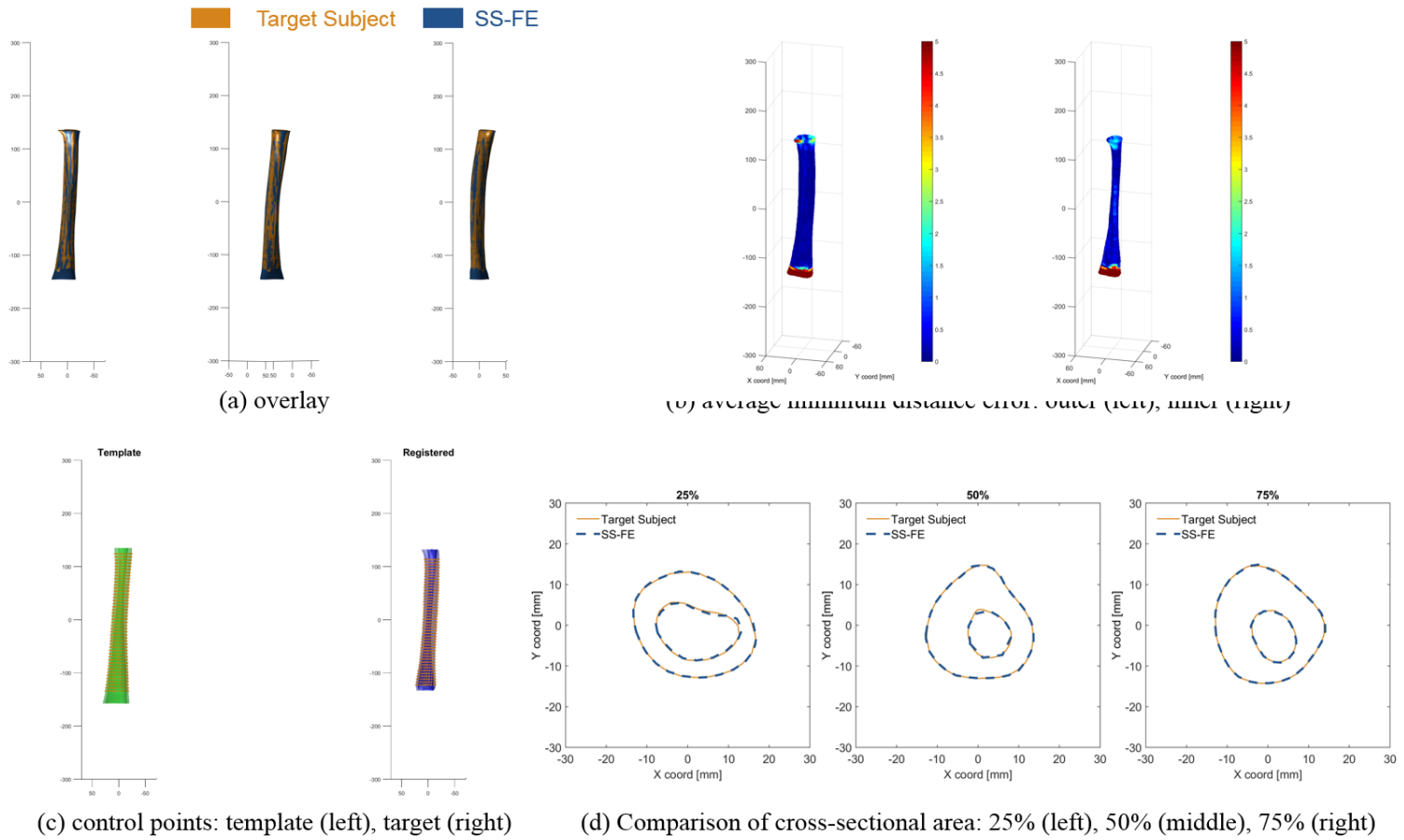
I2012-M02 (age=63)

Figure B2 Comparison of CT and Morphed FE models for combined loadings (continued)



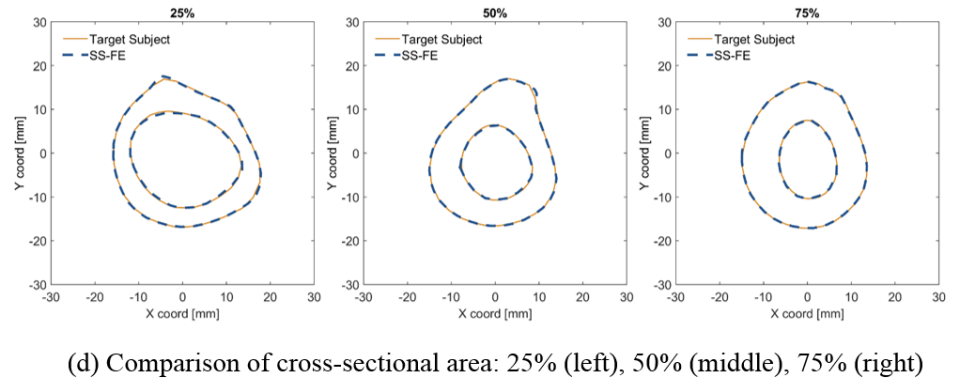
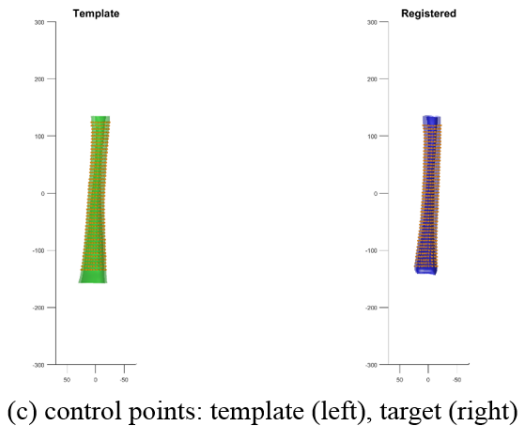
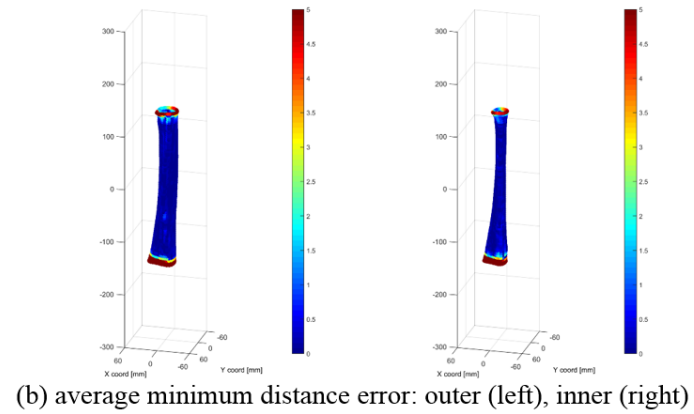
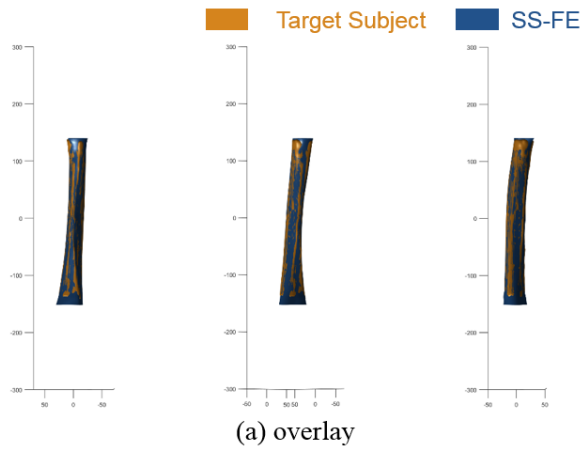
I2012-M03 (age=51)

Figure B2 Comparison of CT and Morphed FE models for combined loadings (continued)



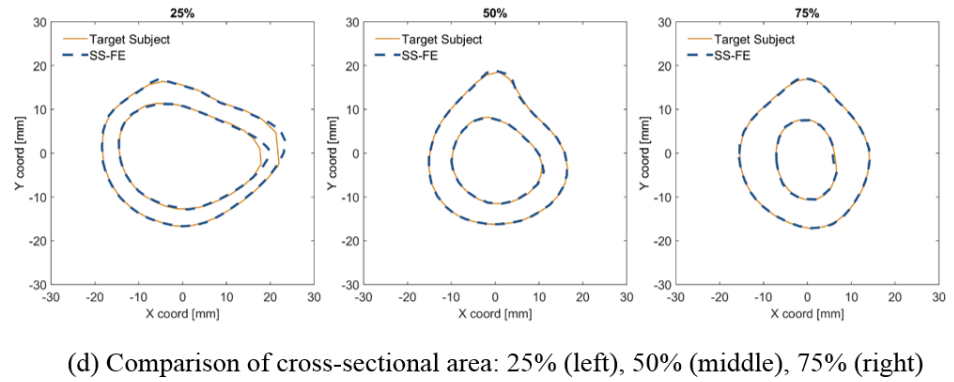
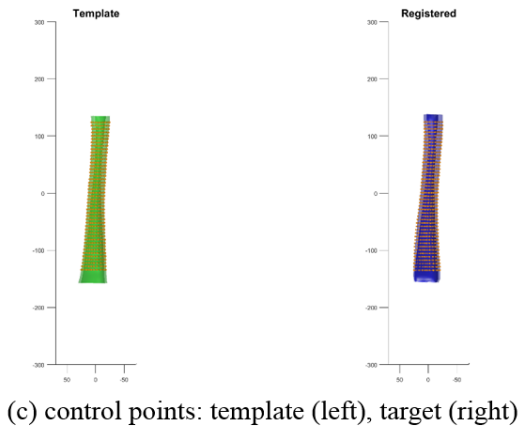
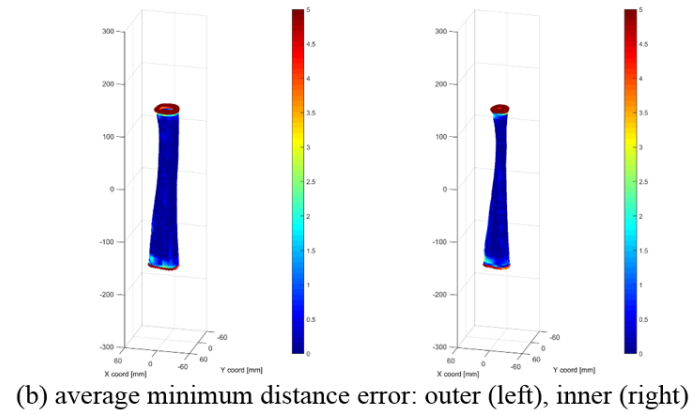
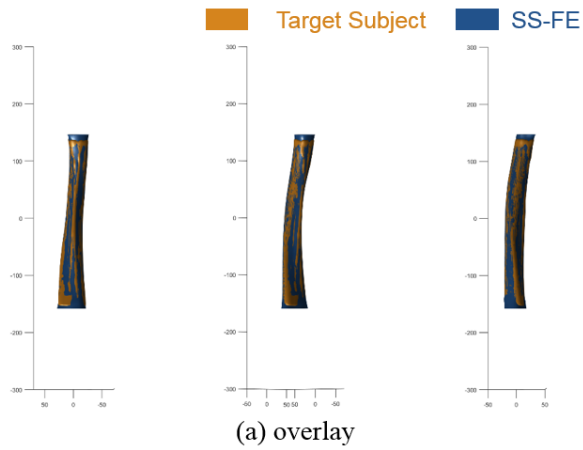
I2012-M04 (age=45)

Figure B2 Comparison of CT and Morphed FE models for combined loadings (continued)



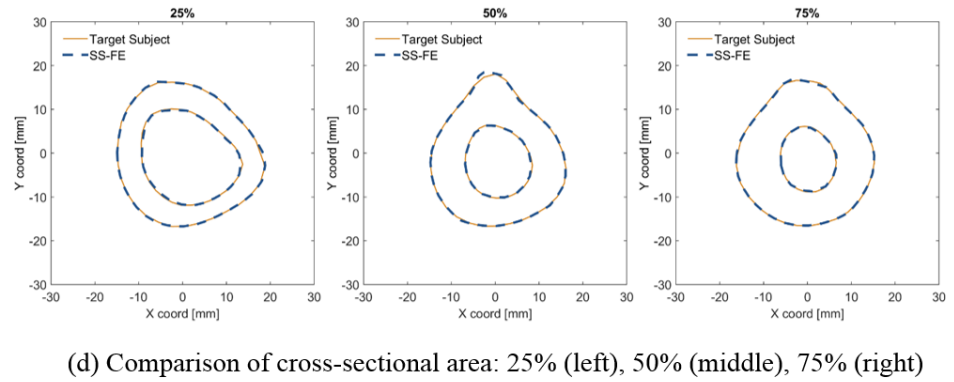
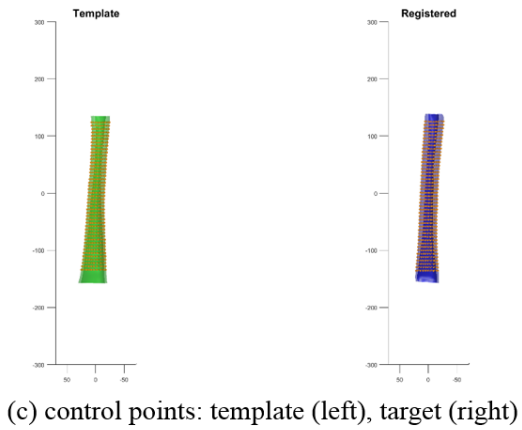
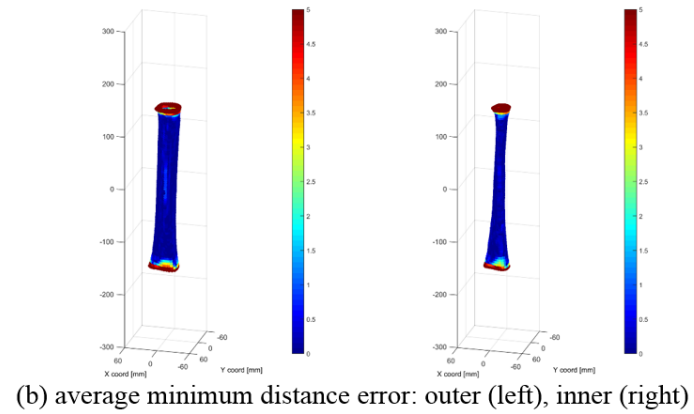
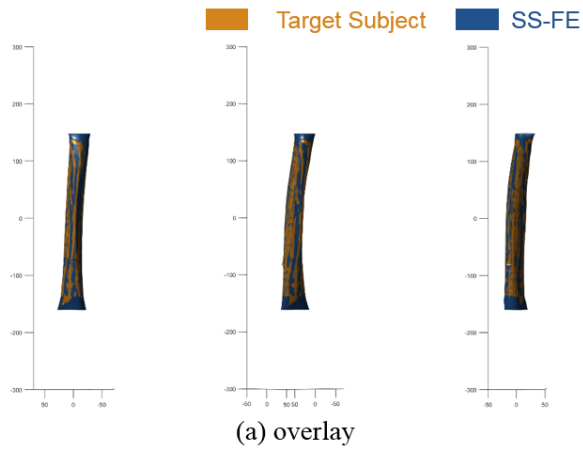
I2012-M05 (age=62)

Figure B2 Comparison of CT and Morphed FE models for combined loadings (continued)



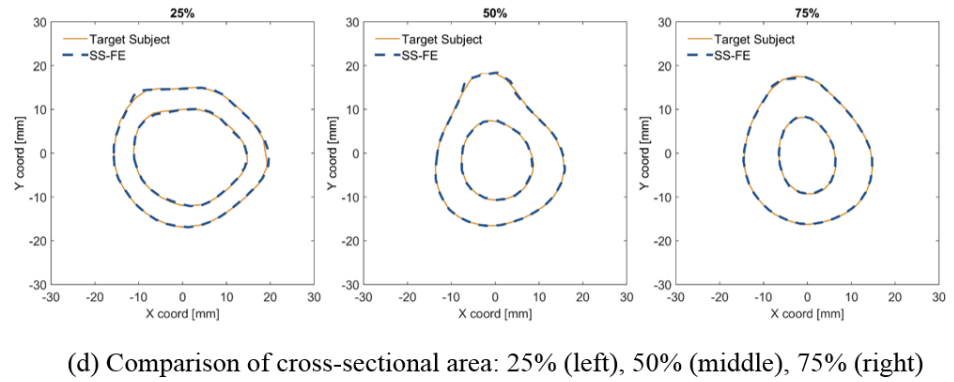
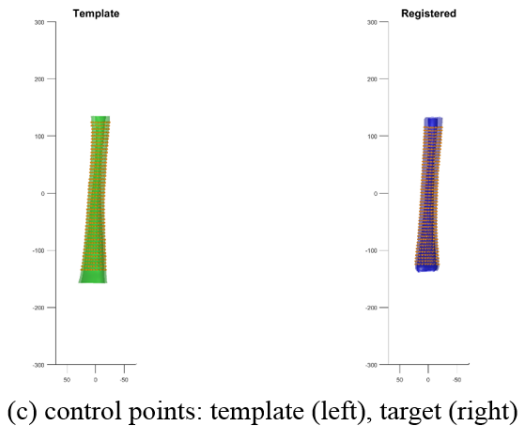
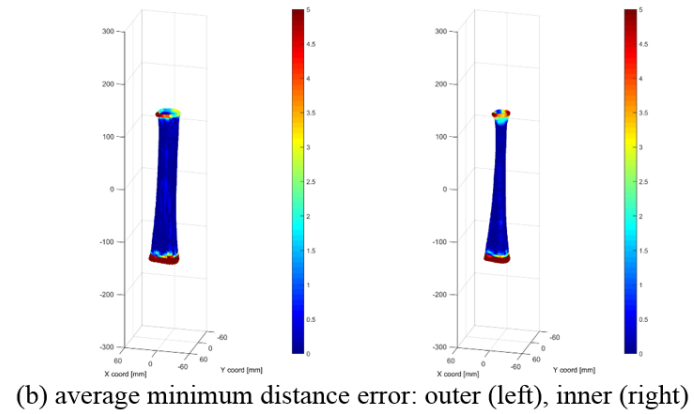
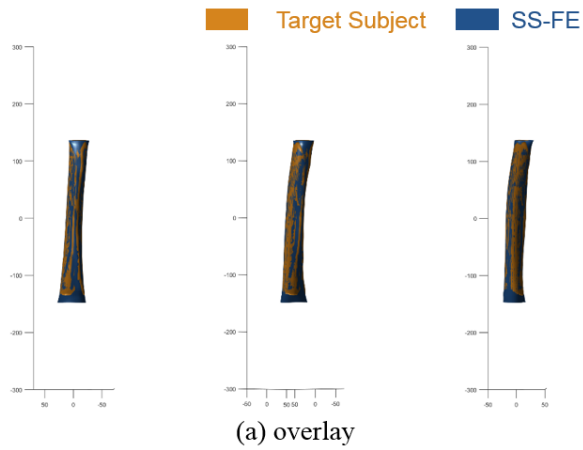
I2012-M06 (age=62)

Figure B2 Comparison of CT and Morphed FE models for combined loadings (continued)



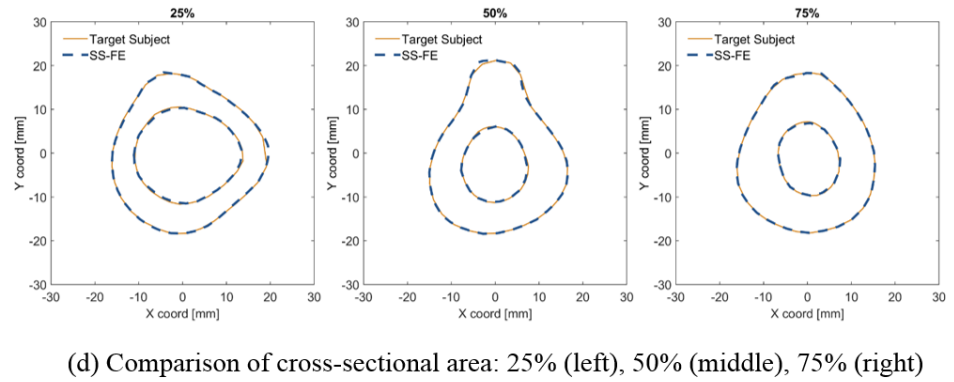
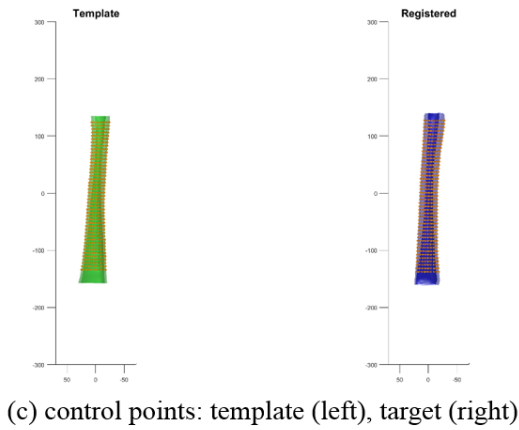
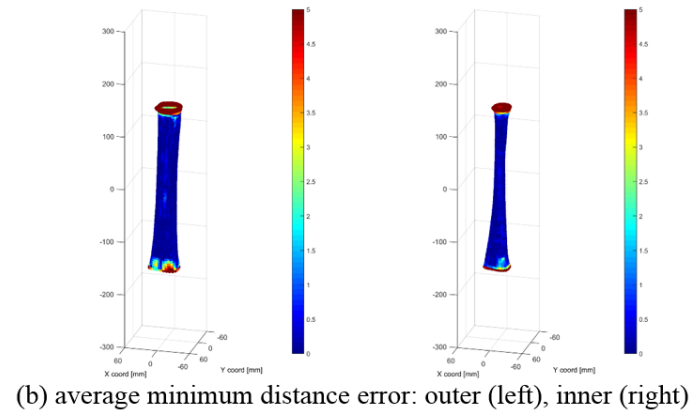
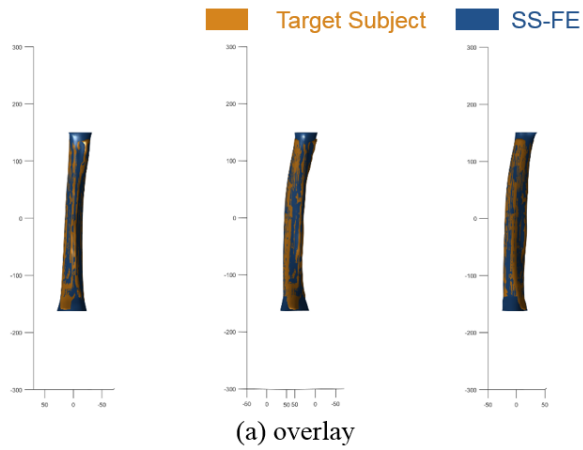
I2012-M07 (age=62)

Figure B2 Comparison of CT and Morphed FE models for combined loadings (continued)



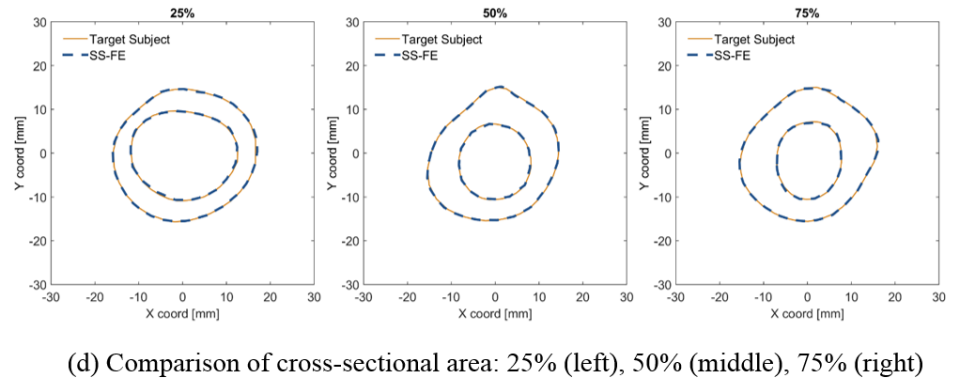
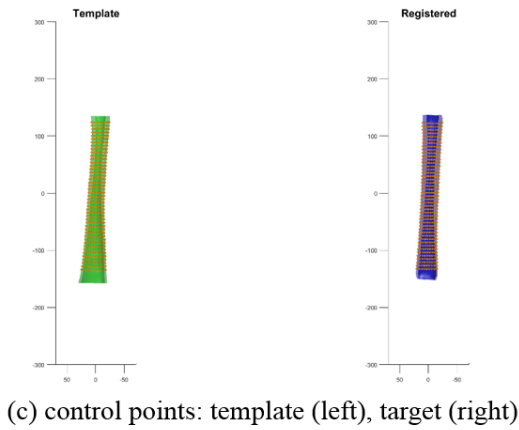
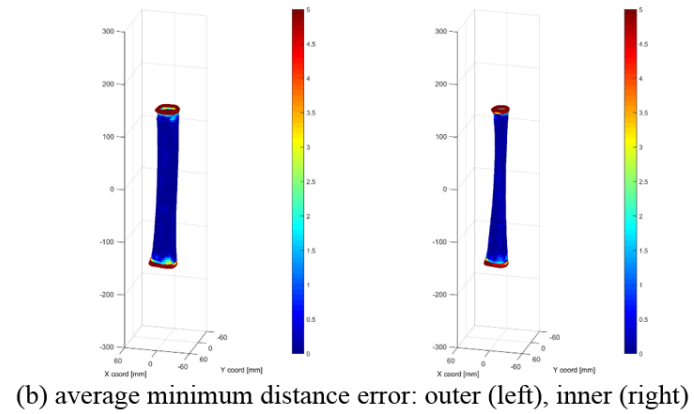
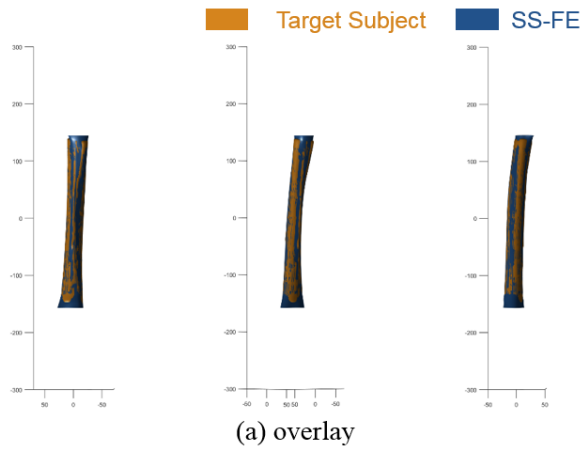
I2012-M08 (age=62)

Figure B2 Comparison of CT and Morphed FE models for combined loadings (continued)



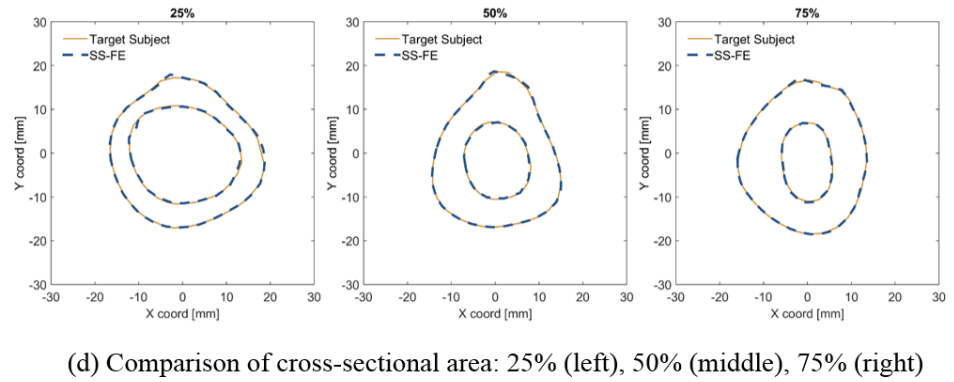
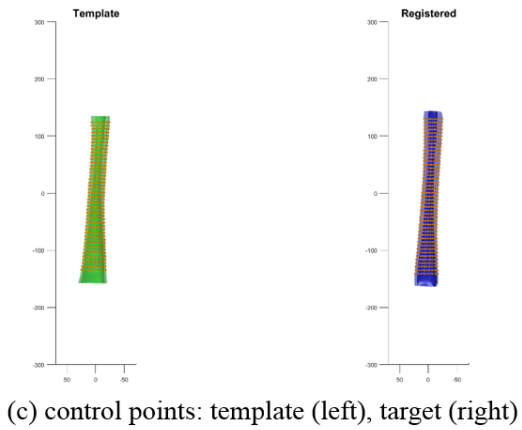
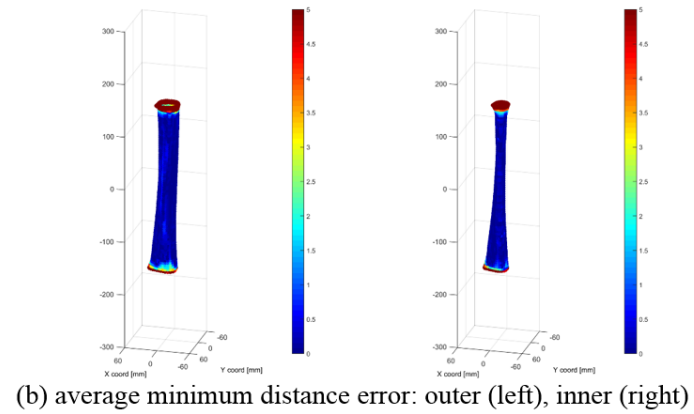
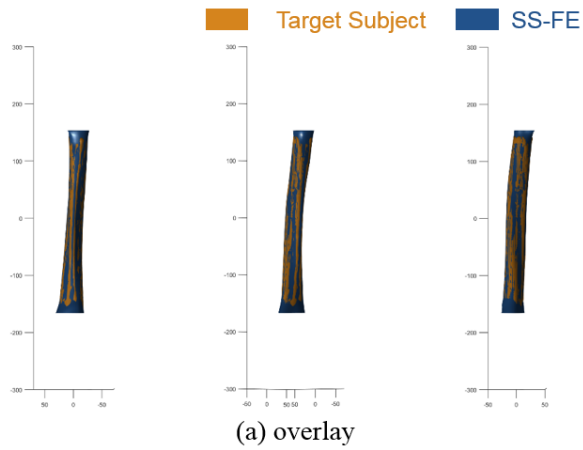
I2012-M09 (age=58)

Figure B2 Comparison of CT and Morphed FE models for combined loadings (continued)



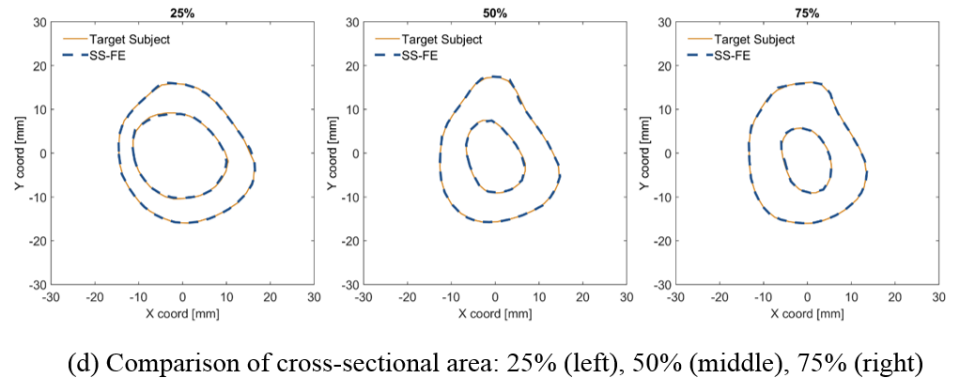
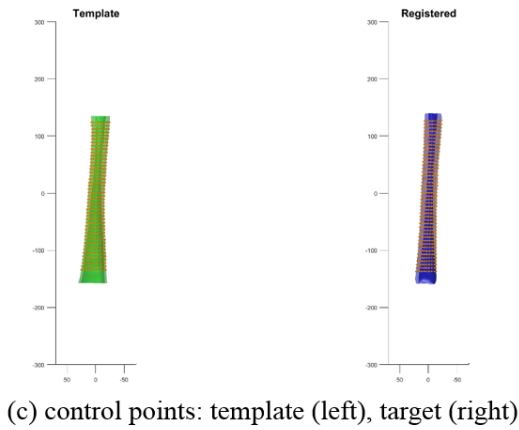
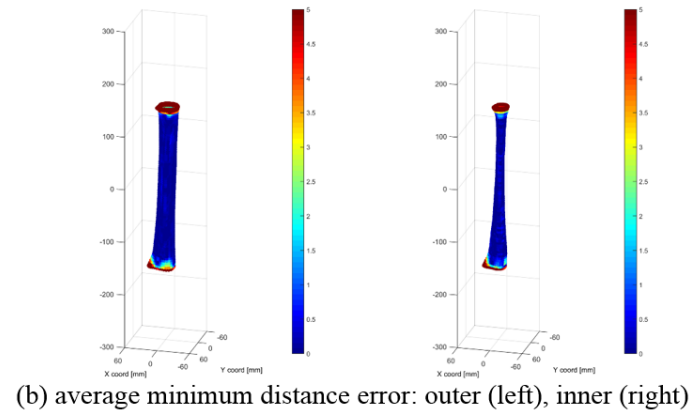
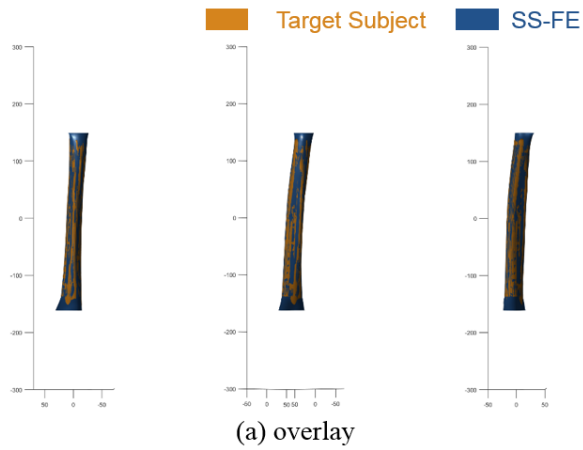
I2012-M10 (age=65)

Figure B2 Comparison of CT and Morphed FE models for combined loadings (continued)



I2012-M11 (age=49)

Figure B2 Comparison of CT and Morphed FE models for combined loadings (continued)



I2012-M12 (age=44)

Figure B2 Comparison of CT and Morphed FE models for combined loadings (continued)

APPENDIX C: MATERIAL PARAMETER IDENTIFICATION

A piecewise linear plastic material model (LSTC, 2013) was used as the material model for the SS-FE models (Table 4). The piecewise linear plasticity material model is defined by the elastic modulus, yield stress, tangent modulus, fracture strain, density, and Poisson's ratio. For a cortical bone of femoral diaphysis, a wide range of elastic modulus has been reported. Thus, to identify a general elastic modulus for simulations, a parametric study for elastic modulus from 11GPa to 21 GPa (every 1 GPa) was conducted using the fifteen SS-FE femur models (targeting the PMHS specimens used in Forman's test (Forman et al., 2012a)). A parametric study for yield stress from 50MPa to 200MPa (every 25MPa) was conducted. Since the yield stress of the cortical bone has not been reported in the literature, the range of the yield stress was assumed in this study. The sum of the RMS errors for fifteen cases was calculated for the material parameters; the 17GPa of the elastic modulus and 125MPa of the yield stress, which gave a minimum RMS error, were selected as the general elastic modulus for the SS-FE models. Also, a parametric study for the ultimate strain from 0.01 to 0.06 (every 0.05) was conducted, and 0.045 of the ultimate strain was selected as the common material parameter which minimizes the both the fracture force differences and the fracture timing. The density and Poisson's ratio of compact bone were assumed as 2000 kg/m³ and 0.3, respectively.

Table C1 Material identification (Elastic Modulus): the sum of RMS error for 15 specimens

		Yield Stress [GPa]							
		0.05	0.075	0.1	0.125	0.15	0.175	0.2	10
Elastic Modulus [GPa]	11	1.99	1.06	0.70	0.60	0.57	0.57	0.57	0.57
	12	1.90	0.95	0.57	0.44	0.41	0.40	0.40	0.40
	13	1.82	0.47	0.44	0.31	0.28	0.27	0.27	0.27
	14	1.74	0.77	0.35	0.21	0.18	0.18	0.19	0.19
	15	1.68	0.71	0.28	0.16	0.14	0.15	0.16	0.17
	16	1.62	0.64	0.23	0.13	0.13	0.16	0.18	0.19
	17	1.56	0.60	0.20	0.12	0.15	0.20	0.24	0.27
	18	1.51	0.56	0.18	0.13	0.20	0.28	0.34	0.39
	19	1.46	0.53	0.18	0.16	0.26	0.39	0.47	0.57
	20	1.42	0.50	0.18	0.19	0.35	0.51	0.63	0.77
	21	1.37	0.48	0.19	0.25	0.45	0.66	0.82	0.98

Table C2 Material identification (Ultimate Strain): the sum of the fracture force and timing differences for 15 specimens

		Ultimate Strain										
		0.01	0.015	0.02	0.025	0.03	0.035	0.04	0.045	0.05	0.055	0.06
Force [kN]		2.60	2.02	1.00	0.80	0.74	0.62	0.54	0.45	0.44	0.43	0.43
Timing [ms]		7.09	5.51	4.41	3.13	2.19	1.70	1.41	1.39	1.76	2.36	3.03

Table C3 Material parameters identified for individual SS-FE models for pure bending cases

code	age	stature	weight	H ^{*a}	Area ^{*b}			E ^{*c}	σ_y ^{*d}	ϵ_u ^{*e}
					25%	50%	75%			
	[cm]	[kg]	[mm]	[mm ²]	[mm ²]	[mm ²]	[GPa]	[GPa]	[%]	
F2012-M01	36	N/A	N/A	448	267	450	534	19.0	0.18	1.7
F2012-M02	20	N/A	N/A	502	239	506	555	16.0	0.15	4.3
F2012-M03	27	N/A	N/A	494	498	574	626	16.0	0.20	2.9
F2012-M04	43	N/A	N/A	467	289	446	498	15.0	0.13	6.0
F2012-M05	35	N/A	N/A	479	283	437	511	16.0	0.13	3.7
F2012-M06	19	N/A	N/A	460	304	501	519	15.0	0.15	3.7
F2012-M07	52	N/A	N/A	475	321	533	590	15.0	0.18	4.0
F2012-M08	27	N/A	N/A	497	340	512	559	16.0	0.13	4.1
F2012-M09	42	N/A	N/A	516	331	494	579	15.0	0.13	4.7
F2012-M10	25	N/A	N/A	443	264	334	363	19.0	0.10	3.8
F2012-M11	28	N/A	N/A	445	303	473	506	16.0	0.20	3.2
F2012-M12	35	N/A	N/A	480	283	448	512	19.0	0.10	3.5
F2012-M13	36	N/A	N/A	458	363	527	596	18.0	0.13	4.7
F2012-M14	28	N/A	N/A	445	246	456	494	18.0	0.13	3.7
F2012-M15	19	N/A	N/A	456	299	495	509	15.0	0.13	4.1
F2004-M01	69	162.6	91.6	453	387	426	437	19.0	0.13	3.1
F2004-M02	70	167.6	73.0	454	404	529	549	16.0	0.10	2.9
F2004-M03	51	188.0	123.4	500	316	639	674	16.0	0.13	3.7
F2004-M04	51	188.0	123.4	502	391	606	638	15.0	0.10	4.5
F2004-M05	69	162.6	91.6	459	375	499	525	16.0	0.13	3.0

N/A = not available

*a: height, *b: cross-sectional area along long bone direction, *c: Elastic modulus, *d: yield stress, *e: ultimate strain

Table C4 Material parameters identified for individual SS-FE models for combined loading cases

code	age	stature	weight	E ^{*c}	σ_y ^{*d}	ϵ_u ^{*e}
I2009-M01	36	184.0	79.4	12.0	0.15	4.0
I2009-M02	20	180.3	89.0	11.0	0.13	3.6
I2009-M03	27	175.0	54.9	10.0	0.15	3.5
I2009-M04	43	175.3	68.1	12.0	0.13	4.9
I2009-M05	35	177.8	81.8	13.0	0.13	2.6
I2009-M06	19	185.4	100.0	14.0	0.13	4.4
I2009-M07	52	182.9	90.9	15.0	0.05	2.1
I2009-M08	27	177.8	81.8	10.0	0.10	5.3
I2009-M09	42	182.9	141.0	16.0	0.18	3.6
I2009-M10	25	182.9	90.9	12.0	0.13	5.3
I2009-M11	28	193.0	100.0	10.0	0.08	3.4
I2009-M12	35	193.0	81.8	10.0	0.10	5.8

*c: Elastic modulus, *d: yield stress, *e: ultimate strain

APPENDIX D: DISTRIBUTIONS FOR POPULATION-BASED FE MODELS

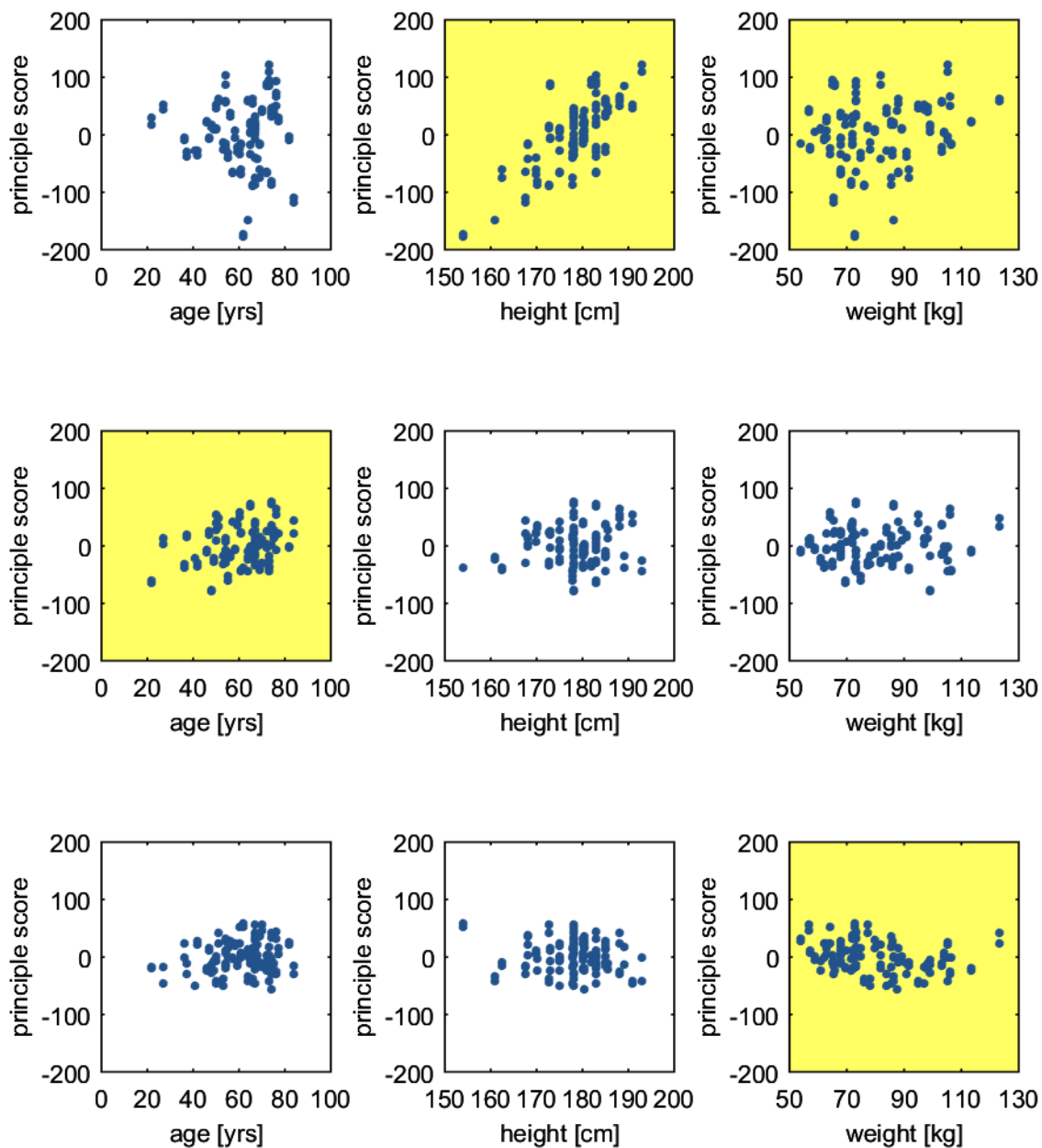


Figure D1 scatter plots (geometric descriptors vs. age, weight, height)

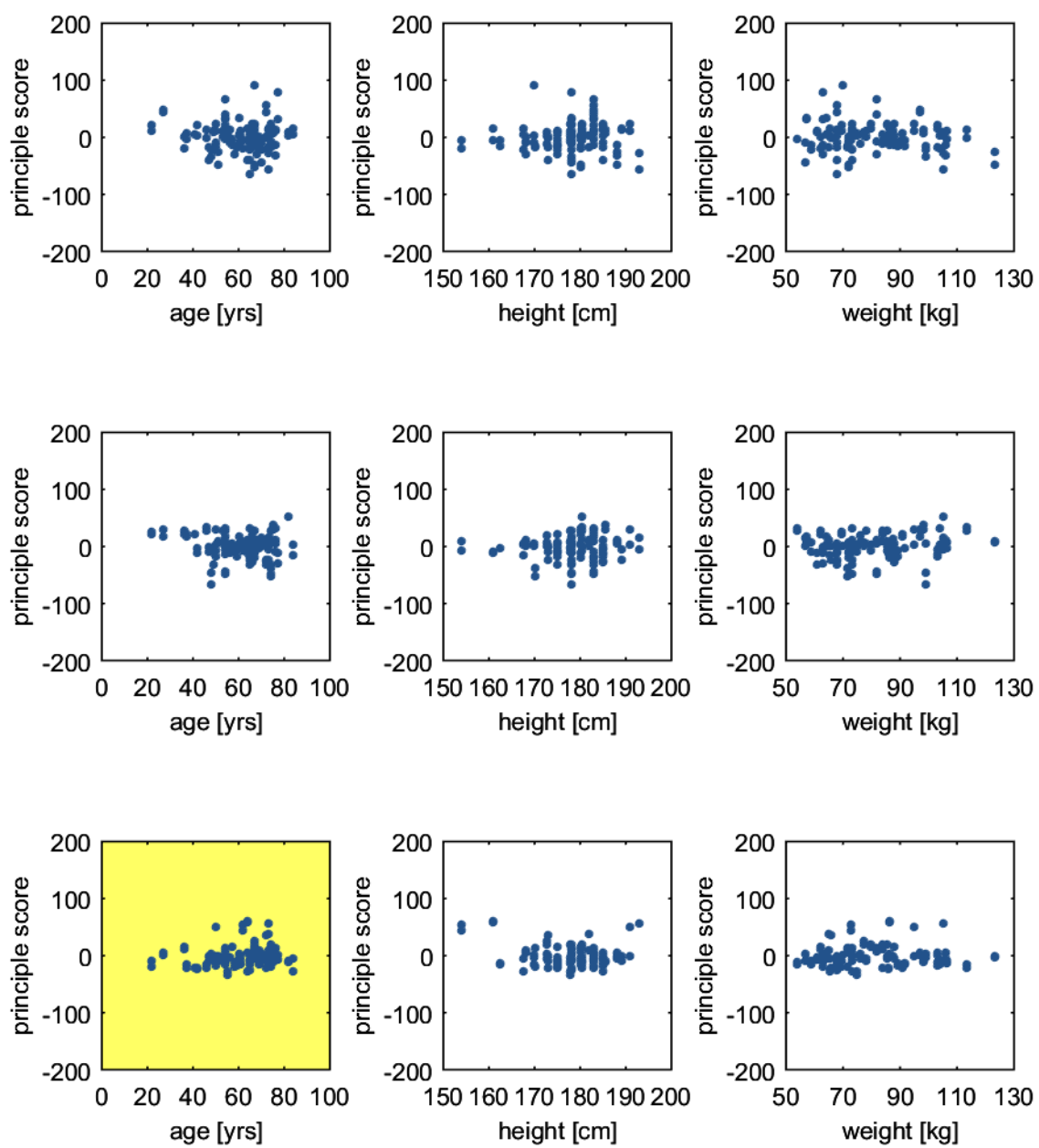


Figure D1 scatter plots (geometric descriptors vs. age, weight, height) (continued)

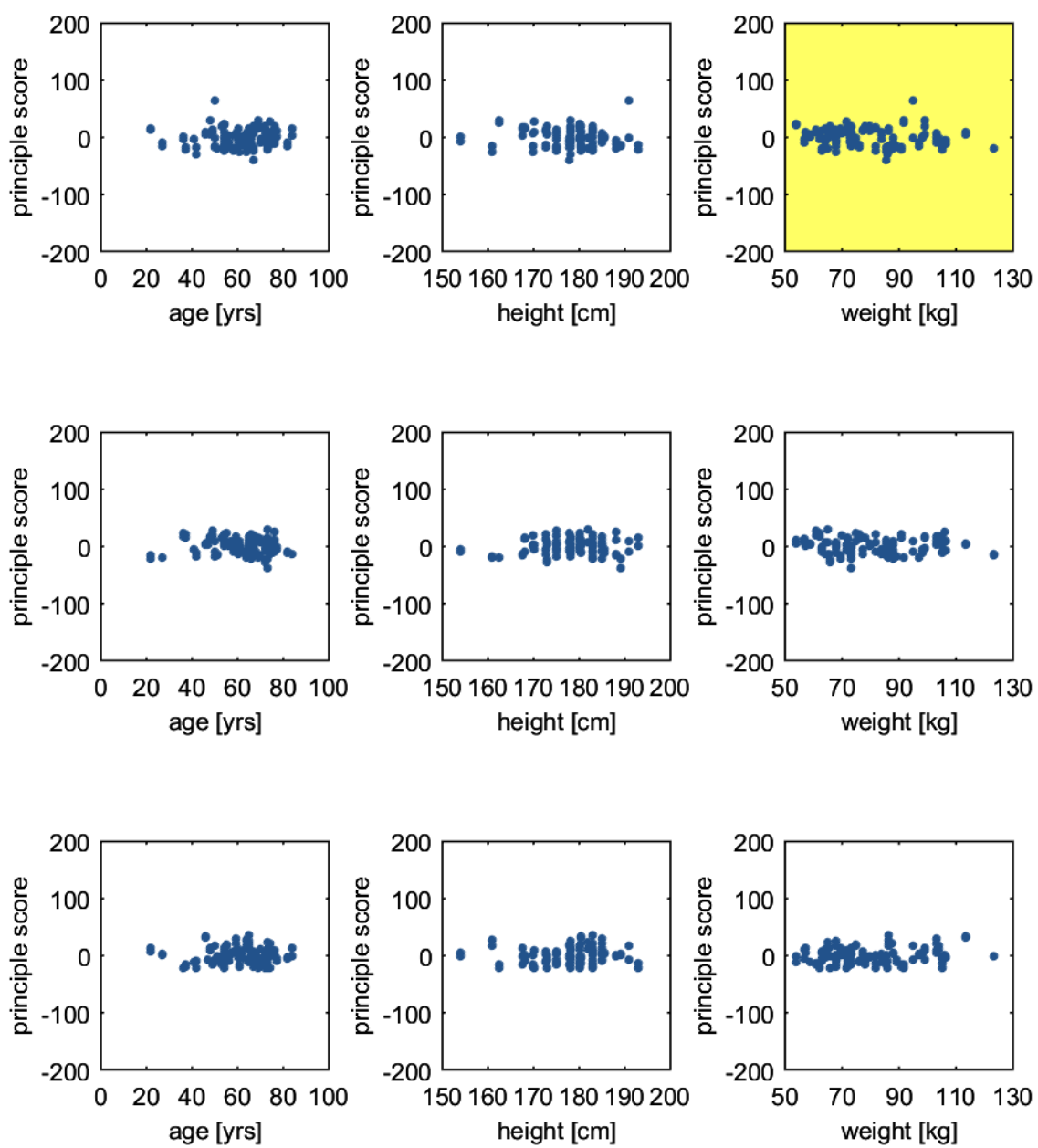


Figure D1 scatter plots (geometric descriptors vs. age, weight, height) (continued)

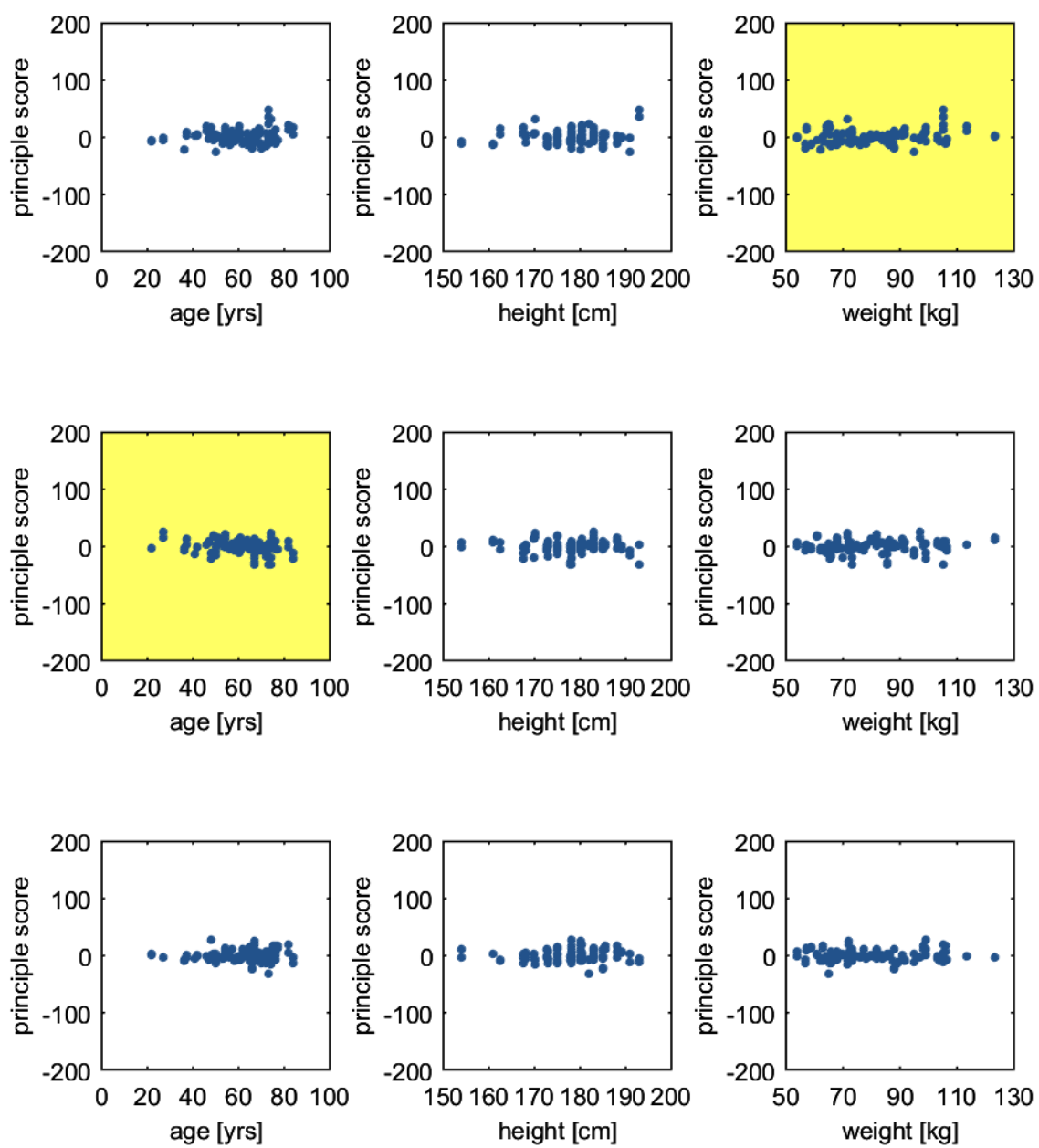


Figure D1 scatter plots (geometric descriptors vs. age, weight, height) (continued)

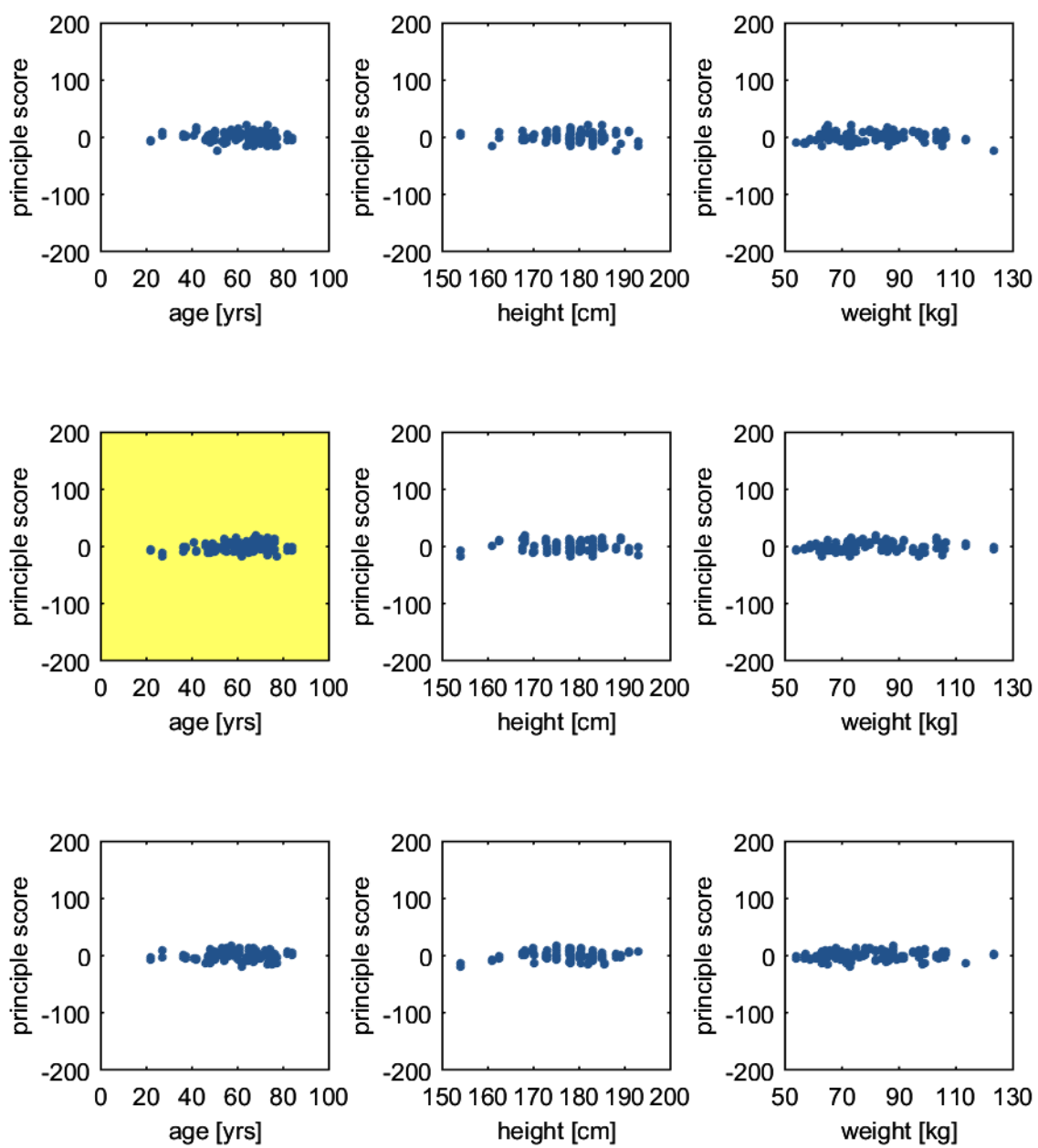


Figure D1 scatter plots (geometric descriptors vs. age, weight, height) (continued)

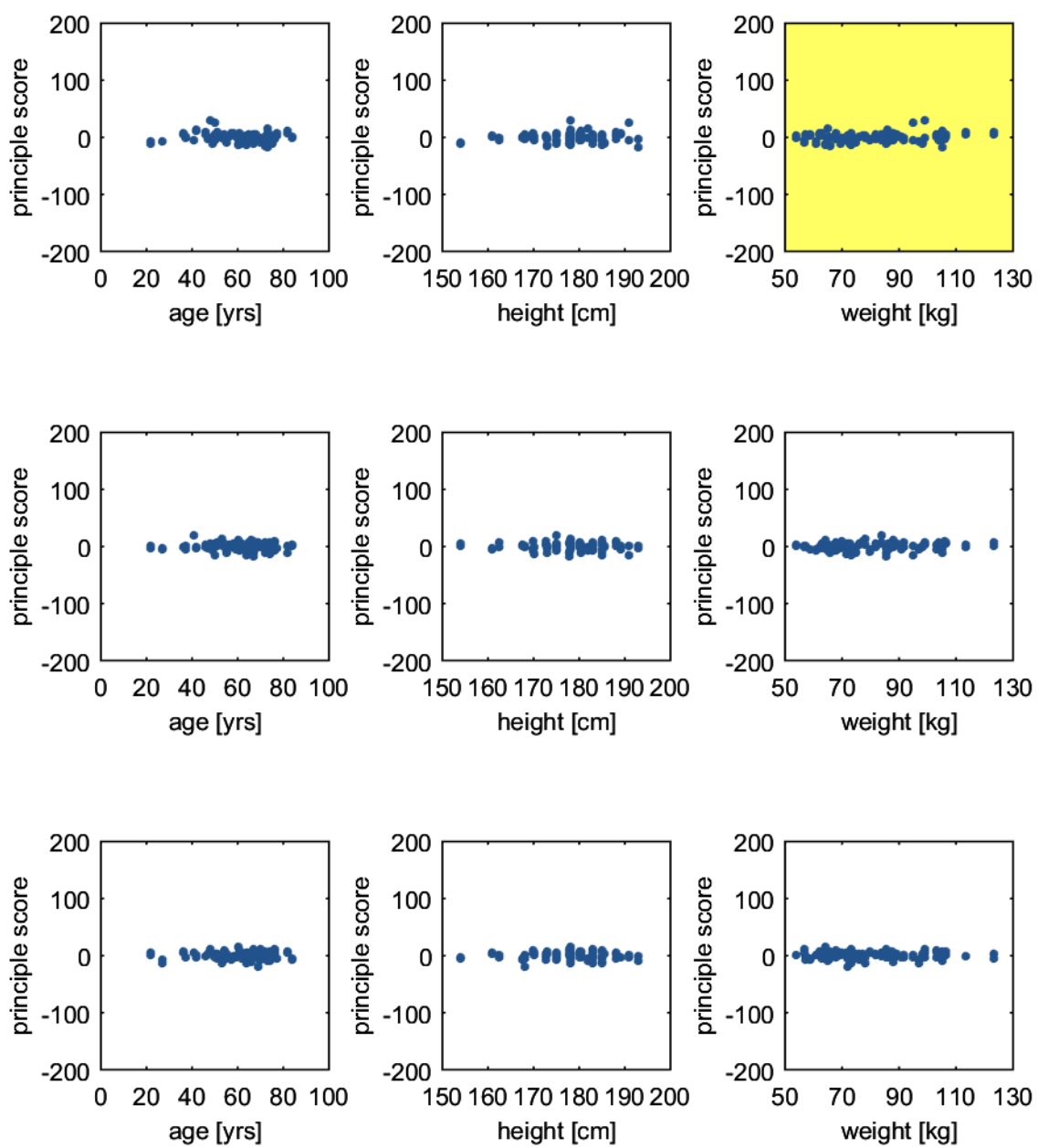


Figure D1 scatter plots (geometric descriptors vs. age, weight, height) (continued)

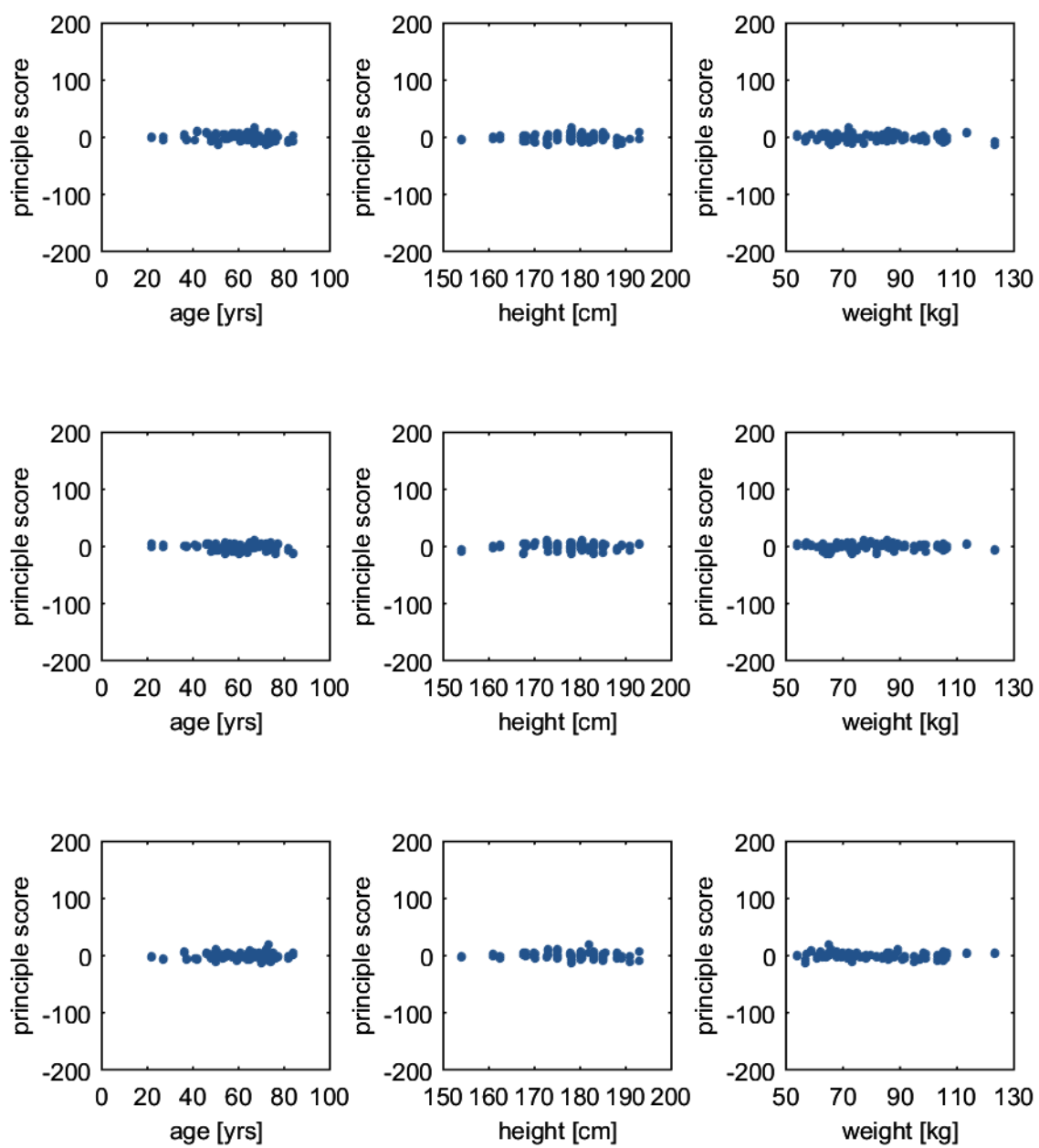


Figure D1 scatter plots (geometric descriptors vs. age, weight, height) (continued)

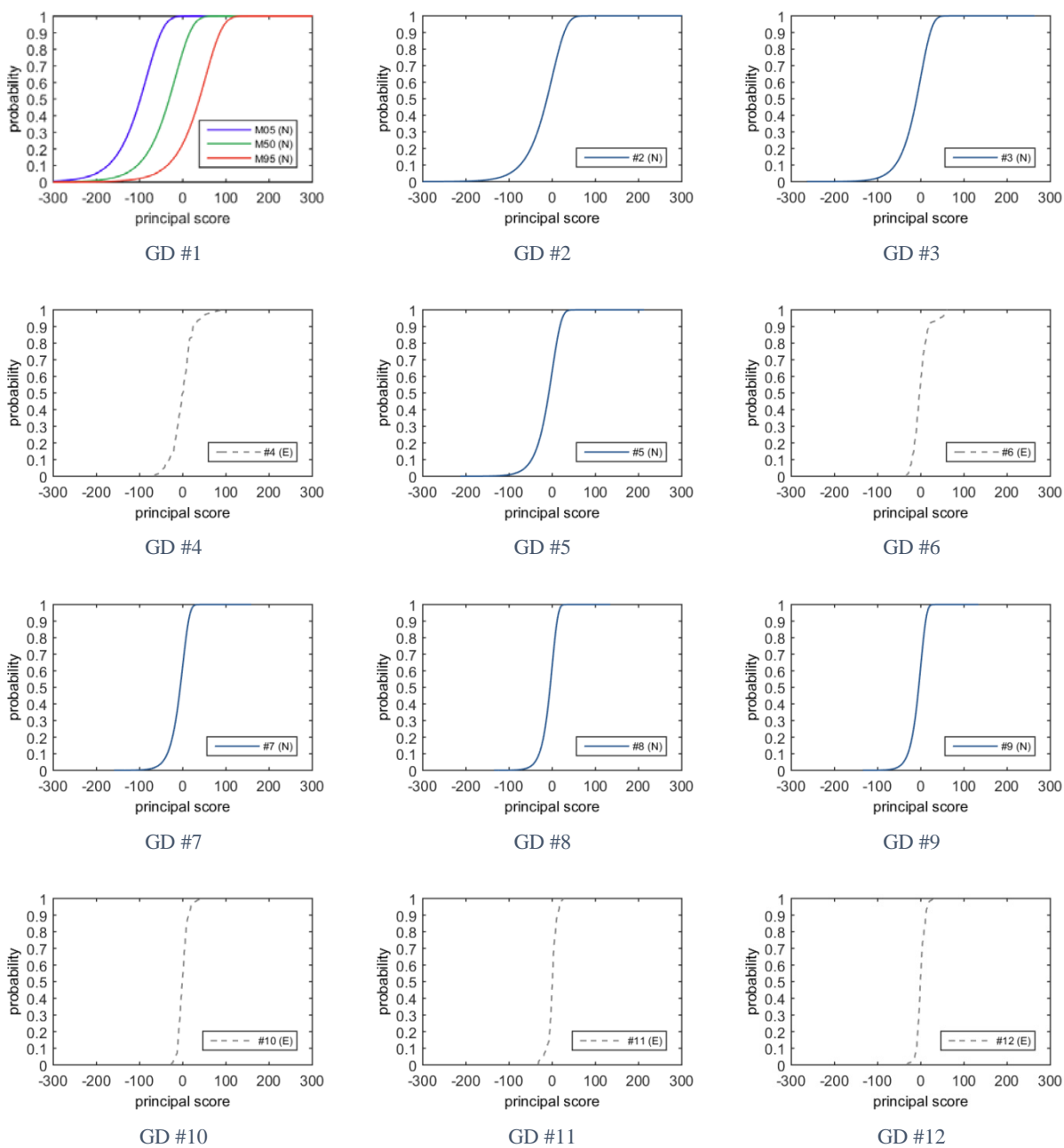
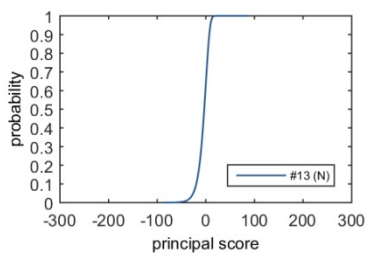
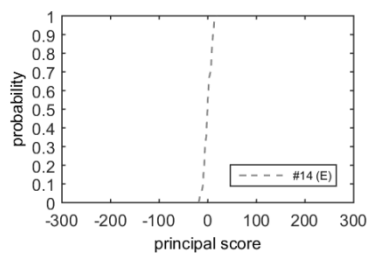


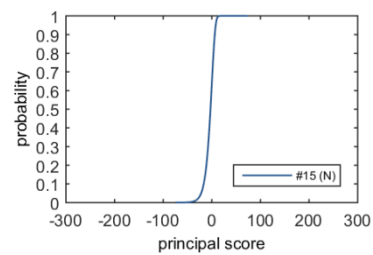
Figure D2 distributions of the geometric descriptors (GD)



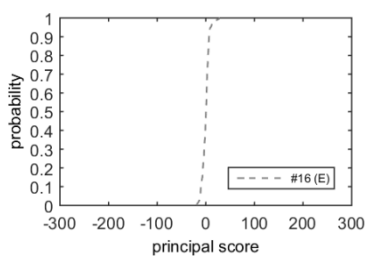
GD #13



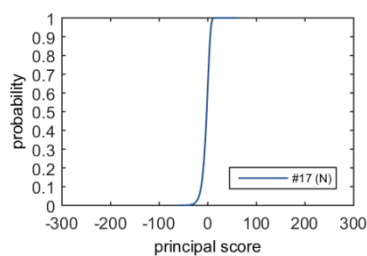
GD #14



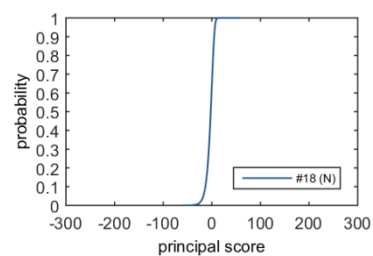
GD #15



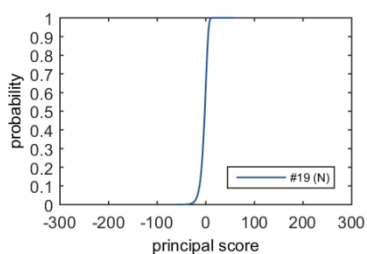
GD #16



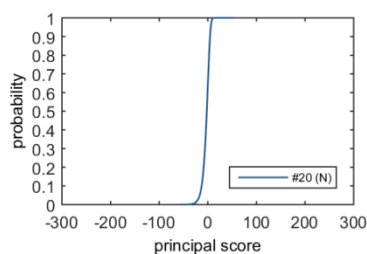
GD #17



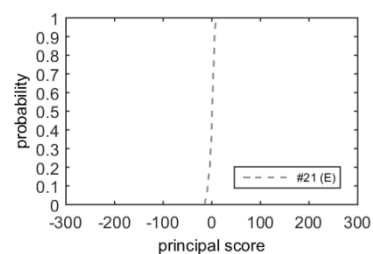
GD #18



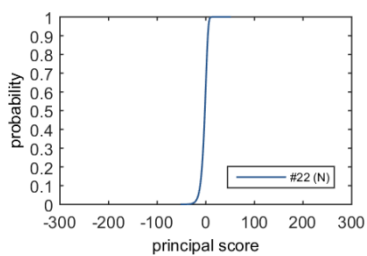
GD #19



GD #20



GD #21



GD #22

Figure D2 distributions of the geometric descriptors (GD) (continued)

Table D1 Normality test (Anderson Darling test) for Input Distributions: p-value less than 0.05 indicates the failure of the normality test (yellow cell)

p-value (Material Parameters)				
Elastic Modulus 0.0791	Ultimate Strain 0.0790	Yield Stress 0.000		
p-value (Geometric descriptors)				
GD #1 0.119	GD #2 0.954	GD #3 0.726	GD #4 0.0119	GD #5 0.0545
GD #6 0.001	GD #7 0.117	GD #8 0.398	GD #9 0.0982	GD #10 0.011
GD #11 0.001	GD #12 0.015	GD #13 0.565	GD #14 0.043	GD #15 0.512
GD #16 0.006	GD #17 0.149	GD #18 0.491	GD #19 0.884	GD #20 0.489
GD #21 0.001	GD #22 0.277			

APPENDIX E: DEVELOPED VPM AND INJURY RISK FUNCTIONS

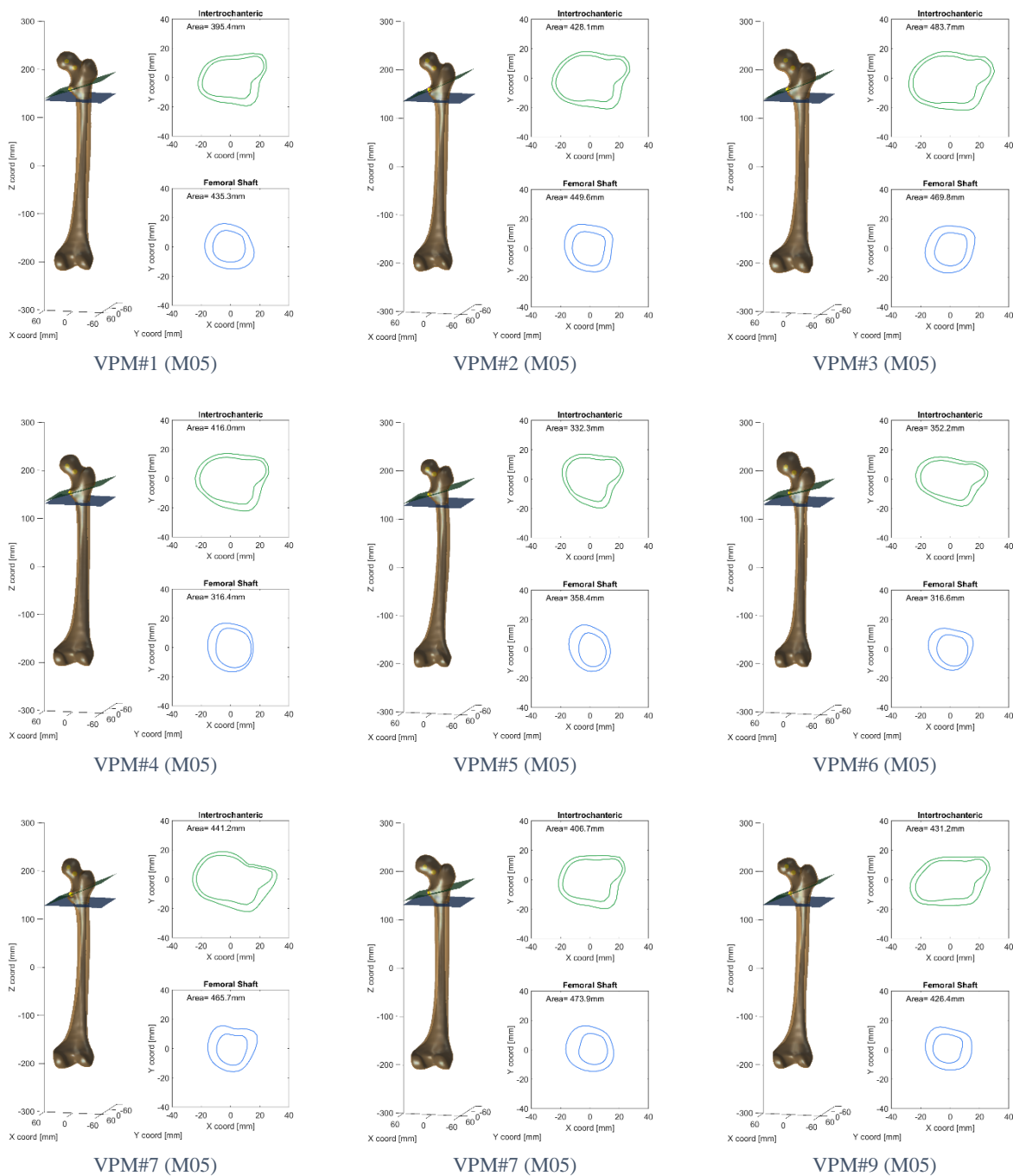
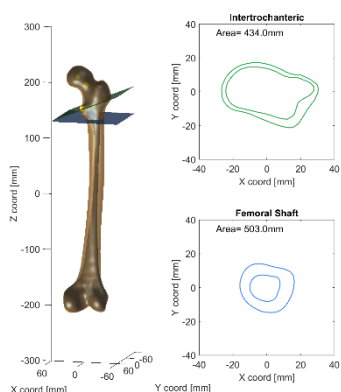
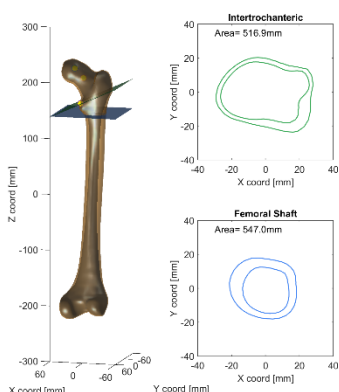


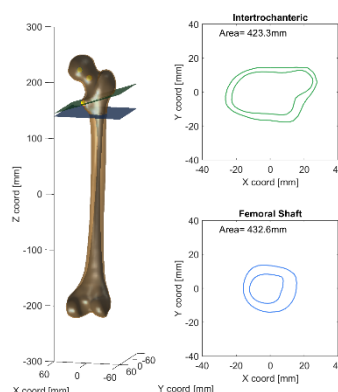
Figure E1 Geometry of VPMs



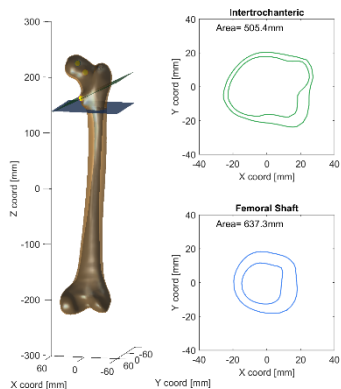
VPM#10 (M05)



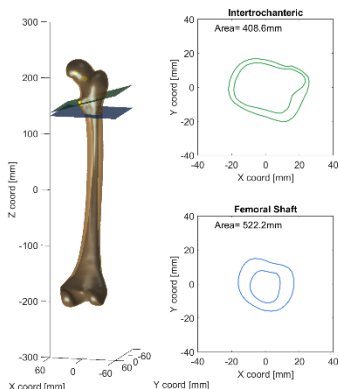
VPM#11 (M05)



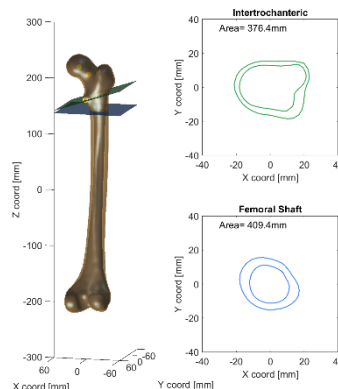
VPM#12 (M05)



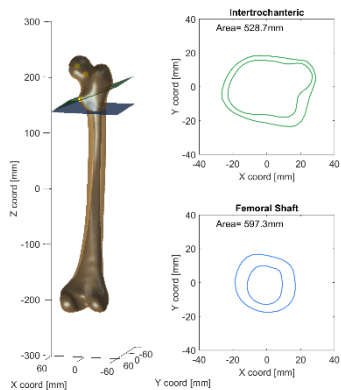
VPM#13 (M05)



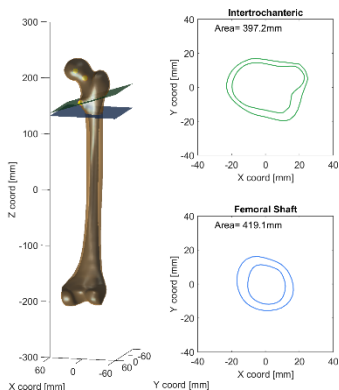
VPM#14 (M05)



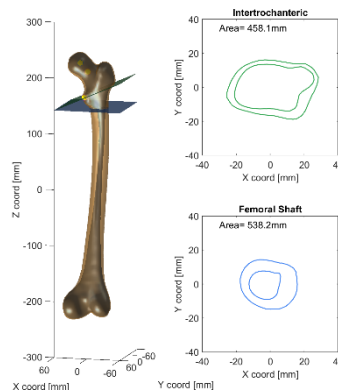
VPM#15 (M05)



VPM#16 (M05)

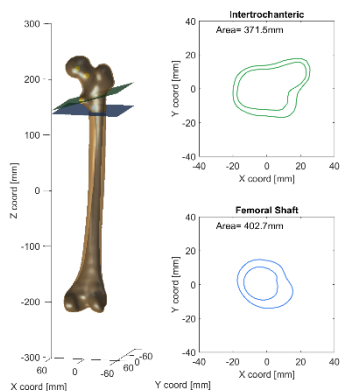


VPM#17 (M05)

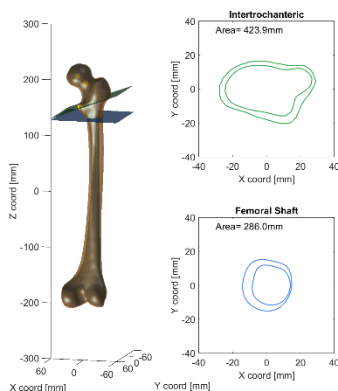


VPM#18 (M05)

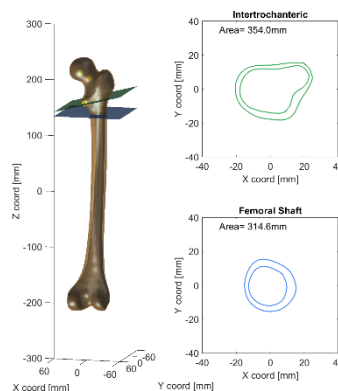
Figure E1 Geometry of VPMs (continued)



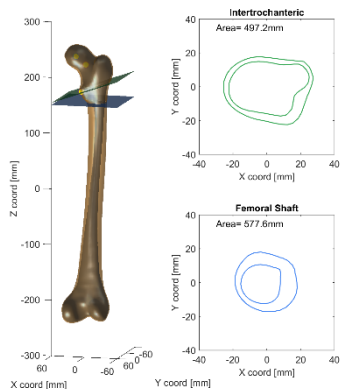
VPM#19 (M05)



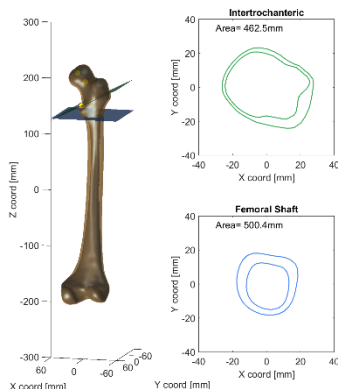
VPM#20 (M05)



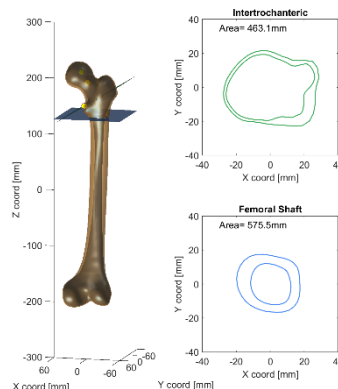
VPM#21 (M05)



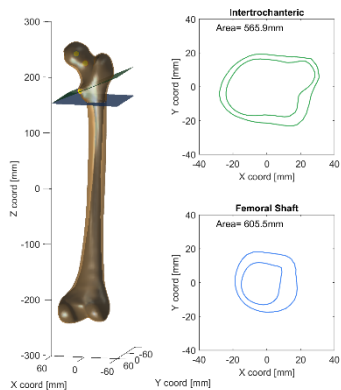
VPM#22 (M05)



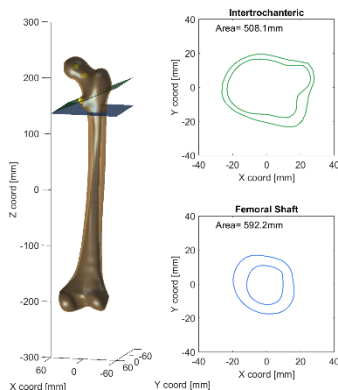
VPM#23 (M05)



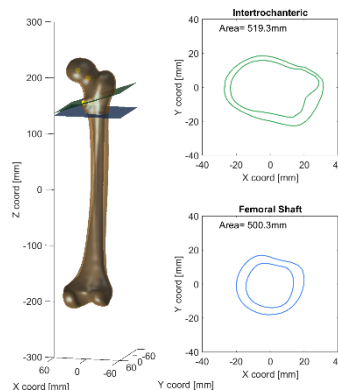
VPM#24 (M05)



VPM#25 (M05)

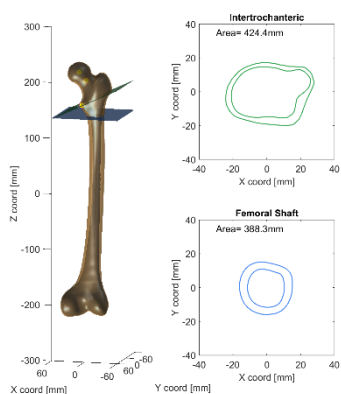


VPM#26 (M05)

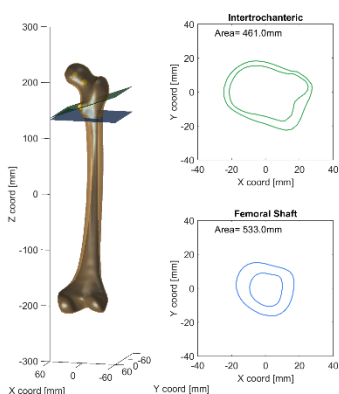


VPM#27 (M05)

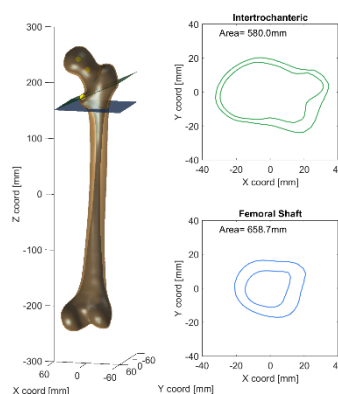
Figure E1 Geometry of VPMs (continued)



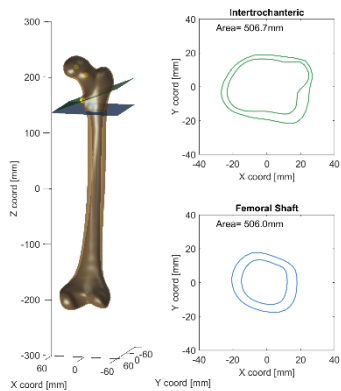
VPM#28 (M05)



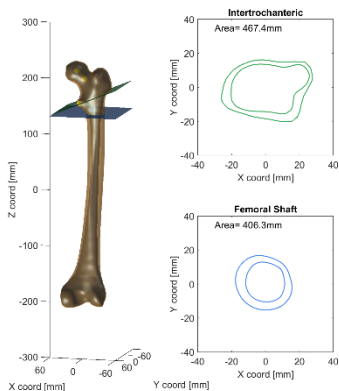
VPM#29 (M05)



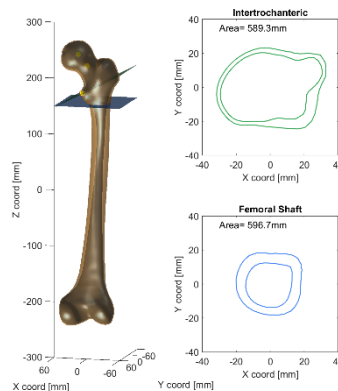
VPM#30 (M05)



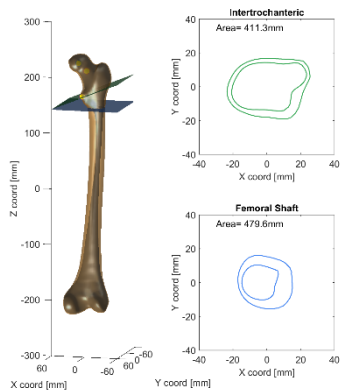
VPM#31 (M05)



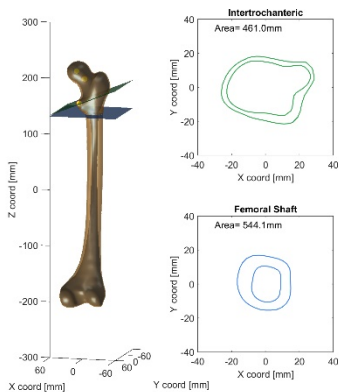
VPM#32 (M05)



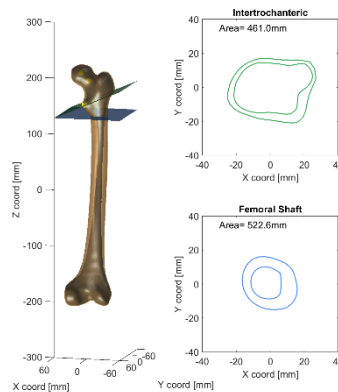
VPM#33 (M05)



VPM#34 (M05)

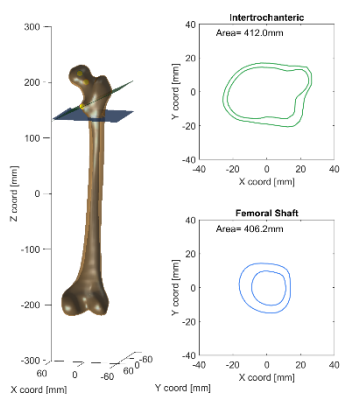


VPM#35 (M05)

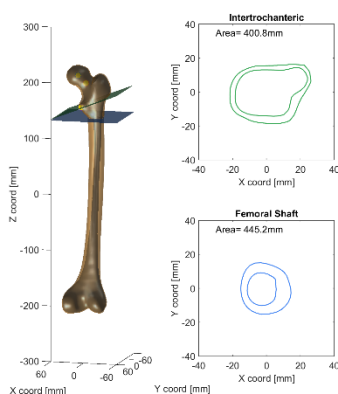


VPM#36 (M05)

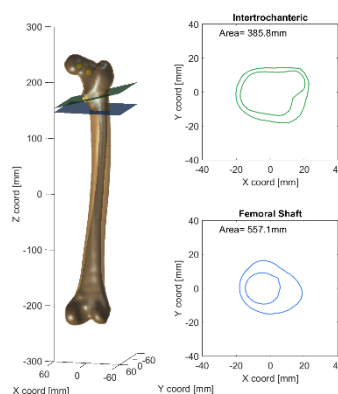
Figure E1 Geometry of VPMs (continued)



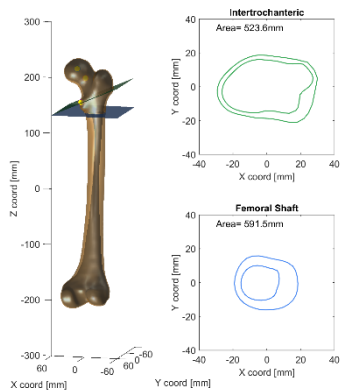
VPM#37 (M05)



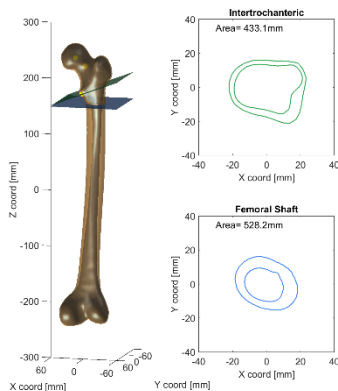
VPM#38 (M05)



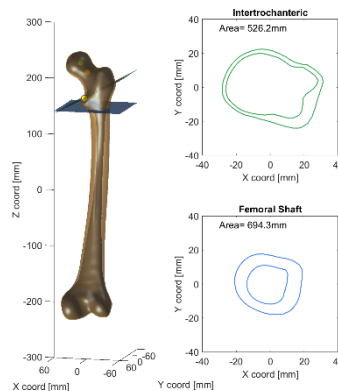
VPM#39 (M05)



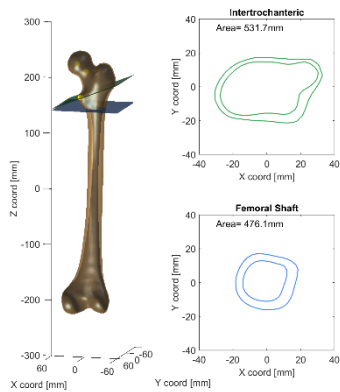
VPM#40 (M05)



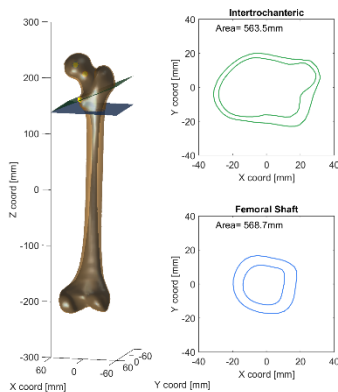
VPM#41 (M05)



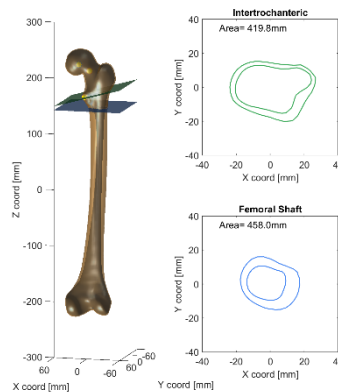
VPM#42 (M05)



VPM#43 (M05)

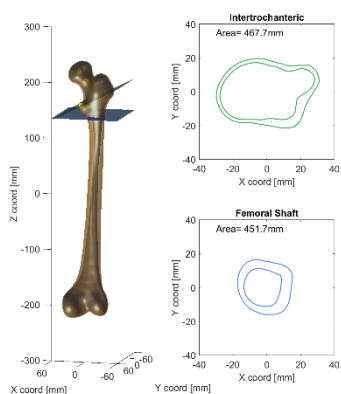


VPM#44 (M05)

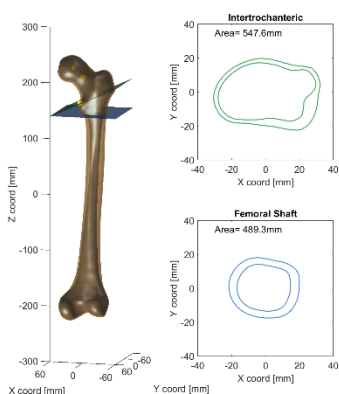


VPM#45 (M05)

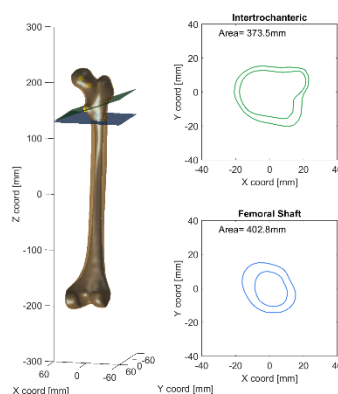
Figure E1 Geometry of VPMs (continued)



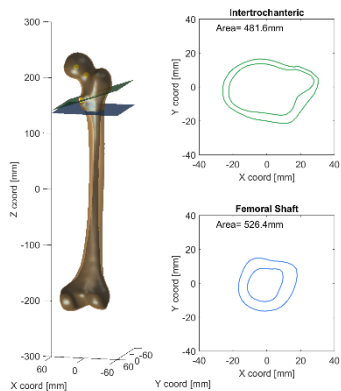
VPM#46 (M05)



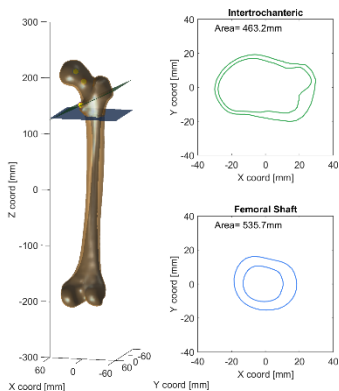
VPM#47 (M05)



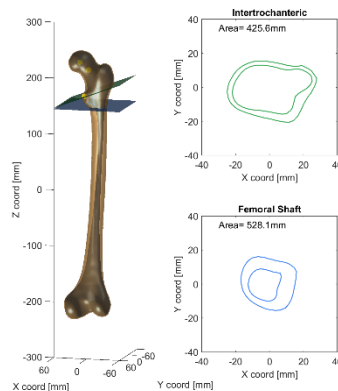
VPM#48 (M05)



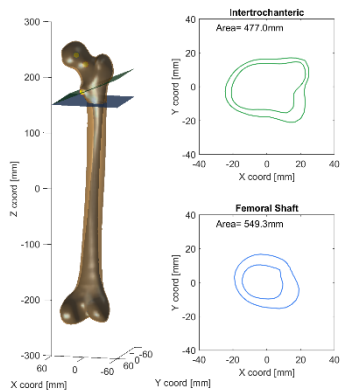
VPM#49 (M05)



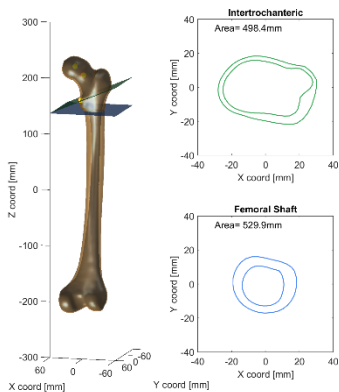
VPM#50 (M05)



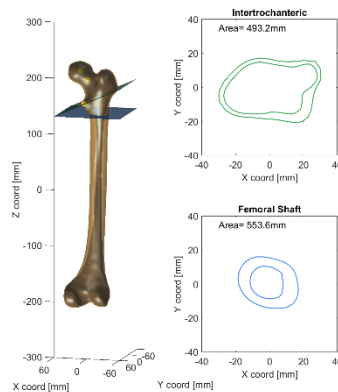
VPM#51 (M05)



VPM#52 (M05)

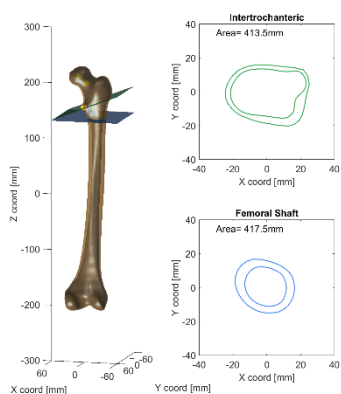


VPM#53 (M05)

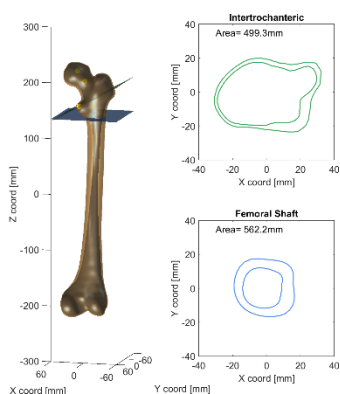


VPM#54 (M05)

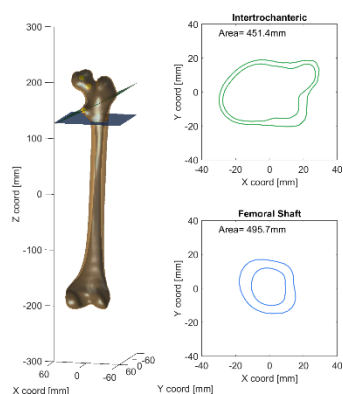
Figure E1 Geometry of VPMs (continued)



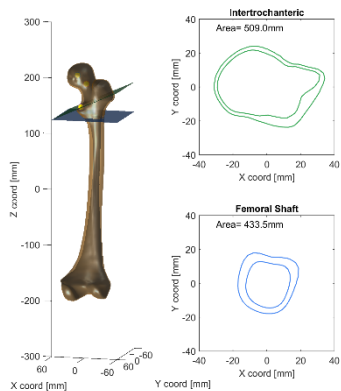
VPM#55 (M05)



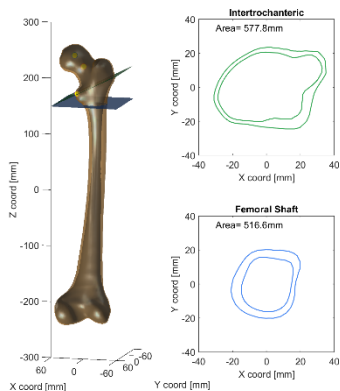
VPM#56 (M05)



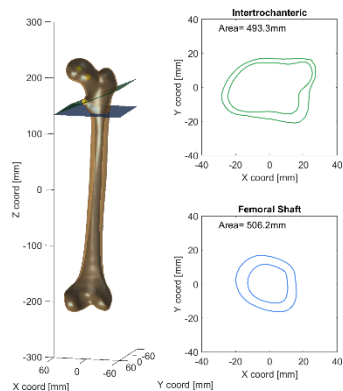
VPM#57 (M05)



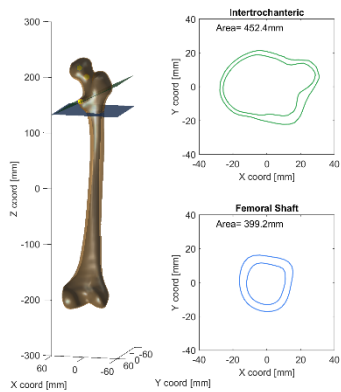
VPM#58 (M05)



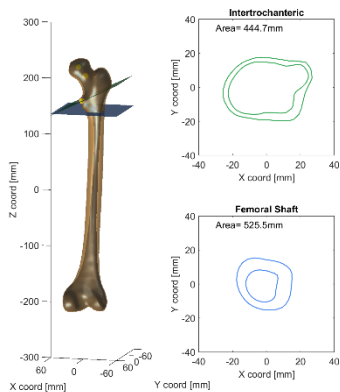
VPM#59 (M05)



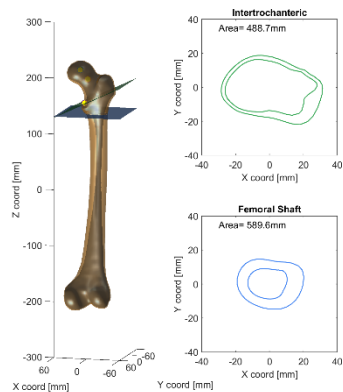
VPM#60 (M05)



VPM#61 (M05)

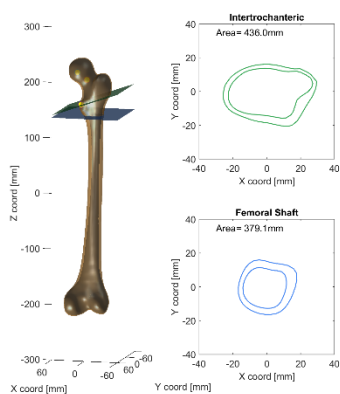


VPM#62 (M05)

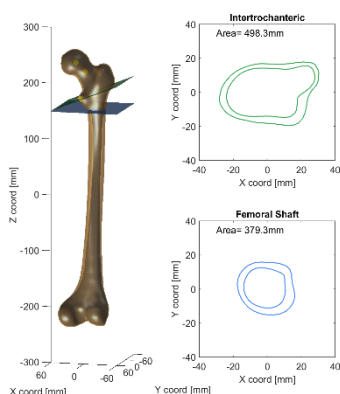


VPM#63 (M05)

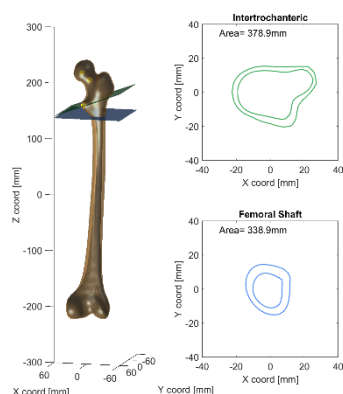
Figure E1 Geometry of VPMs (continued)



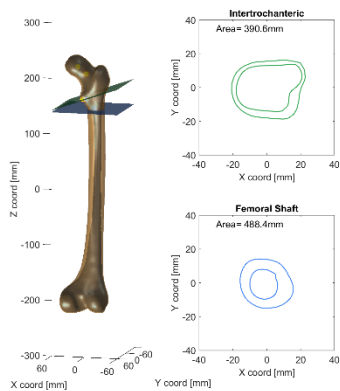
VPM#64 (M05)



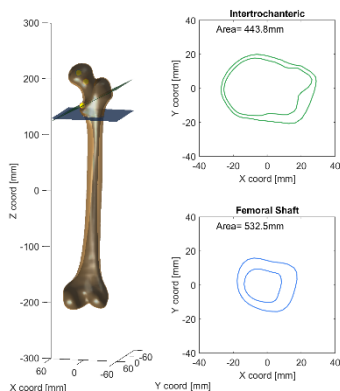
VPM#65 (M05)



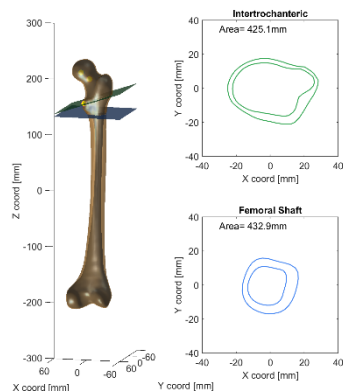
VPM#66 (M05)



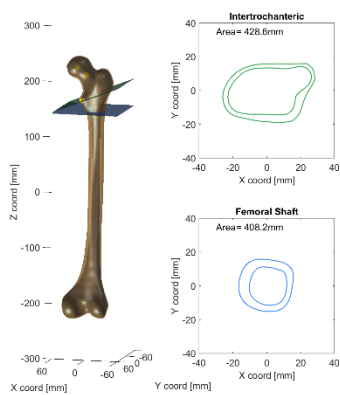
VPM#67 (M05)



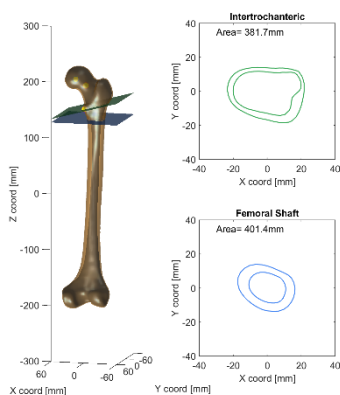
VPM#68 (M05)



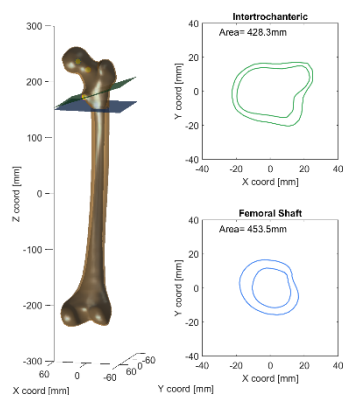
VPM#69 (M05)



VPM#70 (M05)

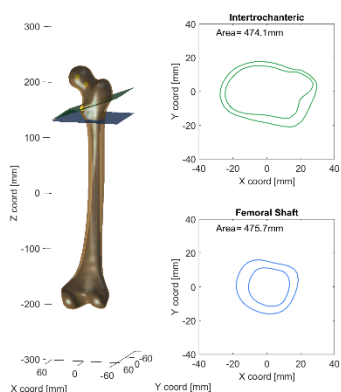


VPM#71 (M05)

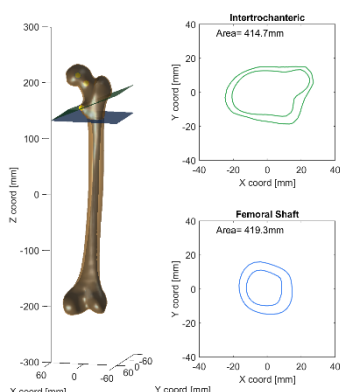


VPM#72 (M05)

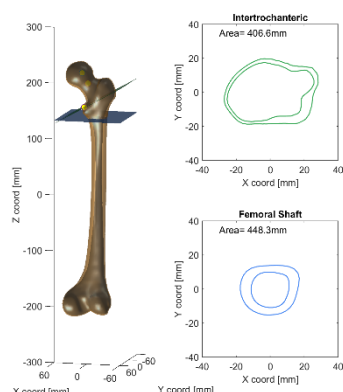
Figure E1 Geometry of VPMs (continued)



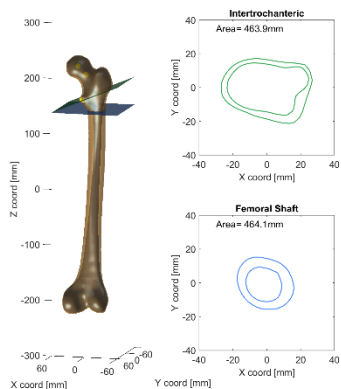
VPM#73 (M05)



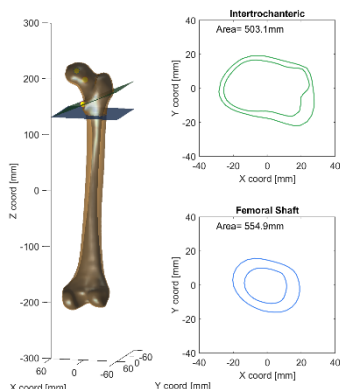
VPM#74 (M05)



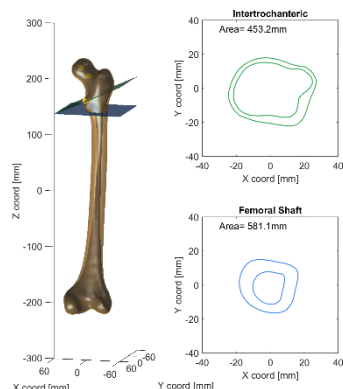
VPM#75 (M05)



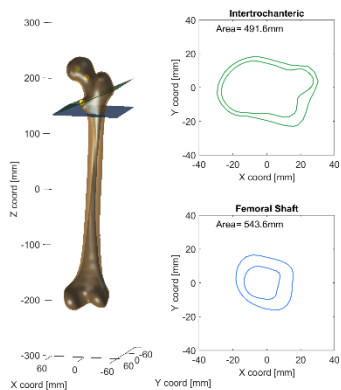
VPM#76 (M05)



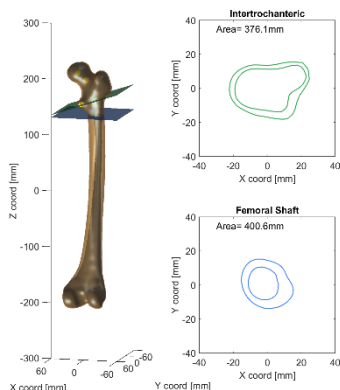
VPM#77 (M05)



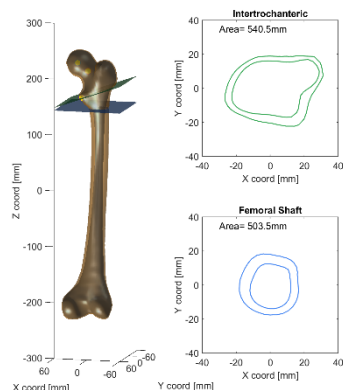
VPM#78 (M05)



VPM#79 (M05)

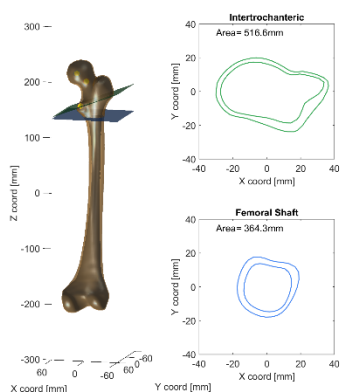


VPM#80 (M05)

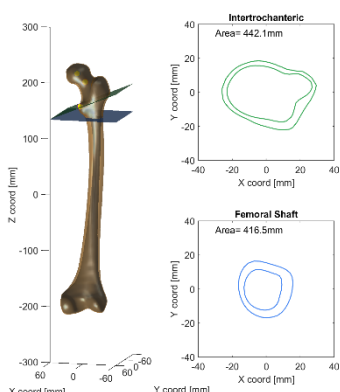


VPM#81 (M05)

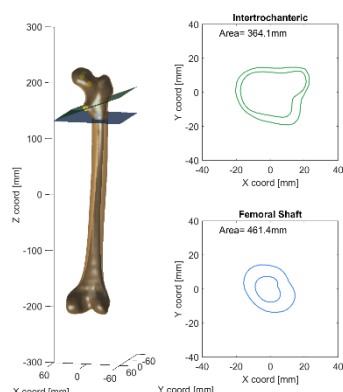
Figure E1 Geometry of VPMs (continued)



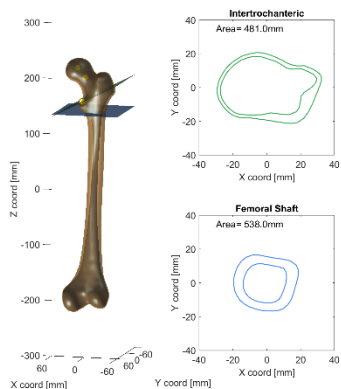
VPM#82 (M05)



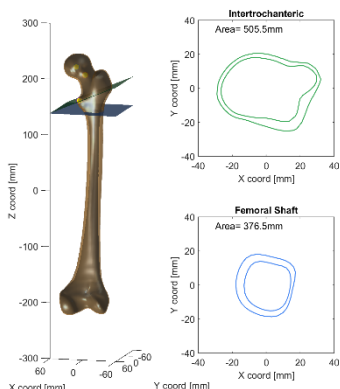
VPM#83 (M05)



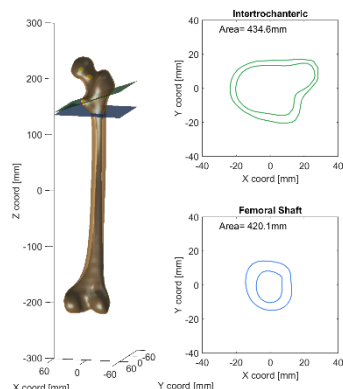
VPM#84 (M05)



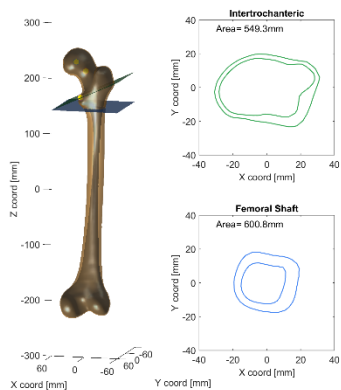
VPM#85 (M05)



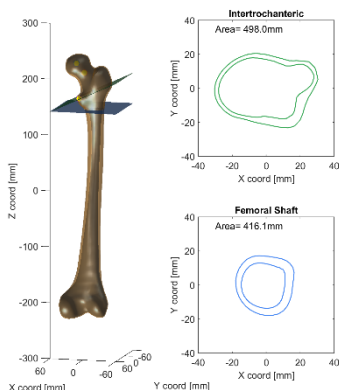
VPM#86 (M05)



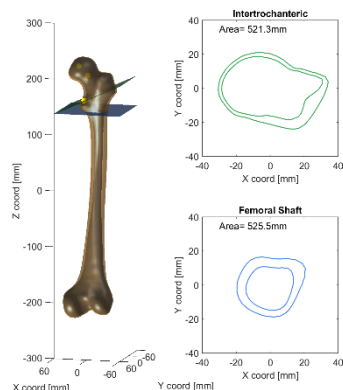
VPM#87 (M05)



VPM#88 (M05)

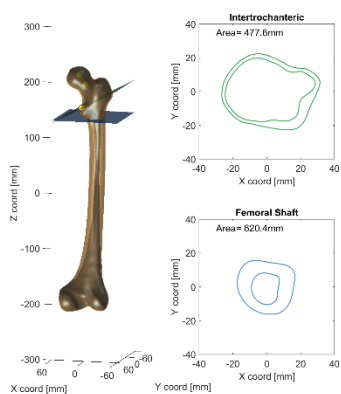


VPM#89 (M05)

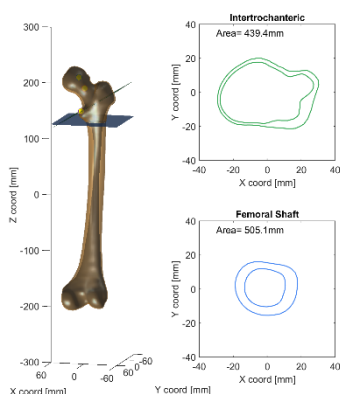


VPM#90 (M05)

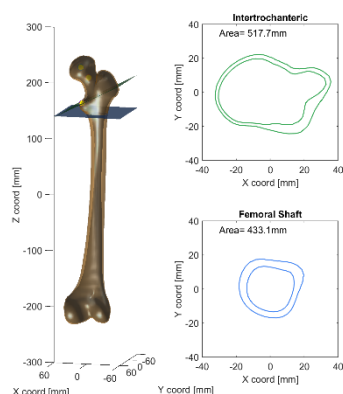
Figure E1 Geometry of VPMs (continued)



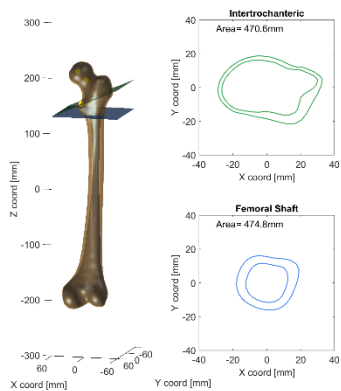
VPM#91 (M05)



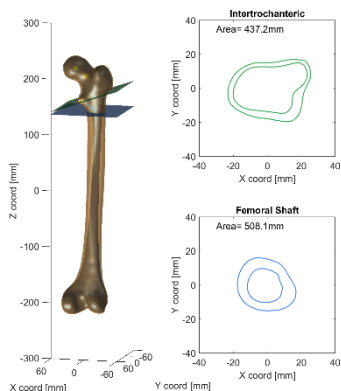
VPM#92 (M05)



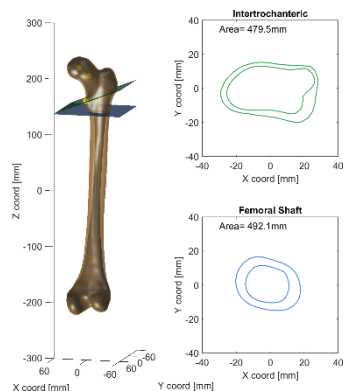
VPM#93 (M05)



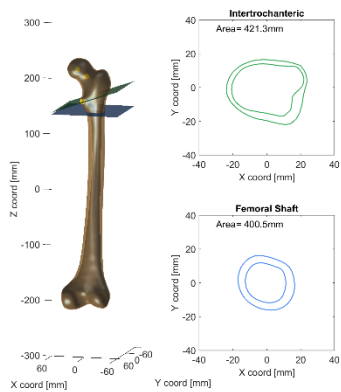
VPM#94 (M05)



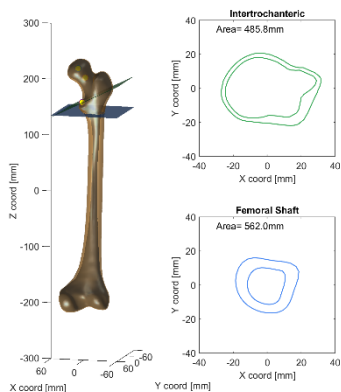
VPM#95 (M05)



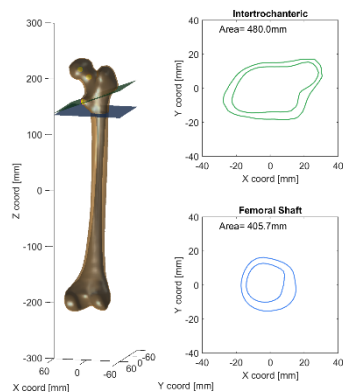
VPM#96 (M05)



VPM#97 (M05)

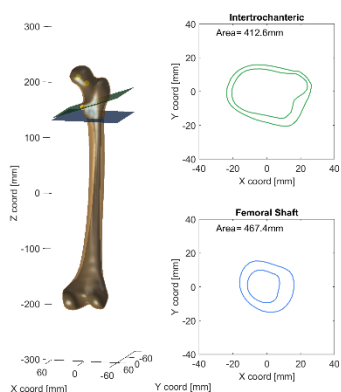


VPM#98 (M05)

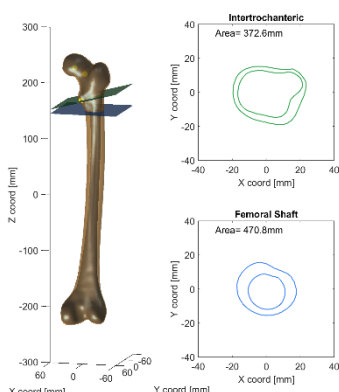


VPM#99 (M05)

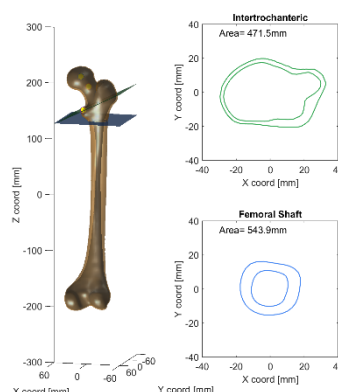
Figure E1 Geometry of VPMs (continued)



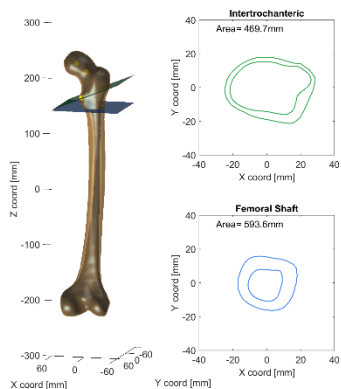
VPM#100 (M05)



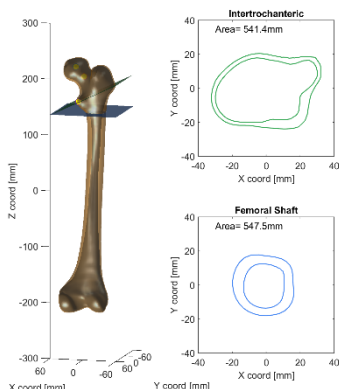
VPM#1 (M50)



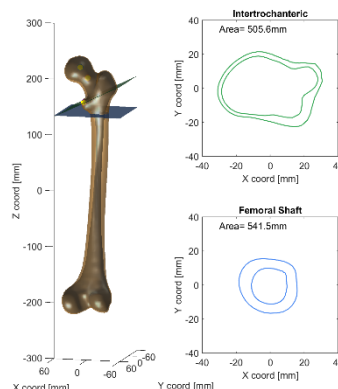
VPM#2 (M50)



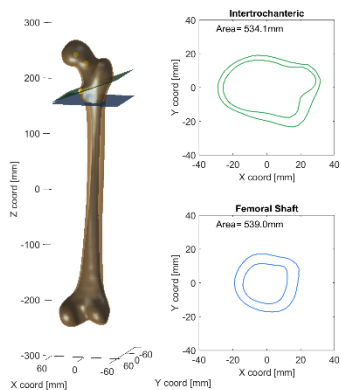
VPM#3 (M50)



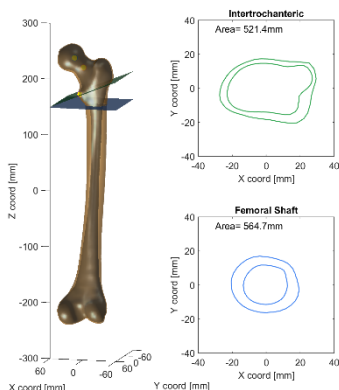
VPM#4 (M50)



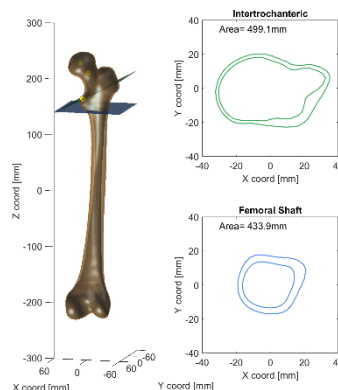
VPM#5 (M50)



VPM#6 (M50)

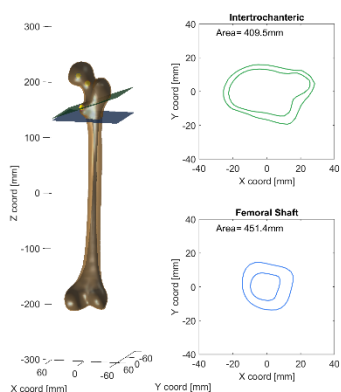


VPM#7 (M50)

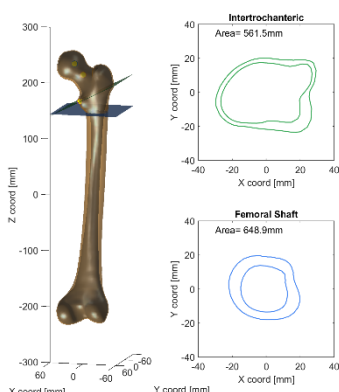


VPM#8 (M50)

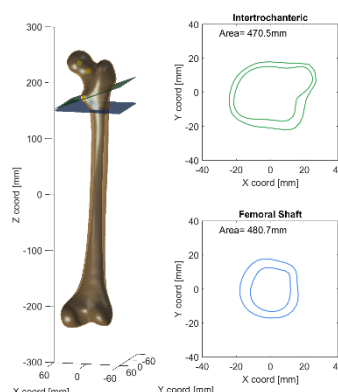
Figure E1 Geometry of VPMs (continued)



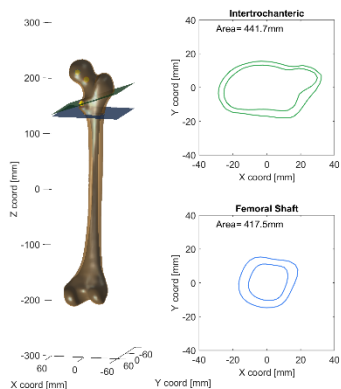
VPM#9 (M50)



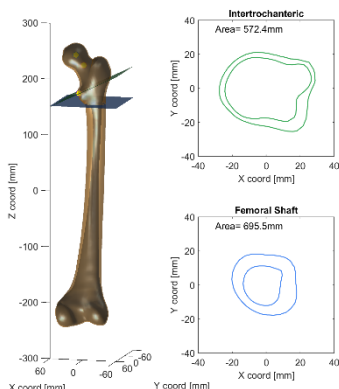
VPM#10 (M50)



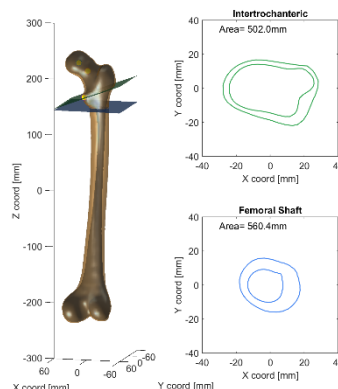
VPM#11 (M50)



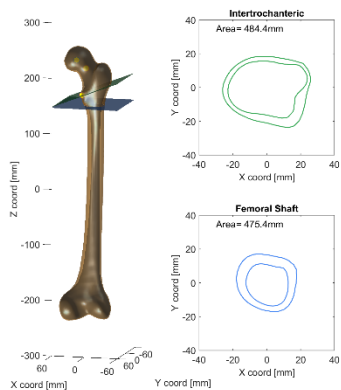
VPM#12 (M50)



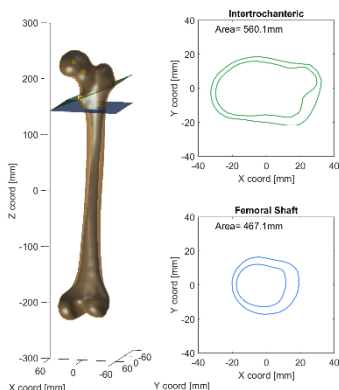
VPM#13 (M50)



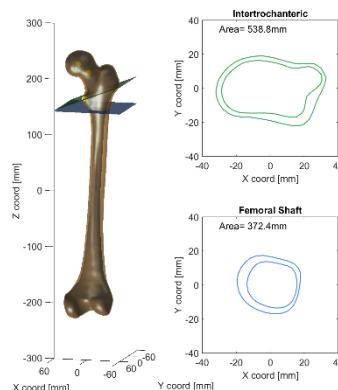
VPM#14 (M50)



VPM#15 (M50)

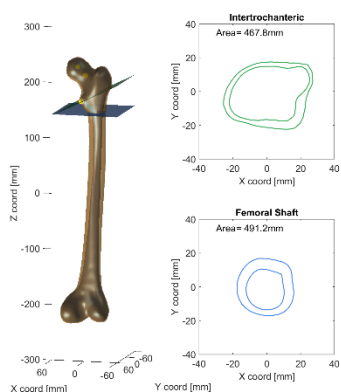


VPM#16 (M50)

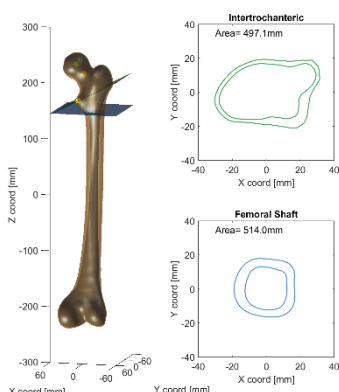


VPM#17 (M50)

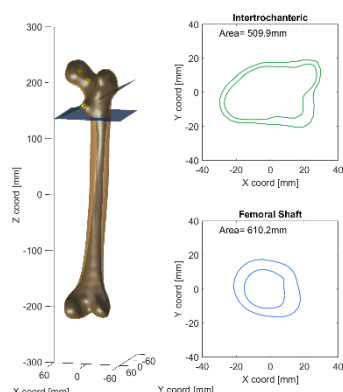
Figure E1 Geometry of VPMs (continued)



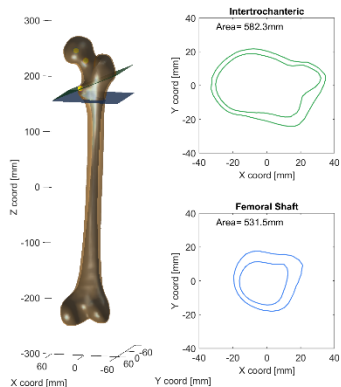
VPM#18 (M50)



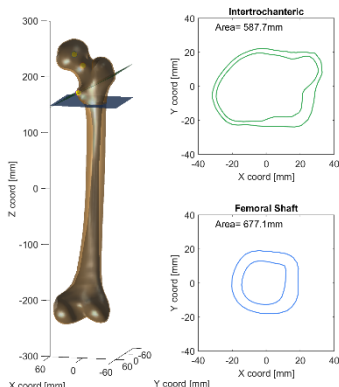
VPM#19 (M50)



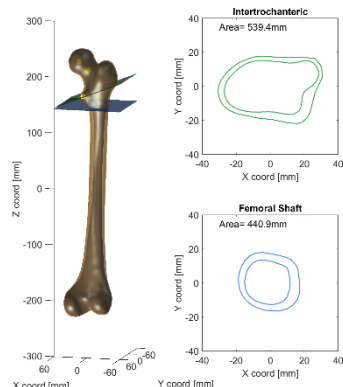
VPM#20 (M50)



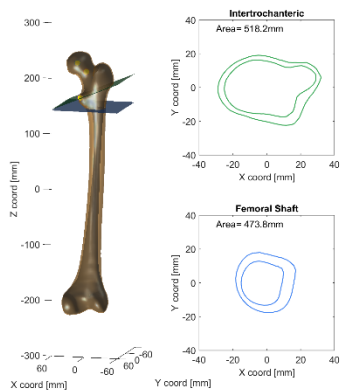
VPM#21 (M50)



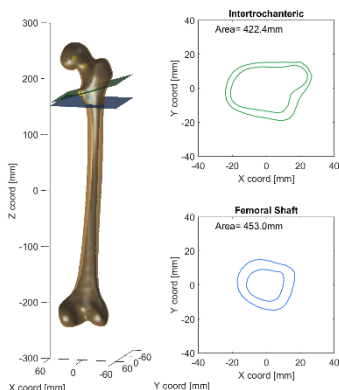
VPM#22 (M50)



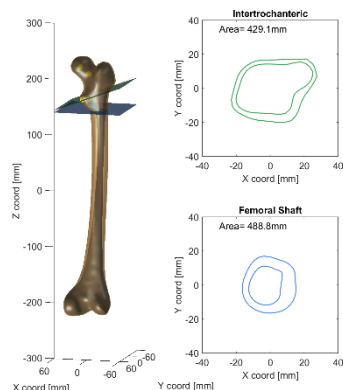
VPM#23 (M50)



VPM#24 (M50)

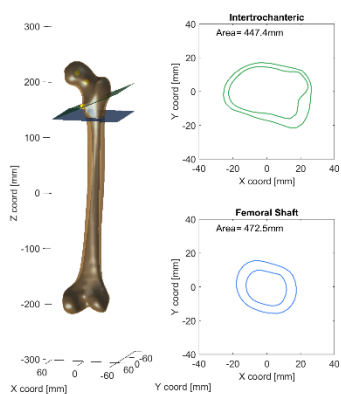


VPM#25 (M50)

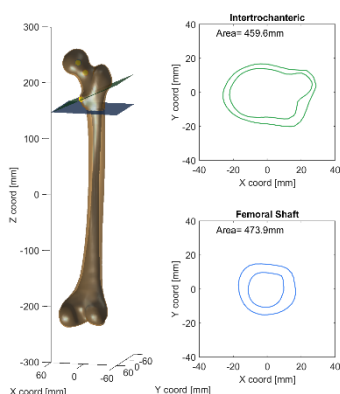


VPM#26 (M50)

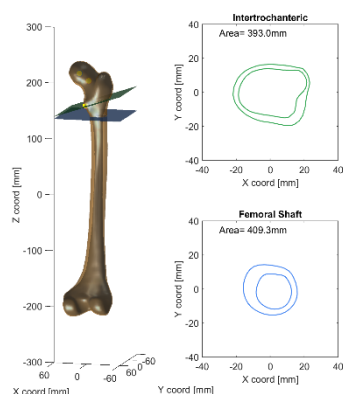
Figure E1 Geometry of VPMs (continued)



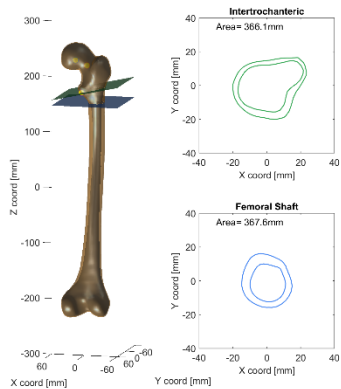
VPM#27 (M50)



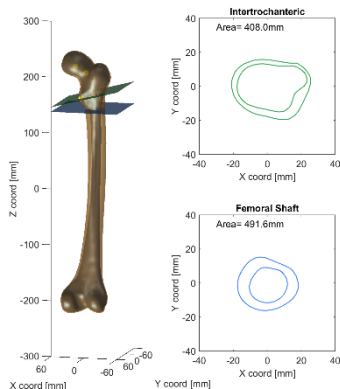
VPM#28 (M50)



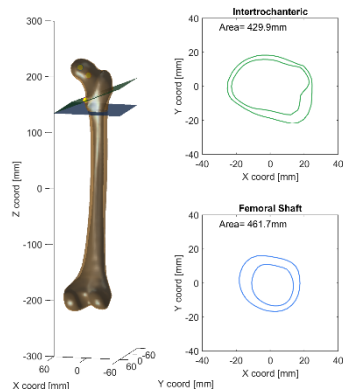
VPM#29 (M50)



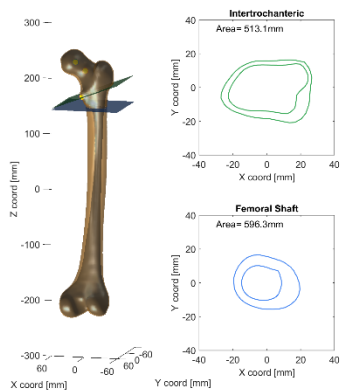
VPM#30 (M50)



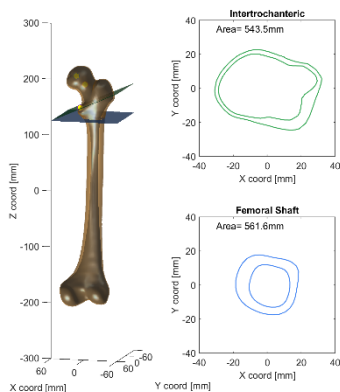
VPM#31 (M50)



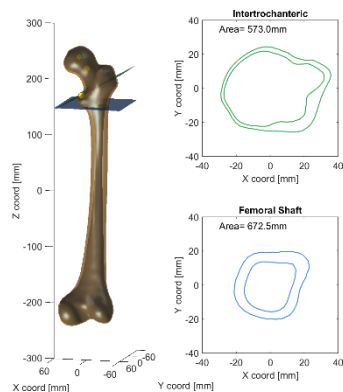
VPM#32 (M50)



VPM#33 (M50)

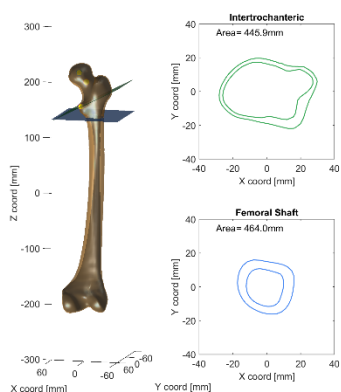


VPM#34 (M50)

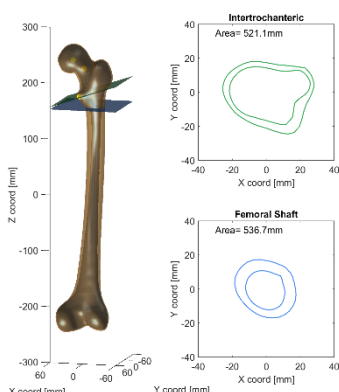


VPM#35 (M50)

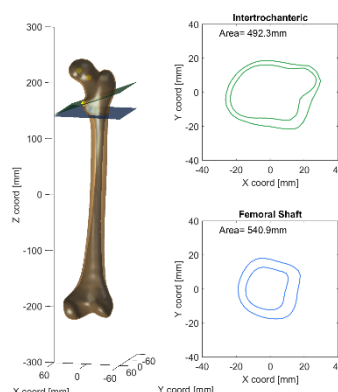
Figure E1 Geometry of VPMs (continued)



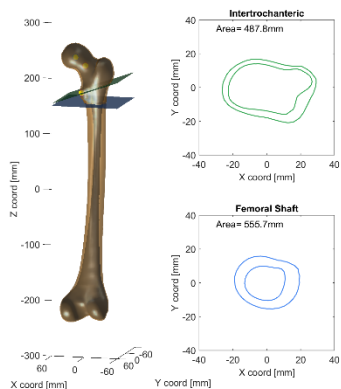
VPM#36 (M50)



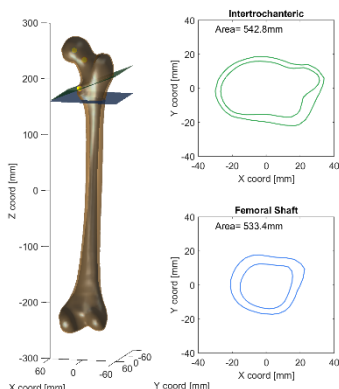
VPM#37 (M50)



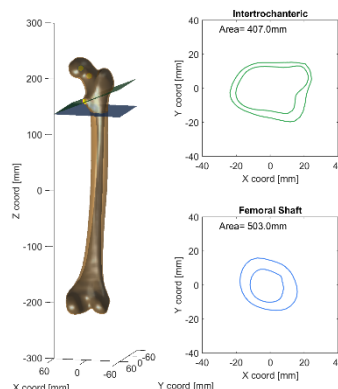
VPM#38 (M50)



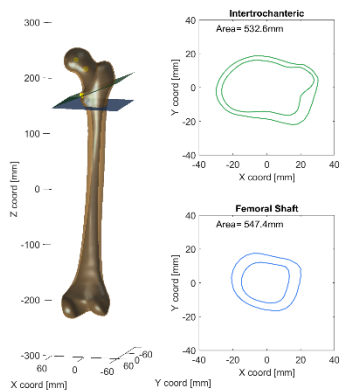
VPM#39 (M50)



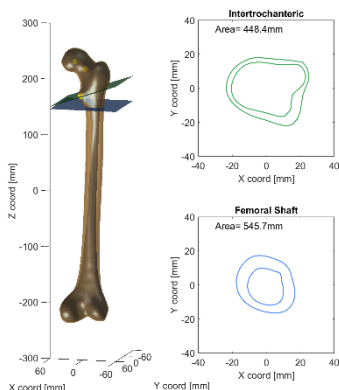
VPM#40 (M50)



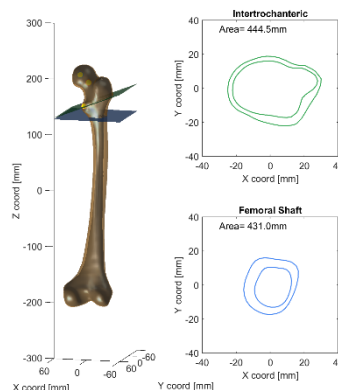
VPM#41 (M50)



VPM#42 (M50)

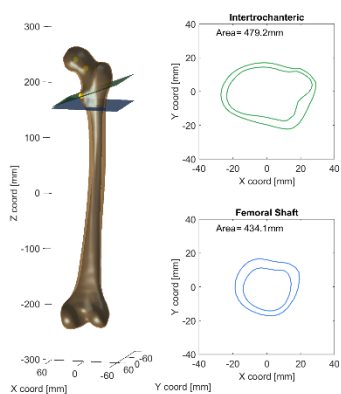


VPM#43 (M50)

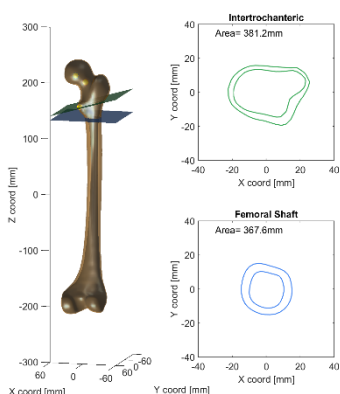


VPM#44 (M50)

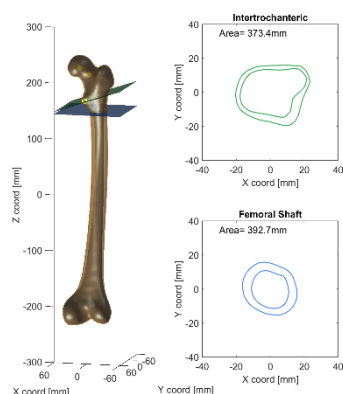
Figure E1 Geometry of VPMs (continued)



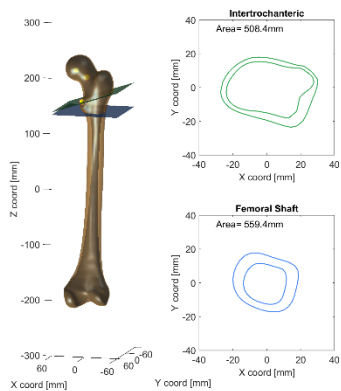
VPM#45 (M50)



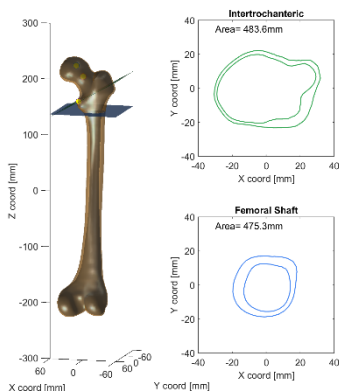
VPM#46 (M50)



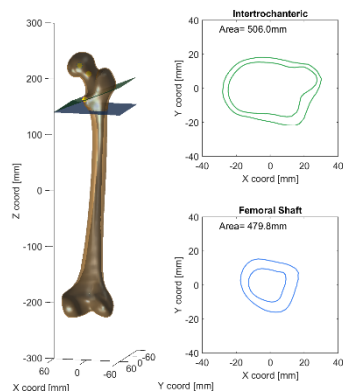
VPM#47 (M50)



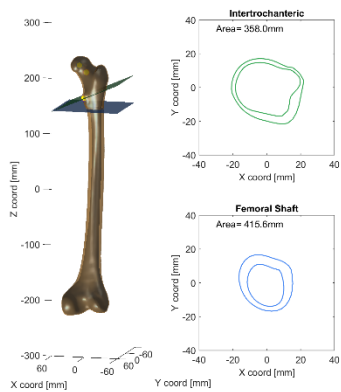
VPM#48 (M50)



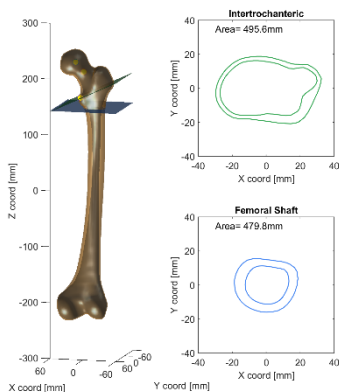
VPM#49 (M50)



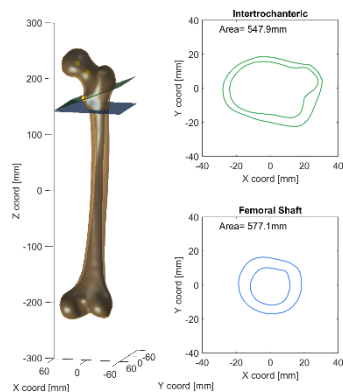
VPM#50 (M50)



VPM#51 (M50)

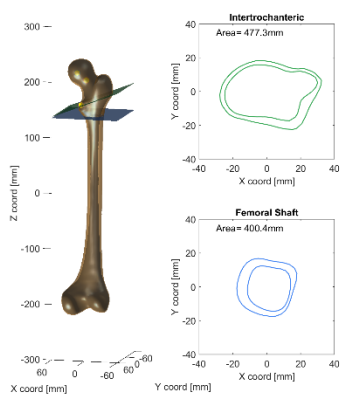


VPM#52 (M50)

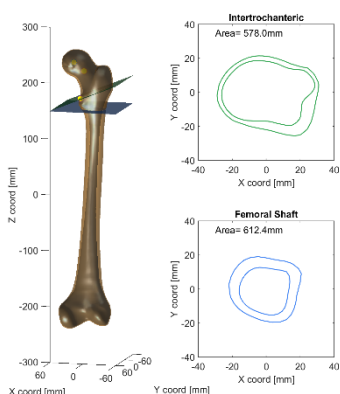


VPM#53 (M50)

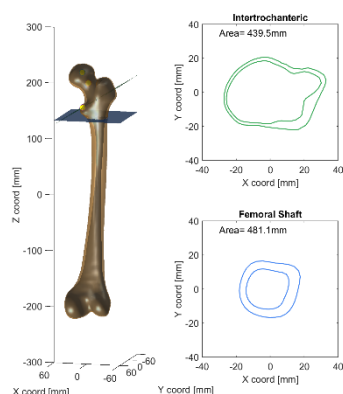
Figure E1 Geometry of VPMs (continued)



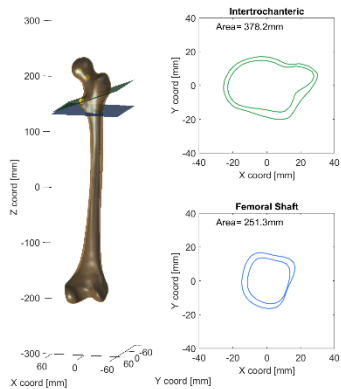
VPM#54 (M50)



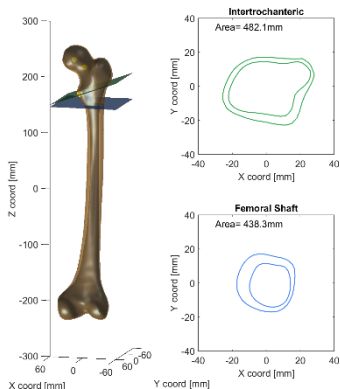
VPM#55 (M50)



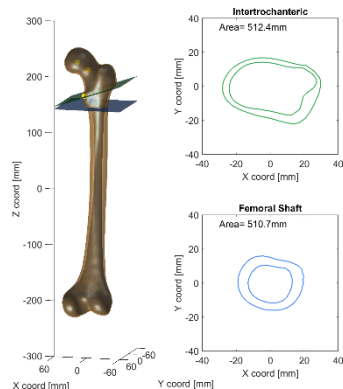
VPM#56 (M50)



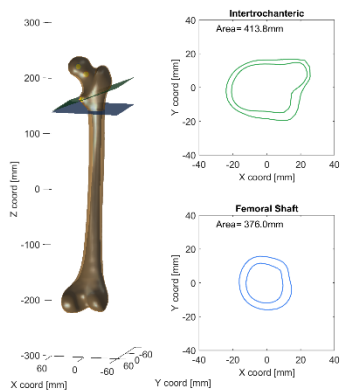
VPM#57 (M50)



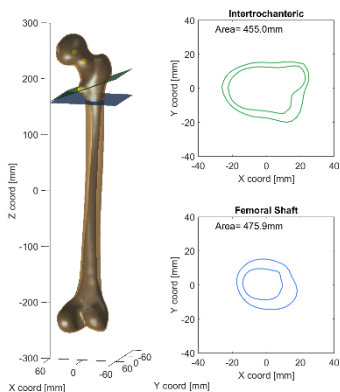
VPM#58 (M50)



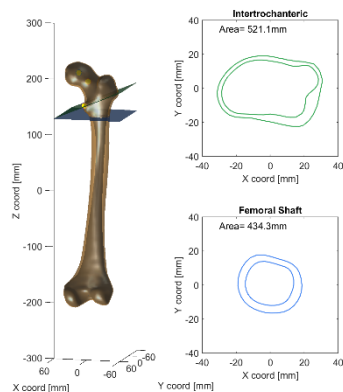
VPM#59 (M50)



VPM#60 (M50)

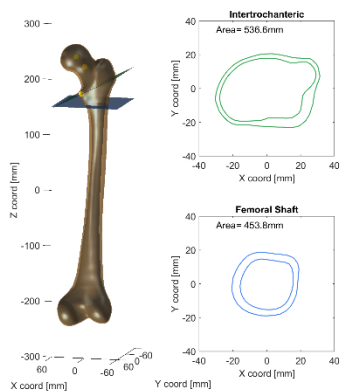


VPM#61 (M50)

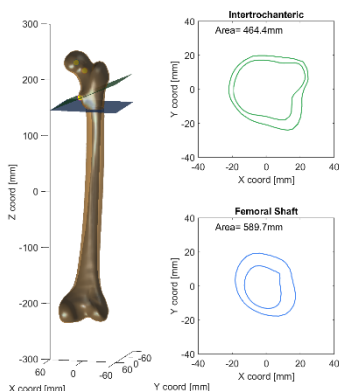


VPM#62 (M50)

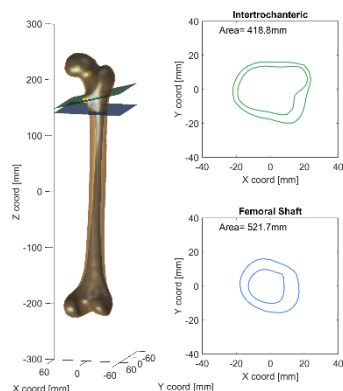
Figure E1 Geometry of VPMs (continued)



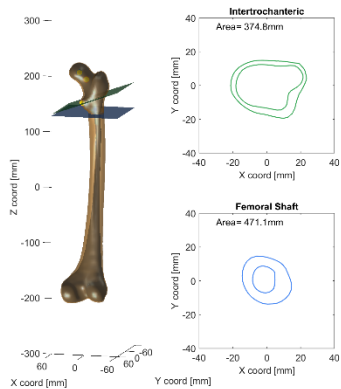
VPM#63 (M50)



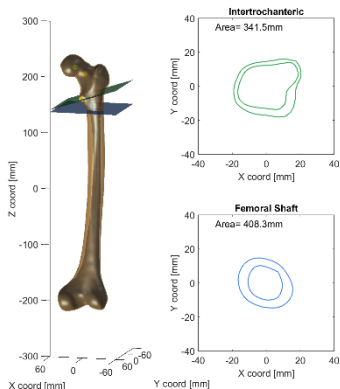
VPM#64 (M50)



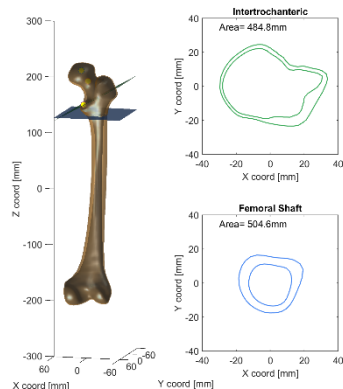
VPM#65 (M50)



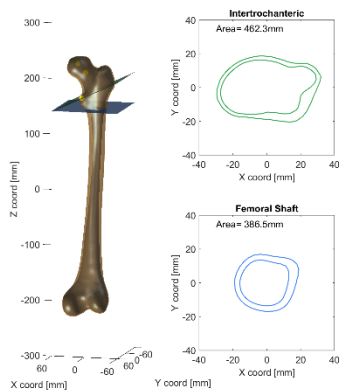
VPM#66 (M50)



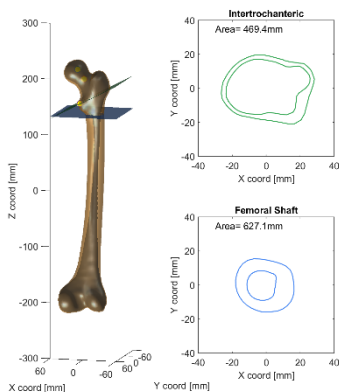
VPM#67 (M50)



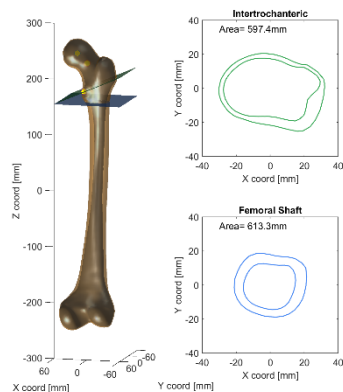
VPM#68 (M50)



VPM#69 (M50)

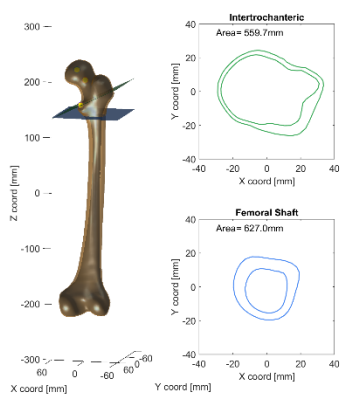


VPM#70 (M50)

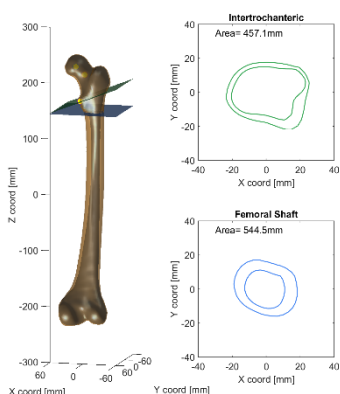


VPM#71 (M50)

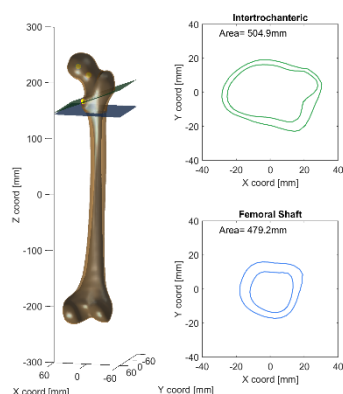
Figure E1 Geometry of VPMs (continued)



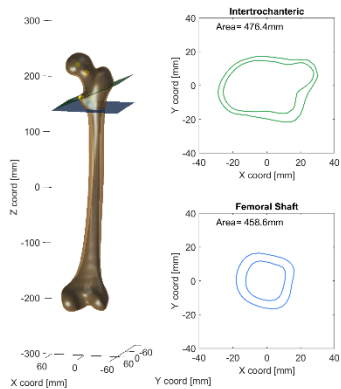
VPM#72 (M50)



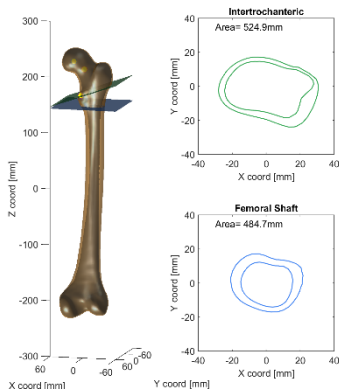
VPM#73 (M50)



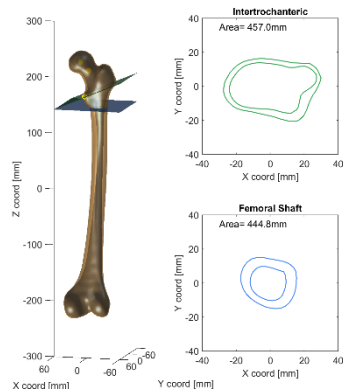
VPM#74 (M50)



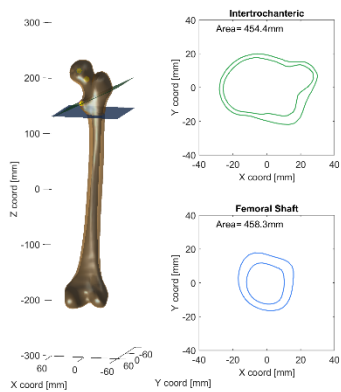
VPM#75 (M50)



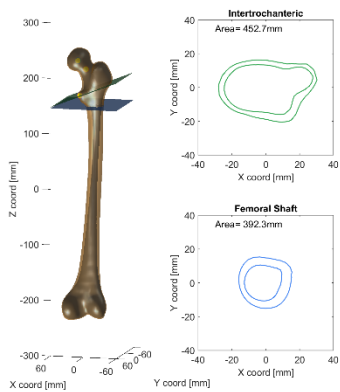
VPM#76 (M50)



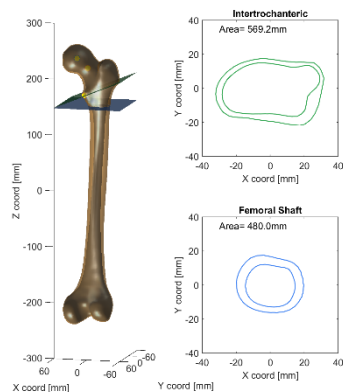
VPM#77 (M50)



VPM#78 (M50)

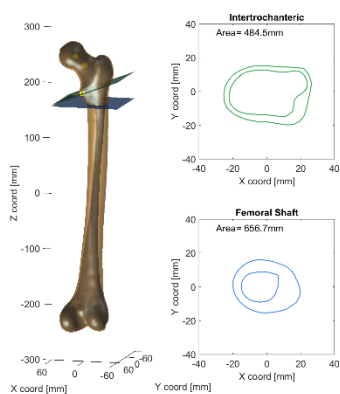


VPM#79 (M50)

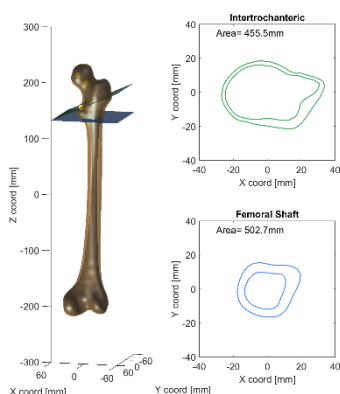


VPM#80 (M50)

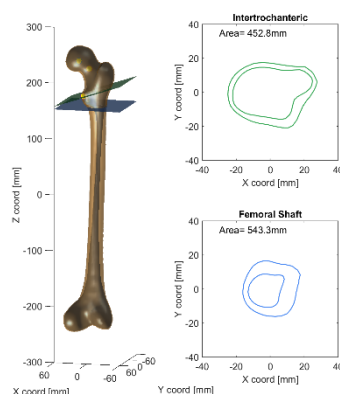
Figure E1 Geometry of VPMs (continued)



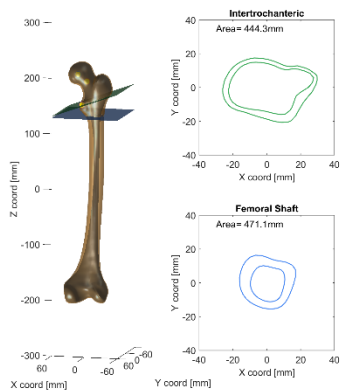
VPM#81 (M50)



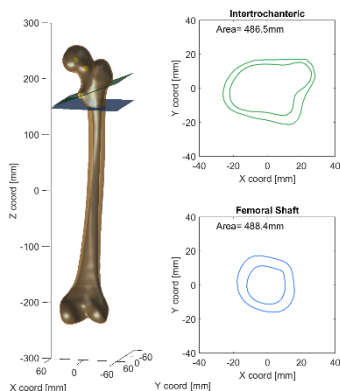
VPM#82 (M50)



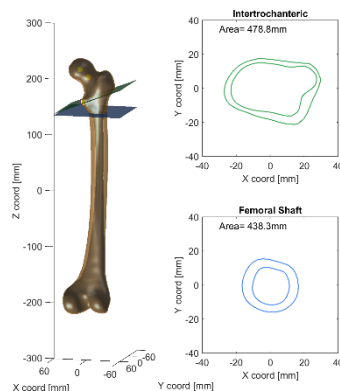
VPM#83 (M50)



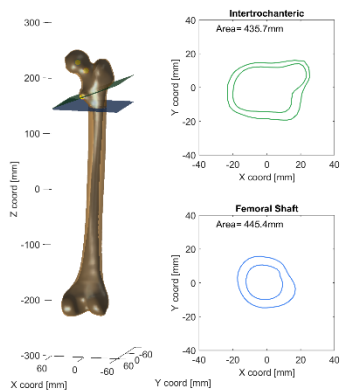
VPM#84 (M50)



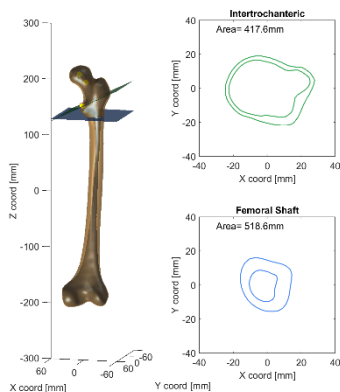
VPM#85 (M50)



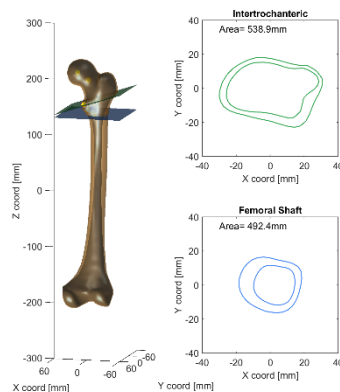
VPM#86 (M50)



VPM#87 (M50)

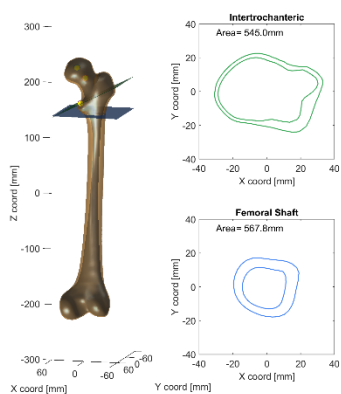


VPM#88 (M50)

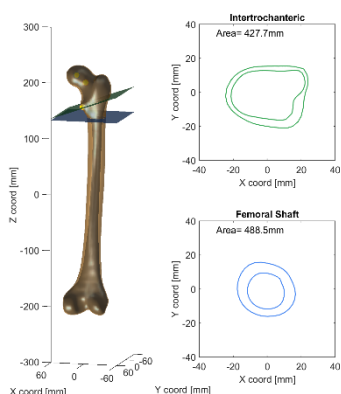


VPM#89 (M50)

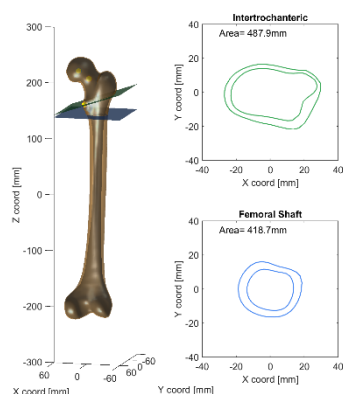
Figure E1 Geometry of VPMs (continued)



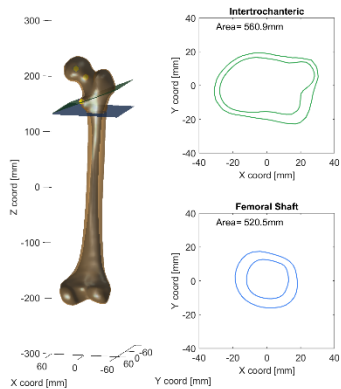
VPM#90 (M50)



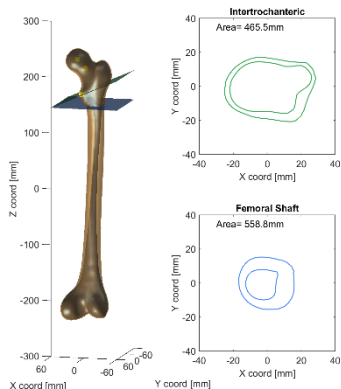
VPM#91 (M50)



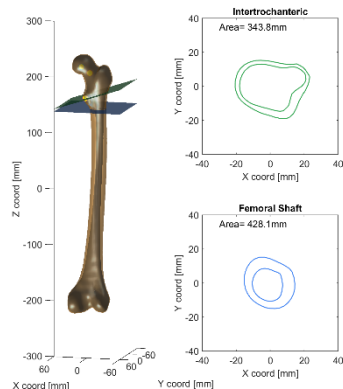
VPM#92 (M50)



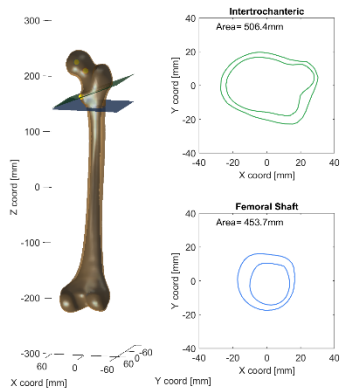
VPM#93 (M50)



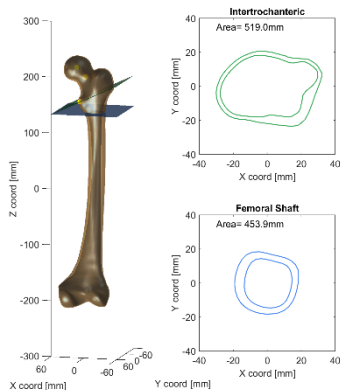
VPM#94 (M50)



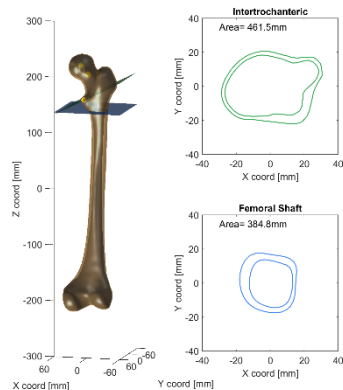
VPM#95 (M50)



VPM#96 (M50)

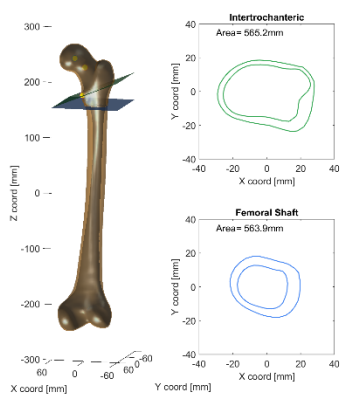


VPM#97 (M50)

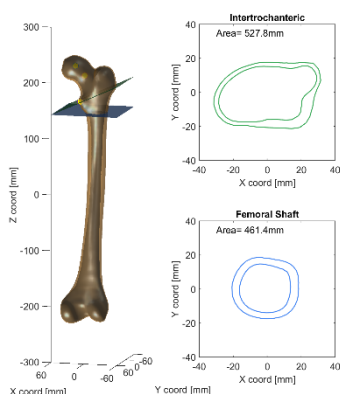


VPM#98 (M50)

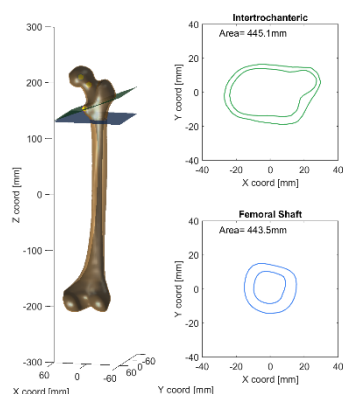
Figure E1 Geometry of VPMs (continued)



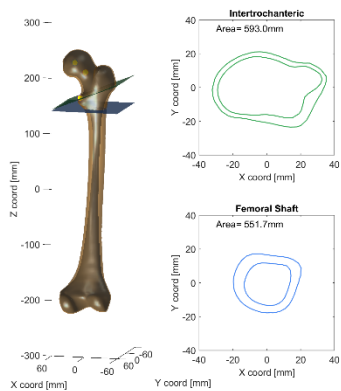
VPM#99 (M50)



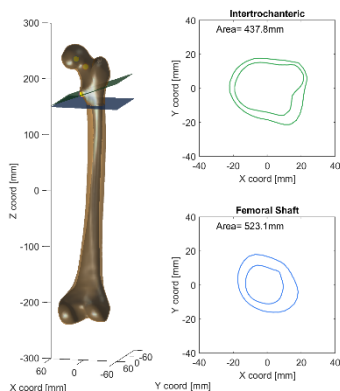
VPM#100 (M50)



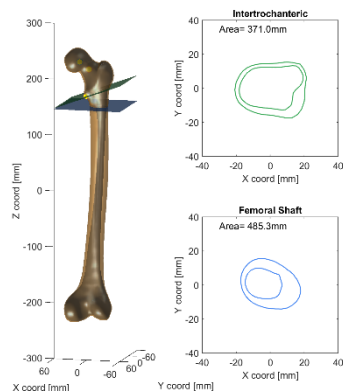
VPM#1 (M95)



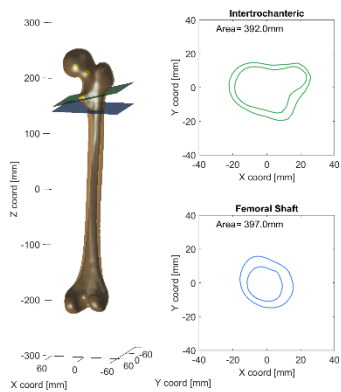
VPM#2 (M95)



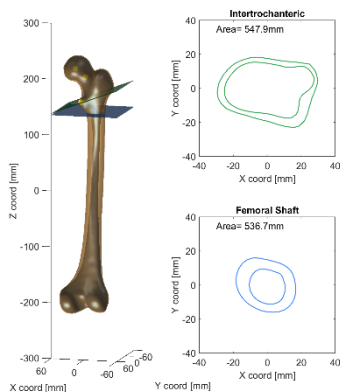
VPM#3 (M95)



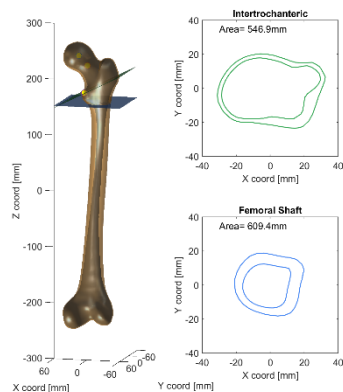
VPM#4 (M95)



VPM#5 (M95)

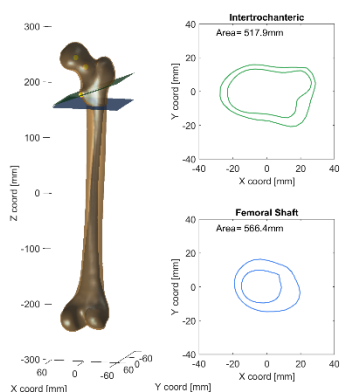


VPM#6 (M95)

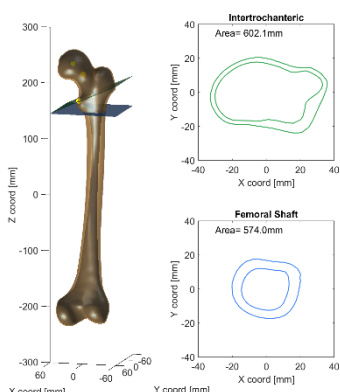


VPM#7 (M95)

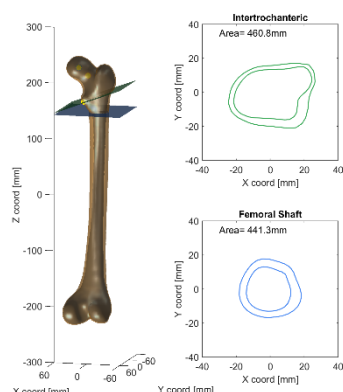
Figure E1 Geometry of VPMs (continued)



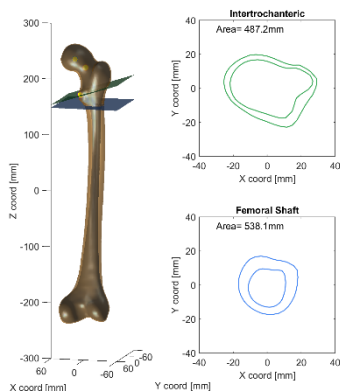
VPM#8 (M95)



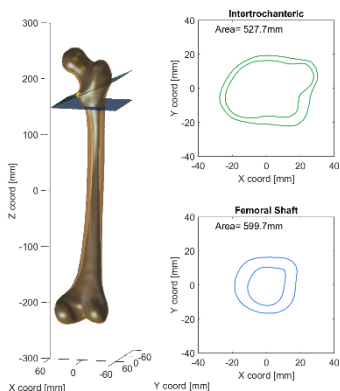
VPM#9 (M95)



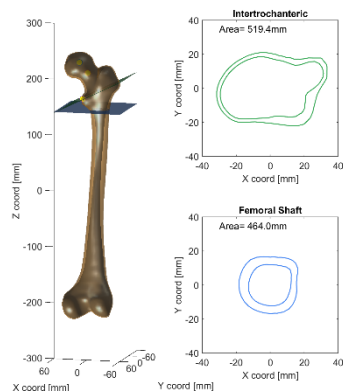
VPM#10 (M95)



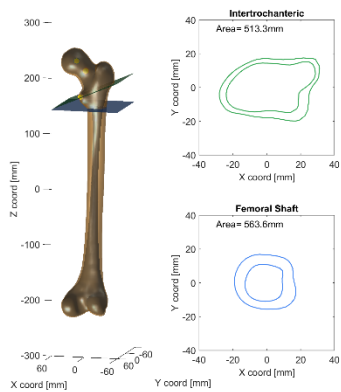
VPM#11 (M95)



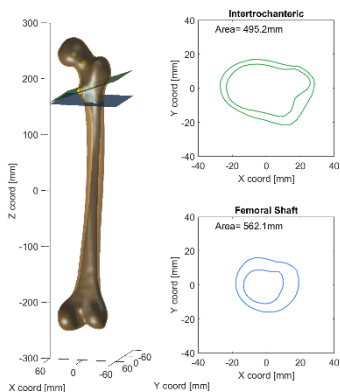
VPM#12 (M95)



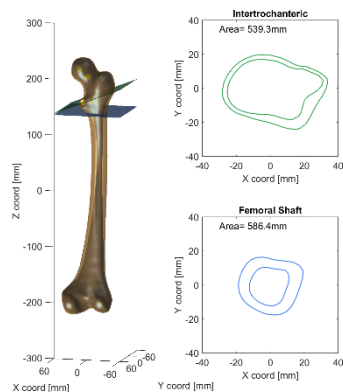
VPM#13 (M95)



VPM#14 (M95)

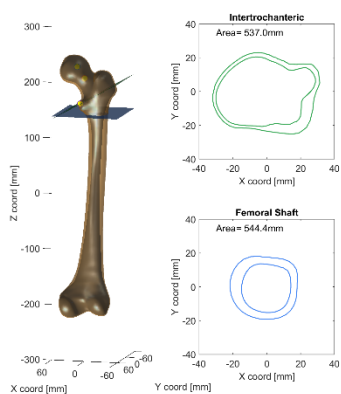


VPM#15 (M95)

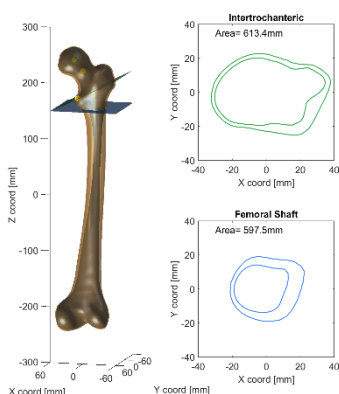


VPM#16 (M95)

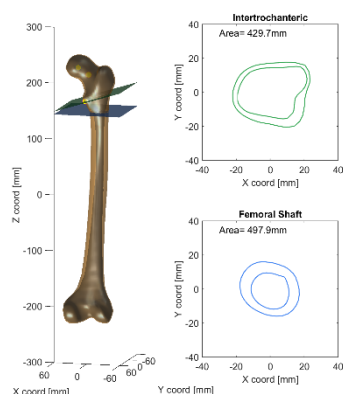
Figure E1 Geometry of VPMs (continued)



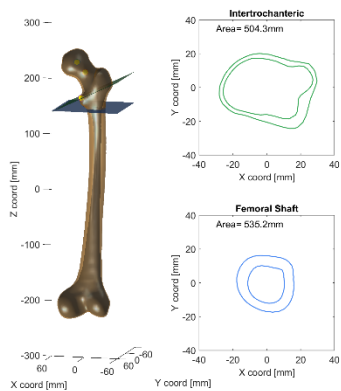
VPM#17 (M95)



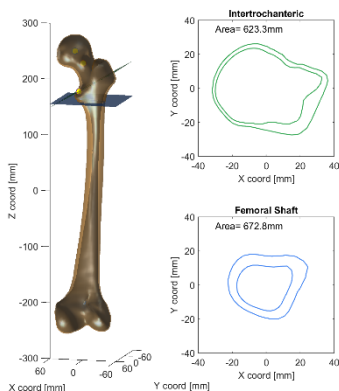
VPM#18 (M95)



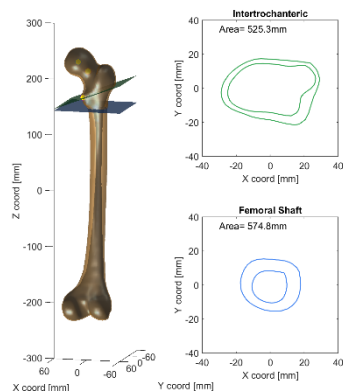
VPM#19 (M95)



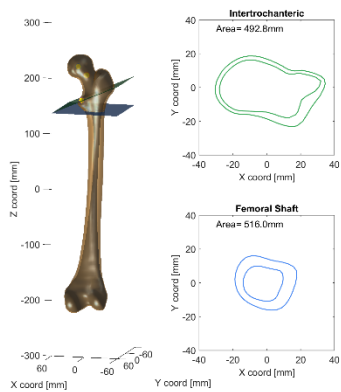
VPM#20 (M95)



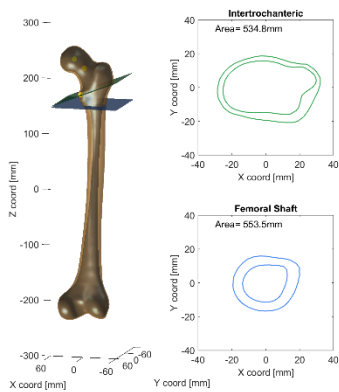
VPM#21 (M95)



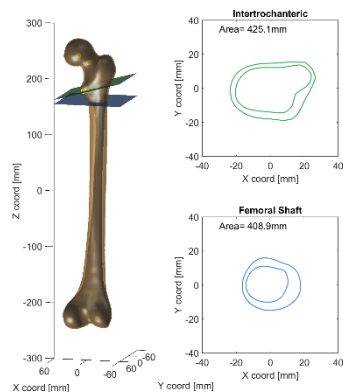
VPM#22 (M95)



VPM#23 (M95)

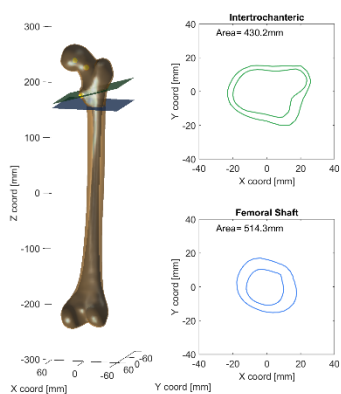


VPM#24 (M95)

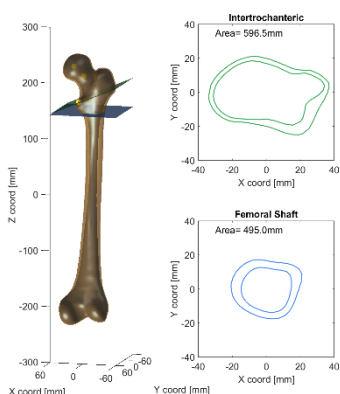


VPM#25 (M95)

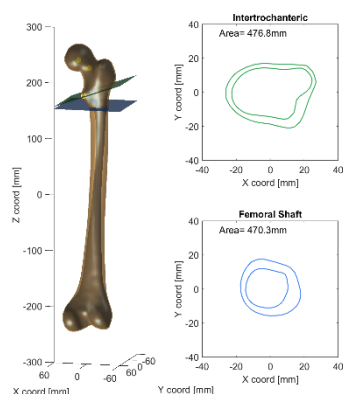
Figure E1 Geometry of VPMs (continued)



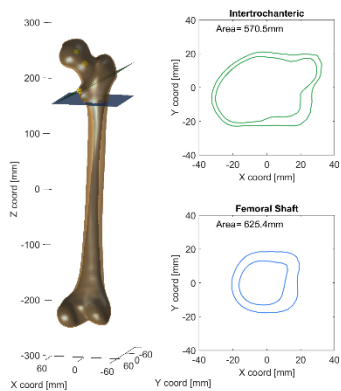
VPM#26 (M95)



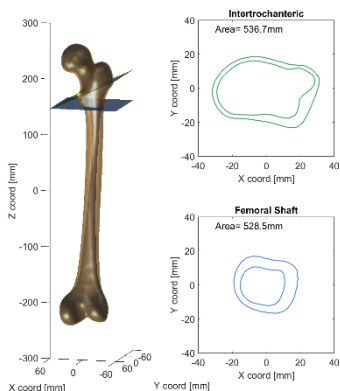
VPM#27 (M95)



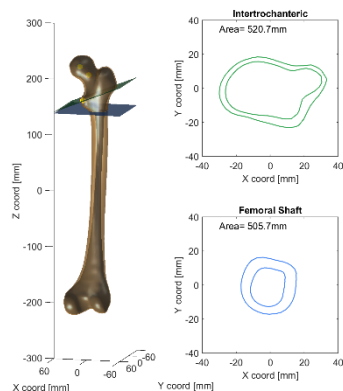
VPM#28 (M95)



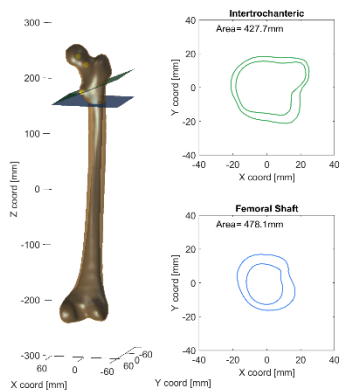
VPM#29 (M95)



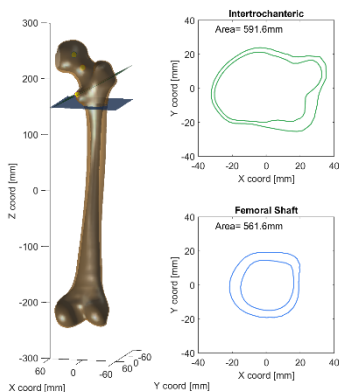
VPM#30 (M95)



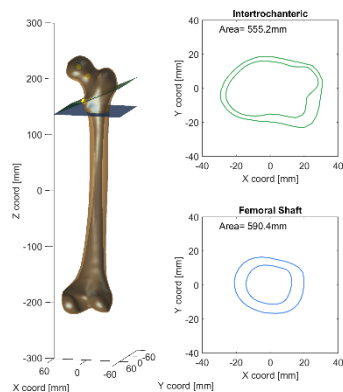
VPM#31 (M95)



VPM#32 (M95)

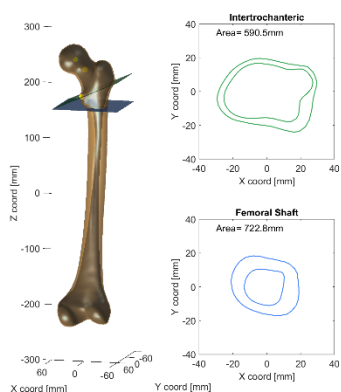


VPM#33 (M95)

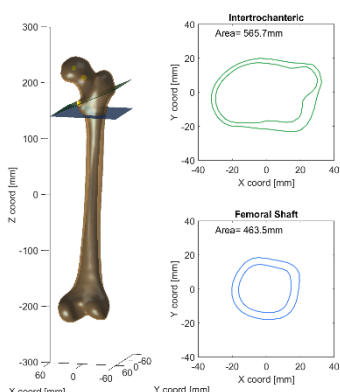


VPM#34 (M95)

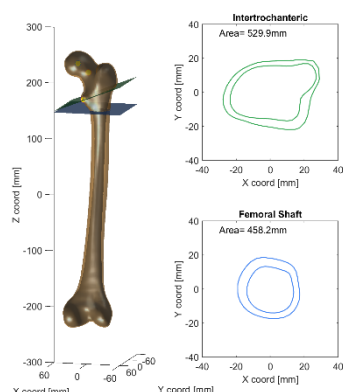
Figure E1 Geometry of VPMs (continued)



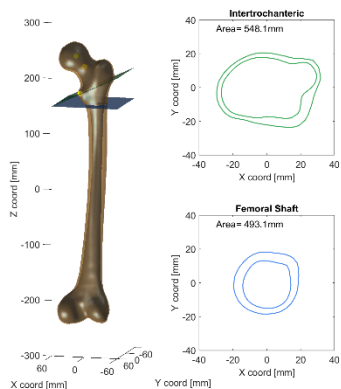
VPM#35 (M95)



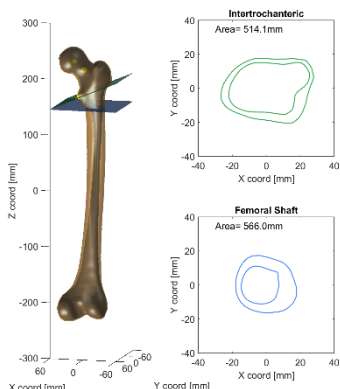
VPM#36 (M95)



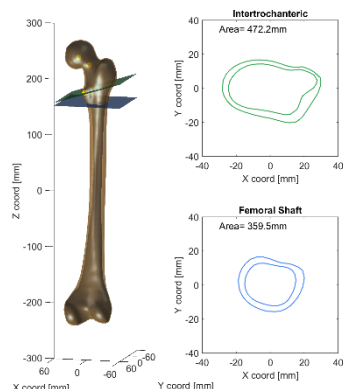
VPM#37 (M95)



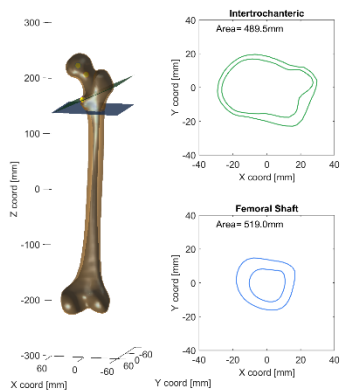
VPM#38 (M95)



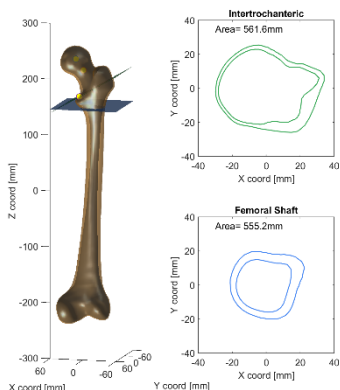
VPM#39 (M95)



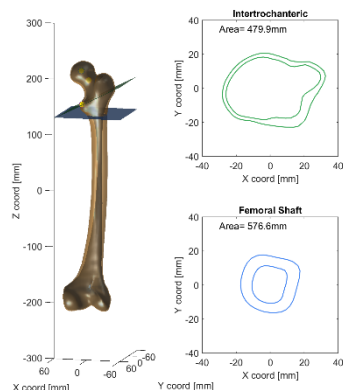
VPM#40 (M95)



VPM#41 (M95)

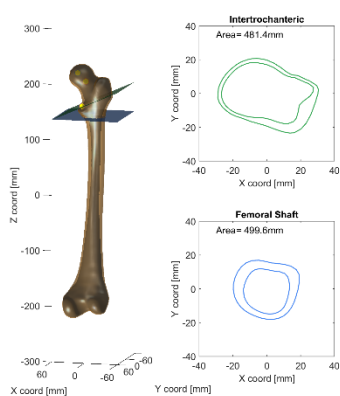


VPM#42 (M95)

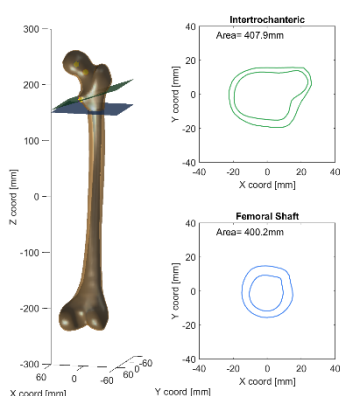


VPM#43 (M95)

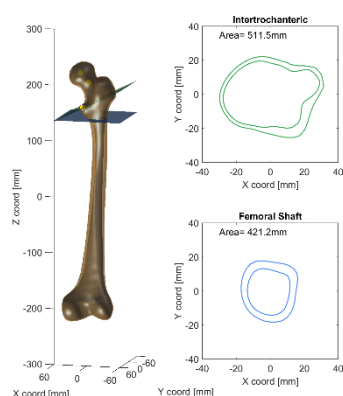
Figure E1 Geometry of VPMs (continued)



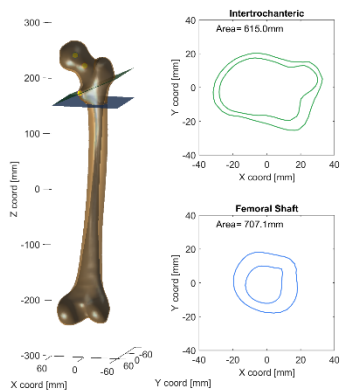
VPM#44 (M95)



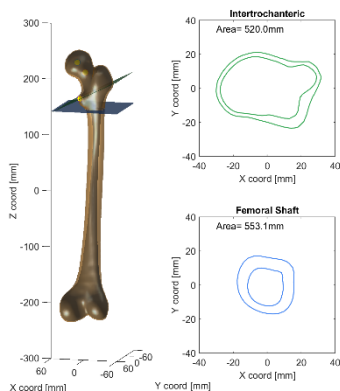
VPM#45 (M95)



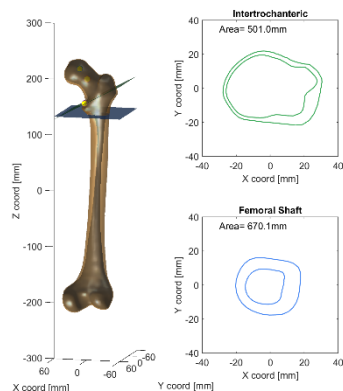
VPM#46 (M95)



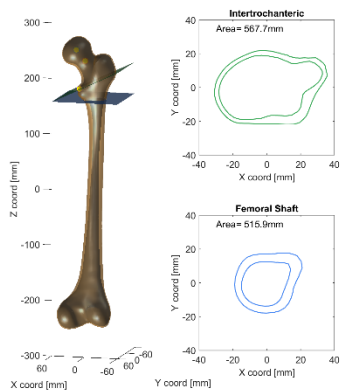
VPM#47 (M95)



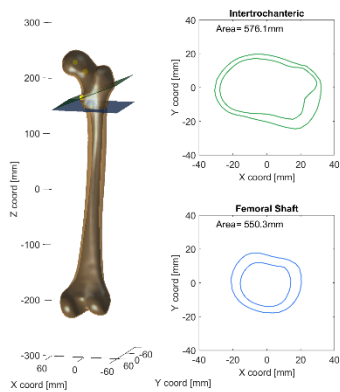
VPM#48 (M95)



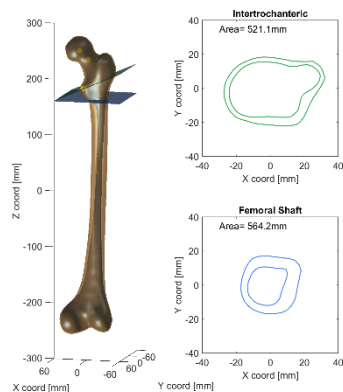
VPM#49 (M95)



VPM#50 (M95)

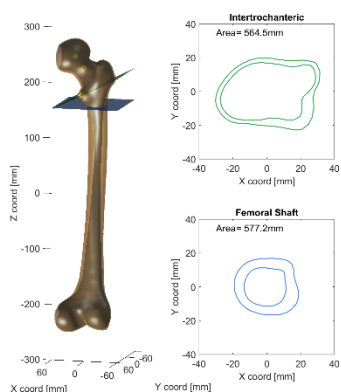


VPM#51 (M95)

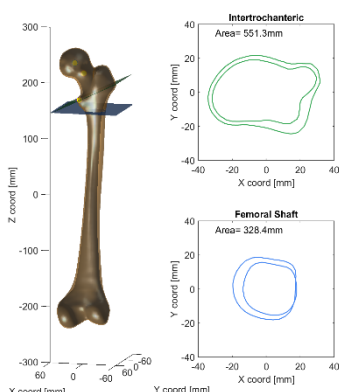


VPM#52 (M95)

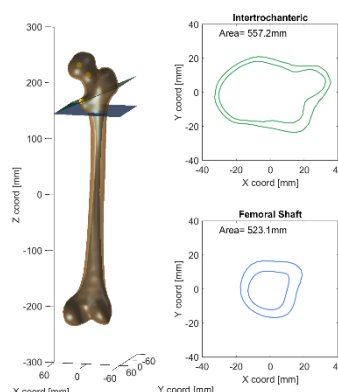
Figure E1 Geometry of VPMs (continued)



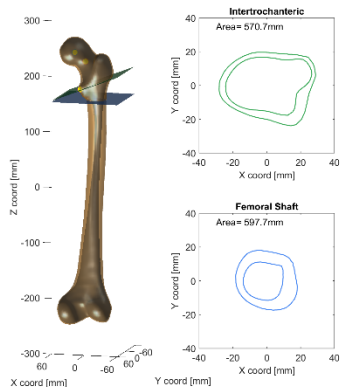
VPM#53 (M95)



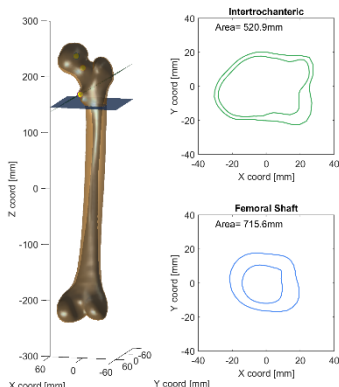
VPM#54 (M95)



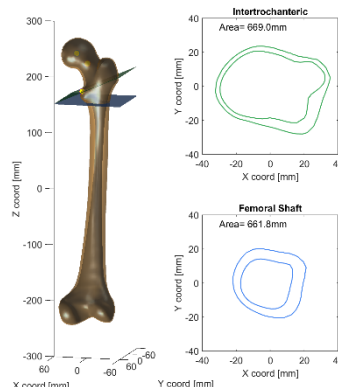
VPM#55 (M95)



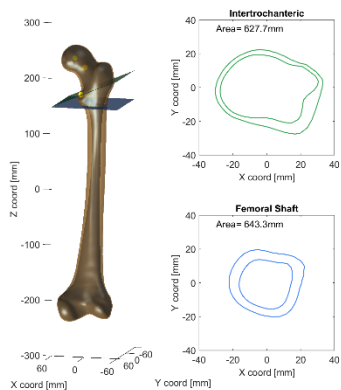
VPM#56 (M95)



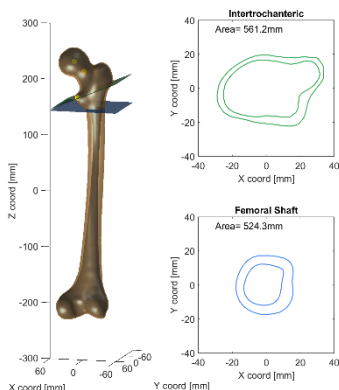
VPM#57 (M95)



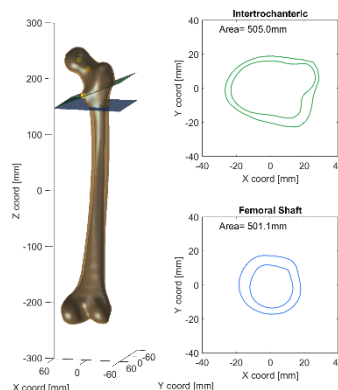
VPM#58 (M95)



VPM#59 (M95)

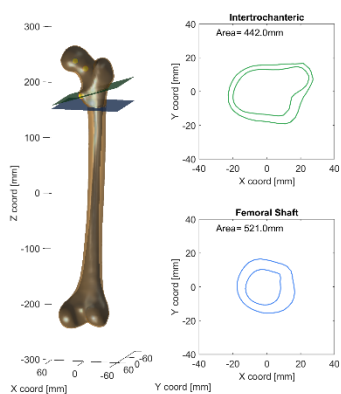


VPM#60 (M95)

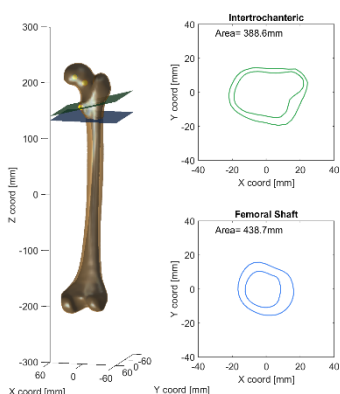


VPM#61 (M95)

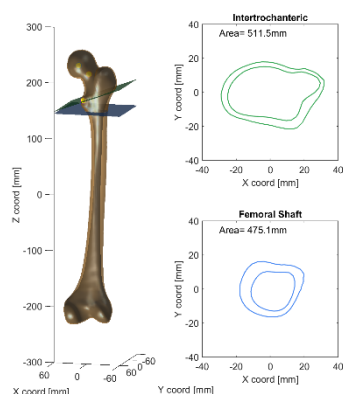
Figure E1 Geometry of VPMs (continued)



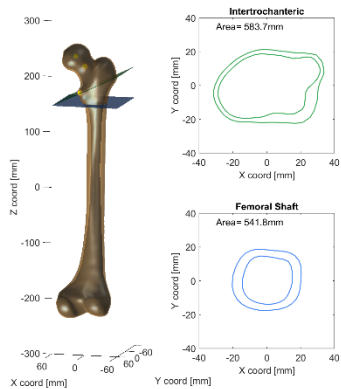
VPM#62 (M95)



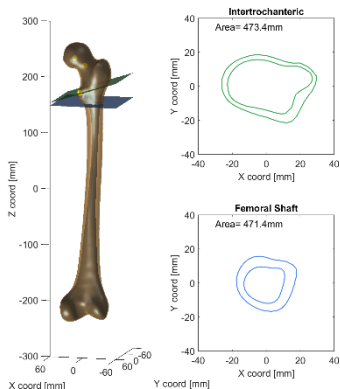
VPM#63 (M95)



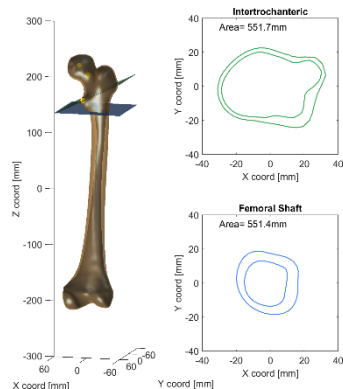
VPM#64 (M95)



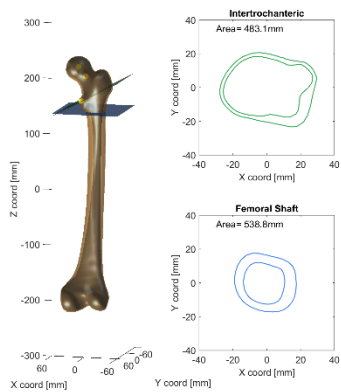
VPM#65 (M95)



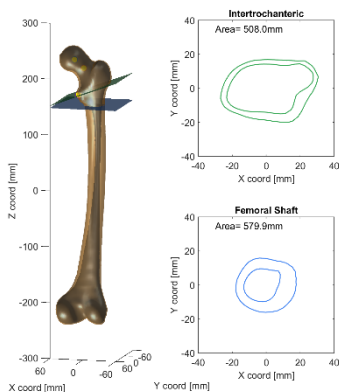
VPM#66 (M95)



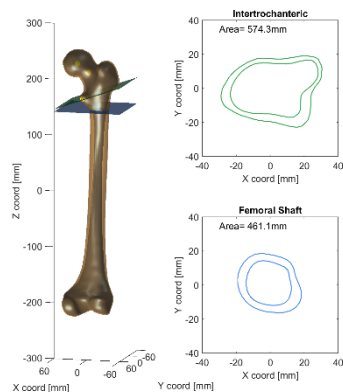
VPM#67 (M95)



VPM#68 (M95)

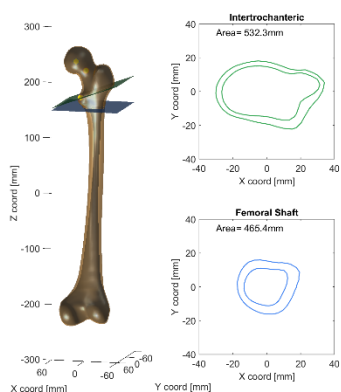


VPM#69 (M95)

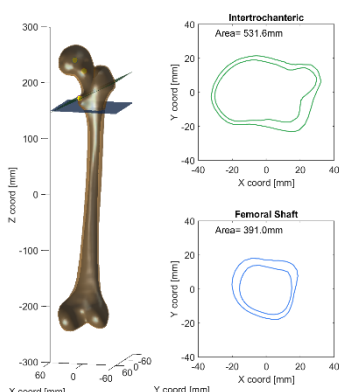


VPM#70 (M95)

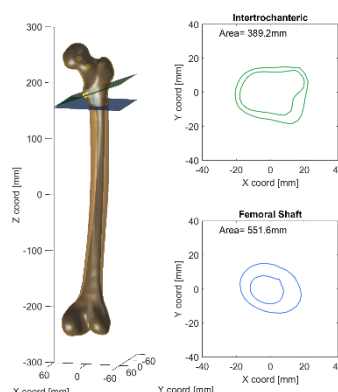
Figure E1 Geometry of VPMs (continued)



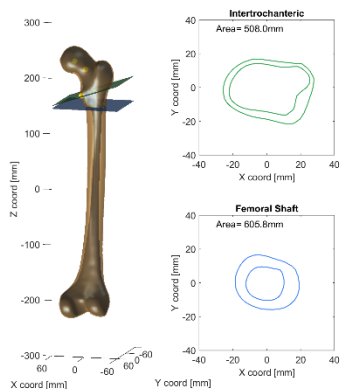
VPM#71 (M95)



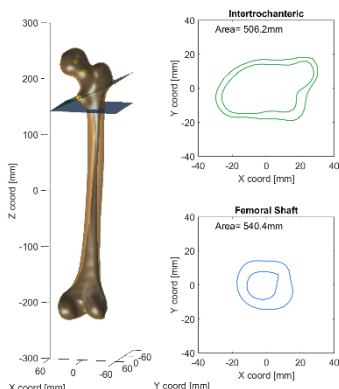
VPM#72 (M95)



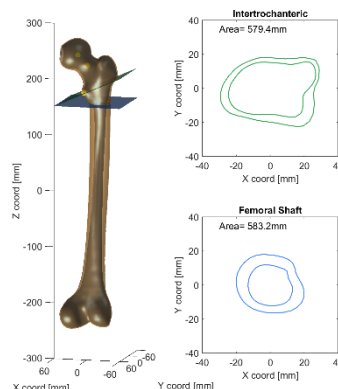
VPM#73 (M95)



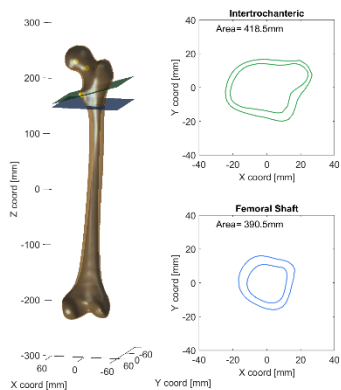
VPM#74 (M95)



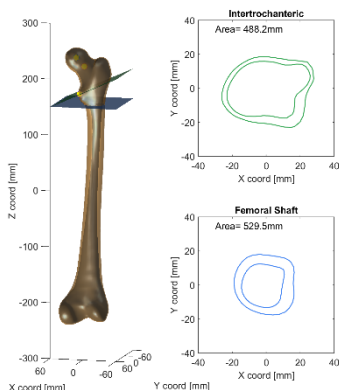
VPM#75 (M95)



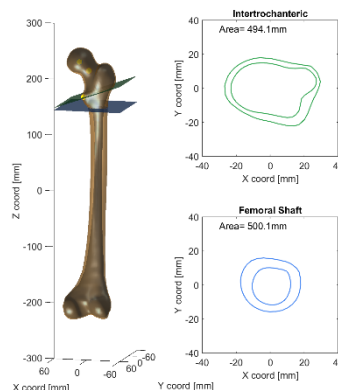
VPM#76 (M95)



VPM#77 (M95)

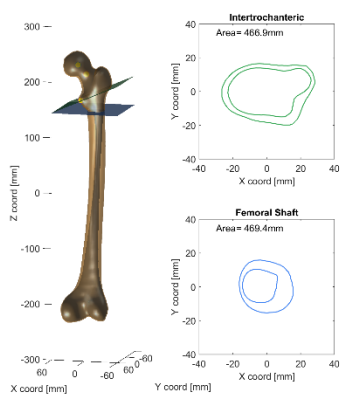


VPM#78 (M95)

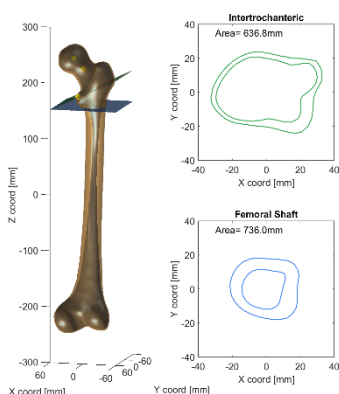


VPM#79 (M95)

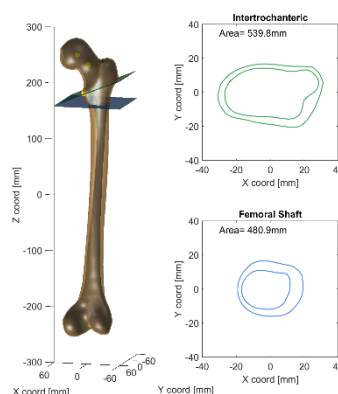
Figure E1 Geometry of VPMs (continued)



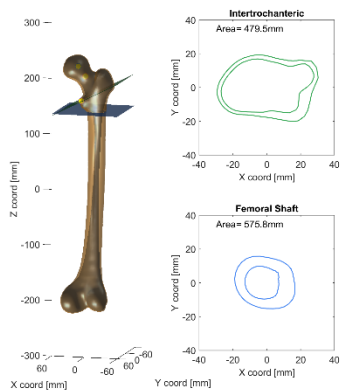
VPM#80 (M95)



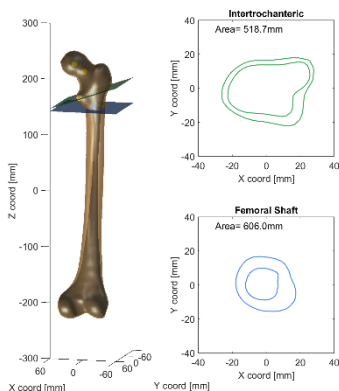
VPM#81 (M95)



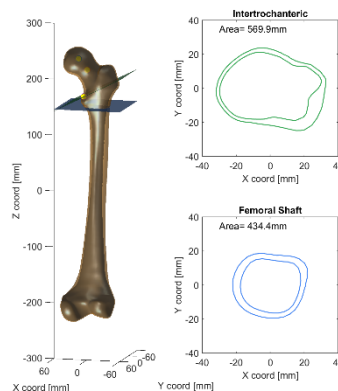
VPM#82 (M95)



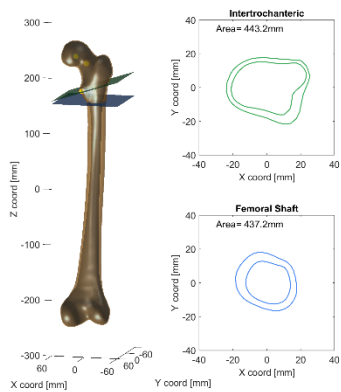
VPM#83 (M95)



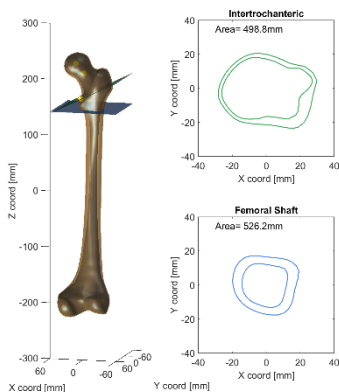
VPM#84 (M95)



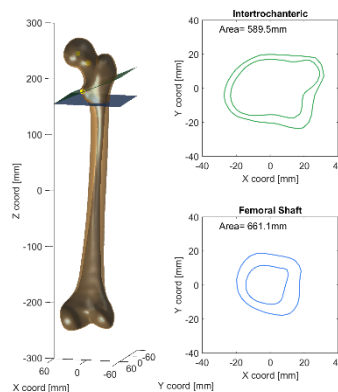
VPM#85 (M95)



VPM#86 (M95)

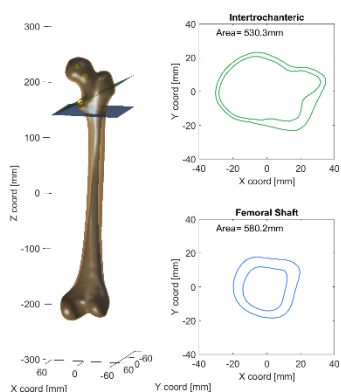


VPM#87 (M95)

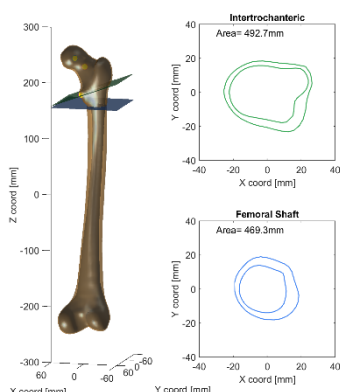


VPM#88 (M95)

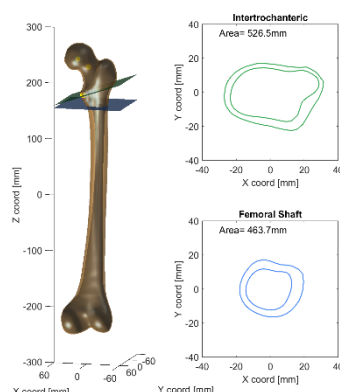
Figure E1 Geometry of VPMs (continued)



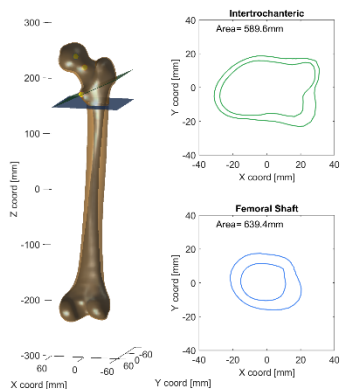
VPM#89 (M95)



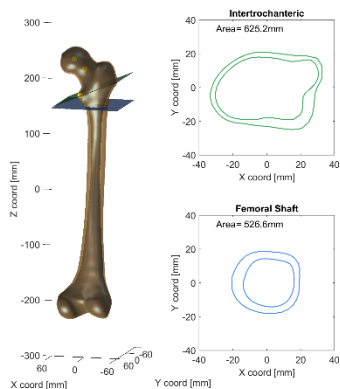
VPM#90 (M95)



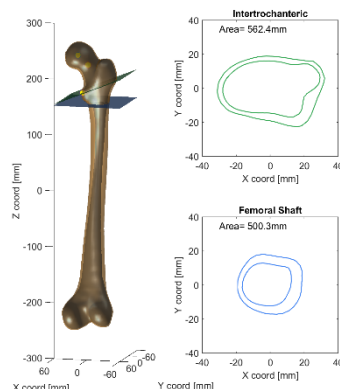
VPM#91 (M95)



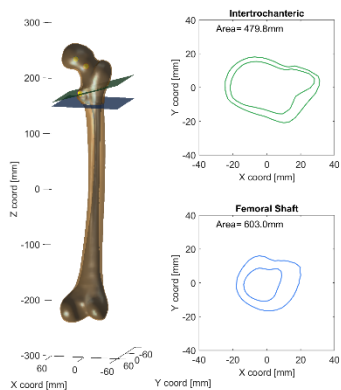
VPM#92 (M95)



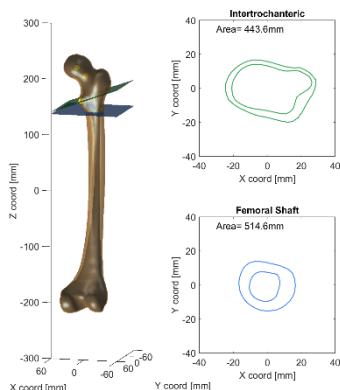
VPM#93 (M95)



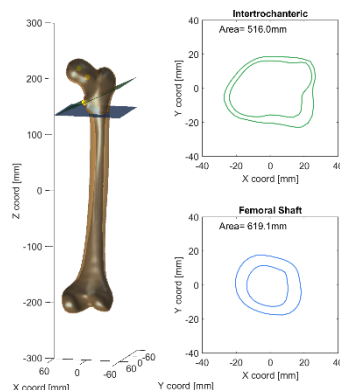
VPM#94 (M95)



VPM#95 (M95)



VPM#96 (M95)



VPM#97 (M95)

Figure E1 Geometry of VPMs (continued)

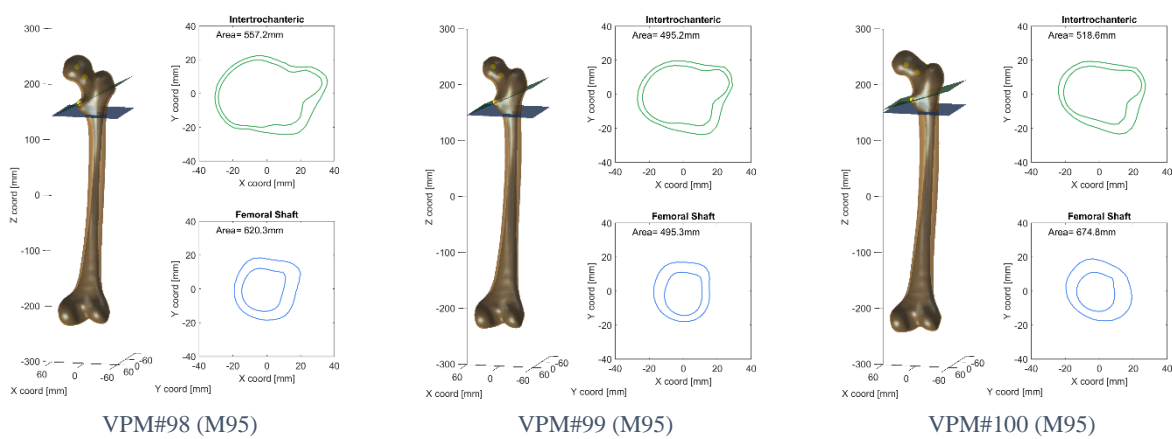


Figure E1 Geometry of VPMs (continued)

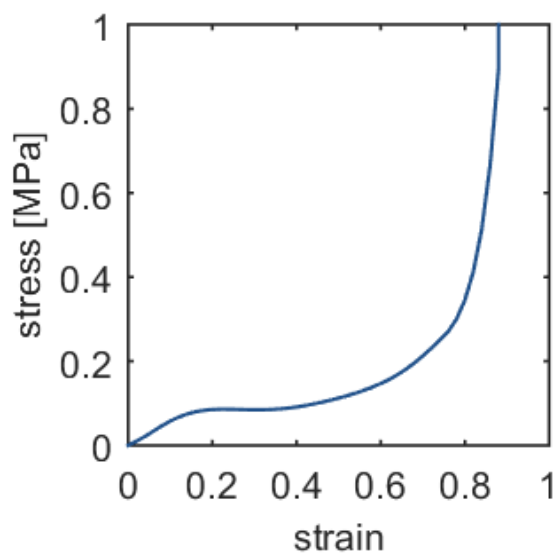
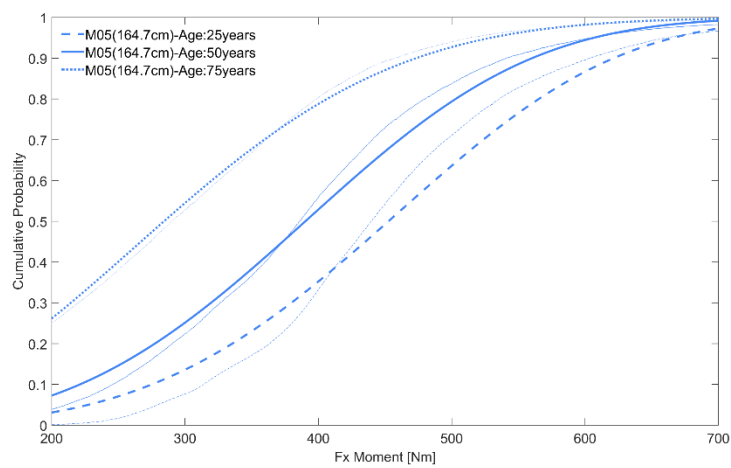
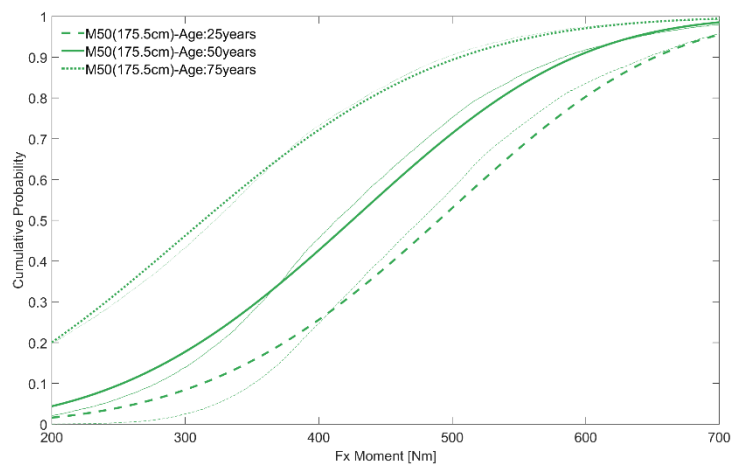


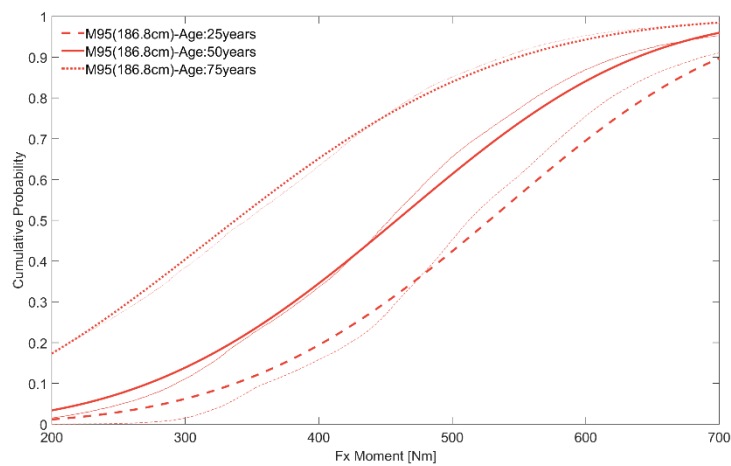
Figure E2 Stress-strain curve for the foam material



(a) M05



(b) M50



(c) M95

Figure E3 IRF for bending with Weibull distribution

APPENDIX F: CRASH DATABASE

Table F1 NHTSA Crash Database

#	Test #	Vehicle		V [kph]	Overlap [%]	Ang [deg]	Side	Dummy
		Model	year					
1	7851	Chevrolet Cruze	2011	90.1	35	15	L	THOR M50
2	7852	Chevrolet Cruze	2011	90.1	35	15	L	THOR M50
3	8089	Hyundai Elantra	2013	90.1	35	15	L	THOR M50
4	8475	Volvo Xc60	2013	90.1	35	15	L	THOR M50
5	8476	Dodge Dart	2013	90.1	35	15	L	THOR M50
6	8477	Honda Civic	2013	90.1	35	15	L	THOR M50
7	8478	Subaru Forester	2014	90.1	35	15	L	THOR M50
8	8488	Volvo S60 Four Door Sedan	2012	90.1	35	15	L	THOR M50
9	8787	Mazda 3	2014	90.1	35	15	L	THOR M50
10	8788	Mazda Cx-5	2014	90.1	35	15	L	THOR M50
11	8789	Honda Accord	2014	90.1	35	15	L	THOR M50
12	8790	Toyota Camry	2014	90.1	35	15	L	THOR M50
13	8791	Honda Odyssey	2014	90.1	35	15	L	THOR M50
14	8998	Mazda Cx-5	2014	90.1	35	15	R	THOR M50
15	8999	Mazda 3	2014	90.1	35	15	R	THOR M50
16	9042	Honda Accord	2014	90.1	35	15	R	THOR M50
17	9043	Honda Fit	2015	90.1	35	15	L	THOR M50
18	9110	Nissan Versa	2013	90.1	35	15	R	THOR M50
19	9121	Toyota Camry	2012	90.1	35	15	R	THOR M50
20	9122	Nissan Versa	2013	90.1	35	15	L	THOR M50
21	9124	Toyota Camry	2012	90.1	35	15	L	THOR M50
22	9125	Ford Taurus	2013	90.1	35	15	L	THOR M50
23	9126	Honda Cr-V	2012	90.1	35	15	L	THOR M50
24	9127	Honda Odyssey	2012	90.1	35	15	L	THOR M50
25	9135	Research Vehicle 8572		90.1	35	15	L	THOR M50
26	9137	Research Vehicle 3A		90.1	35	15	L	THOR M50
27	9138	Research Vehicle 3B		90.1	35	15	L	THOR M50
28	9139	Research Vehicle Cal2661		90.1	35	15	L	THOR M50
29	9140	Research Vehicle 25002		90.1	35	15	L	THOR M50
30	9141	Research Vehicle 25000		90.1	35	15	L	HIII
31	9142	Research Vehicle 9293		90.1	35	15	L	THOR M50
32	9143	Research Vehicle 3100		90.1	35	15	L	THOR M50
33	9144	Research Vehicle 0028		90.1	35	15	L	THOR M50

Table F1 NHTSA Crash Database (continued)

#	Test #	Vehicle		V [kph]	Overlap [%]	Ang [deg]	Side	Dummy
		Model	year					
34	9145	Research Vehicle 4969		90.1	35	15	L	THOR M50
35	9146	Research Vehicle 1236		90.1	35	15	L	THOR M50
36	9147	Research Vehicle Cal2674		90.1	35	15	L	THOR M50
37	9148	Research Vehicle 8200		90.1	35	15	L	THOR M50
38	9149	Research Vehicle Cal2676		90.1	20	7	L	THOR M50
39	9150	Research Vehicle 2677		90.1	35	15	L	THOR M50
40	9151	Research Vehicle 2678		90.1	35	15	L	THOR M50
41	9152	Research Vehicle 2712s		90.1	35	15	L	THOR M50
42	9153	Research Vehicle 3698		90.1	35	15	L	THOR M50
43	9154	Research Vehicle 0304		90.1	35	15	L	THOR M50
44	9155	Research Vehicle 0306		90.1	35	15	L	THOR M50
45	9200	Ford Taurus	2007	90.1	35	15	L	THOR M50
46	9201	Ford Taurus	2007	97.2	18	7	L	THOR M50
47	9202	Toyota Yaris	2010	90.1	35	15	L	THOR M50
48	9203	Toyota Yaris	2010	86.7	20.6	7	L	THOR M50
49	9204	Ford 500	2007	90.1	35	15	L	THOR M50
50	9205	Ford Fusion	2010	90.1	20	7	L	THOR M50
51	9210	Ford Fiesta	2011	90.1	20	7	L	THOR M50
52	9211	Ford Fiesta	2011	90.1	35	15	L	THOR M50
53	9212	Toyota Yaris	2011	90.1	35	15	L	THOR M50
54	9219	Chevrolet Cruze	2011	90.1	20	7	L	THOR M50
55	9220	Chevrolet Cruze	2011	90.1	20	7	L	THOR M50
56	9221	Volvo S60	2012	90.1	20	7	L	THOR M50
57	9222	Fiat 500	2012	90.1	20	7	L	THOR M50
58	9223	Research Vehicle 1A		90.1	35	15	L	THOR M50
59	9226	Small SUV-Research		90.1	20	7	L	THOR M50
60	9228	Honda Accord	2013	90.1	35	15	L	THOR M50
61	9229	Research Vehicle 2175		90.1	35	15	L	THOR M50
62	9354	Subaru Forester	2015	90.1	35	15	R	THOR M50
63	9476	Chevrolet Malibu	2015	90.1	35	15	L	THOR M50
64	9477	Chevrolet Malibu	2015	90.1	35	15	R	THOR M50
65	9478	Ford F-150	2015	90.1	35	15	R	THOR M50
66	9479	Ford F-150	2015	90.1	35	15	L	THOR M50
67	9480	Toyota Highlander	2015	90.1	35	15	R	THOR M50
68	9481	Toyota Highlander	2015	90.1	35	15	L	THOR M50
69	9482	Honda Fit	2015	90.1	35	15	R	THOR M50
70	9483	Volvo S60	2015	90.1	35	15	R	THOR M50
71	9574	Nissan Rogue	2016	90.1	35	15	L	THOR M50

Table F1 NHTSA Crash Database (continued)

#	Test #	Vehicle		V [kph]	Overlap [%]	Ang [deg]	Side	Dummy
		Model	year					
72	9585	Toyota Sienna	2015	90.1	35	15	L	THOR M50
73	9586	Chevrolet Tahoe	2016	90.1	35	15	L	THOR M50
74	9587	Ford F-150	2016	90.1	35	15	L	THOR M50
5	9727	Chevrolet Malibu	2015	90.1	35	15	R	THOR M50

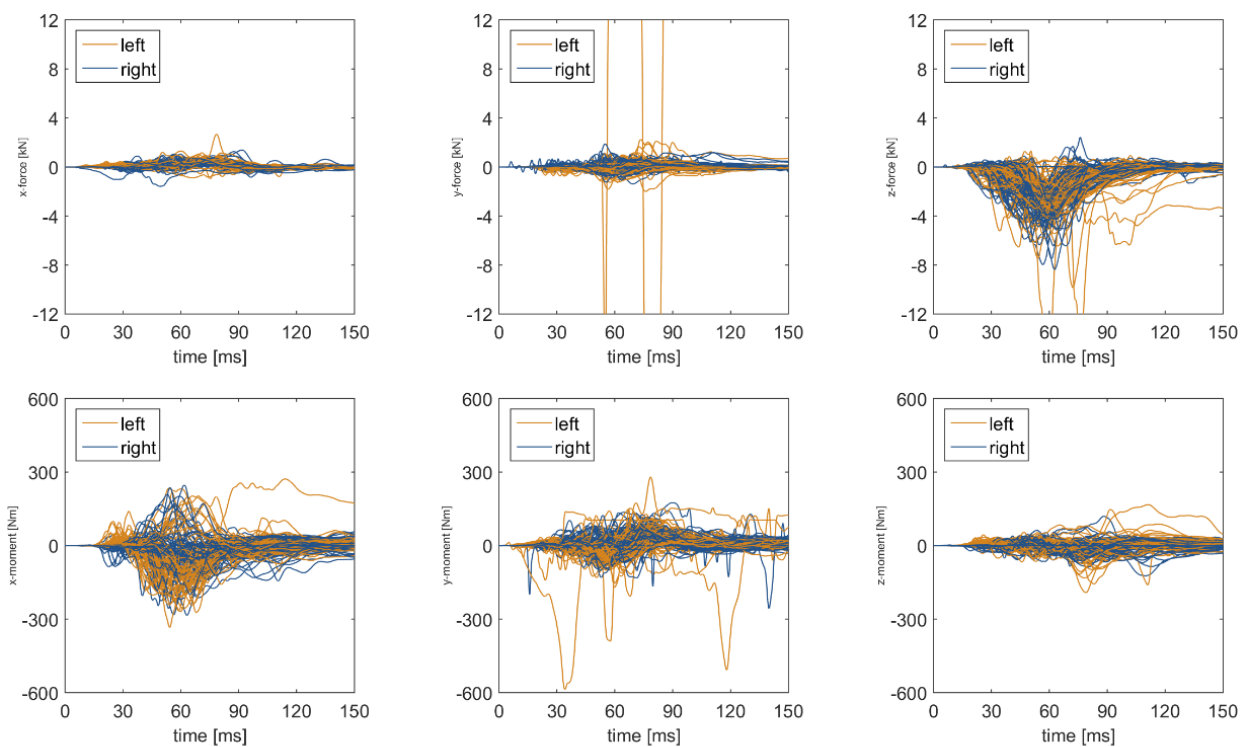


Figure F1 Time histories from Crash Database